Characterization of gas-liquid hydrodynamics and mass transfer in SMX static mixers

Marco Scala

UNIVERSITÉ DE LORRAINE

THÈSE de DOCTORAT DE L'UNIVERSITÉ DE LORRAINE

Opérée au sein de :

Laboratoire Réactions et Génie des Procédés

Ecole Doctorale SIMPPÉ
Numéro d'accréditation 608

Spécialité de doctorat : Génie des Procédés et des Produits et des Molécules
Discipline : Génie des Procédés

Soutenue publiquement le 06/12/2019, par :

Marco SCALA

Characterization of gas-liquid hydrodynamics and mass transfer in SMX static mixers

Devant le jury composé de :

Serge SIMOËNS Professeur, École Centrale de Lyon	**Président**
Daniele MARCHISIO Professeur, École Polytechnique de Turin	**Rapporteur**
Joëlle AUBIN Professeur, École nationale supérieure Toulouse	**Rapporteur**
Mounir BOUAIFI Ingénieur procédés, Solvay	**Examinateur**
Huai-Zhi LI Professeur, Université de Lorraine	**Directeur de thèse**
Lionel GAMET Ingénieur de recherche, IFP Energies nouvelles	**Co-Directeur de thèse**
Louis-Marie MALBEC Ingénieur de recherche, IFP Energies nouvelles	**Co-Directeur de thèse**

Abstract

Keywords : *Multiphase Hydrodynamics, Sulzer static mixer SMX^{TM}, Process intensification, CFD simulations, Particle Image Velocimetry (HF-PIV), Mass transfer.*

The mixing of two or more fluids is a rather common operation in all industrial processes. The main target of the mixing is to increase the interface area between phases in order to improve mass and heat transfer and facilitate then chemical reaction. Among the multiphase mixing stands out the gas liquid dispersion.

The aim of the present work is to examine a specific type of mixers, namely the static mixer. Static mixers are located into a housing or pipeline to ensure a high blending of fluids. They are usually made by a series of inserts, in turn designed by holes, helical elements and oblique blades. These elements cause local accelerations and stretching of the fluid currents to reach a high mixing efficiency.

The wide applications of static mixers in numerous industrial processes require better knowledge of the hydrodynamics in these devices. The gas-liquid flow pattern through a Sulzer static mixer SMX^{TM} mounted in a vertical cylindrical tube was investigated in this study. The main goal was to assess the performance of the Sulzer static mixer SMX^{TM} for gas-liquid applications in industrial processes.

Experimental data were collected from two main optical techniques, Backlight Shadowgraph Technique (BST) and Particle Image Velocimetry (PIV). 3D-printed static mixers were manufactured using transparent plastic in order to provide optical access.

Three different liquids were used as the continuous phase, namely water, water with SDS and normal-heptane. The liquid phase was kept stagnant during the experiments. Five different lengths of mixers (with 1, 2, 5, 10 and 15 elements respectively) and several gaseous nitrogen flow rates from 1 to 10 l/h were analysed.

The behaviour of the simple tube without mixing device, acting like a bubble column, was investigated as a reference, , for comparison purposes with the SMX^{TM}. Bubble diameter distributions at the inlet and outlet of the SMX mixers were evaluated. The velocity fields inside the mixers were quantified. The gas hold-up was also measured.

The oxygen transfer performance in the SMX static mixer in air/water mixture was assessed by measuring the overall oxygen transferred. The mass transfer coefficient to the interfacial area k_La was determined and proved to be larger in the mixer.

Experiments with liquid circulation, both counter-current and co-current, were carried out to verify the impact on the flow pattern. The outcomes highlighted no relevant difference when the liquid flows in a laminar flow regime, corresponding to Reynold numbers lower than 15.

Volume-of-fluid numerical simulations of the mixer were performed with OpenFOAM®. These 3D simulations were mainly focused on the behaviour of the SMX in an organic system at low gas flow rate (1 l/h).

A home-made `functionObject`, called `bubbleTracker`, was implemented in the OpenFOAM® framework. This tool allowed us to collect the bubbles properties. Shapes, sizes, paths and velocities of the bubbles were examined to validate the numerical model.

The numerical simulations were satisfactorily validated by experimental results. The comparison and the combination of the numerical and experimental results bring new insight into the flow pattern in a SMX™ static mixer.

Résumé

Mots clés : *Hydrodynamique multiphasique, Mélangeur statique Sulzer SMX^{TM}, Intensification des procédés, Simulations CFD, Vélocimétrie par images de particules (HF-PIV), Transfert de matière.*

Le mélange de deux ou plusieurs fluides est une opération courante dans tous les procèdes industriels. L'objectif principal du mélange est d'augmenter l'aire interfaciale entre les phases afin d'améliorer le transfert de masse et de chaleur et de faciliter ensuite les réactions chimiques. Parmi les mélanges multiphasiques, on retrouve la dispersion gaz-liquide.

L'objectif de cette thèse est d'examiner un type spécifique de mélangeurs : le mélangeur statique. Un mélangeur statique est un dispositif, placé dans une conduite afin d'assurer un mélange de fluides sans partie mobile. Ils sont généralement constitués d'une série d'éléments qui provoquent des accélérations locales et l'étirement des courants de fluide pour atteindre un mélange souhaité.

Les vastes applications des mélangeurs statiques dans de nombreux procèdes industriels nécessitent une meilleure connaissance de l'hydrodynamique de ces appareils. L'hydrodynamique de l'écoulement gaz-liquide à travers un mélangeur statique Sulzer SMX$^{\text{TM}}$ dans une conduite cylindrique verticale été étudiée. L'objectif principal du présent travail était d'évaluer la performance du mélangeur statique Sulzer SMX$^{\text{TM}}$ dans les procèdes industriels pour les applications gaz-liquide.

Les données ont été recueillies principalement à l'aide de deux techniques optiques, soit la technique Backlight Shadowgraph Technique (BST) et la vélocimétrie par image de particules (PIV). Des mélangeurs statiques imprimés en 3D ont été fabriqués en plastique transparente afin de faciliter la visualisation optique.

Trois différents liquides ont été utilisés comme phase continue : l'eau, l'eau avec SDS et l'heptane. La phase liquide est restée stagnante pendant les expériences. Cinq différentes longueurs de mélangeurs (avec 1, 2, 5, 10 et 15 éléments) et plusieurs débits d'azote gazeux de 1 à 10 l/h ont été analysés.

Le comportement d'un tube vide, agissant comme une colonne à bulles, a été étudié comme référence de comparaison. La distribution des diamètres des bulles à l'entrée et à la sortie des mélangeurs SMX a été évaluée. Les champs de vitesse à l'intérieur des mélangeurs ont été quantifiés. La rétention du gaz a également été examiné.

L'efficacité de transfert d'oxygène dans un mélangeur statique SMX a été évaluée en

mesurant l'oxygène global transféré. Le coefficient de transfert de masse vers la zone interfaciale $k_L a$ a été déterminé et s'est avéré être plus élevé dans le mélangeur.

Des expériences avec circulation de liquide tant à contre-courant qu'à co-courant ont été réalisées pour vérifier son effet sur l'hydrodynamique. Les résultats n'ont mis en évidence aucune différence pertinente lorsque le liquide s'écoule en régime d'écoulement laminaire, c'est-à-dire lorsque le Re < 15.

Des simulations numériques du mélangeur ont été effectuées grâce à OpenFOAM®. Ces simulations 3D étaient principalement axées sur le comportement de la SMX avec un liquide organique à faible débit de gaz (1 l/h).

Un `functionObject` fait maison, appelé `bubbleTracker`, a été implémenté sous OpenFOAM®. Cet outil nous a permis de collecter les propriétés des bulles. Les formes, tailles et vitesses des bulles ont été examinées pour valider le modèle numérique.

Les résultats expérimentaux ont été largement confirmés par des simulations numériques et vice versa. La comparaison entre les résultats numériques et expérimentaux apporte un nouvel éclairage au fonctionnement d'un mélangeur statique SMX™.

Résumé étendu

1 Introduction

Les procédés industriels forment un ensemble d'opérations qui, par des étapes chimiques, physiques, électriques ou mécaniques, permettent la réalisation d'un ou de plusieurs éléments ou produits. Les procédés industriels sont généralement destinés à la fabrication de produits finis ou semi-finis.

Dans l'industrie chimique, le mélange ou la dispersion de deux ou plusieurs phases fluides est une opération très courante et largement répandue. L'objectif principal du processus de mélange est d'augmenter l'aire interfaciale entre les phases afin d'améliorer les transferts de matière et de chaleur.

Depuis des décennies, et en particulier pour les dispersions gaz-liquide, l'une des idées les plus populaires dans la littérature est que les agitateurs et les colonnes à bulles (avec ou sans garnissage structuré) constituent les dispositifs les plus efficaces pour obtenir le mélange requis (Sánchez Pérez et al. 2006 [1]). Cependant, des développements théoriques plus récents ont révélé que les mêmes résultats peuvent être obtenus à l'aide de dispositifs différents, tels que des mélangeurs statiques (Thakur et al. (2003) [2]).

Ce dispositif est un équipement de mélange inséré dans une conduite pour le mélange de flux de fluides [2]. Les mélangeurs statiques se composent d'une série d'éléments. Chacun de ces éléments est conçu pour diviser et recombiner le flux (Heyouni et al. 2002 [3]).

Les mélangeurs statiques ont été examinés en profondeur au cours des dernières décennies à partir des travaux de Grace (1982) [4] et ensuite dans les recherches menées par de nombreux auteurs tels que Li et al. [5], Legrand et al (2011) [6], Fradette et al (2006) [7], Madhuranthakam et al (2009) [8]. Ces recherches ne sont que quelques-unes des centaines de références qui ont abordé les mélangeurs statiques. Malheureusement, malgré une littérature abondante sur le sujet, le cas de la dispersion gaz-liquide dans les mélangeurs statiques n'est pas complètement couvert. D'autres travaux, tant expérimentaux que numériques, sont nécessaires pour améliorer la compréhension de tels systèmes dispersés.

Par exemple, l'étude approfondie des phénomènes de dispersion, de rupture et de coalescence de bulles de gaz en phase organique à l'intérieur d'un mélangeur statique Sulzer SMX^{TM} n'a pas encore été abordée.

Le but ultime de la présente étude est de répondre aux questions suivantes : un mélangeur statique peut-il représenter une alternative à un réacteur agité ou à une colonne à bulles ? Ce dispositif peut-il assurer un bon mélange entre un gaz montant et un liquide stagnant ?

Cet appareil fonctionne-t-il convenablement lorsqu'il est utilisé avec des fluides organiques ?

Comme point de départ de l'étude, le liquide est maintenu immobile et son mouvement est induit par l'ascension des bulles de gaz qui le traversent. L'effet négligeable d'une circulation liquide lente a permis de se concentrer sur le cas d'un liquide stagnant. Des expériences de circulation liquide, à contre-courant et à co-courant, ont néanmoins été menées pour vérifier la similitude des résultats.

L'objectif initial de cette étude est d'analyser la faisabilité de l'utilisation des mélangeurs statiques pour des applications gaz-liquide en génie chimique. L'hydrodynamique à l'intérieur du SMX^{TM} a été caractérisée en utilisant deux méthodes optiques : la vélocimétrie par image de particules (PIV) et la technique d'ombroscopie par rétro-éclairage (BST, Backlight Shadowgraph Technique). Nous avons ici appliqué ces techniques afin de caractériser l'écoulement à l'intérieur du mélangeur statique SMX. L'effet des éléments du mélangeur SMX sur le champ de vitesse a été quantifié.

La rétention gazeuse dans différentes conditions opératoires a ensuite été estimée. C'est un paramètre important car il est lié à la zone interfaciale entre les phases.

Le transfert d'oxygène à l'intérieur du mélangeur statique a également été analysé. L'effet du mélangeur statique a été quantifié. Cette analyse a fourni une indication de l'augmentation de l'efficacité du transfert de matière due au mélangeur statique SMX.

Des simulations numériques avec la méthode volume de fluide ont été effectuées. Grâce à OpenFOAM®, une analyse complète du système a été effectuée. Les résultats ont été comparés aux résultats expérimentaux afin d'obtenir une validation de notre modèle CFD.

2 Méthodologie

2.1 Analyses expérimentales

Deux campagnes expérimentales principales ont été réalisées. Elles visaient à caractériser le comportement des dispersions de gaz dans les solutions aqueuses et dans l'heptane en présence du mélangeur SMX^{TM} inséré dans une colonne cylindrique. Différentes concentrations de SDS en solution aqueuse ont été étudiées : 0% (eau pure), 0,1% (tension superficielle : 50,3 mN/m) et 3% (tension superficielle : 35,4 mN/m).

Deux types de techniques de vélocimétrie par image de particules ont été utilisés afin de recueillir les champs de vitesse des liquides, à savoir la HFPIV (haute fréquence) et la PIV (standard). Cinq longueurs de SMX différentes ont été utilisées, avec 1, 2, 5, 10 et 15 éléments. Le comportement de la colonne vide a également été analysé. Cette longueur d'élément "0" nous a permis d'obtenir des résultats utiles afin de les comparer aux mélangeurs statiques SMX.

Les techniques PIV/HFPIV et BST nécessitent un accès optique. Cela nous a conduit à utiliser des matériaux transparents. La colonne cylindrique en verre a été placée à l'intérieur d'une boîte également en verre de section carrée contenant le même liquide afin de réduire la distorsion de l'image (voir la figure 1). Le mélangeur statique et la colonne sont donc pratiquement invisibles de l'extérieur de la boîte cubique. La minimisation de distorsion de

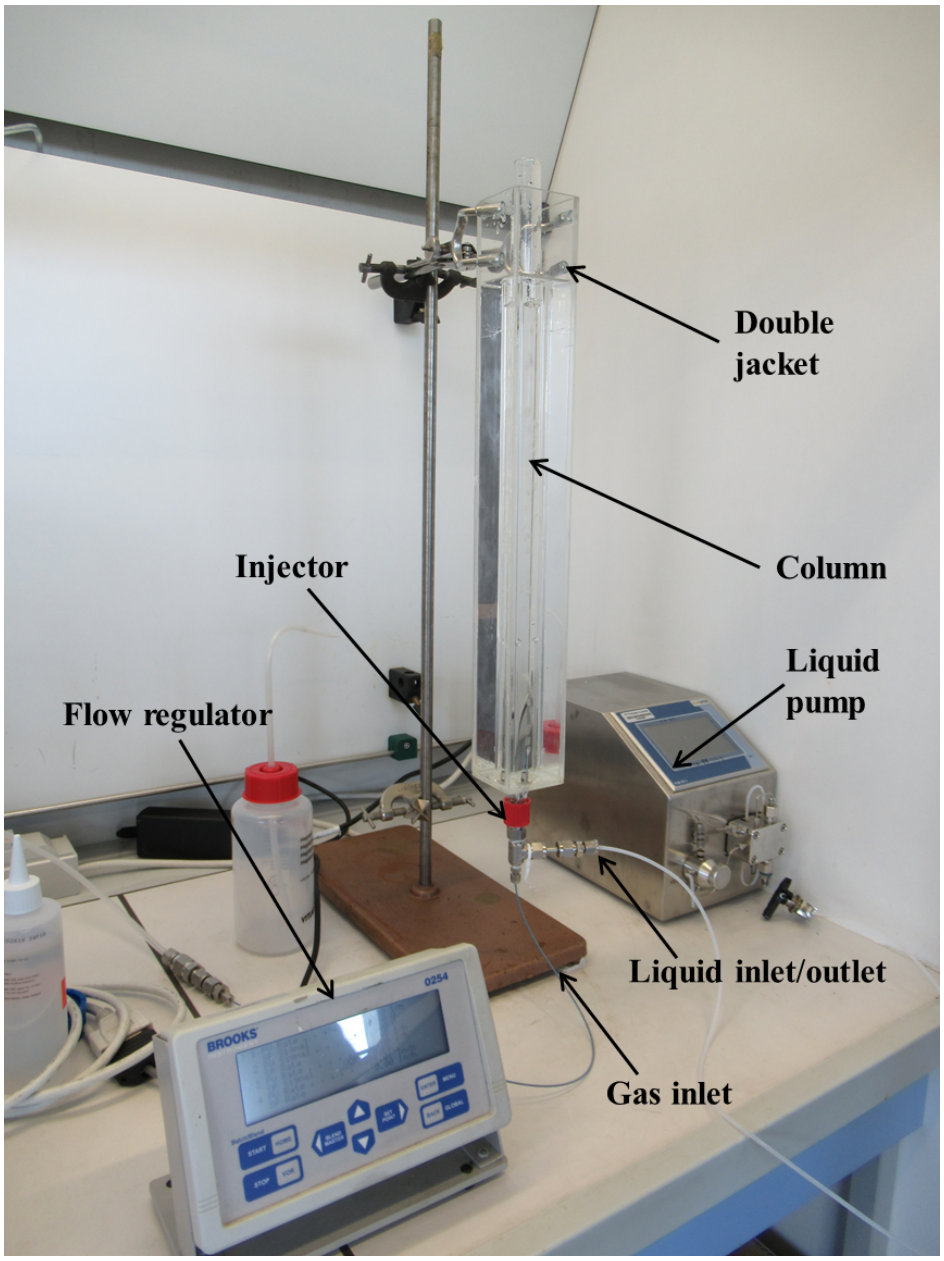

Figure 1 – Dispositif utilisé pour les analyses de laboratoire menées sur la colonne.

l'image a été vérifiée expérimentalement.

La colonne utilisée pour les expériences est illustrée dans la figure 1. La colonne a un diamètre de 16,2 mm.

L'objectif principal de ce travail est l'étude des fluides organiques, et plus précisément de l'essence. Le normal-heptane a été choisi en raison de ses similitudes physico-chimiques avec l'essence. L'heptane représente un bon compromis entre la similitude des propriétés de l'essence, les problèmes de sécurité dans les laboratoires, l'inertie chimique et la reproductibilité des expériences.

En premier lieu, des expériences sur l'eau ont été menées pour obtenir des résultats préliminaires, principalement en raison de questions de sécurité et de facilité de montage. La plupart des expériences avec l'eau ont été réalisées en ajoutant un petit pourcentage de

sulfate de dodécyle de sodium (SDS), soit 0,1% et 3%. Cela nous a permis de diminuer la tension superficielle entre la solution aqueuse et la phase gazeuse dispersée pour s'approcher de celle de l'heptane dans l'air.

L'azote a été utilisé en tant que phase dispersée dans l'heptane parce qu'il s'agit d'un composé stable non réactif. Ce choix a garanti un plus grand nombre de réutilisations de la même solution ainsi qu'une sécurité accrue.

Le débit de gaz était contrôlé avec une vanne électronique reliée à un boîtier de contrôle. Ce dispositif de régulation de débit est précis et a un temps de réponse rapide. Les pressions d'entrée d'air et d'azote ont été réglées à 2 bars à l'aide d'une vanne de régulation de pression. Le débit de liquide a été induit grâce à une pompe doseuse (voir figure 1).

Une géométrie de mélangeur statique Sulzer SMX a été utilisée dans toutes les expériences effectuées. La figure 2 représente la structure du mélangeur à 10 éléments. Chaque élément est pivoté de 90 degrés par rapport au précédent. De plus, les éléments sont constitués d'une série de lames inclinées à 45 degrés par rapport à l'axe. Tous les éléments sont identiques.

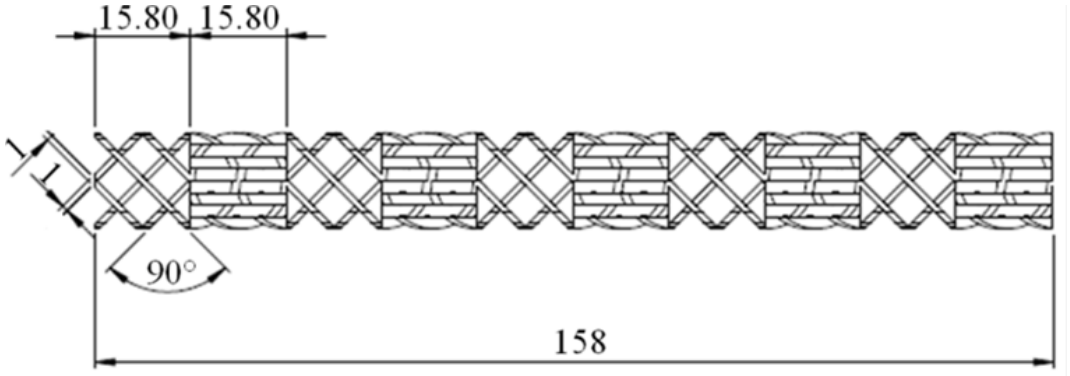

Figure 2 – Détails du mélangeur statique SMX 10 éléments. L'unité de longueur est mm. Tiré de Scala et al. (2019) [9].

Les mélangeurs étudiés dans le présent travail ont été créés par impression 3D à partir de fichiers CAO en matériau Accura ClearVue^{TM}. Ce matériau nous a permis d'obtenir un mélangeur SMX en plastique entièrement transparent en solution.

2.1.1 L'ombroscopie

La technique d'ombroscopie a été mise en œuvre pour estimer les caractéristiques des bulles. Cette méthode d'analyse est fréquemment utilisée pour étudier les systèmes dispersés caractérisés par un contraste élevé entre les phases. Avec un éclairage de fond, cette technique repose sur l'enregistrement des ombres créées par les bulles qui montent dans la phase liquide. Afin d'obtenir des ombres bien délimitées, un panneau led a été monté derrière la colonne.

L'enregistrement de ces ombres a été obtenu par une caméra rapide située devant la colonne. Pour l'estimation des diamètres, des formes et des centres des bulles, la fréquence d'acquisition de la caméra a été fixée à 500 images par seconde. Le logiciel Halcon® a été choisi pour le post-traitement des images et pour estimer la taille, la vitesse de déplacement et la position des bulles.

Les trajectoires préférentielles de bulles dans le mélangeur SMX et la colonne ont également été analysées. Ces trajectoires préférentielles représentent des zones dans lesquelles le passage des bulles est plus fréquent.

2.1.2 La rétention gazeuse

La rétention gazeuse peut être définie comme la quantité de gaz contenue dans un liquide à un moment donné. C'est une des variables qui caractérise l'intensité et la durée du contact entre la phase gazeuse et la phase liquide. La rétention e du gaz est donc liée à l'aire interfaciale entre les phases.

La méthode d'analyse utilisée est basée sur l'acquisition et le post-traitement des images. Grâce à la caméra rapide, une série d'images ont été acquises avec une fréquence très basse, soit 5 Hz. La première image de la série a été acquise en l'absence de gaz dans la colonne. Cette première image a été utilisée pour obtenir une estimation du niveau initial de liquide à l'intérieur de la colonne. Ensuite, en injectant le débit de gaz, les images avec un nouveau niveau de liquide ont été sauvegardées. Le gaz présent dans la colonne augmente le volume global. La différence de volume n'est rien d'autre que la rétention gazeuse.

2.1.3 La PIV

La PIV est couramment utilisée pour quantifier l'écoulement liquide ou l'écoulement gaz-liquide (Sathe et al. 2010 [10]). Les images PIV ont été acquises grâce à la caméra rapide et un laser pulsé à haute puissance. Le laser possède un résonateur optique double avec un cycle de répétition élevé.

Le schéma numérique PIV adaptatif a été choisi afin d'obtenir la plus grande précision, la robustesse la plus importante et la meilleure résolution spatiale possibles (voir le site internet LaVision). Cette méthode permet l'utilisation de l'option multi-pass. Cette dernière nous a permis de diminuer progressivement la taille de la fenêtre d'interrogation. La taille de la fenêtre variait de 64×64 pixels à 8×8 pixels.

2.1.4 Le transfert de matière

La mesure du transfert de matière est un facteur clé pour évaluer l'efficacité des mélangeurs statiques dans la dissolution ou le stripage des gaz. Cependant, une estimation précise du coefficient de transfert peut être délicate, notamment en phase organique. Nous avons utilisé une sonde à oxygène pour les solutions aqueuses.

La méthodologie que nous avons utilisée est basée sur le transfert d'oxygène entre l'air et une solution aqueuse. Une fois la sonde fixée à la sortie de la colonne, un stripage de l'oxygène présent dans l'eau a été effectué en injectant de l'azote dans la colonne. La concentration de O_2 lue par la sonde a diminué jusqu'à zéro. Un étalonnage était nécessaire à ce moment-là. L'alimentation de la colonne est ensuite passée de l'azote à l'air. La concentration de O_2 a augmenté dans le temps jusqu'à une valeur de saturation.

2.2 Analyse numérique

Pour la présente thèse, la version ESI-OpenCFD OpenFOAM® + a été choisie. Ce choix a été motivé par la plus grande quantité de solveurs et d'outils de post-traitement disponibles dans la version OpenFOAM+ par rapport aux autres. En particulier, le solveur VoF `interIsoFoam`, qui utilise la méthode *isoAdvector* avec *isoAlpha* a été utilisé [11].

Le solveur `interIsoFoam` a été utilisé dans cette étude. Il repose sur une méthode volume de fluide (VoF) géométrique appelée *isoAdvector* avec *isoAlpha*. L'algorithme a été implémenté dans le solveur `interIsoFoam` qui est disponible dans OpenFOAM+ depuis la version v1706.

Le solveur `interIsoFoam` (*isoAdvector*) résout le système d'équations de la quantité de mouvement et de la continuité de manière découplée en utilisant l'algorithme PIMPLE (une combinaison des algorithmes SIMPLE et PISO) pour le couplage pression-vitesse.

2.2.1 Définition de la géométrie et du processus de maillage

Une géométrie similaire à celle utilisée pour les expériences a été utilisée. Le maillage a été généré par `snappyHexMesh`, un utilitaire fourni avec OpenFOAM®. `SnappyHexMesh` génère des maillages tridimensionnels contenant principalement des hexaèdres (hex) et des hexaèdres divisés (split-hex). Le processus de génération de maillage est automatiquement réalisé à partir de géométries de surface triangulées au format STL. Tous les fichiers STL ont été produits par Pointwise® à partir de CAO des géométries.

`snappyHexMesh` nous a permis d'obtenir une grille très uniforme et structurée. Le taux de recouvrement par des cellules hexahédriques a atteint environ 99% (selon les cas). La distorsion des cellules près de la surface du mélangeur SMX a été largement contenue. Les cellules dont le volume se trouvait inférieur à 10^{-15} m^3 ont été supprimées du domaine.

L'analyse de la sensibilité au maillage a été réalisée sur le benchmark de Hysing afin de trouver le nombre optimal de cellules par diamètre de bulle. Les résultats suggèrent une valeur optimale comprise entre 20 cellules/diamètre et 40 cellules/diamètre. Une estimation préliminaire du nombre total de cellules obtenues dans le domaine informatique a révélé que le critère des 40 cellules/diamètre ne pouvait être respecté. Pour cette raison, une discrétisation spatiale intermédiaire de 0,1 mm a été utilisée (environ 30 cellules/diamètre).

2.2.2 Fonction Objet

Le processus et l'analyse des résultats est un aspect fondamental des simulations CFD. Une `functionObject` faite maison a été ajoutée dans le fichier `controlDict`. Cette dernière, appelée `bubbleTracker`, est capable d'isoler les bulles présentes dans le domaine et de calculer leurs caractéristiques. `bubbleTracker` génère et stocke un `scalarField` appelé `VoFColor` basé sur le champ de fraction volumique. Ce champ est composé d'entiers représentant l'identifiant des bulles.

Les cellules appartenant à la même bulle reçoivent un numéro d'identification identique. Ensuite, chaque bulle détectée est post-traitée individuellement afin d'obtenir ses

caractéristiques (diamètre, vitesse, position, forme, surface, volume). Les propriétés de la bulle sont sauvegardées dans des fichiers au format texte pendant le calcul.

3 Résultats

3.1 Résultats expérimentaux

La rétention gazeuse dans le mélangeur statique SMX est environ deux fois plus élevée que dans une simple colonne à bulles. Dans la colonne à bulles, la dispersion de gaz dans l'eau pure présente une rétention inférieure à celle observée pour les solutions SDS, indépendamment du débit du gaz considéré. En fait, l'SDS induit une tension superficielle plus faible qui entraîne la formation de bulles de plus petit diamètre, ce qui conduit à une vitesse d'ascension moyenne plus faible et donc un temps de séjour plus long.

La présence du mélangeur statique a une influence significative sur les valeurs de rétention gazeuse. Les tendances observées suggèrent que les mélangeurs statiques sont plus performants dans les solutions d'eau pure. Cependant, une analyse plus détaillée met en évidence que le niveau de rétention gazeuse plus élevé atteint dans l'eau pure est principalement dû à la quantité de bulles qui restent collées sur la surface du mélangeur statique, ou pour être plus précis, sur les barres transversales de la structure du mélangeur.

La figure 3 et la figure 4 illustrent les principaux résultats obtenus avec l'heptane. La comparaison des valeurs de la retention gazeuse avec et sans mélangeur statique montre une augmentation substantielle causée par la présence du mélangeur.

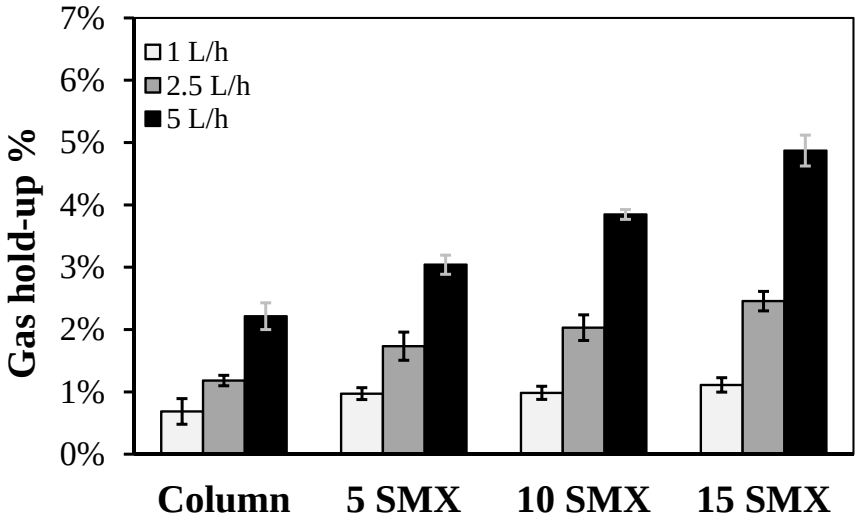

Figure 3 – Valeurs de rétention gazeuse pour l'injecteur de 0,25 mm.

Les résultats obtenus pour la colonne vide sont conformes par rapport à la littérature. Les valeurs de rétention du gaz mesurées pour la buse de 0,25 mm (figure 3) suggèrent que l'emploi d'un plus petit injecteur est à l'origine de la formation de bulles de plus petite taille, de vitesses d'ascension plus faibles, d'un temps de séjour plus long ainsi que d'une retenue plus importante d'azote.

Différentes considérations peuvent être déduites des données collectées en utilisant les mélangeurs SMX. Les valeurs de la rétention gazeuse résultant de la plus petite buse (d_n = 0,25 mm) et du plus faible débit du gaz (Q_G = 1 l/h) semblent être presque constantes. La taille des bulles dans ces conditions peut expliquer ce comportement particulier. Les petites bulles générées peuvent potentiellement monter plus rapidement dans le mélangeur, sans interagir les unes avec les autres, sauf dans les premiers éléments du mélangeur. Ceci pourrait s'expliquer soit par l'état de surface du mélangeur, soit par un sillage plus confiné autour de ces bulles. Des résultats similaires ont été obtenus avec le plus gros injecteur.

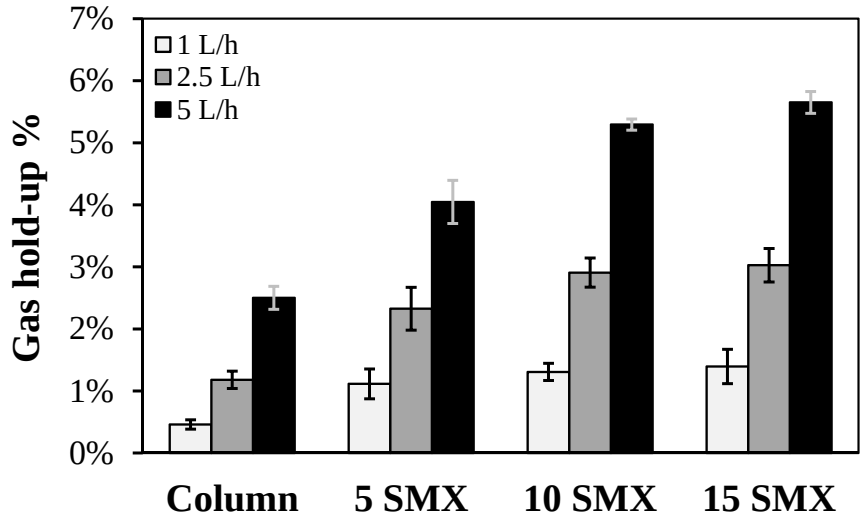

Figure 4 – Valeurs de rétention gazeuse pour l'injecteur de 1 mm.

En comparant la forme et le diamètre des bulles dans la colonne vide avec ceux détectés avant l'entrée du SMX, aucune différence significative n'a été identifiée. Cela suggère que le mélangeur n'affecte pas la forme et la vitesse des bulles dans la région de formation des bulles, en amont. Cette observation reste valable dans les régions éloignées d'au moins deux diamètres de colonne du mélangeur statique.

Dans la colonne sans mélangeur, la distribution de diamètres de bulles obtenue en utilisant l'injecteur de 1 mm est assez étroite autour du diamètre de Sauter. La distribution résultant de d_n = 0,25 mm présente une tendance différente, avec un pic secondaire correspondant à des petites bulles (d_e environ 0,8 mm). Cela s'explique par un différent régime de formation pour les bulles.

Les diamètres de bulles équivalents ont également été mesurés à la sortie des mélangeurs statiques. Les distributions des bulles ont considérablement évolué à la sortie de mélangeurs de trois longueurs, en comparaison avec la colonne à bulles. Les distributions globales sont généralement plus larges. Les pourcentages de petites bulles (d_e <1 mm) et de grosses bulles ($d_e >$ 4 mm) ont sensiblement augmenté.

Les vitesses des bulles ont été obtenues en suivant le déplacement de bulles. Pendant les expériences, il a été constaté que la montée en zigzag et en spirale des bulles provoquait leur déformation et une instabilité de la vitesse. Les vitesses instantanées des bulles à l'intérieur du mélangeur sont sur la plage 0-24 cm/s.

La vitesse axiale moyenne des bulles mesurée à l'intérieur du mélangeur est d'environ 8

cm/s ($d_n = 1$ mm. $Q_G = 1$ l/h Une valeur similaire a été retrouvée pour la composante horizontale de la vitesse dans tous les éléments faisant face à la caméra. La vitesse moyenne dans le premier élément (12 cm/s) est relativement plus élevée que dans les autres, ce qui révèle le rôle d'obstacle du mélangeur statique. De plus, aucun changement significatif de la vitesse moyenne des bulles n'a été observé à l'intérieur du mélangeur après le troisième élément. Une quantité considérable de bulles à proximité des barres transversales SMX présente une vitesse négligeable.

Dans la colonne à bulles sans mélangeur des trajectoires en zigzag et/ou en spirale ont souvent été observées. Une analyse statistique de la probabilité de trouver des bulles dans une zone a été effectuée. Les résultats obtenus sur la colonne sans SMX ont révélé que la probabilité de trouver une bulle au centre de la colonne est plus élevée que près des parois.

La présence du mélangeur statique change le comportement des bulles : il diminue le diamètre des bulles et augmente donc leur temps de séjour. Une autre observation ressort de cette analyse : les bulles montent dans le SMX en suivant les trajectoires préférentielles. Ces trajectoires préférentielles sont principalement proches des barres inclinées du mélangeur.

La technique PIV a été utilisée pour mesurer les champs de vitesse de la phase liquide (eau ou heptane) tant dans la colonne vide que dans la colonne avec le SMX. Le champ moyen collecté indique un comportement caractéristique du système : les bulles ont tendance à passer par le centre de la colonne. Ce résultat, confirmé par la technique de l'ombroscopie, se traduit par un débit moyen ascendant près de l'axe. Par contre, les régions proches de la paroi de la colonne présentent un débit moyen descendant.

Les résultats PIV sont complètement différents lorsque les mélangeurs SMX sont utilisés. Par exemple, la figure 5 illustre un champ de vitesse instantanée mesuré dans le SMX. Le mouvement de la phase liquide dû à un passage de bulle peut être identifié en observant scrupuleusement l'image à droite de la figure 5. Par exemple, un écoulement ascendant peut être observé à proximité des trois bulles les plus à droite. Dans certains cas, les champs de vitesse liquide peuvent ne pas correspondre à la configuration du plan de coupe médian attendu à travers une bulle, comme c'est le cas pour les bulles les plus à gauche.

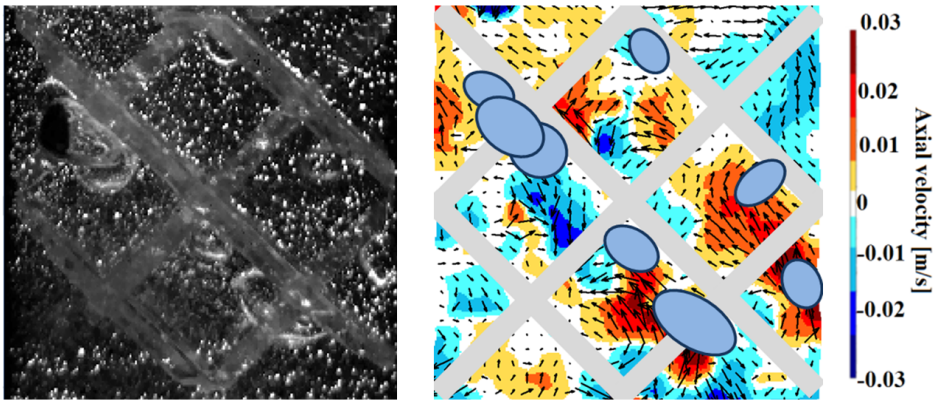

Figure 5 – Image PIV brute et champ d'écoulement instantané dans le premier élément SMX (coloré par la composante axiale de la vitesse). $d_n = 0.25$ mm. $Q_G = 1$ l/h.

Les écoulements deviennent plus compliqués à interpréter pour des débits de gaz plus grands en raison de la présence de nombreuses bulles suite à l'augmentation de la rétention

gazeuse. Les principaux écoulements de liquide sont situés dans la zone de passage des bulles. Des écoulements ascendants ont généralement été observés à proximité des bulles, devant une bulle et dans son sillage, en regardant dans un plan de coupe médian de la bulle. Des courants descendants sont mesurés sur les côtés latéraux des trajectoires des bulles. A l'intérieur du mélangeur, on a observé une diminution des vitesses du liquide, due à la réduction des vitesses des bulles. Les vitesses des bulles sont environ 2 à 3 fois plus petites à l'intérieur du mélangeur.

Les résultats PIV suggèrent que les bulles s'élèvent dans le sillage laissé par les précédentes. Ce comportement implique la présence de certains chemins préférentiels dans le mélangeur statique SMX. Il est à noter que l'écoulement peut être difficile à mesurer dans certaines zones du mélangeur statique en raison de la présence de plusieurs bulles. Les interfaces gaz-liquide des bulles reflètent le laser, ce qui rend difficile le suivi des particules d'ensemencement.

Le transfert de matière global est estimé à l'aide des deux équations du bilan matière. Le K_La est généralement obtenu en exprimant les résultats sur un graphique semi-logarithmique utilisant des données entre 20% et 80% de la concentration maximale en oxygène. Cette méthode a été présentée par Niewon (2015) [12].

Le coefficient de transfert de matière global k_La est la pente des droites représentées sur la figure 6. En augmentant le débit de gaz, la recirculation de la solution aqueuse devient de plus en plus intense. La quantité d'oxygène dissout augmente également plus rapidement. Par conséquent, le coefficient de transfert de matière volumétrique k_La augmente. Ce comportement est décrit par la figure 6.

La figure 6 montre les améliorations apportées au transfert de matière par le mélangeur statique. La comparaison entre les lignes montre que la pente (et donc k_La) est deux fois plus forte. On peut donc en déduire que le transfert de matière global dans le mélangeur est environ deux fois plus efficace que dans la colonne à bulles.

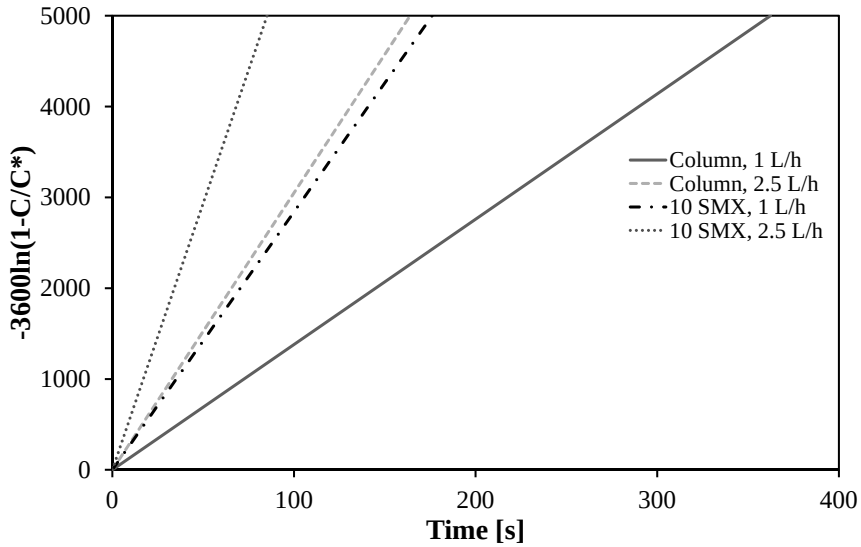

Figure 6 – Représentation par lignes d'interpolation de l'évolution dans le temps de $-3600\ \ln(\frac{1-C}{C^*})$ dans plusieurs conditions de fonctionnement. $d_n = 1$ mm.

3.2 Résultats numériques

Les valeurs de la rétention gazeuse ont été évaluées aussi avec des simulations numériques. Grâce à la `FunctionObject bubbleTracker`, le volume total des bulles dans la dispersion était disponible à tout instant. Le volume de la phase liquide était également connu. La rétention du gaz a donc été estimée comme étant le rapport entre le volume de gaz et le volume total de la dispersion.

Une comparaison des résultats obtenus à partir de simulations numériques et d'xpériences a été effectuée. Les valeurs obtenues montrent une concordance satisfaisante entre les résultats expérimentaux et numériques. L'écart maximum rencontré est inférieur à 10 %.

Le diamètre moyen des bulles entre l'entrée et la sortie du mélangeur a été étudié par des simulations numériques. La variation du diamètre obtenue par expérience numérique est en accord avec les observations expérimentales. Même si les diamètres moyens sont restés pratiquement inchangés entre l'entrée et la sortie du mélangeur, la distribution a sensiblement évolué. Par exemple, une grande quantité de bulles (environ 19%) d'un diamètre moyen inférieur à 2 mm a été détectée à la sortie du mélangeur statique de 5 éléments. Ces bulles ont été générées par des ruptures dans le mélangeur. De même, une quantité non négligeable de bulles (environ 8%) avec un diamètre moyen de 4 mm a été trouvée. Ces bulles ont été produites par des phénomènes de coalescence.

La vitesse des bulles a été quantifiée par les simulations CFD. Dans la colonne à bulles, les vitesses axiales des bulles variaient de 12 à 27 cm/s. Ces gammes sont identiques à celles des expériences. Les vitesses instantanées des bulles à l'intérieur du mélangeur SMX ont été mesurées en CFD sur une plage de 0 à 24 cm/s. Les simulations suggèrent donc que les bulles ont traversé le mélangeur SMX avec une vitesse moyenne similaire à l'observation expérimentale.

Les trajectoires préférentielles ont été évaluées de deux manières différentes, notamment en analysant le centre de gravité de la bulle $\overrightarrow{x_G}$ et en faisant la moyenne dans le temps des valeurs du champ de fraction volumique. Les deux méthodes ont donné des résultats similaires. Les trajectoires préférentielles obtenues par les simulations numériques sont analogues à celles des expériences. Les trajectoires des bulles passent préférentiellement par la zone centrale de la colonne. A proximité de l'injecteur et sur les premiers centimètres après le détachement, les bulles avancent sur une trajectoire rectiligne. Des trajectoires en zigzag et/ou en spirale ont ensuite été observées pour certaines tailles de bulle.

Les simulations numériques ont mis en évidence des trajectoires préférentielles des bulles dans le mélangeur SMX. Comme le montrent les résultats expérimentaux, ces trajectoires préférentielles sont principalement proches des barres inclinées du mélangeur. De plus, des zones avec une probabilité nulle (environ 0.8%) de trouver des bulles ont été identifiées. Le résultat dans le mélangeur de 2 éléments et 5 éléments SMX est illustré sur la figure 7.

Les résultats de l'étude numérique se comparent favorablement avec ceux obtenus expérimentalement par la PIV. Par exemple, la figure 8 (gauche) illustre une vue détaillée du champ de vitesse axiale moyenne obtenu à l'entrée du SMX à 10 éléments avec le PIV. Le champ de droite montre le champ de vitesse axiale de la même région obtenu par les simulations numériques.

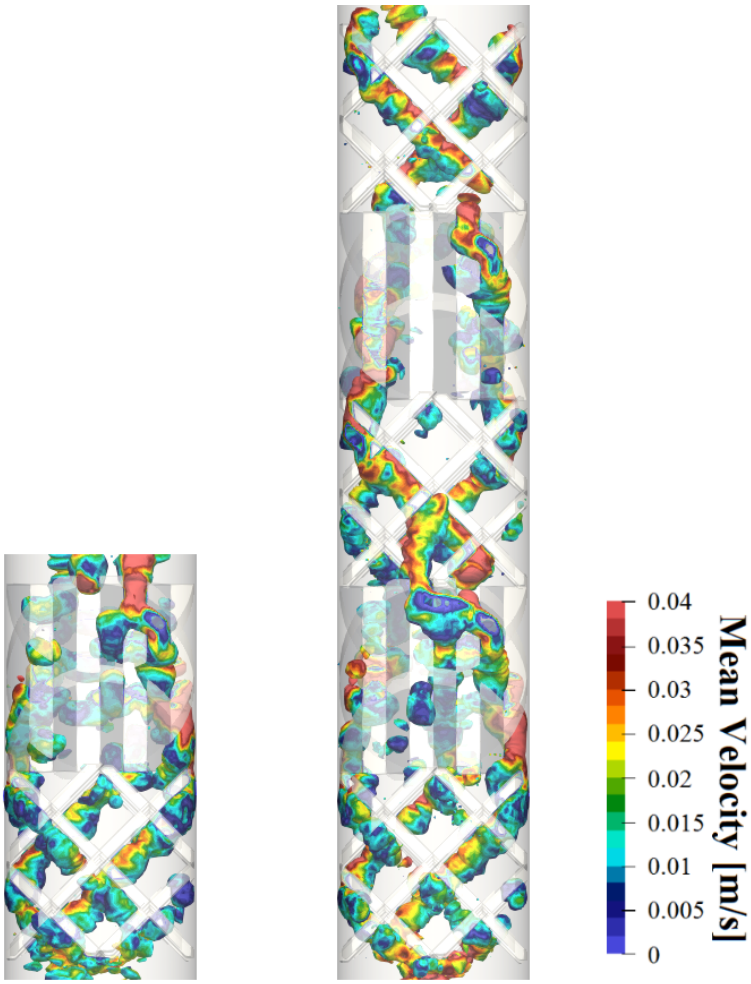

Figure 7 – Trajectoires préférentielles détectées dans la colonne bulles avec les SMX à 2 éléments et 5 éléments alimentés par $d_n = 1$ mm. Débit de gaz $Q_G = 1\,\mathrm{l/h}$. Carte en couleurs du champ de vitesse.

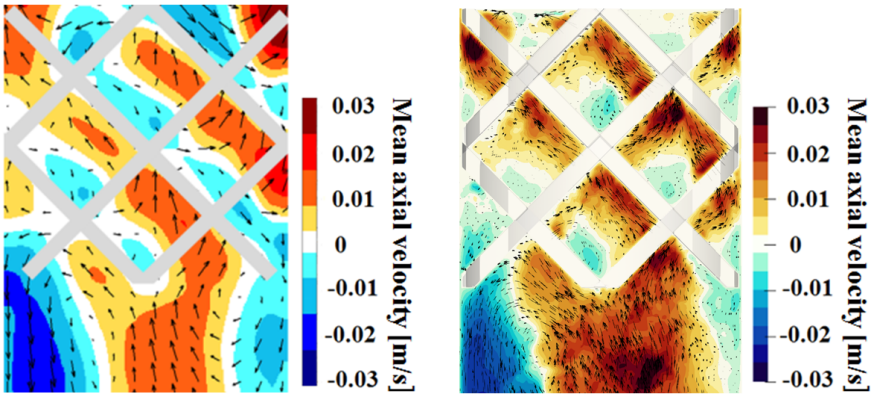

Figure 8 – Vue détaillée du premier élément des 10 éléments SMX : résultats expérimentaux (gauche) et numériques (droite). Plan de coupe passant par le centre de l'élément décrivant les valeurs de la vitesse axiale moyenne. $d_n = 1$ mm. $Q_G = 1\,\mathrm{l/h}$.

On remarque peu de différences significatives dans ces champs. De plus, les vitesses moyennes et instantanées variaient dans le même intervalle dans les expériences et les simulations CFD. Une portion significative de vitesses allant de -0,02 m/s à 0,02 m/s a été trouvée

dans le mélangeur, soit environ 55%. Une analyse plus détaillée des champs d'écoulement à l'intérieur du mélangeur statique a largement validé les résultats expérimentaux.

4 Conclusion

L'objectif principal du présent travail était de caractériser l'hydrodynamique diphasique dans les mélangeurs statiques Sulzer SMX^{TM} de différentes longueurs. La majorité des travaux ont été concentrés sur une dispersion de bulles dans du n-heptane. Cependant, des expériences avec des solutions aqueuses ont également été réalisées pour affiner les techniques d'investigation et obtenir des résultats préliminaires, notamment dans le domaine du transfert de matière.

L'étude expérimentale a été réalisée par l'injection d'azote dans un liquide stagnant sous différentes conditions opératoires : différents débits de gaz, différentes longueurs de mélangeur, différents fluides (eau, eau + SDS et heptane normal) et deux tailles de buses.

La taille, la forme, la vitesse et la position des bulles ont été quantifiées à l'aide de plusieurs techniques expérimentales, notamment PIV et ombroscopie. Un post-traitement d'image a été mis au point pour estimer le diamètre moyen de Sauter des bulles à l'entrée et à la sortie des mélangeurs SMX. La capacité d'estimer la taille réelle, la forme et la vitesse des bulles a été vérifiée en effectuant plusieurs comparaisons avec les corrélations empiriques et les données présentées dans la littérature.

Les vitesses du liquide ont été mesurées par la technique PIV pour la première fois dans un mélangeur statique grâce à l'impression 3D transparente. Les résultats obtenus révèlent que le SMX^{TM} augmente substantiellement la rétention de gaz et le temps de séjour des bulles pour toutes les conditions opératoires exploitées.

L'analyse détaillée sur la dispersion azote-heptane a révélé des informations importantes. Par exemple, cette étude suggère que le mélangeur SMX à 15 éléments est suffisamment long pour assurer un équilibre dynamique entre la coalescence et la rupture des bulles dans le mélangeur, quelles que soient les conditions en entrée.

La performance du transfert d'oxygène air/eau dans le mélangeur statique SMX a été évaluée en calculant l'oxygène global transféré. Cette analyse a mis en évidence que l'efficacité du transfert de matière global dans le mélangeur est environ deux fois plus élevé que dans une colonne à bulles simple.

Des simulations numériques volume de fluide de l'écoulement diphasique dans le mélangeur ont été effectuées grâce à OpenFOAM®. Ces simulations 3D s'intéressaient principalement aux effets des éléments SMX sur les bulles dans un liquide organique à faible débit de gaz (Q_G = 1 l/h). La comparaison des résultats numériques et expérimentaux apporte un nouvel éclairage sur l'hydrodynamique diphasique complexe dans un mélangeur statique SMX^{TM}. La vitesse, le diamètre moyen des bulles et la rétention gazeuse mesurés par les simulations numériques sont en bon accord avec les expériences. Les trajectoires préférentielles simulées par les simulations ont aussi été confirmées par les expériences dans le mélangeur.

Remerciements

Je tiens tout d'abord à remercier Madame Joëlle AUBIN et Monsieur Daniele MARCHISIO pour leur lecture détaillée de mon manuscrit de thèse. La version finale de ce mémoire a bénéficié de leur lecture très attentive et de leurs remarques précieuses. Je remercie également Monsieur Serge SIMOËNS et Monsieur Mounir BOUAIFI pour l'honneur qu'ils m'ont fait d'être dans mon jury de thèse. Je remercie également tous les membres du jury d'avoir accepté d'assister à la présentation de ce travail ainsi que pour les remarques qu'ils m'adresseront lors de cette soutenance afin d'améliorer mon travail.

Je remercie Monsieur Huai-Zhi LI, Professeur à l'Université de Lorraine, qui m'a encadré tout au long de cette thèse et qui a partagé avec moi ses brillantes intuitions. Qu'il soit aussi remercié pour sa gentillesse, sa disponibilité permanente et pour les nombreux encouragements qu'il m'a prodigués. J'aimerais également lui dire à quel point j'ai apprécié sa grande disponibilité et son respect sans faille des délais serrés de relecture des documents que je lui ai adressés.

Je tiens à remercier mon superviseur de thèse, monsieur Lionel GAMET, pour la confiance qu'il m'a accordée, pour ses multiples conseils et pour toutes les heures qu'il a consacrées pour mon projet. Je le remercie du fond du cœur pour m'avoir accompagné, conseillé et écouté lors de ce dur travail. Je tiens a lui remercier aussi pour avoir lu et relu tous mes manuscrits. Merci aussi pour son optimisme à toute épreuve et pour son investissement au quotidien ; on peut être fier du travail qui a été accompli lors de ces trois années.

Je souhaiterais exprimer ma gratitude à mon co-superviseur de thèse, monsieur Louis-Marie MALBEC, pour m'avoir donné des conseils et des idées indispensables. Je le remercie également pour son accueil chaleureux dans son département et à chaque fois que j'ai sollicité son aide, ainsi que pour ses multiples encouragements, notamment lors de mes expériences dans les laboratoires de Rueil et pendent la période de rédaction.

J'exprime tout particulièrement encore une fois ma gratitude à Monsieur Huai-Zhi LI, Monsieur Lionel GAMET et Monsieur Louis-Marie MALBEC aussi pour leur soutien, leur enthousiasme et leur investissement tout au long de ces trois années de travail. Merci de vous être tant impliqués pour que ma thèse se déroule bien, et d'avoir toujours été présents. Je suis également reconnaissant à Vania SANTOS-MOREAU pour avoir participé à la naissance de ce projet de thèse. J'adresse également mes remerciements à Matthieu ROLLAND pour son intérêt et son suivi de mon travail.

Les nombreuses expériences présentées dans ce manuscrit de thèse n'auraient pu voir le jour sans la participation et l'engagement de plusieurs ingénieurs et techniciens IFPEN et LRGP. Leur expertise m'a permis d'obtenir des résultats expérimentaux de grande qualité.

Je remercie le LRGP et IFPEN pour l'accueil que j'ai reçu au sein des laboratoires, ainsi que pour les importants moyens techniques qui ont été mis à ma disposition. Je remercie fortement tous les membres des groupes LRGP-ENSIC pour les moments de convivialité que nous avons partagés.

Un grand merci aussi à tous les collègues d'IFPEN et en particulier à tous les thésards et mes co-bureaux qui ont partagé avec moi des moments inoubliables.

Merci enfin à tous ceux qui m'ont soutenu et accompagné dans le reste de ma vie. J'adresse une pensée particulière à Lorena et Barbara pour leur soutien. Un grand merci également à ma famille surtout mes parents et mes grands-parents, en particulier ma mère Rossana, mon père Paolo et ma nièce Agata, qui ont été toujours présents. Enfin, et peut-être surtout, merci à mon grand-père Vincenzo de m'avoir donné la motivation et la force de faire des choix importants.

Contents

List of Figures

List of Tables

List of Symbols

Symbol	Units	Description
A_p	m^2	Particle surface
$\mathcal{C}$	-	Circularity
C_α	mol/l	Concentration of α in a liquid
C_α^*	mol/l	Concentration of α in a liquid at equilibrium
Ca	-	Capillary number
D	m	Characteristic diameter
d_{32}	m	Sauter diameter
D_a	m	Deformation at drop burst
d_b	m	Bubble diameter
D_c	m	Column diameter
D_d	m	Drop deformation
d_{eq}	m	Equivalent bubble diameter
D_i	m	Impeller diameter
d_n	m	Orifice (nozzle) diameter
d_A	m	Equivalent bubble diameter based on surface
d_V	m	Equivalent bubble diameter based on volume
E	-	Bubble aspect ratio
Fr	-	Froude number
f	-	Fanning friction factor
$\mathbf{F}_\sigma$	N/m	Surface tension force per unit of volume
G_B	-	Shear rate at drop burst
H	$\frac{\mathrm{l\ atm}}{\mathrm{mol}}$	Henry constant
h_i	m	Initial liquid level in the column
h_f	m	Final liquid level in the column
k_G	m/s	Mass transfer coefficient (gas-side)
k_i	-	Interface curvature
K_L	$\frac{\mathrm{mol}/(\mathrm{s\ m}^2)}{\mathrm{mol}/\mathrm{m}^3}$	Overall Mass transfer coefficient (liquid-side)
k_L	$\frac{\mathrm{mol}/(\mathrm{s\ m}^2)}{\mathrm{mol}/\mathrm{m}^3}$	Mass transfer coefficient (liquid-side)

Symbol	Units	Description
$k_L a$	s^{-1}	Mass transfer coefficient
J_{O_2}	mol/m^2	Oxygen flux at interface
L	m	Characteristic length (tube/column/mixer)
Mo	-	Morton number
Ne	-	Newton number
P	atm	Pressure
P_G	atm	Pressure of gas phase
P_L	atm	Pressure of liquid phase
P_α	atm	Partial pressure of α
p_μ	atm	Viscosity ratio
Pe	-	Peclet number
Q_V	m^3/s	Volumetric flow-rate
Q_G	m^3/s	Volumetric gas flow-rate
Q_L	m^3/s	Volumetric liquid flow-rate
R_ρ	-	Density ratio
r_A	m	Equivalent radius based on surface
r_V	m	Equivalent radius based on volume
Re	-	Reynolds number
St	-	Stanton number
Stk	-	Stokes number
$\mathbf{u}$	m/s	Velocity vector in the momentum equation
U	m/s	Magnitude of the characteristic velocity
$\mathbf{U_b}$	m/s	Bubble velocity
U_G	m/s	Gas velocity
U_L	m/s	Liquid velocity
U_T	m/s	Bubble terminal velocity
$u_{s,p}$	m/s	Particle sedimentation velocity
u_x	m/s	Horizontal component of the velocity
u_y	m/s	Vertical (axial) component of the velocity
u_z	m/s	z-direction component of the velocity
V_b	m^3	Bubble volume
V_G	m^3	Gas volume
V_L	m^3	Liquid volume
V_p	m^3	Particle volume
V_{SMX}	m^3	SMX mixer volume
$\mathbf{x_G}$	-	Bubble centroid of mass
We	-	Weber number
Z	-	Drop pressure ratio factor

Symbol	Units	Description
α	-	Volume fraction
α_p	-	Volume fraction of the component p
γ	s^{-1}	Shear rate
γ_{avg}	s^{-1}	Average shear rate
γ_{eff}	s^{-1}	Effective shear rate
γ_w	s^{-1}	Shear rate at the wall
η	m^2/s	Aapparent fluid viscosity
μ	Pa s	Dynamic viscosity
μ_G	Pa s	Gas dynamic viscosity
μ_L	Pa s	Liquid dynamic viscosity
Δh	m	Mesh size : edge length (3D) and face length (2D)
Δt	s	Generic time step
ΔP	atm	Pressure drop
Δt_{CFL}	s	Time step based on CFL condition
Δt_μ	s	Time step based on viscous force
Δt_g	s	Time step based on gravity force
Δt_σ	s	Time step based on surface tension force
$\Delta\rho$	kg/m^3	Density difference between the two phases
δ_G	m	Gas-side film
δ_L	m	Liquid-side film
ϵ_G	-	Gas hold-up
ϵ_{SMX}	-	SMX mixer porosity
θ	$^\circ$	Contact angle
τ	s^{-1}	Space time
ρ	kg/m^3	Density
ρ_G	kg/m^3	Gas density
ρ_L	kg/m^3	Liquid density
ρ_p	kg/m^3	Particle density
σ	N/m	Surface tension
ν	m^2/s	kinematic viscosity
ψ	-	Sphericity
Ω	-	Drop rotation

Abbreviation	Description
2D	Two-dimensional
3D	Three-dimensional space
AMR	Adaptive mesh refinement
BST	Backlight Shadowgraph Technique
CAD	Computer Aided Design
CARPT	Computer-automated radioactive particle tracking
$Cells/d_B$	Cells on the bubble diameter
CFD	Computational fluid dynamics
CFL	Courant-Friedrichs-Lewy condition
CICSAM	Compressive interface-capturing scheme for arbitrary meshes
CPU	Central processing unit
CSF	Continuum surface force
CSS	Continuum surface stress
CT	Computed tomography
HFPIV	High Frequency Particle Image Velocimetry
HRIC	High resolution interface capturing
ISG	Interfacial Surface Generator Ross^{TM}
LLPD	Low-Low-Pressure-Drop Ross^{TM}
LPD	Low-Pressure-Drop Ross^{TM}
LS	Level Set method
MULES	Multidimensional Universal Limiter with Explicit Solution
PDF	Probability Density Function
PIV	Particle Image Velocimetry
RTD	Residence Time Distribuition
SDS	Sodium Dodecyl Sulfate
SLIC	Simple Line Interface Calculation method
SMV	Sulzer static mixer SMV^{TM}
SMX	Sulzer static mixer SMX^{TM}
THINC	Tangent of Hyperbola for Interface Capturing method
UNS	Unstructured mesh
VoF	Volume of fluid
WLIC	Weighed Line Interface Calculation

Chapter 1

Introduction

The aim of this chapter is to provide the reader with a quick overview of the issues addressed in this thesis, as well as a general overview of the applications of the present work.

Methodology of problem approach, issues found, and solutions proposed are briefly described in the following sections to give more details which may be useful for the reader. A detailed outline of the thesis was added in the last section 1.4 below.

This Ph.D. thesis was financially supported by IFP Énergies Nouvelles (IFPEN) and aims at improving fundamental knowledge related to hydrodynamics and mass transfers inside Sulzer SMX^{TM} static mixer. The initial promoter of IFPEN for this research was Vania Santos-Moreau, who was then replaced by Lionel Gamet and Louis-Marie Malbec. In addition, this study was carried out in collaboration with the Laboratoire Réactions et Génie des Procédés (LRGP) in Nancy (University of Lorraine) under the supervision of Professor Huai-Zhi Li.

1.1 Industrial context and issues, scientific strategy

Industrial processes are a set of operations that through chemical, physical, electrical or mechanical steps permit the realization of one or more elements or products. Industrial processes aim at the realization of finished or semi-finished products.

In chemical industry applications, the mixing of two or more fluids phases is a very common and widely spread operation. The main objective of the mixing process is to increase the interface area between the phases in order to improve mass and heat transfer and facilitate heterogeneous chemical reaction. For decades, especially for gas liquid dispersions, one of the most popular ideas in the literature was that stirred tanks and bubble columns (with or without structured packings) were the most suitable and efficient devices to achieve the required mixing (Sánchez Pérez et al. 2006 [1]). But more recent theoretical developments revealed that the same results can be obtained using different devices, such as static mixers (Thakur et al. (2003) [2]).

Static mixers are mixing equipment inlaid into a housing or pipeline for the blending of fluid flows [2]. The static mixers consist of a series of elements. Each of them is designed

to split and recombine the flow (Heyouni et al. 2002 [3]). A more detailed explanation and description of such devices is provided in section 2.2.2 of chapter 2. Over the last two decades, the research on static mixers gained renewed interest due to an increasing demand for efficient mixing devices in the industry. Compared to stirred tanks, the static mixers do not have any mobile part and present good mixing performance for a reduced energy consumption (Thakur et al. 2003 [2]). Furthermore, they present low maintenance cost and easy installation (Madhuranthakam et al. 2009 [8]).

A common strategy used to study these blending devices is to perform examinations of mixing capacity on liquid/liquid systems. For example, by using epoxide resins, several authors analysed and obtained an estimation of the mixing performances of several static mixer geometries. Most of the theories and results present in the literature are thus focused on explaining the performance of such devices for liquid-liquid dispersions, and for systems in which the continuous phase is flowing into the blending device. Fewer researches were carried out on gas-liquid systems. The hydrodynamics of such systems are often complex, and their study is also complicated (see chapter 2).

In recent decades, the growing number of studies led to the birth of more and more geometries to cover a wide range of industrial applications. Several designs of static mixers are available nowadays. A considerable number of studies sought to determine the most suitable device conformation for each industrial application (Hobbs and Muzzio (1998) [39] ; Byrde and Sawley (1999) [40] ; Rauline et al. (2000) [25] ; Ugwu et al. (2002) [41] ; Regner et al. (2006) [42] ; Meijer et al. (2012) [21]). In gas-liquid dispersions, an open geometry with blades is usually recommended and employed (Thakur et al. (2003) [2] ; Madhuranthakam et al. (2009) [8]).

It is, however, necessary that further studies be carried out in order to enhance static mixers performance and to uncover possible future applications of these devices, particularly in the gas-liquid regime. In fact, these static mixers could potentially be used for stripping of gases in a liquid or, inversely, for saturation of a gas into a liquid.

1.2 Objective of the study

As stated above, the dispersion of a gas into a liquid phase is a widely spread operation in different branches of the industry, going from the production of fuels, to their purification from pollutants up to the food industry or even in the cosmetic processes. All the aforementioned fields have dispersive processes in common. Several types of dispersion devices are required in the industry, depending on to the type of compounds involved and on the products.

Static mixers were deeply examined during the last decades starting from the work of Grace (1982) [4] and continuing with the research of many authors such as Li et al. [5], Legrand et al. (2011) [6], Fradette et al. (2006) [7], Madhuranthakam et al. (2009) [8]. These researches are just some among the long list of references who addressed this topic. Unfortunately, the abundant literature about this subject does not cover completely the case of gas-liquid dispersion in static mixers. Further experimental campaigns are necessary to address this issue.

Researches on hydrodynamics inside static mixers remain limited. There are key questions and notions that are still not well discussed in the literature such as the behaviour of the static mixer when the liquid is stationary (or when the liquid velocity is negligible compared to the gas one) and also the behaviour of static mixers in the gas-liquid regime. An in-depth study of the phenomena of dispersion, rupture and coalescence of gas bubbles in organic phases inside the Sulzer static mixer SMX^{TM} has not yet been fully uncovered.

Therefore, the ultimate goal of the present study is to answer to the following questions regarding the applicability of static mixers to stripping or saturation of gases into a liquid : Can a static mixer represent an alternative to a stirred tank or a bubble column ? Can this device ensure a good mixing between a rising gas and a stagnant liquid ? What is the performance of this device when used with organic fluids ?

1.3 Approach to the problem

The ultimate aim of this research is to address the relevance of static mixers for gas-liquid applications in chemical engineering, like saturation or stripping (e.g. stripping of sulphur compounds in gasoline). Experimentations with water were performed to collect preliminary data. Heptane tests were however at the heart of this research. This compound may be considered comparable, in terms of physical properties, to gasoline.

As a starting point of the investigation, the liquid is kept stationary and its motion is induced by gas bubbles rising through it. Among classical gas-liquid contactors, the liquid phase is usually stagnant in bubble columns while it can be either stagnant or mobile in structured packings (Engel et al. (2001) [43] ; Wild et al. (2003) [44] ; Luo et al. (2008) [45]). Static mixers are quite similar to packings. Even if the liquid motion was effectively considered in this work, its negligible effect compared to a stagnant liquid allowed to focus only on the case of a stagnant liquid. Experiments with liquid circulation, both counter-current and co-current, were nevertheless carried out to verify the congruence of results. Furthermore, the stagnant liquid allowed either to perform the analysis with fewer errors or to serve as a reference for further investigation with a flowing liquid.

The characterization of the hydrodynamics of the SMX was conducted by using two optical experimental methods : the Particle Image Velocimetry (PIV) and the Backlight Shadowgraph Technique (BST). These techniques were commonly employed to investigate the hydrodynamics of multiphase flows (Chen and Fan (1992) [32] ; Delnoij et al. (2000) [46] ; Boëdec et al. (2001) [47], Boyer et al. (2002) [48] ; Aubin et al. (2004) [49], Zaruba et al. (2005) [50] ; Aubin et al. (2010) [51], Sathe et al. (2010) [10] ; Sobieszuk et al. (2012) [52] ; Sathe et al. (2013) [53] ; Ayati et al. (2015) [54] ; Laupsien et al. (2017) [29]). Most of the previous studies used these optical techniques for studying bubble columns, microreactors and gas-liquid-solid fluidized beds. In the present study, we applied these techniques to quantify the flow pattern inside the SMX static mixer. Furthermore, the main advantages and drawbacks of the Backlight Shadowgraph Technique (BST) and Particle Image Velocimetry (PIV) were reported. The gas hold-up in different operating conditions was also experimentally estimated. This is an important parameter as it is related to the interfacial area between the phases. The effect of the SMX mixing elements on the velocity flow field is quantified.

The oxygen transfer inside the static mixer was measured in aqueous phase. The effect of

the static mixer was quantified. This analysis provided an indication of the increase in mass transfer due to the SMX static mixer. This investigation was performed using an oxygen microsensor.

Finally, numerical simulations were performed with the aim of "completing" the experimental data with detailed insights onto the hydrodynamics. Thanks to OpenFOAM®, a complete analysis of the system was performed. The numerical results were compared with the experiments in order to obtain a validation of our CFD model. Several parameters, which are difficult to monitor through experimental techniques, could be obtained with the CFD.

1.4 Organization of the dissertation

The present dissertation was divided in two main parts containing a total of eight chapters. This layout allowed us to maintain a coherent structure and to make it possible to find the desired and interesting parts in a convenient way. The first part reports and describes the experimental results, while the second part illustrates the numerical methods used and the CFD results obtained.

Chapter 1 is the introduction to the thesis. Chapter 2 summarizes the main researches and results concerning the static mixers available in the literature. This chapter is divided into sections, starting from generalities to static mixers literature, and ending with experimental techniques as used in the present work.

Chapter 3 handles and deepens the experimental analysis techniques adopted. Details on operating principles and experimentation strategies can be found in this chapter. The problems encountered and the solutions implemented to stem them were also illustrated. Specific sections deal with each techniques and associated settings used in the laboratory experiments, briefly gas hold-up, mass transfer, PIV and shadowgraph techniques. Chapter 4 is devoted to the discussion of the achieved results. The methods used to obtain the results and their reliability were also addressed. In this chapter, a broad discussion was opened about important results that can be further developed in future research.

Chapter 5 provides details on the main numerical methods available for CFD simulations, and more specifically on the methods implemented in OpenFOAM®. Chapter 6 describes in details the elementary test cases that were performed to obtain and define the parameters and settings of our simulations. Chapter 7 presents the main results obtained by CFD simulations on the full 3D static mixer. These results were compared with the experimental ones in order to validate the model and to provide additional information and analyses.

Chapter 8 briefly summarizes this work. In addition, recommendations for future work were added.

Chapter 2

Literature review

The aim of chapter 2 is to report the main results of previous studies and experiments concerning static mixers and others which may be useful to the present work. The wide scope of the literature led us to divide the information found in sections.

As explained in the introduction, many industrial processes require gas/liquid dispersions. The section 2.1 is dedicated to generalities on dispersions. A series of studies was done to improve the efficiency of mixing and to point out which is the best mixing device for each industrial application. This is discussed in section 2.2.

This thesis is focused on the SMX static mixer, a device with high mixing efficiency and low energy required. The section 2.3 presents a literature review on static mixers. The behaviour of static mixers in the laminar flow regime was deeply studied in the past for liquid/liquid systems. In the last decades, a series of studies were carried out to point out the main physical mechanisms that rule drop's behaviour inside mixers. Grace (1982) [4] lays the groundwork for uncover how drops behave inside a helical static mixer. Grace (1982) [4] presents a part focused on drop deformation and breakup in rotational shear fields (Couette) and in irrotational (extensional) shear fields. Understanding the behaviour of a single drop is essential to understand the complete system acting. The results were correlated with the results in presence of a helical mixer. Then, further research works were performed on the same topic. During the last years, the transition to turbulence regimes and the turbulent flow were analysed too.

The present study will examine gas/liquid laminar flows inside static mixers with local near to turbulent transition perturbations. Even today, the mechanisms of breakage and coalescence of gas bubbles inside a static mixer are not completely covered.

In addition, many authors deemed the pressure drop as one of the most important parameters that should be caught during the experiments [2, 5, 26]. The pressure drop allows to assess the required energy for the mixing. Pressure drop measurements are also useful for the validation of CFD models.

2.1 Dispersions

In the field of mixing, dispersions are common required operations. A dispersion composed of two or more phases can be stable or unstable. Usually, one secondary phase is dispersed in a continuous primary phase. The main feature of dispersions is the heterogeneous composition of the system. Besides, the characteristic size of the dispersed phases has to be greater than the colloidal sizes (diameter $> 1\,\mu m$) [55].

Many types of dispersions are required in the industrial processes depending on the nature of substances involved and the tasks of the production. Moreover, different kinds of units can be used to achieve the dispersion, the choice among them being motivated mostly by the properties of the system and the nature of the substances involved. One of the most widespread process is the gas-liquid dispersion. This particular dispersion is usually achieved from two phases in which the dispersing phase is liquid, and the dispersed phase is gas. However, the opposite configuration, in which the liquid is dispersed in the gas, is also possible, like in sprays.

Dispersion of gas bubbles in a liquid is used in many processes in order to increase mass and heat transfers between the involved phases. In fact, at the same gas fraction, reducing of the diameter of the bubbles conducts to a considerable increase of the interfacial area. Usually, the gas-liquid dispersions are used to facilitate the mass transfer of a component from the gaseous phase to the liquid phase.

To point out the influence of the bubble diameter, it is convenient to introduce a particular case as an example : the dissolution of a gas at constant temperature. The Henry law can be used to calculate the concentration of the gas component in the liquid solution [55] :

$$P_\alpha \, H_\alpha = C_\alpha \tag{2.1}$$

where P_α is the partial pressure of the component α, H_α is the Henry constant and C_α is the concentration of α in the liquid. The Henry constant strictly depends on the nature of the gas, the temperature and the liquid. Therefore, each time that a gas is in contact with a liquid phase, the amount of mass transfer is proportional to the partial pressure of the gas component. Moreover, if the gas is considered ideal, it is possible to apply the Dalton's law and express the partial pressure as [55] :

$$P_\alpha = X_\alpha \, P \tag{2.2}$$

where X_α is the molar fraction of the component α and P is the total pressure of the mixture, i.e. the sum of all the partial pressures of all gas components. It is worth remembering also the importance of capillary pressure difference across the interface between a gas and a liquid. The Young-Laplace law can be applied [55] :

$$P_G - P_L = \sigma \left(\frac{1}{R_1} + \frac{1}{R_2} \right) \tag{2.3}$$

where P_G is the gas pressure inside the bubble and P_L is the pressure inside the surrounding liquid. The Young-Laplace equation says that the pressure drop between two immiscible phases is proportional to the surface tension and the two radii of curvature (R_1, R_2) of the surface, generated by the intersection of the surface with two orthogonal planes. Assuming

a spherical geometry of the gas bubble ($R_1 = R_2$), equation 2.3 can be written as follows [55] :

$$P_G = P_L + \sigma \left(\frac{2}{R_b} \right) \tag{2.4}$$

where R_b is the bubble radius. Supposing a constant pressure of the liquid phase p_l, it appears clear that decreasing R_b increases the bubble pressure P_G. Thus, the partial pressure of the component α increases, conducting to an increase of mass transfer.

In addition to the bubble pressure, other factors have to be taken into account when investigating the mixing performances of a dispersion : the overall surface of exchange, which is inversely proportional to the bubble diameters, the contact angle, and the liquid flow regime (laminar or turbulent).

2.1.1 Contact angle

The contact angle is one of the most important parameters for the dispersion. In fact, each time a bubble or a drop is in contact with a solid surface, a complex triple line is encountered. The angle formed between the phases is called contact angle. As can be seen from figure 2.1, the contact angle is a function of the phases involved, namely the physical characteristics of the substances. This parameter is also influenced by the kind of dispersion. For example, by switching the continuous phase with the dispersed phase, very different values of contact angle can be obtained [14].

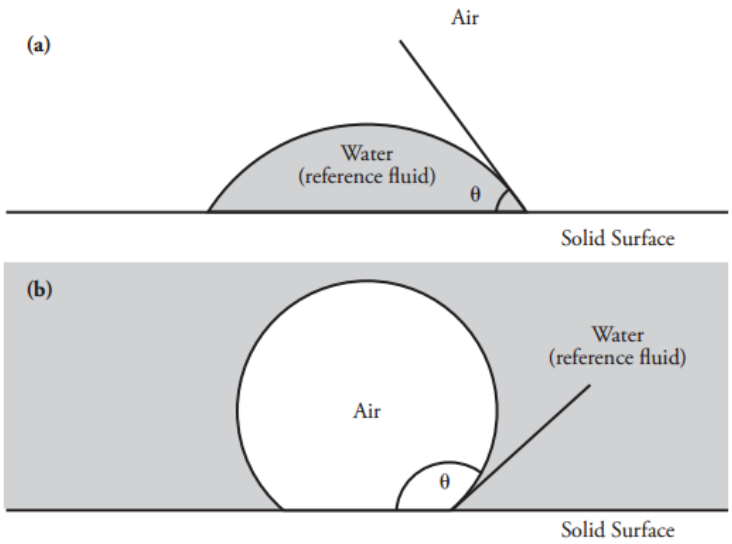

Figure 2.1 – Three-phase system in two different configurations. Taken from Akbulut et al (2012) [13]

The relationship between physical properties of the phases and the contact angle is given by the Young's equation (see equation 2.5). This equation represents the three-phase force equilibrium along the parallel direction to the surface (Di Marco (2005) [14]).

$$\sigma_{SG} = \sigma_{SL} + \sigma_{LG} \cos \theta_O \tag{2.5}$$

where σ_{SG}, σ_{SL} and σ_{LG} are respectively solid-gas, solid-liquid and liquid-gas surface tensions and θ_O is the contact angle. The contact angle in equation 2.5 can be used only for an estimation of the contact angle in *static condition* and once the system reaches the equilibrium. The modelling of the dynamical contact angle is more complicated and affected by numerous factors such as surface roughness, moving velocity, etc. [14].

2.1.2 Detachment models : bubble diameter estimation

Predicting the diameter of the bubble at the exit of the injector is essential to analyse the dispersive systems. Several models were proposed. Generally, the detachment bubble diameter should be a function of the parameters shown in the equation 2.6 below (Di Marco 2005 [14]) :

$$d_{eq,D} = f(Q_G, d_n, \rho_L, \rho_G, \mu_L, \mu_G, \sigma, K_{ori}, V_{ch}, g, \theta_O, h_{liq}) \tag{2.6}$$

where Q_G is the volumetric gas flow rate, d_n the orifice diameter, ρ the density, μ the viscosity, σ the liquid-gas surface tension, K_{ori} an orifice constant, V_{ch} the gas chamber volume, g the gravity, h_{liq} the liquid head and θ_O the static contact angle. Index L refers to the liquid and index G refers to the gas. The liquid head parameter could be neglected if it is greater than a few bubble diameters. If the gas density and gas viscosity are negligible compared to the liquid ones, then the equation 2.6 is reduced to [14] :

$$d_{eq,D} = f(Q_G, d_n, \rho_L, \mu_L, \sigma, K_{ori}, V_{ch}, g, \theta_O) \tag{2.7}$$

Of course, an increase of the gas flow rate causes an enhancement of the detaching frequency. When continuing the increase of the gas flow rate, dynamics effects come into play and the detachment volume increases. It should be highlighted that very high gas flow rates lead to bubble coalescence close to the nozzle and to a jet regime [14].

Gerlach et al. (2007) [56] distinguished two modes of the bubble growth at an orifice, which was also reproduced by CFD models. Figure 2.2 shows these two different patterns of growth of the bubbles. The way bubbles or drops grow up strongly affect their diameters. Figure 2.2(a) highlights a situation that may be characteristic for a thin nozzle. On the r.h.s. of figure 2.2(b) is shown a situation in which the bubble grows from an orifice on a surface [14].

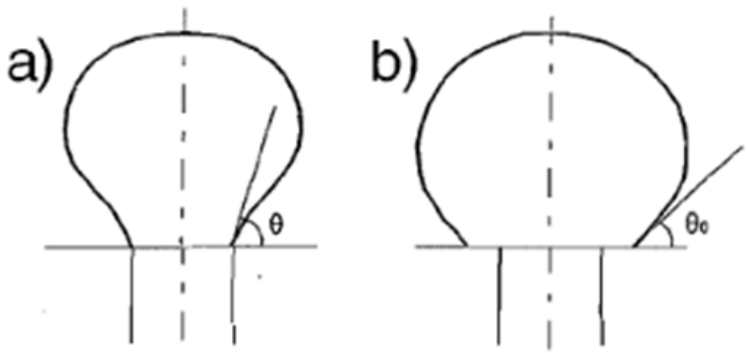

Figure 2.2 – Two different patterns of growth of the bubbles. Taken from Di Marco 2005 [14].

2.1.3 Laminar regime

As stated before, the flow regime affects significantly the mixing/blending capacity. There are two main types of flow : laminar and turbulent. The limit between them is not perfectly delineated. There is a transition zone which shows intermediate properties between the two regimes. The laminar flow is a condition that occurs when a fluid flows in parallel layers, without interaction between the different layers. This occurs at very low velocities [57].

In a laminar flow, there are no swirls nor eddies and no currents perpendicular to the main flow streamlines. The fluid particles have very uniform motions, in particular the particles near the wall, which flow in parallel lines to the wall surface. This translates into high momentum diffusion and very low momentum convection [57].

On the opposite, a chaotic movement of fluid particles governs the turbulent flow regime. The molecules in the fluid move in different directions and at different speeds [57]. Swirls and eddies are prevalent and cause a high shuffling of molecules. Figure 2.3 shows how an external body can change the flow condition and highlight the difference between the two kinds of flows.

The transition between a laminar and a turbulent regime is dependent upon the Reynolds number, defined as :

$$Re = \frac{\rho U L}{\mu} \tag{2.8}$$

where ρ is the fluid density, L and U are characteristic lengths and velocity of the system, and μ is the fluid viscosity.

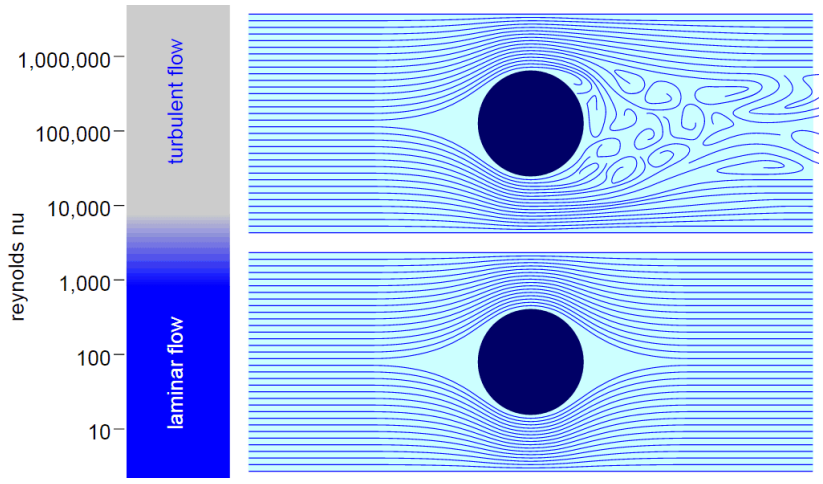

Figure 2.3 – Different flows : laminar and turbulent. Taken from Reactor Physics website [15].

Let's consider now a flow in a pipe, without any obstacles inside the pipe. At low Reynolds number, the flow is strictly laminar. Without obstacles, there is no perturbation and the fluid flows in straight multi-layers. By taking under examination a flow in a pipe, downstream the hydrodynamic entrance region, a transition region occurs where the velocity profile is not constant. Then, there is a region with a fully developed velocity profile. The length of the initial zone depends on the system properties. Figure 2.4 summarizes and explains the concepts illustrated before.

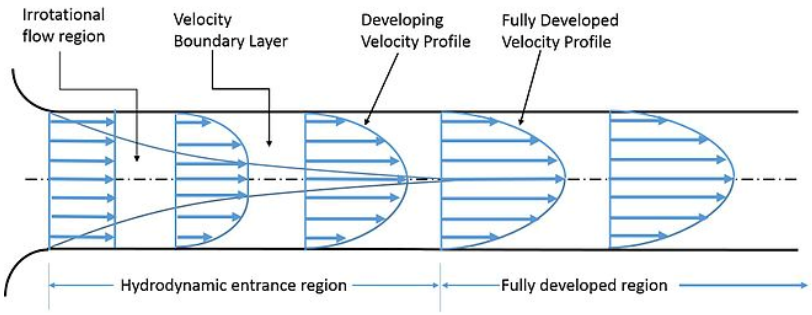

Figure 2.4 – Velocity profile in a tube. Taken from Cengel and Cimbala (2006) [16]

Figure 2.4 also shows that the tube inlet has a pure irrotational flow region. This behaviour is due to the feeding system and its extension is very short. Obviously, a velocity profile as shown in figure 2.4 does not allow radial mixing. By supposing two different liquid streams, one black and another white, each distributed in a semi-circular section of the pipeline, there will be no mixing of the two streams while crossing the tube (Thakur et al. 2003 [2]).

In fact, due to the undisturbed laminar flow, the two layers remain straight, and the two fluids will exit from the pipeline as they entered. Limited mixing at the interface could be caused by the molecular diffusion. Under these assumptions, it will be impossible to have an efficient mixing in a laminar pipe flow without a suited device (Thakur et al. 2003 [2]).

2.1.4 The capillary number

One of the most important parameters that can be used to figure out the stability of a gas-liquid dispersion is the capillary number. This dimensionless number is linked to the probability to obtain drops/bubbles break-up. It characterizes the relative effect of viscosity forces over the surface tension that act at the interface between two immiscible fluids. This definition can be applied between a liquid and a gas or two immiscible liquids (Marculescu et al. 2016 [58]).

In the case of a gas dispersed in a liquid, a bubble tends to be deformed by the friction of the liquid flow due to viscosity effects. On the other hand, the surface tension forces tend to decrease the surface. For Newtonian fluids, the dimensionless capillary number is defined as :

$$Ca = \frac{\mu_L U}{\sigma} \tag{2.9}$$

where U and μ_L are respectively the velocity and the viscosity of the liquid (or continuous phase) and σ is the surface tension or interfacial tension between the two fluid phases. For high values of Ca, the capillary forces are negligible with respect to the viscous forces. For low value of Ca (less than 10^{-5}), the system behaviour is dominated by capillary forces. The inertial forces do not dominate due to the laminar flow regime. The capillary number can also be defined as the ratio of Weber (see equation 2.29) to Reynolds number (see equation 2.39) [7].

$$Ca = \frac{We}{Re} = \frac{\mu_L U}{\sigma} \tag{2.10}$$

To summarize, the capillary number is defined as the dimensionless representation of the relative effect of viscous forces related to surface tension acting across an interface. This interface can be made up between a liquid and a gas or two immiscible liquids (Marculescu et al. 2016 [58]). By analysing the capillary number, Grace [4] and other authors predicted bubbles instability region ($Ca > Ca_{Critical}$) [7]. All their experimentations were done in steady state conditions (see chapter 2.3.1).

2.2 Mixing and dispersion units

The growing energy demand of industries and the decreasing availability of energy sources clearly orients the industry towards the choice of more energy-efficient systems. Like other processes, gas-liquid dispersion processes are required to be improved in terms of efficiency. This aim can be reached by increasing the interface between the phases, using as little energy as possible. In order to achieve this objective, in the last years, many studies were done. The most used devices for gas-liquid dispersions are the bubble columns and stirred tanks. However, it is not possible to identify a recommended unit type for all applications.

Theron et al. (2010) [38] performed experimentations to get a qualitative comparison of the energy required for mixing. In this study, the energy required to reach a specific value of the Sauter diameter was measured by testing a liquid-liquid dispersion in two different devices : the SMX static mixer and the stirred tank [38]. The study highlighted a higher mixing efficiency in the SMX due mainly to the uniform dissipation of the energy. Each drop undergoes the same shear stress and, furthermore, less energy per mass unit is required to mix the two liquids. Other studies brought similar results [38].

The industrial processes for which are required a high mixing efficiency in synergy with a low cost and a low maintenance, may be performed through a static mixer (Thakur et al. 2003 [2]). Table 2.1 resumes the principal advantages of the static mixer compared with mechanically agitated vessels.

Table 2.1 – Striations generated by some commercial static mixers. Taken from Thakur et al. (2003) [2].

Static mixer	**CSTR**
Small space requirement	Large space requirement
Low equipment cost	High equipment cost
No power required except pumping	High-power consumption
No moving parts except pump	Agitator drive and seals
Small flanges to seal	Small flanges plus one large flange to seal
Short residence times	Long residence times
Good mixing at low shear rates	Locally high shear rates can damage sensitive materials
Fast product grade changes	Product grade changes may generate waste
Self-cleaning, interchangeable mixers or disposable mixers	Large vessels to be cleaned

It appears clear that static mixers are more energy saving than stirred tanks. Experimentations, simulations and data analysis collected useful results to better understand the suitable static mixer for each particular case. The complexity of the flow through a static mixer leaves undiscovered physical behaviours [2], which limits their application range in the industrial field.

2.2.1 Bubble column and packings

A bubble column is constituted by a cylindrical vessel with a gas distributor at the bottom. This kind of device is extensively employed in the chemical industry, namely, to achieve gas-liquid (or gas-liquid-solid) dispersions. The bubble column reactors belong to the general class of multiphase reactors. Multiphase reactors might be divided into three main categories : trickle bed reactors (fixed or packed bed), fluidized bed reactors, and bubble column reactors [59, 60].

The mass transfer is a critical parameter for many industrial processes. Bubble columns packed with static mixers or packings are extensively used to increase the mass transfer. We then talk about packed column category of reactors. Fan et al. (1975) [61] affirmed that the mass-transfer coefficient is almost doubled by using a static mixer while the pressure drop only increases slightly. The packing enables to control the hydrodynamics and to enhance the mass transfer of bubble columns. Moreover, it might be used to support the catalyst, especially with extreme operating conditions, namely at high pressure and temperature (Bhatia et al. (2004) [62]. The mass transfer coefficients for gas absorption and desorption in packed columns were deeply investigated by several authors, for instance, Onda et al. (1968) [63], Goto et al.(1975) [64], Charpentier (1976) [65] and Wang et al (1978) [66].

The fluid dynamic characterization of bubble column reactors has a significant effect on the bubble column performance [60]. According to literature, the mixing efficiency strictly depends on the regime prevailing in the column [60]. Figure 2.5 depicts the flow regimes in bubble columns.

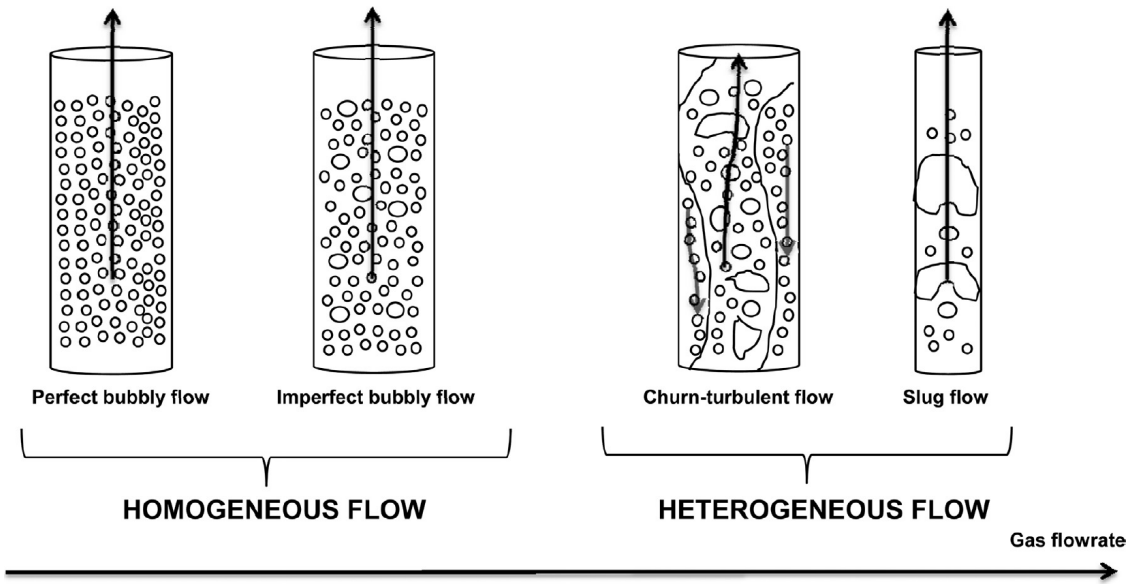

Figure 2.5 – Main flow regimes in bubble columns. Taken from Leonard et al. [17].

The flow regimes in bubble columns are classified according to the superficial gas velocity. Three types of flow regimes are commonly observed, namely the homogeneous (bubbly flow) regime, the heterogeneous (churn-turbulent) regime and the slug flow regime (Hyndman et al (1997) [67], Kantarci et al (2005) [60]). These flow regimes are illustrated in figure 2.6. The shared areas in figure 2.6 indicate the transition regions. The exact boundaries of these regions strongly depend on the system considered [60].

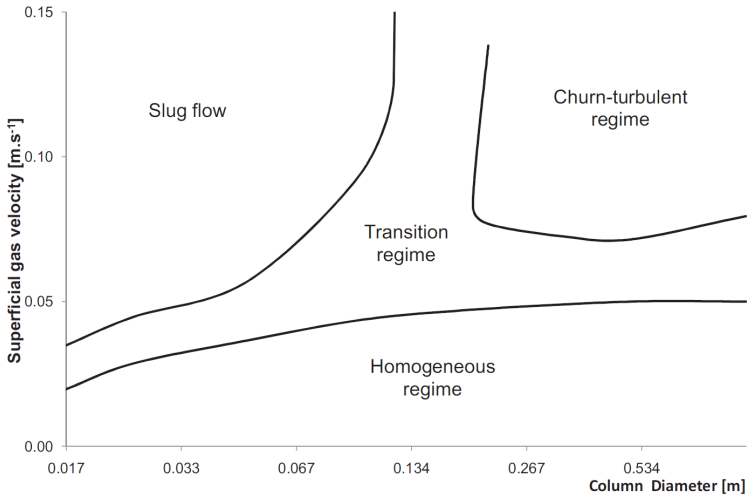

Figure 2.6 – Flow regime diagram at ambient pressure and temperature. Air/water system. Taken from Leonard et al. (2015) [17].

The bubbly flow regime or homogeneous flow regime is obtained at low superficial gas velocities (less than 0.05 m/s). This flow regime is characterized by bubbles of relatively uniform small sizes and rise velocities [60]. Moreover, this regime is marked by a uniform bubble distribution and gentle mixing. There is almost no bubble coalescence or break-up. The bubble sizes are thus dictated by the injector/nozzle design and system properties (Thorat et al. (2004) [68]). The gas hold-up (ϵ_G) increases linearly with increasing superficial gas velocity [60].

The churn-turbulent regime or heterogeneous regime is observed at higher superficial gas velocities (greater than 0.05 m/s). This regime is characterized by zones with homogeneous gas-liquid regime and liquid recirculation. The unsteady flow patterns lead to large bubbles and therefore short residence times [60]. These large bubbles are formed by coalescence due to high gas throughputs. A wide bubble size distribution is caused by coalescence and break-up phenomena. The bubble size might range from a few millimetres to a few centimetres. The mass transfer coefficient k_La is lower at heterogeneous regime as compared to homogeneous flow [60].

The slug flow regime is mainly observed in small diameter laboratory columns at high gas flow rates. This regime is characterized by the formation of bubble slugs [60]. In micro-reactors, we talk about Taylor flows (Abadie et al. (2011) [69]).

The gas hold-up is a dimensionless parameter that characterizes transport and dispersion phenomena of bubble column systems (Luo et al. (1999) [70]). Gas hold-up is strongly dependent of the operating conditions (pressure, temperature, system, superficial gas velocity, gas sparger, column design etc...). The superficial liquid velocity was reported to be a relevant

parameter for the determination of the gas hold-up [17]. Several authors investigated the gas hold-up for air in aqueous system. For instance, Hikita et al. (1980) [71] studied the effect of various electrolytes on the gas hold-up. A common trend of the gas hold in aqueous system is reported in figure 2.7.

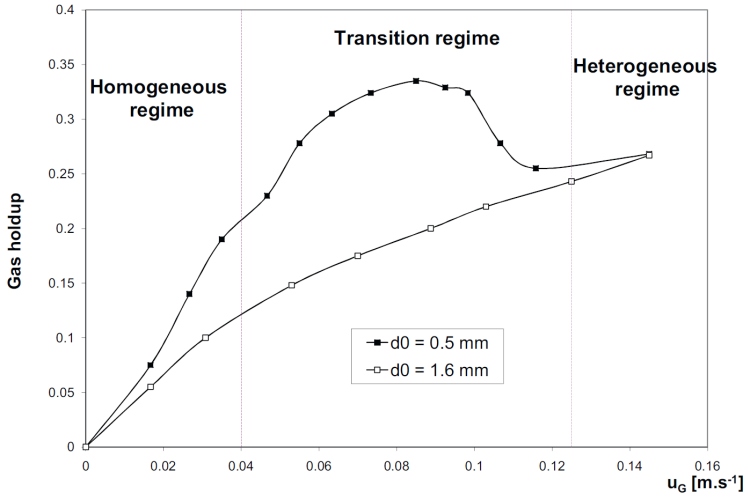

Figure 2.7 – Gas hold-up (ϵ_G profile versus superficial gas velocity, $D_c = 0.14$ m. Air/water system. (Zahradnik et al., 1997 : Duality of the gas-liquid flow regimes in bubble column reactors). Taken from Leonard et al. (2015) [17].

2.2.2 Static mixers

A static mixer is a device which has to be inserted into a housing or pipeline to ensure mixing of fluids. It is composed by a series of inserts, containing holes, channels, helical elements and oblique blades which cause local accelerations and stretching of the fluids. These recombination, splitting, accelerations and decelerations considerably increase the mixing of the currents flowing through it.

The energy required for mixing derives from the pressure drop of the fluids which flow through the static mixer. Higher pressure drops yield higher flow rates and better mixing efficiency. Nowadays, static mixers are commonly used in many industrial applications, because of their ease to install or maintain, and because they can operate at high temperatures or pressures. Compared to stirred tanks, static mixers do not have any mobile part and present better mixing performances at lower energy requirements [2].

The small space required, low cost, high efficiency in mixing, low maintenance and surface area generation in the dispersion processes contributed to the development of static mixers in recent years. Even mixing with processes that use corrosive substances can be carried out with these classes of devices [2].

In recent years, different geometries of static mixers were developed, to meet and to satisfy all the requirements of the market. The main static mixer models are the helical static mixers (e.g. the Kenics), the low-pressure drop static mixers, the corrugated plates and the crossbar static mixers (e.g. the SMX and the SMXL). All models listed above are based on the same principle, namely the mode of division and recombination of the currents, illustrated previously [2].

Static mixers are all characterized by a different structure, to allow their application in various industrials fields. Usually the static mixer body is made up of elementary structural units, "plates, baffles, helical" or "geometric grids", which are repeated several times to form the complete device. It goes from low-pressure drop in the helical static mixers, accompanied by modest mixing efficiencies, to high-pressure drop and high mixing efficiencies to the static mixer SMX. Figure 2.8 portrays the main models of static mixers available on the market today.

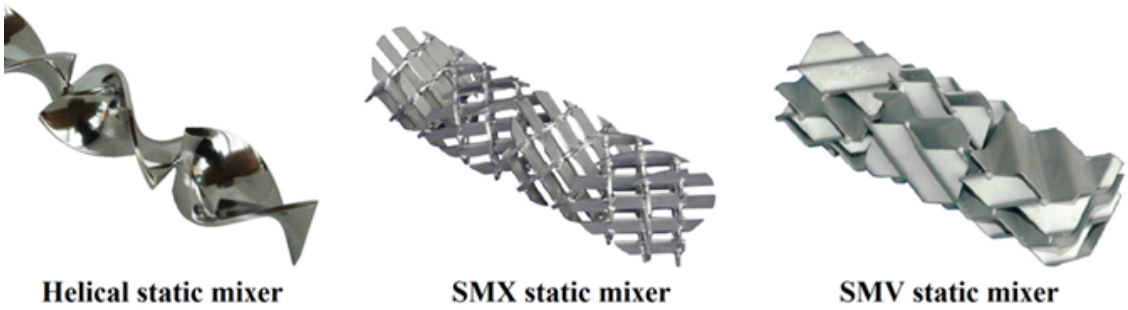

Figure 2.8 – Main models of static mixers. Taken from StaMixCo website [18].

Even in laminar regime, the static mixer can ensure a good degree of mixing. By increasing both the axial and radial mixing, this device leads to homogenization of the fluids which flow through it. Some devices are made up of elements rotated at 90 degrees from the previous one. This feature enables a better mixing efficiency [72].

Figure 2.9 gives an overview of the mixing efficiency by doing a comparison between liquids flow in an empty pipeline or through a static mixer. After four elements, a good mixing degree is reached between the white and blue fluids in the static mixer.

The presence of the static mixer changes a lot the velocity profile. As can be seen from figure 2.4, in an empty tube the fully developed velocity profile is tightly parabolic (Poiseuille flow). It appears clear that, with the static mixer, the velocity profile is strongly different. This allows flow mixing in the tube. Through the element units (holes, channels, blades etc.) the static mixer causes local stretching and radial flows that are never present in undisturbed laminar flows [2].

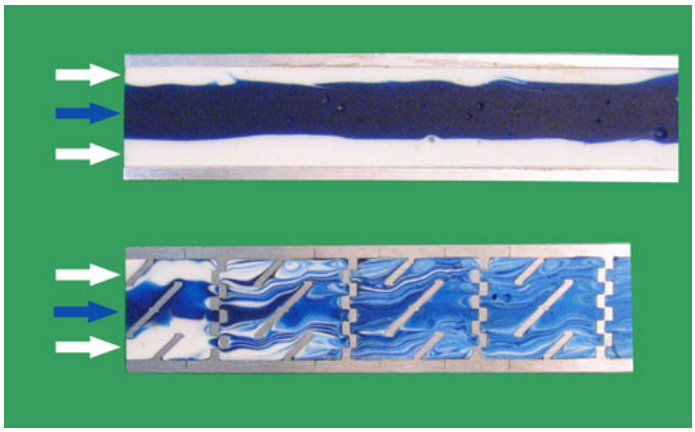

Figure 2.9 – Mixing in presence of a static mixer. (Laminar flow). Taken from StaMixCo website [18].

Geometry and applications

Over the years, many shapes of static mixers were developed. Such growth was mainly dictated by the willingness to cover different industrial applications. In the last years, existing geometries were optimized [42, 73].

Even though the number of static mixers on the market is high, these devices may be grouped in three major categories whose main exponents are the KMX, SMX and SMV, as illustrated in figure 2.8. These three mixers were studied by V. Stamilla (2016) [74] through the use of a high-speed camera. The objective of this experimental campaign performed at IFPEN in Solaize, was to explore static mixer behaviour for a gas/liquid two-phase system conducted with nitrogen bubbles flowing into heptane.

The SMV and SMX mixers conducted to better efficiency in case of gas liquid dispersion. A considerable increase of the residence time of the gas in the liquid and bubble rupture was noted (V. Stamilla 2016 [74]). In contrast to this, the Kenics does not influence much the residence time and leads to bubble coalescence only for high gas flow rates. The SMV mixer shown a higher residence time than the other devices. This is mainly due to the higher pressure drop through it [74]. These considerations led to the choice of the SMX deemed the most suitable to the nitrogen dispersion in heptane, or more generally to the gas-liquid dispersion with similar characteristics.

The standard SMX

The SMX static mixer is constituted by an elementary unit repeated along the axis. The number of these elements depends on the required application of the device. Each element is rotated at 90 degrees with respect to the previous one. SMX elements are formed by a series of inclined blades to 45 degrees from the axis (see figure 2.10). The standard version of this device presents geometric constraints such as the length to diameter ratio of an element is equal to one [38].

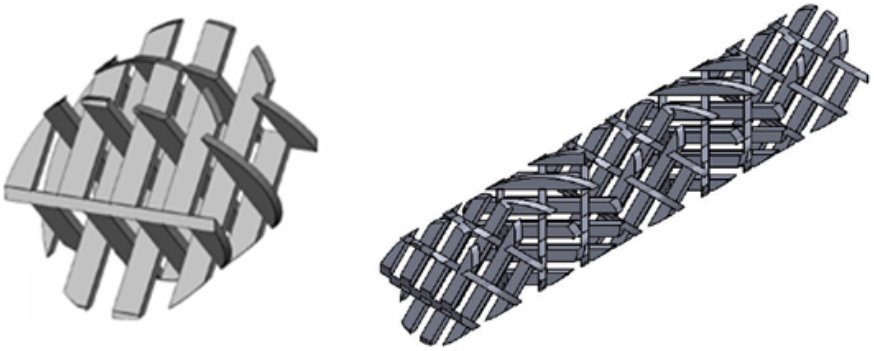

Figure 2.10 – Single SMX element (left) and series of five SMX elements (right) - Scala M. 2016 [19]

The standard Sulzer SMX is also called SMX (2, 3, 8). This is a proper nomenclature for classifying unequivocally the device geometry [19]. The first number represents the number

of crosses over the height of the channel, the second one the number of parallel bars over the length of one element and the last one the number of crossing bars over the width of the channel (Meijer et al. (2012) [21]).

2.3 Literature review of Static mixers

The main purpose of section 2.3 is to resume the available data in the literature concerning dispersion in presence of static mixers. This data collection also validates the choice of the current study, namely the examination of just one static mixer geometry : the SMX. Experimental data and numerical simulations tend to affirm that this device is one of the most suitable for the gas liquid dispersion.

Gas liquid dispersion in presence of the SMX was deeply analysed by several authors, for instance by Liu et al. (2005) [28], Fradette et al. (2006) [7], Madhuranthakam et al. (2009) [8]. Fradette et al. [7] performed a significant work concerning the gas-liquid dispersion with the SMX in the laminar regime. This work allowed a better understanding of the rules governing this particular biphasic system (see section 2.3.1).

2.3.1 Dispersion phenomena

Drops deformation and breakup are correlated to the shear field. The drop behaviour is strongly influenced by the type of flow : simple shear, Couette, extensional etc. A Couette shear occurs when a viscous fluid flows in laminar regime between two parallel planes that are moving in opposite direction. Figure 2.11 shows a drop under a simple shear flow (Ioannoua et al. (2016) [20]).

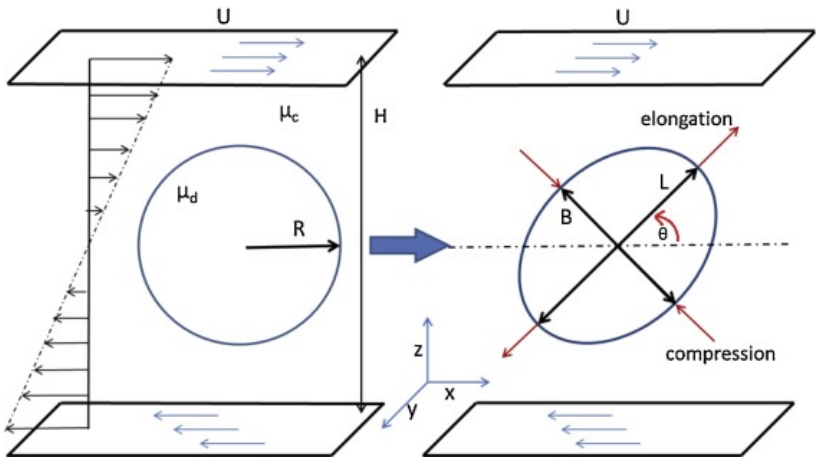

Figure 2.11 – Bubble/drop deformation under simple shear. Taken from Ioannoua et al. (2016) [20].

Under the shear flow the drop deforms and takes an ellipsoidal shape. We can define the drop deformation D_d (or D) as [4, 20] :

$$D_d = \frac{L - B}{L + B} \tag{2.11}$$

where L and B are the two the principal semi-axes of the ellipsoid. In order to better classify the system, many researchers introduced the viscosity ratio p_μ, defined as the ratio between the viscosity of dispersed phase and the viscosity of the continuous phase [4] :

$$p_\mu = \frac{\mu_d}{\mu_c} \tag{2.12}$$

where μ_d and μ_c are respectively the viscosity of the dispersed and the continuous phase. The parameter E was introduced by Grace [4], as stated in equation 2.13. E is defined as the ratio of viscous to interface tension forces necessary for burst :

$$E = \frac{G\ r_d\ \mu_c\ f(p_\mu)}{\sigma} \tag{2.13}$$

where G is the shear rate, r_d the drop radius and σ the surface tension among the involved phases.

Taylor demonstrated that for small deformations D is equal to E. Furthermore, he suggested a function of the viscosity ratio f (reported in equation 2.14) which varies from 1 to 1.2 [4, 75] :

$$f(p_\mu) = \frac{19p_\mu + 16}{16p_\mu + 16} \tag{2.14}$$

If the viscosity ratio p_μ ranges from 0.1 to 1.0, the deformation at the burst (D_a) is equal to E at burst (E_B). The shear rate at the burst (G_B), the drop radius (r_d) and the surface tension (σ) impact thus on the required deformation to reach the drop break-up. These information are resumed in the equation 2.15 (see [4]) hereafter :

$$D_a = E_B = \frac{G_B\ r_d\ \mu_c\ f(p)}{\sigma} \tag{2.15}$$

Grace (1982) [4] observed the effects of single drop deformation until its burst by using a Couette device. He used equation 2.13 to model the results. Figure 2.12 illustrates that there exists a linear correlation between G and drop deformation for small deformation value.

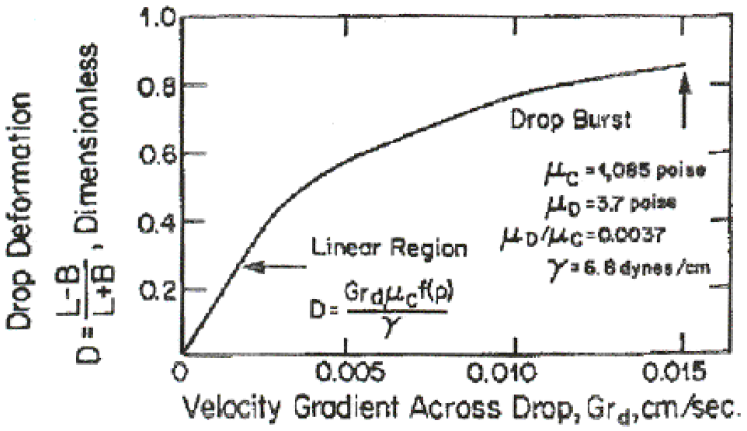

Figure 2.12 – Correlation between velocity gradient across drop and the drop deformation. Taken from Grace [4]

Grace [4] proved experimentally that at very low, or very high, value of viscosity ratios, it becomes indeed difficult to break drops with uniform rotational shear. That explains why the gas dispersion in high viscosity liquids is a complex operation. Figure 2.13 shows the aforementioned behaviour. From figure 2.13, it can be deduced further that the required deformation for drop break-up has a minimum when the viscosity ratio ranges from 0.1 to 1.

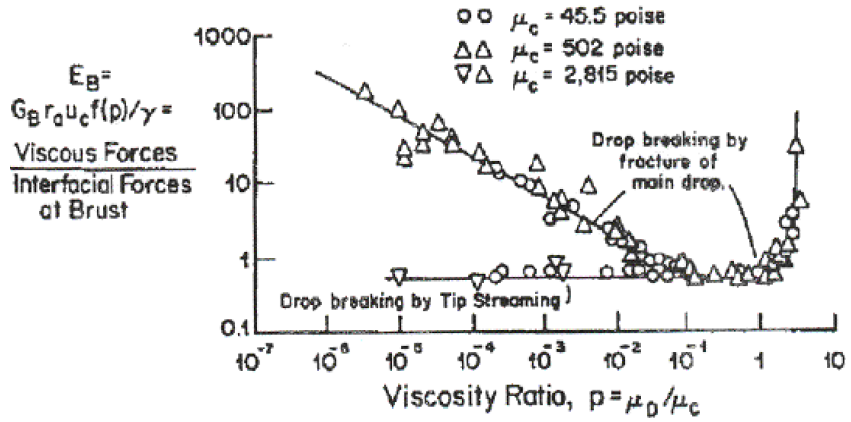

Figure 2.13 – Effect of viscosity ratio on ratio of viscous force to interfacial tension forces necessary for drop burst. Taken from Grace [4]

Other important results were obtained for irrotational flows by Grace [4]. The flow is irrotational when the vorticity is equal to zero everywhere in the system. The experimental results reported in figure 2.14 points out that, with an irrotational shear, it is simpler to break up the drops than with simple rotational shear (Couette). The data were extrapolated from a four-roll device.

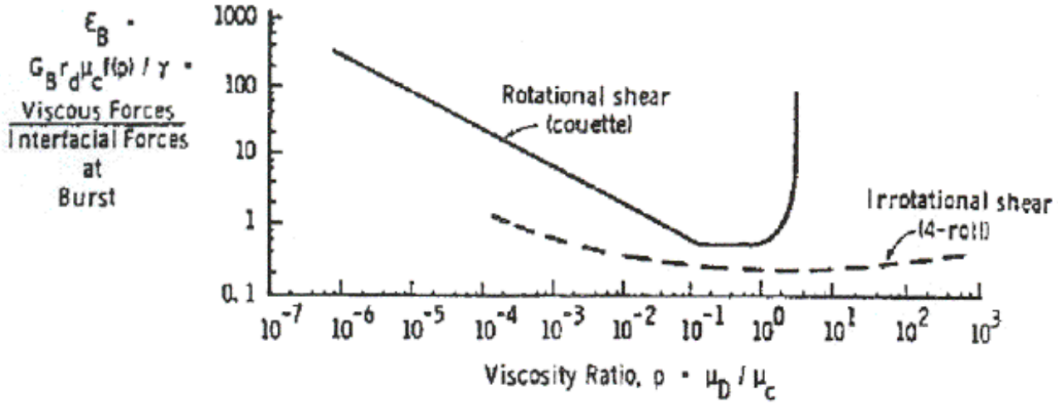

Figure 2.14 – Comparison of different shear fields : rotational and irrotational. Taken from Grace [4].

Grace shown that drops contained in high viscosity ratio systems (greater than 3.5) cannot be broken with a simple rotational shear [4]. The break-up can be achieved with an irrotational shear. Furthermore, he quantified the irrotational shear component in the Kenics mixer.

Grace noticed that the irrotational shear component is weaker than the rotational component. However, the irrotational component is sufficient to enable the mixer to be used for dispersion at viscosity ratios above 3.5 [4]. Lastly, Grace affirmed that the generation of the irrotational shear within the Kenics static mixer is related to the inter-laminar transfer occurring thanks to the radial circulation in the twisting elements (see figure 2.8).

Rallison in 1984 [76] proved that the extensional components are more efficient among all the irrotational component of a flow field to get dispersions. In 1994, Manas-Zlockzower [77] provided a scheme for the flow characterization. This scheme is based on the division of the velocity gradient tensor $\ddot{u}$ into its anti-symmetric and symmetric parts :

$$\ddot{u} = \frac{1}{2}[(\nabla v + \nabla v^T) + (\nabla v - \nabla v^T)] \tag{2.16}$$

$$\ddot{u} = D + \Omega \tag{2.17}$$

In her study, Manas-Zlockzower [77] defined the extensional efficiency parameter α as :

$$\alpha = \frac{|D|}{|D| + |\Omega|} \tag{2.18}$$

where D is the deformation and Ω is the rotational component of the velocity gradient tensor. α allows the characterization of the flow field. Although *alpha* can take any intermediate value, particular border values are illustrated below ([2, 7]) :

- $\alpha = 0$ pure rotational ;
- $\alpha = 0.5$ simple shear ;
- $\alpha = 1$ pure extensional.

In summary, the superficial force, namely the surface tension, leads to drops and bubbles coalescence and is opposed to their break-up. In a non-moving system, the equilibrium configuration is reached when the phases are completely separated, and the interfacial area is minimum. Dynamic systems have a different behaviour. As a matter of fact, a fluid flow causes drop and bubble break due to different local conditions. In the laminar flow, the Rayleigh-Taylor and the Kelvin-Helmholtz instabilities are the principal mechanisms which govern the drop break-up due respectively to surface tension and viscosity difference [78,79].

Elongated structures, that are formed in laminar flows, are metastable and will break in smaller drops. Different sizes of drops can be obtained [4]. In a biphasic dispersion, small drops which are close can coalesce and as opposed big drops can break-up. When the two mechanisms have the same rate, a dynamic equilibrium is reached. In this particular case, the drops distribution is almost constant [4].

Fradette et al. [7] obtained from the curves of Grace (1982) [4] the following two equations able to predict the critical capillary number in simple shear (equation 2.19) and elongation shear (equation 2.20) as conditions function of the viscosity ratio p_μ :

$$Ca_{cri} = 0.18 p_\mu^{-0.536} \tag{2.19}$$

$$Ca_{cri} = 0.2 p_\mu^{-0.142} \tag{2.20}$$

The effective shear rate γ_{eff} can be obtained from equation 2.21 below, once the critical capillary number was calculated :

$$\gamma_{eff} = Ca_{cri} \frac{\sigma}{d_{32}\ \eta_{proc}} \tag{2.21}$$

where η_{proc} designs the process viscosity value which is obtained from the pressure drop combined to the total flow rate (Fradette et al. 2006 [7]). d_{32} is the Sauter diameter obtained experimentally. Fradette et al. provided a correlation between the mixing energy inside the SMX and the effective shear rate (equation 2.21) required to reach the critical capillary number in two different situations : simple shear (equation 2.19) and elongation (equation 2.20). The results are illustrated in figure 2.15.

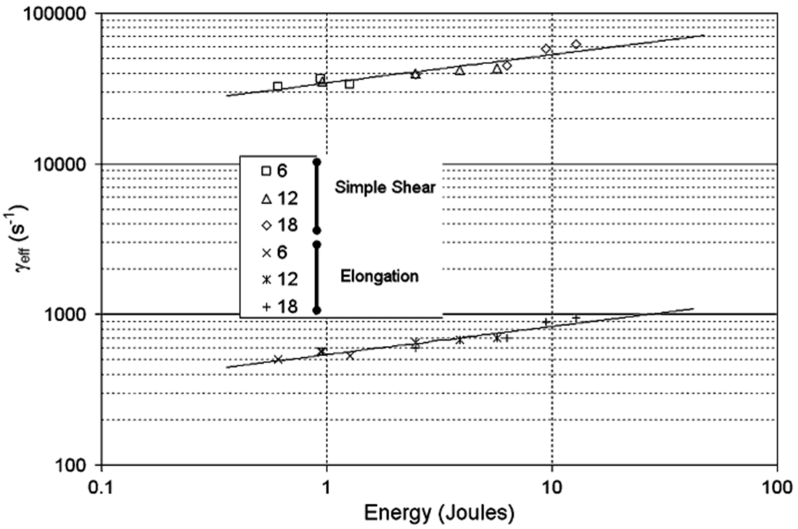

Figure 2.15 – Energy in the SMX in function of the shear rate required to reach the Ca_{cri}. Taken from Fradette et al. (2006) [7].

In figure 2.15, the effective shear was calculated using the mean diameter at the exit of the SMX. The effective shear rates based on the elongation shear, namely calculated by using equations 2.20 and 2.21, have a range between $500\,s^{-1}$ and $1000\ 1000\,s^{-1}$. These values are reachable inside static mixers [7].

Simple shear cannot be the dominant shear inside the device. In fact, when looking at the values of effective shear rates, these are too high for SMX mixing devices. Such high values are typically reached in high speed rotating equipment. This implies that, in the SMX static mixer, the elongation shear is the predominant shear type [7]. Thus, Fradette et al. (2006) [7] shown that the elongation shear is the major contribution to the bubbles size reduction and the simple shear has not a significant effect on it.

Furthermore, Fradette et al. (2006) [7] did a comparison between their results and those obtained by Grace (1982) [4] who had examined the Kenics static mixer. The comparisons were made by analysing the shear rate required to reach the same average diameter in each mixer, of course, operating in different conditions. Table 2.2 summarizes the experimental conditions used in the Grace work, listed in the second and third column, while the results coming from Fradette et al. are listed in the last column.

Table 2.2 – Experimental condition used in Grace's work (Kenics) and Fradette et al.'s work [7].

	Kenics #1	**Kenics #2**	**SMX**
Dispersion type	L/L	L/G	L/G
σ [N/m]	0.0085	0.0144	0.07
η_c [Pa s]	108	108	0.8
p_μ	$1.2\ 10^{-2}$	$4.6\ 10^{-4}$	$2.3\ 10^{-5}$
σ_2/σ_{ref}	1.0	1.7	8.0
η_2/η_{ref}	1.0	1.0	135.0
Ca_2/Ca_{ref}	1.0	7.1	36.0
γ_2/γ_{ref}	1	12	39532

It should be noted that the first case was taken as a reference case for the table. By analysing Table 2.2, it can be deduced that a factor of 12 in the shear rate is necessary to reach the same mean diameter in the two Kenics mixers. On the other hand, by doing a comparison between the Kenics and the SMX, it can be seen that there is a factor 40 000 times which is needed to produce the same sizes distribution [7]. It is worth pointing out that this case is far from industrial processes where an important number of drops or bubbles flow in the mixer with consistent interactions between them [7].

A work about the Sulzer SMX static mixer was done by Mutsakis et al. (1986) [80]. They evaluated the critical capillary numbers for Newtonian fluids with viscosity ratio below than 1. Figure 2.16 reports the experimental data obtained from Mutsakis et al. (1986) [80]. They established that, in presence of the SMX, the critical capillary numbers are close to the 2D elongation region, which was identified by Grace (1982) [4].

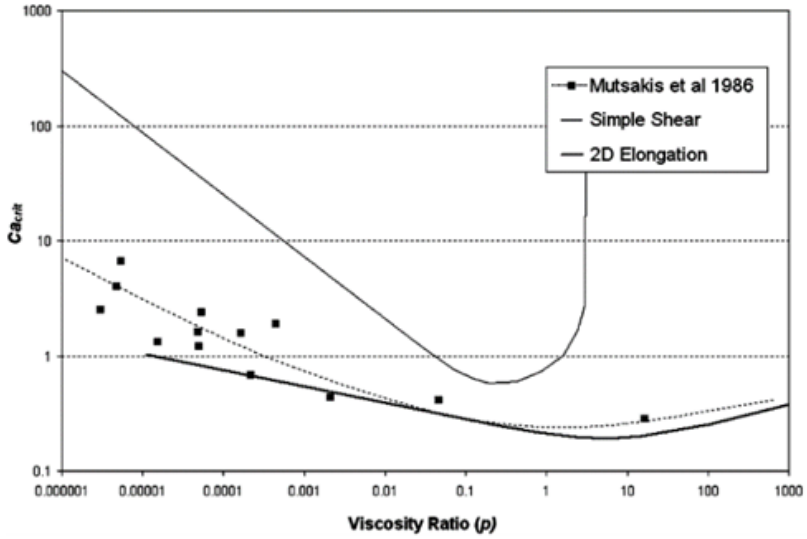

Figure 2.16 – Experimental results from Grace (1982) and Mutsakis et al. (1986). Taken from Fradette et al [7].

The curves obtained are function of the viscosity ratio and were made in steady state

two-dimensional flow conditions. The flow in presence of the SMX is very different : three-dimensional, non-symmetric and with non-constant shear stress [7]. Numerical investigations of the performance of several static mixers were done by Rauline et al. (1998) [24]. This study highlighted that the mean extensional efficiency parameter α for the SMX is approximately 0.6, which is close to the simple shear value (0.5). However, this is only a mean value of the extensional efficiency parameter that does not portray local phenomena [7].

2.3.2 Liquid-Liquid mixing through static mixer

Static mixers were initially designated for blending liquids in laminar flow. Other industrial applications appeared later. The main goal was to find something that could enhance axial mixing by splitting the inlet fluids in multi layers [2]. The SMX and SMXL make use of blades and baffles to split the fluid in multiple layers. They produce a distributive mixing. This type of mixing is due to convection rather than molecular diffusion. Homogeneity on molecular scale may be achieved by increasing the distributive mixing degree.

The striation thickness was provided by Mohr et al. (1957) [81] to explain and quantify the distributive mixing in a liquid-liquid system. Figure 2.17 illustrates how the striation thickness decreases when the fluids are sheared in axial direction, namely perpendicularly to the striations [2].

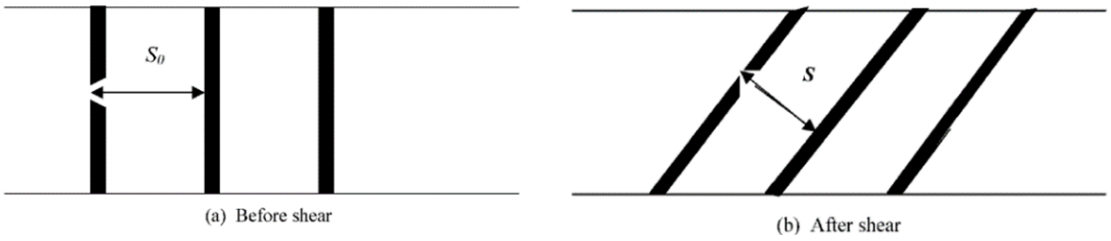

Figure 2.17 – Striation thickness under simple shear. Taken from Thakur et al. (2003) [2].

By increasing the shear, the interfacial area will increase. However, the simple shear efficiency decreases much when the striations are aligned with the shear direction. Higher mixing efficiencies could be achieved by changing the shear direction periodically. In addition, splitting and recombination of the striations improve the mixing efficiency. All these mechanisms can be found within static mixers. Figure 2.18 shows how a static mixer works in laminar regime [2].

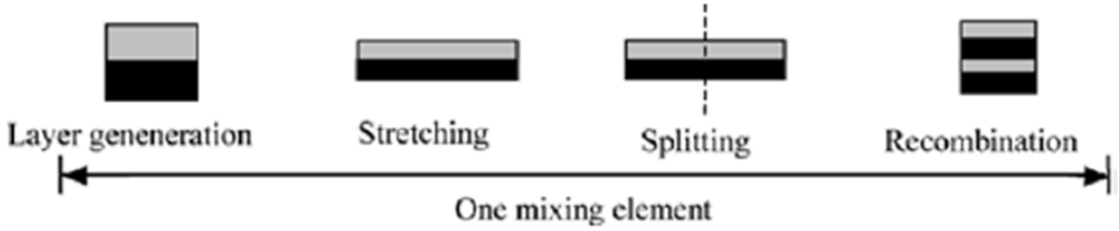

Figure 2.18 – Mechanism of mixing in a static mixer in laminar flow. taken from Thakur et al. (2003) [2].

Figure 2.17 and figure 2.18 refer to a $2N$ mixing process, where, every element of the static mixer increases by a factor 2 the number of layers, and N is the number of elements. This specific configuration is characteristic of the Kenics and the LPD (low-pressure drop) static mixer. Other theoretical numbers of striations generated by static mixers are illustrated in table 2.3 [2].

Table 2.3 – Striations generated by some commercial static mixers. Adapted from Thakur et al. (2003) [2]

Kenics	**ISG**	**Inliner**	**SMV**
2^N	4^N	$3\,(2)^{N-1}$	$n_c\,(2\,n_c)^{N-1}$

Furthermore, figure 2.19 illustrates the main mixing mechanisms proposed by Edwards et al. (1992) [82] in laminar flow conditions. In their description of these phenomena, Edwards et al. [82] considered three ideal flows inside the mixer : simple shear, uni-axial extension and planar extension [2]. Edwards et al. [82] also noted that the extensional flow is much more effective at low shear than the simple shear and become even more efficient when the shear is large. This behaviour is due to the unfavourable orientation of the striations that occurs in the case of simple shear.

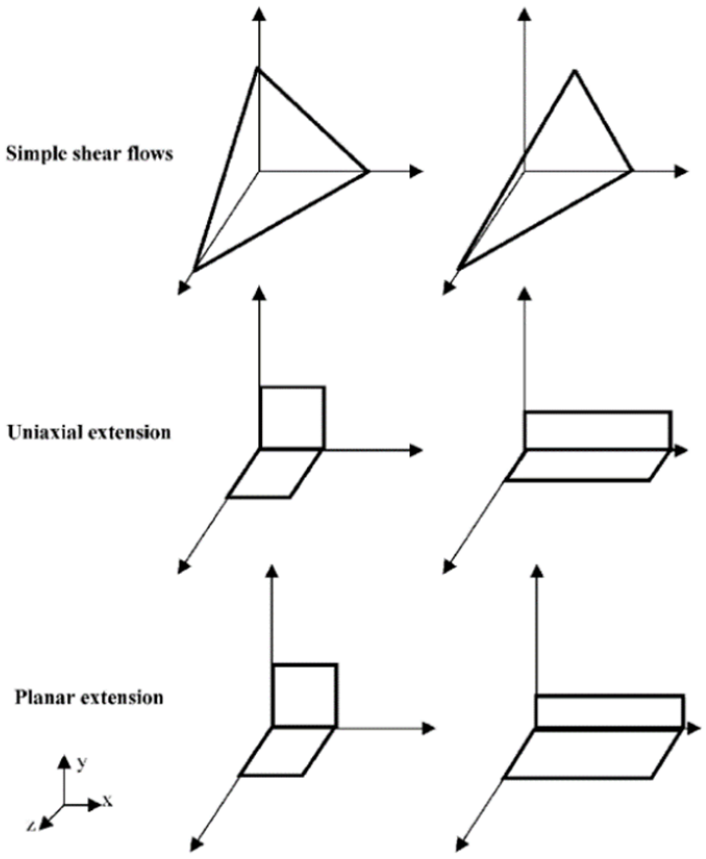

Figure 2.19 – Mechanisms which increase the area under ideal laminar flow condition. Taken from Thakur et al. (2003) [2]

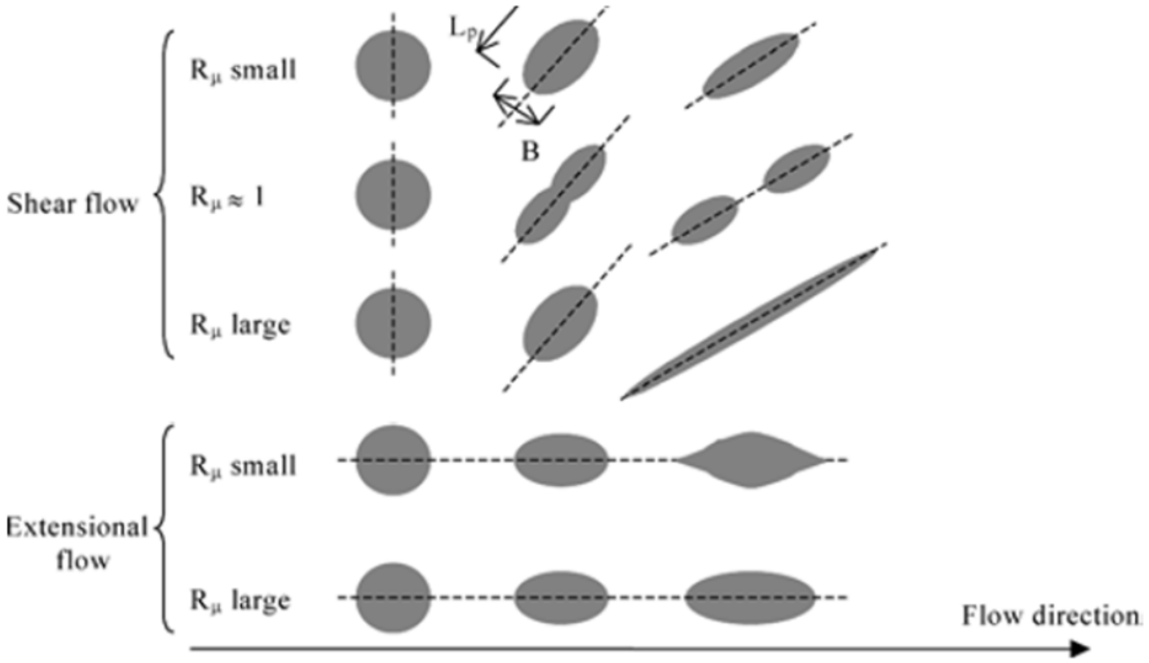

Figure 2.20 – Drop deformation under different flows condition. Taken from Thakur et al. (2003) [2]

The above considerations were carried out for liquid-liquid mixing systems. However, they can also be applied to drops and bubbles dispersions. To summarize, a series of static mixer elements generates a periodic flow pattern and might lead to an enhancement of drops and bubbles breakup mechanisms. Figure 2.20, taken from Thakur et al.'s work, may help to understand the drops deformation in different flows and for different viscosity ratios [2].

2.3.3 Interface generation in Static Mixers

The breakup of bubbles and drops allows a substantial increase of the interface area : This is favourable to mass and heat transfers. Biphasic immiscible systems are usually identified using the viscosity ratio p_μ (see equation 2.12) and the volumetric flow rate ratio ϕ_Q defined as [2] :

$$\phi_Q = \frac{Q_d}{Q_c} \tag{2.22}$$

where Q is the volumetric flow rate of a phase. The d and c indices refer to the dispersed or the continuous phase. Generally, the respective flow rates of the phases involved in the system are known so that ϕ_Q can be easily defined. We also introduce the density ratio R_ρ as :

$$R_\rho = \frac{\rho_d}{\rho_c} \tag{2.23}$$

Any change of the volumetric flow rate ratio will induce a change of the dispersion degree of the system. Furthermore, the dispersion is also highly influenced by the surface tension. Some applications require the use of a surfactant to enhance the quality of the dispersion.

Dispersions of drops and bubbles demand the introduction of a characteristic diameter to facilitate comparison between different mixing units and to figure out the dispersion efficiency

of the system [2]. The Sauter mean diameter (d_{32}) is often used for that purpose. It can be roughly viewed as the average of bubbles/particles/drops size. The Sauter diameter is defined as the diameter of a sphere that has the same volume/surface ratio as the considered particle. Mathematically, d_{32} is defined as [83] :

$$d_{32} = \frac{\int_{d_{min}}^{d_{max}} d^3\, \phi(d)\, \mathrm{d}d}{\int_{d_{min}}^{d_{max}} d^2\, \phi(d)\, \mathrm{d}d} \tag{2.24}$$

where d indicates the particle diameter, d_{max} and d_{min} indicates the maximum and minimum diameters of the particle distribution, $\phi(d)$ is a particle-size distribution function. Several methods were conceived to get a good estimate of the Sauter diameter. The most common method defines d_{32} through two main parameters, namely the sphere surface equivalent diameter d_A and the sphere volume equivalent diameter d_V :

$$d_A = \sqrt{\frac{A_p}{\pi}} \tag{2.25}$$

$$d_V = \left(\frac{6V_p}{\pi}\right)^{\frac{1}{3}} \tag{2.26}$$

In the former equations, A_p and V_p are respectively the surface and the volume of the particles. This method is particularly used in experimentations, as it is easy to obtain the area of the particles (e.g. using shadowgraphy). The particle volume can also be easily estimated with the volume fraction of the dispersed phase. Then, d_{32} can be calculated as :

$$\frac{V_p}{A_p} = \frac{\frac{4}{3}\pi\left(\frac{d_V}{2}\right)^3}{4\pi\left(\frac{d_A}{2}\right)^2} = \frac{\left(\frac{d_V}{2}\right)^3}{3\left(\frac{d_A}{2}\right)^2} = \frac{d_{32}}{6} \tag{2.27}$$

Drop-size and bubble-size distributions produced in bubble column and stirred tank in different flow regimes were experimentally and theoretically studied by many authors (Daly et al. 1992 [84] ; Schäfer et al. 2002 [85] ; Bouaifi et al. 2001 [86] ; Evans et al. 1992 [87]). The results of these studies allow to predict the behaviours of dispersion knowing the physical properties of the system and macroscopic flow variables.

The situation is rather more complex in presence of a static mixer. Every geometry has a different influence on the Sauter diameter. Drop size distributions for several static mixer geometries were examined over the past few years (Theron et al. 2010 [38]).

Empirical correlations allowed to reproduce drops and bubbles behaviour in different conditions. Through the correlations found in the literature, it is possible to predict the Sauter diameter. These correlations are usually derived from those originally developed for stirred tanks (Legrand et al. 2001 [6]). In the low viscosity dispersions commonly reported in the literature the correlations follow a power law of the Weber number :

$$\frac{d_{32}}{D_i} \propto We^{-0.6} \tag{2.28}$$

where D_i is the impeller diameter and We is the Weber number defined as :

$$We = \frac{\rho_L U^2 L}{\sigma} \tag{2.29}$$

ρ_L is the density of the liquid, U is its velocity, L is a characteristic length, typically the impeller diameter, and σ is the surface tension. The correlation 2.28 directly connects the Sauter diameter d_{32} to the impeller diameter. Additional terms that take into account the physical properties are usually involving the Reynolds number [6].

The considerations arising from the stirred tanks were applied to the static mixer, replacing the impeller diameter by a characteristic diameter of the system, like the diameter of the tube enclosing the mixer. Empirical correlations for the Sauter diameter were found by analysing experimental data of the static mixers to be functions of the form [2] :

$$\frac{d_{32}}{D} = f(Re_c, We, p_\mu, \phi_Q, R_p) \tag{2.30}$$

Several authors, mostly for gas-liquid dispersions, employed the capillary number to fit the experimental data [2].

$$\frac{d_{32}}{D} = f(Re_c, Ca, p_\mu, \phi_Q, R_p) \tag{2.31}$$

In both the above equations 2.30 and 2.31 appear Re_c, the Reynolds number based on mixer diameter but with the physical properties of the continuous phase.

$$Re_c = \frac{\rho_c U D}{\mu_c} \tag{2.32}$$

Data fitting of static mixer experimental conducted to correlation functions of two factors [88] :

$$\frac{d_{32}}{D} \propto We_c^{\alpha}\ Re_c^{\beta} \tag{2.33}$$

where We_c is the Weber number based on the physical properties of the continuous phase :

$$We_c = \frac{\rho_c U^2 D}{\sigma_c} \tag{2.34}$$

Over the last decades, several authors investigated the drops/bubbles size at the static mixers' outlet. Some of the proposed correlations are reported in table 2.4 (see also Theron, et al. (2010) [38]).

authors	mixer design	characteristic diameter	Φ	equation	regime	α	β
Middleman[9]	Kenics	D	0.005−0.01	$\frac{D_{32}}{D} = K_4 We_c^{-0.6} Re^{0.1}$	turbulent	−0.6	0.1
Streiff[12]	Sulzer SMV	D_h	≤0.25	$\frac{D_{32}}{D_h} = 0.21 We_h^{-0.5} Re_h^{0.15}$	transient, turbulent	−0.5	0.15
Haas[30]	Kenics	D		$\frac{D_{43}}{D} = 1.2 We^{-0.65} Re^{-0.2} \left(\frac{\mu_d}{\mu_c}\right)^{0.5}$	laminar	−0.65	−0.2
Legrand et al.[21]	SMX	d_p	0.05−0.25	$\frac{D_{32}}{D_p} = 0.29 We_p^{-0.2} Re_p^{-0.16}$	laminar, transient and turbulent	−0.2	−0.16
Chen and Libby[10]	Kenics	D		$\frac{D_{32}}{D} = 1.14 We^{-0.75} \left(\frac{\mu_d}{\mu_c}\right)^{0.18}$	turbulent	−0.75	0
Matsumura et al.[13]	Hi Mixer	D	0.2	$\frac{D_{32}}{D} = K We_c^{-n} \qquad n = 0.56-0.67$	turbulent	−0.67to −0.67	0
Al Taweel and Walker[14]	Lightnin	D_h	0.01	$\frac{D_{32}}{D_h} = K We^{-0.6} f^{-0.4}$	turbulent	−0.6	
Berkman and Calabrese[11]	Kenics	D	<0.1	$\frac{D_{32}}{D} = 0.49 We^{-0.6} \left(1 + 1.38 Vi \left(\frac{D_{32}}{D}\right)^{0.33}\right)^{0.6}$	turbulent	−0.6	0
Al Taweel and Chen[15]	Woven Screens		0.01−0.04	$D_{32} = 0.682 (We_{jet}^{-0.859} \varphi^{0.875}) \left(\frac{b}{M}\right)^{0.833}$	turbulent	−0.859	0
Streiff et al.[20]	SMV, SMX, SMXL		0.01	$d = C_n (1 + K\varphi) \left(\frac{(1 + BVi) We_c}{2}\right)^{0.6} \left(\frac{\sigma}{\rho_c}\right)^{0.6} \left(\frac{\rho_c}{\rho_d}\right)^{0.1} \varepsilon^{-0.4}$ $d_{max} = 0.94 \left(\frac{\sigma}{\rho_c}\right)^{0.6} \varepsilon^{-0.4}$			
Lemenand et al.[16–18]	HEV	D	0.025−0.15	$\frac{D_{32}}{D} = 0.57 We^{-0.6}$	turbulent	−0.6	0
Das et al.[29]	SMX	D_p	0.05−0.25	$\frac{d_{max}}{d_p} = C We_p^{-0.33}$	laminar, transient	−0.33	0
Hirschberg et al.[22]	SMX plus		0.05	$d = C_n (1 + K\varphi) \left(\frac{(1 + BVi) We_c}{2}\right)^{0.6} \left(\frac{\sigma}{\rho_c}\right)^{0.6} \left(\frac{\rho_c}{\rho_d}\right)^{0.1} \varepsilon^{-0.4}$	turbulent		

Table 2.4 – Correlations proposed by different authors for the calculation of D_{32} or D_{43} under different operative conditions. Taken from Theron, et al. (2010) [38]

2.3.4 Dispersions and hydrodynamics in SMX Static Mixers

Meijer et al. (2012) [21] analysed the performance of several static mixers making a quantitative comparison of their efficiency. They used high viscosity liquids that flow inside the most common industrial statics mixers in laminar flow. In their work, Meijer et al. studied the Ross Low-Pressure-Drop (LPD), the Low-Low-Pressure-Drop (LLPD), the standard Sulzer SMX and a series of new designs of SMX. These devices were quantitatively compared through several characteristics : energy consumption, pressure drop, compactness and mixing efficiency. Although liquid-liquid systems are not the object of our study, it was considered useful to introduce the work of Meijer et al. (2012) [21] in order to give hints about the mixing efficiency and the pressure drop inside different static mixers.

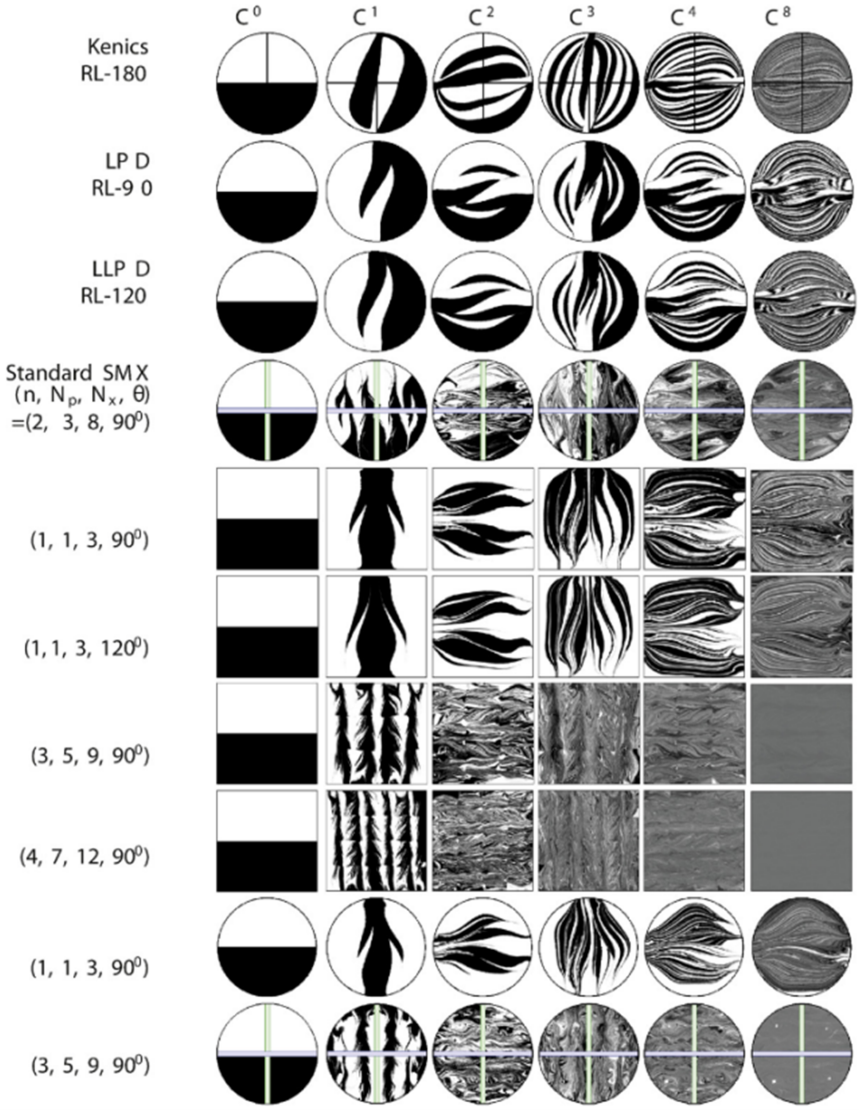

Figure 2.21 – Mixing profiles in static mixers : Kenics, Ross, Sulzer and their modified profiles. Taken from Meijer et al. (2012) [21].

Figure 2.21 illustrates the major results obtained by these authors. These images were obtained by analysing the cross-section distribution of a white and black liquid/liquid fluid system, flowing through the different mixers. It should be noted that the inlet conditions are the same for all tests. The pictures are taken after 1, 2, 3, 4 and 8 elements, corresponding respectively to columns C1, C2, C3, C4 and C8 [21].

The first four mixers, reported in the first four rows of figure 2.21, are the most common commercial devices for industrial applications. Among them, it clearly appears that the Standard Sulzer SMX has a higher mixing efficiency. The other mixers come out from a modification of the standard Sulzer SMX. From the fifth to the eighth row are shown quadrangular section mixers [21].

The plots, shown in figure 2.22 and figure 2.23, report what is easy to guess by observing figure 2.21. The left graphic shows the static mixers efficiency by drawing the number of layers generated along various static mixer lengths. Figure 2.22 shows clearly that the Standard SMX, the SMX (3, 5, 9) and the SMX (4, 7, 12) have higher mixing efficiency than the other devices. The last one cited, the SMX (4, 7, 12), reveals the highest mixing efficiency [21].

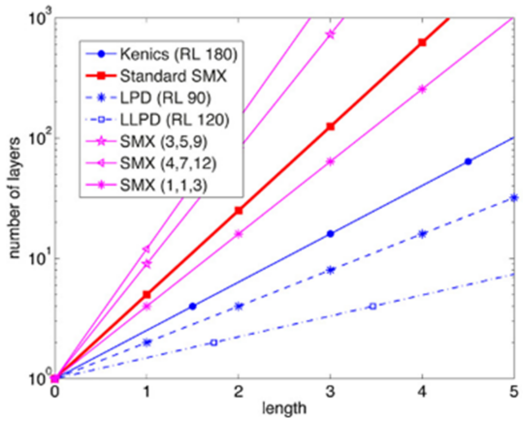

Figure 2.22 – Influence of the length of the device on the number of layers generated (Meijer et al. 2012) [21]

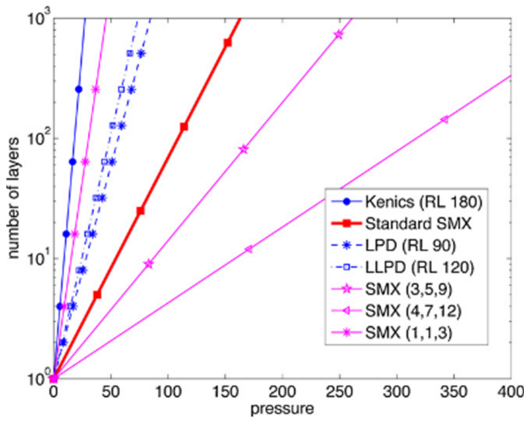

Figure 2.23 – Influence of pressure drop into the device on the number of layers generated (Meijer et al. 2012) [21]

The second graph, on figure 2.23, illustrates the pressure drop through different static mixers as a function of the number of layers generated. The Standard SMX, the SMX (3, 5, 9) and the SMX (4, 7, 12) have a higher-pressure drop compared with the other devices. The SMX (3, 5, 9) and the SMX (4, 7, 12) show the highest mixing efficiency at the expense of the highest pressure drop. The standard SMX depicts an intermediate situation : high mixing efficiency and acceptable pressure drop. A lower efficiency and pressure drop were highlighted by the other static mixers [21].

Additional works regarding liquid-liquid mixing were done. Theron et al. (2010) [38] studied the pressure drop in a liquid-liquid dispersion in Sulzer SMX mixer. Legrand et al. (2001) [6] analysed the liquid-liquid dispersion in the Sulzer SMX by focusing on the pressure drop in the system and on the mean Sauter diameters. Many other authors treated liquid-liquid systems and reported results for a wide range of applications.

The complexity of the gas-liquid dispersions led to have fewer studies treating such systems. Fradette et al. (2006) [7] performed a work aimed at quantifying the SMX (Sulzer) dispersion capacity in the laminar regime and at comparing its performance with other static mixers. Fradette et al. [7] did a series of experiments by dispersing nitrogen gas in Newtonian and Non-Newtonian fluids. Different flow rates were examined. The volume fraction of the gas was maintained between 0 % and 7 %. The bubbles size distribution was measured in all the experimentations. Pacek et al. [89] analysed some photos which were taken through the

vessel wall in a stirred tank. They determined that the diameter distributions obtained by the images recorded with the camera are compatible with the real distributions inside the stirred tank.

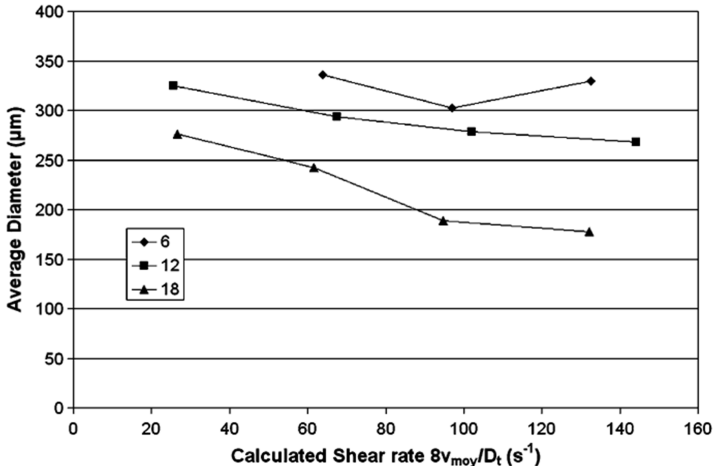

Figure 2.24 – Nitrogen bubble average diameter for different SMX lengths (Fradette et al. 2006)

Fradette et al. measured the mean diameters with a camera by recording the outlet of the SMX. Some authors added a rectangular transparent box around the tank or column to minimize the optical deformations during the image acquisition. The box is filled with the same continuous phase as the one used in the experimentation. The main results of Fradette et al. [7] are shown on figure 2.24. They are useful to make considerations for gas-liquid systems. In the abscissa axis, the average shear is shown following equation 2.35 below, where U_{avg} is the mean fluid velocity and D_t is the diameter of the tube. In the ordinate axis, the average diameter of the bubbles is represented.

$$\gamma_{avg} = 8 \, \frac{U_{avg}}{D_t} \tag{2.35}$$

Three different SMX static mixers lengths were examined, with respectively : 6, 12 and 18 number of elements. When the number of elements increases, there is a decrease of the bubbles mean diameter. On the other hand, by keeping constant the number of elements, the bubbles diameter decreases if the shear rate increases, i.e. when the fluid flow rate increases (Fradette et al. 2006 [7]).

2.3.5 Pressure drop across a static mixer

In the static mixer, the mixing energy is provided by the pressure drop. Static mixers thus lead to higher pressure drop than an empty tube. The efficiency of the process and the amount of energy required can be evaluated by analysing the evolution of pressure drop across the mixer.

Several correlations for the pressure drop in single phase flow are available for different types of static mixers [22, 90–95]. Many authors proposed a comparison between pressure drop in static mixers and in a simple tube (also called empty column in the following). They

defined thus the Z factor (Zalc et al. 2002 [90]) :

$$Z = \frac{\Delta P_{Mixer}}{\Delta P_{Column}} \tag{2.36}$$

where ΔP_{Mixer} and ΔP_{Column} are respectively the pressure drop in the static mixer and the empty column. A second way of correlating pressure drop in static mixer is through the definition of Fanning friction factor f or the Newton number Ne :

$$Ne = 2f = \frac{\Delta P}{\rho U_0^2} \frac{D}{L} \tag{2.37}$$

where U_0 is the superficial velocity of the fluid, ρ is the fluid density, D the tube diameter and L the mixer length. The friction factor can be written as a function of the Reynolds number Re (Li et al. 1997 [22]) :

$$\frac{f}{2} = \text{function}\left(Re, \frac{D}{L}\right) \tag{2.38}$$

where the Reynolds number is defined as :

$$Re = \frac{\rho U_0 D}{\mu} \tag{2.39}$$

Several authors defined the Reynolds numbers accounting for the porosity ϵ_{SMX} of the static mixer. For example, Shah and Kale proposed a Reynolds number and a Fanning friction factor defined as [96] :

$$Re_i = \frac{\rho U_0 D}{\mu \epsilon_{SMX}} \tag{2.40}$$

$$f_i = \frac{\Delta P}{2 \rho U_0^2} \frac{D}{L} \epsilon_{SMX}^2 \tag{2.41}$$

Equation 2.40 led to define the interstitial velocity U_i :

$$U_i = \frac{U_0}{\epsilon_{SMX}} \tag{2.42}$$

Equations 2.41 and 2.40 allowed the comparison between mixers with different porosity. Streiff et al. expressed the Reynolds number (Re_h) as [97] :

$$Re_h = \frac{\rho U_0 D_h}{\mu \epsilon_{SMX}} \tag{2.43}$$

where D_h represents the hydraulic diameter of the mixer. Equation 2.43 seems more appropriate to perform comparison of different mixers geometry. Li et al. [22] defined the Reynolds number in terms of apparent fluid viscosity at the wall $\eta_w(\gamma_w)$ where γ_w is the shear rate at the wall :

$$Re_g = \frac{\rho U_0 D}{\eta_w(\gamma_w)} \tag{2.44}$$

Li et al. (1997) [22] conducted experiments on four fluids with different properties. They proposed mathematical correlations fitting their experimental data. The correlation for the Fanning factor works over a wide range of Reynolds. The finding of Li et al. [22] are summarized in figure 2.25.

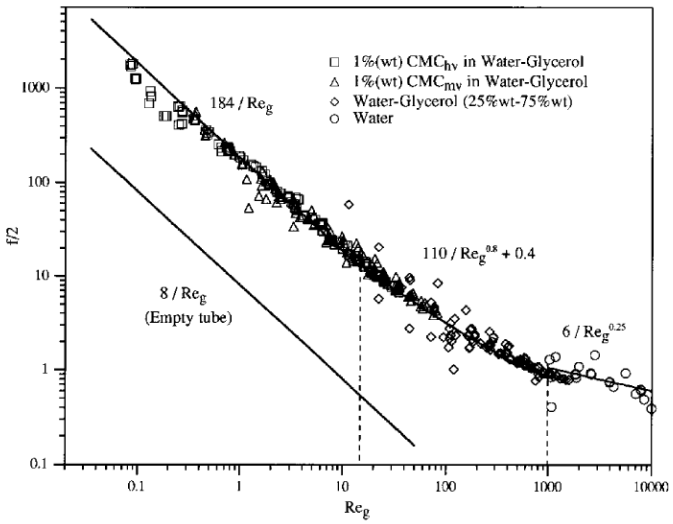

Figure 2.25 – Mathematical correlation between $f/2$ and Re_g in different flow regime proposed by Li et al. [22].

Figure 2.25 can be summarized in this way :

- Laminar flow regime ($Re_g \leq 15$) :

$$\frac{f}{2} = \frac{184}{Re_g} \tag{2.45}$$

- Transient flow regime ($15 < Re_g \leq 1000$) :

$$\frac{f}{2} = \frac{110}{Re_g^{0.8}} + 0.4 \tag{2.46}$$

- Turbulent flow regime ($Re_g > 1000$) :

$$\frac{f}{2} = \frac{6}{Re_g^{0.25}} \tag{2.47}$$

The correlations found by Li et al. (1997) [22] are also in agreement with other experimental data from other studies. The comparison between Li et al. [22] correlations and experimental results of Müller and Kalbitz is illustrated in figure 2.26.

In the same paper, Li et al. [22] reported the influence of temperature (figure 2.27) and the number of elements on the pressure drop (figure 2.28).

In conclusion, the pressure drop increases with the number of elements N. On the other hand, the pressure drop decreases when increasing the wall temperature of the static mixer. Other correlations were proposed by other authors. Table 2.5 sums up the main correlations present in the literature (Theron et al. [38]).

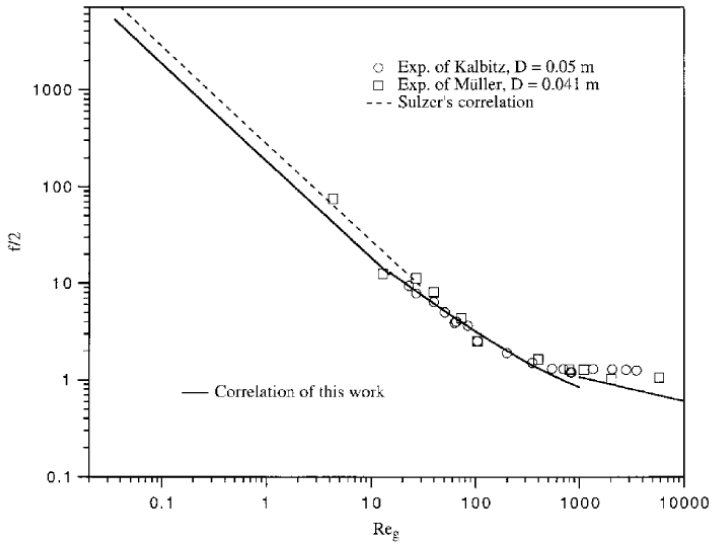

Figure 2.26 – Comparison between Li et al.'s correlations and experimental data of Müller and Kalbitz. Taken from Li et al. [22].

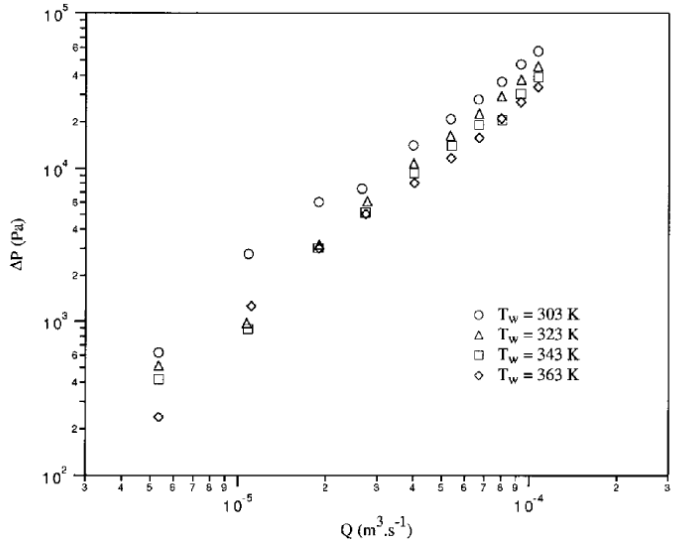

Figure 2.27 – Influence of wall temperature on the pressure drop. Substances : 25% water, 75% glycerol (wt fraction). Taken from Li et al. [22].

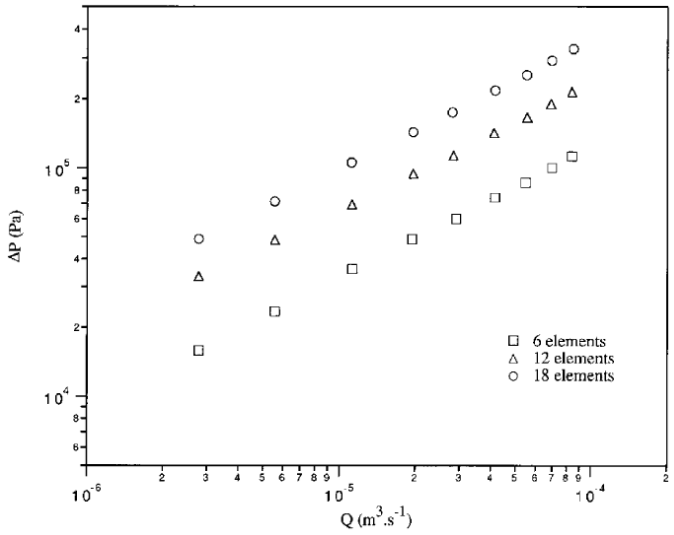

Figure 2.28 – Influence of the number of mixing elements N on the pressure drop. Substances : 49.5% water, 49.5% glycerol, 1% CMChv (wt fraction), $T_w = 293$K. Taken from Li et al. [22].

authors	SMX mixer characteristics	correlation	Z	Reynolds range
Pahl and Muschelknautz[4]	$D = 50$ mm; $L/D = 1.5$; 5, 7, 9 elements		10−100	$Re \leq 50$
Pahl and Muschelknautz[5,6]	$D = 50$ mm; $L/D = 1.5$; 5, 7, 9 elements	$Ne = 6$	10−60	$Re \leq 50$ $Re \geq 1000$
Bohnet et al.[7]	$D = 50$ mm	$\frac{f}{2} = \frac{236.6}{Re}$	30	$1.8 < Re < 20$
		$\frac{f}{2} = \frac{217.6}{Re} + 1.0$		$20 < Re < 1350$
		$\frac{f}{2} = \frac{9.1}{Re^{0.25}}$	230	$1350 < Re < 4000$
Shah and Kale[1]	$D = 26.54$ mm; L/D =1.5; 24 elements; $\varepsilon = 0.87$	$f_i = \frac{350}{Re_i} + \frac{5.13}{Re_i^{0.58}}$		$Re_i < 10$ ($\approx Re < 10$)
Li et al.[3]	$D = 16$ mm; $L/D = 1.25$; 6, 8, 12 elements; $\varepsilon = 0.84$	$\frac{f}{2} = \frac{184}{\mathrm{Re}}$	23	$Re < 15$
		$\frac{f}{2} = \frac{110}{\mathrm{Re}^{0.8}} + 0.4$		$15 < Re < 1000$
		$\frac{f}{2} = \frac{6}{\mathrm{Re}^{0.25}}$	152	$1000 < Re < 10000$
Streiff et al.[8]		$Ne = \frac{1,200}{Re} + 5$	38	laminar: $Re_h < 20$ turbulent: $Re_h > 2300$
Yang and Park[2]	$D = 40$ mm; $L/D = 1$; 4, 8, 12 elements	$\frac{f}{2} = \frac{8.55}{Re^{1.61}}$		$Re < 20$

Table 2.5 – Correlations of pressure drop in SMX Mixer available in the literature. Taken from Theron, et al. (2010) [38]

2.3.6 Residence Time Distribution (RTD) model for the SMX

Several Residence Time Distribution (RTD) models for the static mixer were proposed in the last decades. For instance, Li et al. (1996) [5] examined the RTD, the mixing mechanism, the pressure drop and the heat transfer in the SMX static mixer. By analysing the fluids rheology, Li et al. (1996) [5] built a RTD model able to predict the behaviour within the SMX for a wide range of fluids. By fitting experimental data, they showed that the RTD can be described by a two-parameters model, both affected by the geometry of each element.

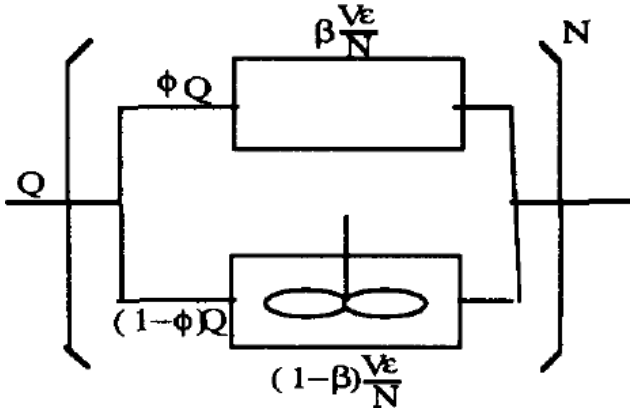

Figure 2.29 – Model proposed by Li et al. (1996). Taken from Li et al. (1996) [5]

The model proposed and reported in figure 2.29 consists of an association in parallel of a

CSTR and a plug flow. The main advantage of this model is its flexibility towards the number of mixing elements N. Equation 2.48 shows the transfer function used by Li et al. [5] :

$$G(s) = \left[\frac{1 - \phi_{p.f.}}{1 + \frac{1-\beta_{p.f.}}{1-\phi_{p.f.}} \tau^1 s} + \phi \; exp\left(-\frac{\beta_{p.f.}}{\phi_{p.f.}} \tau^1 s \right) \right]^N \tag{2.48}$$

where $\phi_{p.f.}$ is the volumetric fraction of the flow rate in plug flow, $\beta_{p.f.}$ the volumetric fraction in plug flow and N represents the number of mixing elements. The quantity τ^1 is the space time in each element and it can be written as [5] :

$$\tau^1 = \frac{V_{SMX} \; \epsilon_{SMX}}{N \, Q} \tag{2.49}$$

where V_{SMX} is the total volume of the SMX, ϵ_{SMX} its porosity. Q represents the flow rate. Li et al. (1996) [5] affirmed that the two parameters of the model (equation 2.48) are functions of the generalized Reynolds number Re_g (equation 2.44) based on a characteristic viscosity. The latter parameter was introduced for taking in account the specific rheology of the fluids into the SMX. The influence of the Reynolds number Re_g on the model parameters $\phi_{p.f.}$ and $\beta_{p.f.}$ is logical. On the other hand, the effect of the number of elements on fraction of plug flow $\beta_{p.f.}$ is less straightforward [5].

Li et al. (1996) proposed two empirical correlations for the estimation of the volumetric fraction of the flow rate in plug flow ($\phi_{p.f.}$) and the volumetric fraction in plug flow ($\beta_{p.f.}$) [5].

$$\phi_{p.f.} = 0.86 + 2.72 \; 10^{-3} \, Re_g \tag{2.50}$$

$$\beta_{p.f.} = 1 - \left(1.62 - 2.64 \; 10^{-2} \, Re_g\right) \; N^{-0.39} \tag{2.51}$$

With these two parameters (equations 2.50 and 2.51), Li et al. [5] obtained an excellent agreement between mathematical model (equation 2.48) and experimental data. The results are reported in figure 2.30.

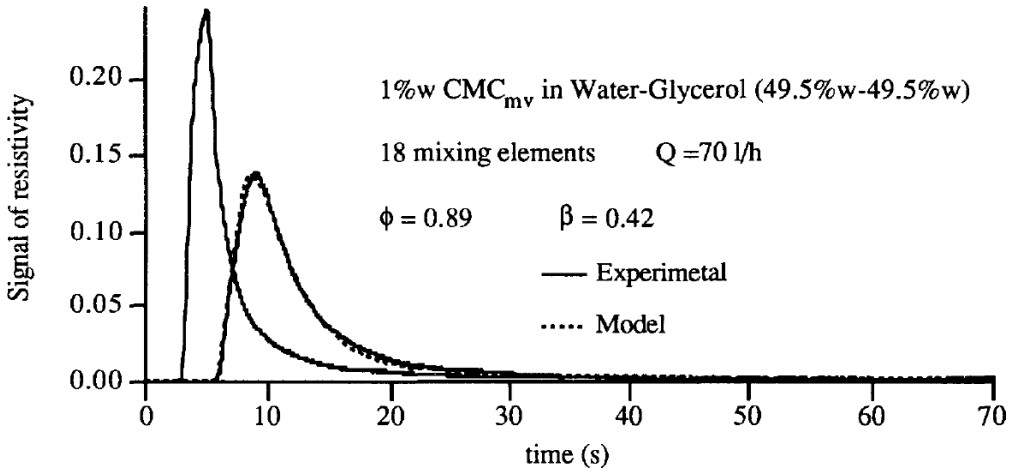

Figure 2.30 – Comparison between the experimental signals and the fitting mathematical model. Taken from Li et al. (1996) [5].

To summarize, Li et al. [5] provided a RTD model of two parameters that is able to predict the behaviours of Newtonian and non-Newtonian fluids in presence of the SMX static mixer. The model shown a good agreement with the experimental data obtained with four different fluids. Furthermore, they studied the effect of the number of elements N on the two model parameters.

They concluded that the influence of N on the volumetric fraction of plug flow is probably due to a feedback effect [5]. Madhuranthakam et al. (2009) [98] used a similar RTD model to predict the gas hold-up in the SMX.

2.3.7 Mass transfers in the SMX

The mass transfer is a movement of mass from one phase to another. The driving force which controls the mass transfer is usually a concentration difference. Other factors may contribute to the mass transfer, such as a chemical reaction. The mass transfer is often described using the volumetric transfer coefficient, namely the K_La (Gourich et al. 2008 [99]).

In the design and in the scale-up of bubble columns, the mass transfer coefficient is a decisive factor. The quantity of dissolved gas is limited by the gas solubility in the liquid phase, the gas consumption rate by an eventual chemical kinetics and K_La coefficient (Gourich et al. 2008 [99]).

Madhuranthakam et al. (2009) [8] studied the mass transfer improvement in presence of the static mixer by analysing the decrease of the amount of air oxygen flowing through the SMX in deoxygenated water. The differential mass balance in the liquid phases can be written as :

$$\frac{\partial(Co_2)}{\partial t} = Da\,\frac{\partial^2(Co_2)}{\partial z^2} - \hat{U}\,\frac{\partial(Co_2)}{\partial z} + K_La\,(Co_2^* - Co_2) \tag{2.52}$$

where Da is the axial diffusion coefficient, K_La is the overall mass transfer coefficient on the liquid side, Co_2 and Co_2^* are respectively the oxygen concentration in water at any time and the oxygen concentration in water reached at equilibrium. The above equation can be made dimensionless by scaling the time with the space time τ, the length with the reactor length L and the oxygen concentration with the equilibrium concentration Co_2^* :

$$\frac{\partial\xi}{\partial\theta} = \frac{1}{Pe}\,\frac{\partial^2\xi}{\partial\lambda^2} - \frac{\partial\xi}{\partial\lambda} + St(1-\xi) \tag{2.53}$$

The dimensionless variables introduced are detailed below :

$$\xi = \frac{Co_2}{Co_2^*};\quad Pe = \frac{\hat{U}\,L}{Da};\quad \lambda = \frac{z}{L};\quad \theta = \frac{t}{\tau};\quad \tau = \frac{L}{\hat{U}};\quad St = K_La\,\tau \tag{2.54}$$

The Stanton number St permits to determine the K_La. The K_La obtained from experiments for several gas and liquid flow rates is shown in figure 2.31 [8].

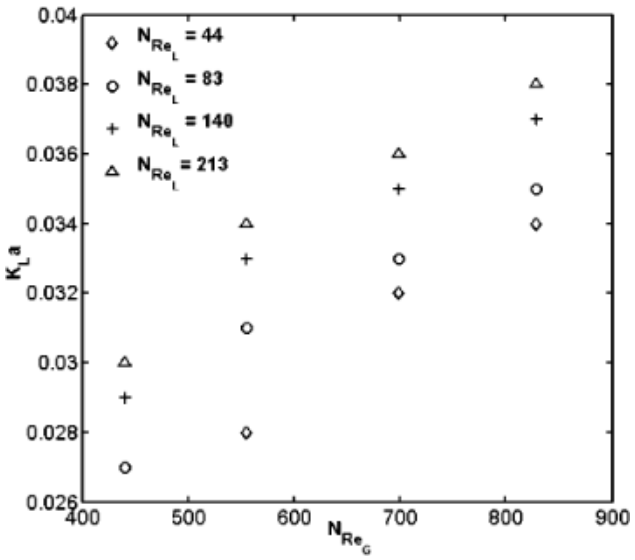

Figure 2.31 – Effect of liquid and gas Reynolds number on $K_L a$ in the SMX (Madhuranthakam et al. [8])

The Peclet number Pe was determined using the RTD model with open-open as boundary conditions. These authors linked the $K_L a$ with the Reynolds number in the liquid-side (N_{Re_L}) and the Reynolds number in the gas-side (N_{Re_G}) by using this correlation :

$$K_L a = A\, N_{Re_L}^{\alpha}\, N_{Re_G}^{\beta} \tag{2.55}$$

where there are three constants : $A = 0.003\ \mathrm{s}^{-1}$, $\alpha = 0.099$ and $\beta = 0.307$. Both Reynolds numbers are calculated through equation 2.39 using respectively liquid and gas properties. The values found for power constants revealed that the gas side Reynolds number has more impact than the liquid Reynolds number. In fact, for a given liquid flow rate, an increase in gas flow rate increases the interfacial area and thus the mass transfer [8].

In their research, Madhuranthakam et al. [8] examined the mass transfer characteristic at high gas velocities and relative low liquid velocities. Consequently, a moderate dependence of liquid velocity (U_L) on the mass transfer was observed in their work. These authors correlated the $K_L a$ to the gas velocity (U_G) [8] :

$$K_L a = A\, U_G^{\beta} \tag{2.56}$$

where $A = 0.737$ and $\beta = 0.92$. With almost the same air/water system, Lakota et al. (2002) [100] found that the effect of the superficial gas velocity on the mass transfer is higher than the effect of the liquid velocity [8]. Madhuranthakam et al. [8] also reported an important graph, shown in figure 2.32, representing a comparison between different mixing units. A Rushton turbine in a stirred tank, a SMX and a SMV were compared to identify which is the most efficient mixing device. The mass transfer coefficients were compared for different situations by varying the energy dissipation and keeping constant the superficial gas velocity [8]. The Rushton turbine had the same power dissipation and superficial gas velocity than the static mixers. The plot shows that the mass transfer coefficients in the SMX are higher than the coefficients in dynamic mixer and SMV [8]. In the same year, Madhuranthakam et al. [8] also did a similar research about the residence time distribution and liquid hold-up in the Kenics KMX static mixer.

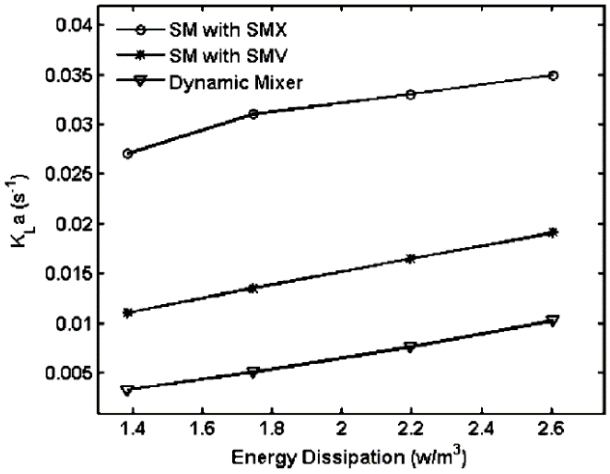

Figure 2.32 – Comparison of the mass transfer values from different mixing device.

2.3.8 Influence of injectors on the dispersion

An injector is required to spread the dispersed phase into the continuous phase. This device has a strong influence on the bubble/drop diameters distribution. In fact, its geometry plays an important role in the bubbles/drops' formation mechanisms (see section 2.1.2). Rauline et al. (1998) [24] demonstrated, by running dedicated simulations that the centre of the pipe is the most favourable position for the injector. Besides, according to Rauline et al. (1998) [24], the SMX and the Ross ISG mixers are not much affected by the position of the injector.

Zalc et al. (2003) [23] analysed the trajectory of passive tracer particles through the SMX static mixer to classify the mixing dynamics as a function of the injection position. The results are illustrated in figure 2.33 and 2.34. In the case of a centreline injection (figure 2.33), the distribution inside the SMX is more uniform, which conducts to a higher mixing efficiency.

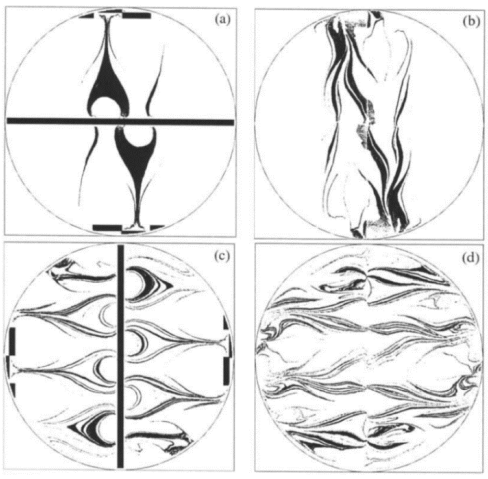

Figure 2.33 – Mixing patterns for a centreline tracer injection at $Re = 1$ (Zalc et al. 2003 [23].)

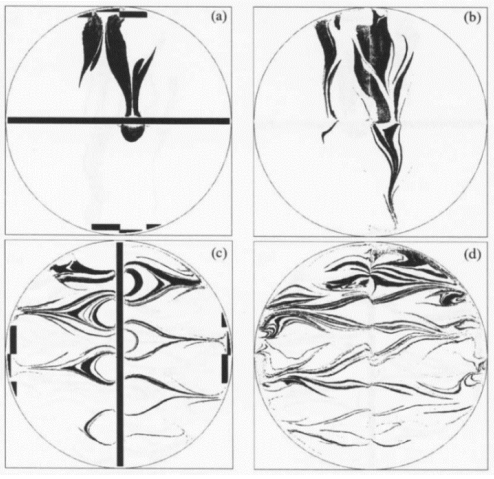

Figure 2.34 – Mixing patterns for an off-centre tracer injection at $Re = 1$ (Zalc et al. 2003 [23].)

It appears clear from figure 2.34 that the tracer is not perfectly distributed when the injection is off-centred. In both experiments, the same operating conditions was used. In addition, Zalc et al. (2003) [23] found that the mixing rate is relatively insensitive to Reynolds number for the low Reynolds they studied (Re >100) for a centreline injection, but is strongly dependent on the flow rate in the case of off-centre injection. Therefore, the centreline is preferable to achieve higher overall mixing efficiencies [23].

2.3.9 CFD simulations of static mixers

In the last decades, several authors conducted numerical study to evaluate the performance of static mixers. For instance, Rauline et al. (1998) [24] compared several static mixers by numerical simulations, the Kenics, Inlier, LPD, Cleveland, ISG and SMX. Numerical pressure drops were compared with the experimental values in order to validate their model. That comparison shown an overall good agreement between numerical and experimental results.

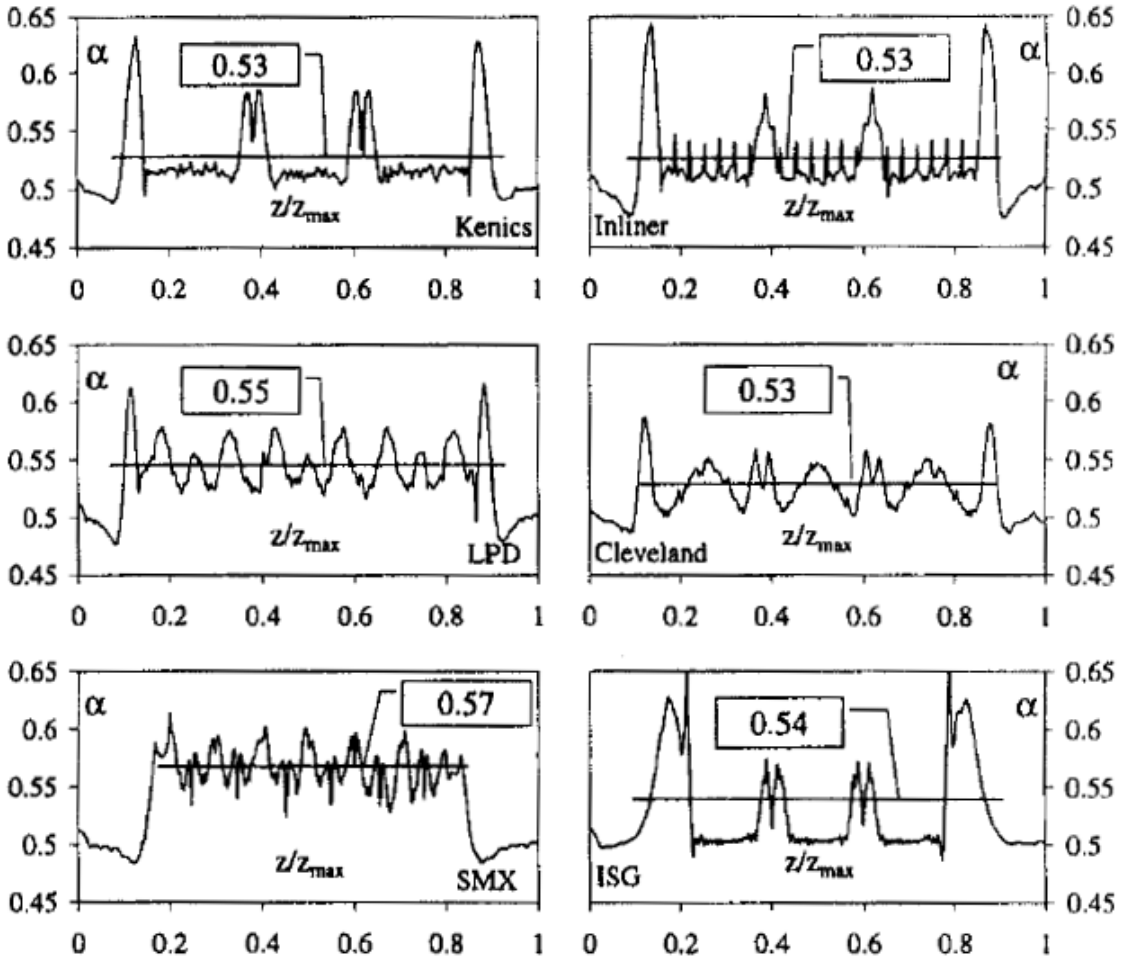

Figure 2.35 – Comparison of the extensional efficiency in several static mixer devices. Numerical simulations made by Rauline et al. (1998) [24]

Simulations were performed using no slip boundary conditions for the reactor walls and for the mixer elements. The extensional efficiency α quantifies the relative strength of pure elongational flow. $\alpha = 1$ corresponds to pure extension, $\alpha = 0.5$ to simple shear and $\alpha = 0$ to pure rotation. The extensional efficiency of several mixers is shown in figure 2.35. In this figure, each graphic represents a different mixer. In the abscissa is reported the dimensionless

length of the mixer and in the ordinate the average extensional efficiency at the cross-section plane located at the corresponding normalized length. It appears clear that the exit and entry effects are not negligible : two higher peaks are present for all mixers, which means that the mixer would be more efficient if some space was left between its elements. Furthermore, Kenics, Inlear and Clevend mixers shown a lower extensional efficiency, which means lower mixing efficiency. The two other devices presented higher extensional efficiency. In particular, the SMX static mixer has the highest one. In addition, the SMX presents a smaller amplitude of oscillations of the α parameter (Rauline et al. 1998 [24]).

Figure 2.36 shows the cumulative volumetric distribution of the extensional efficiency. For each abscissa value of α, this figure depicts the volume percentage in which α is greater than the abscissa value. The SMX is more efficient than the ISG and the Kenics by having higher values of α parameter in a greater volume percentage.

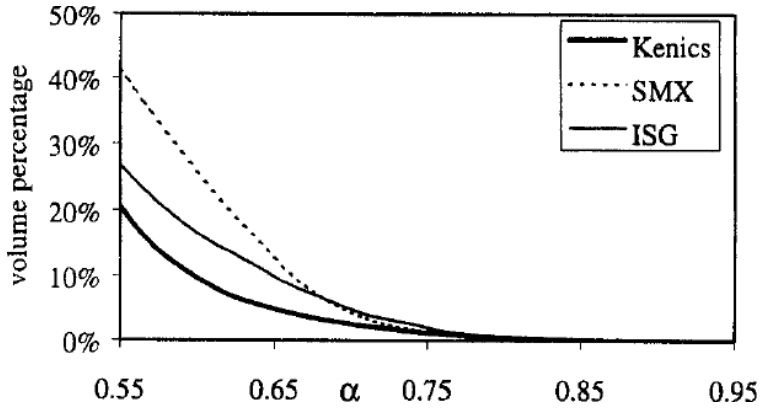

Figure 2.36 – Volumetric distributions of the extensional efficiency for three different mixers. Taken from Rauline et al. (1998) [24]

In conclusion, Rauline et al. (1998) [24] showed that in creeping laminar flow regime the Kenics, Inliner, LPD and Cleveland are rather similar, and the ISG mixer had better performance but its pressure drop is too high compared to the other advantages. The SMX was shown to be the most efficient [24].

In a more recent study, Rauline et al. (2000) [25] investigated the performance of the Kenics and SMX mixers in the laminar flow regime through 3D numerical simulations. In their research, Rauline et al. (2000) [25] distinguished two mixing : "easy" mixing and "difficult" mixing. In the case of "easy" mixing, the Kenics might be more suitable than the SMX. The Kenics should be 3.3 times longer than the SMX mixer in that case. Besides, the Kenics mixer is generally less expensive than the SMX. The Kenics mixer might thus be chosen for "easy" mixing tasks if space constraints are not restrictive (Rauline et al. 2000 [25]).

On the other hand, a "difficult" mixing requires the use of the SMX. This emerges from a balance between capital cost (higher for the SMX) and operating cost (higher for the Kenics). Furthermore, Rauline et al. (2000) [25] claimed that to achieve a "difficult" mixing task, the SMX mixer is more efficient than the Kenics mixer.

Moreover, Rauline et al. 2000 [25] showed that from a distributive mixing point of view, one element of the SMX is equivalent to approximately 2 or 3 Kenics elements (depending of the operating conditions). These results can be seen from the figures 2.37 and 2.38.

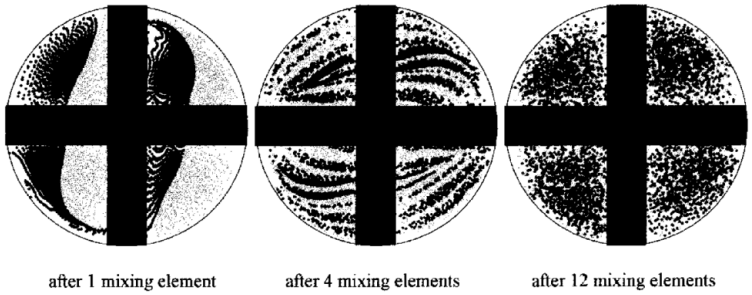

Figure 2.37 – Tracer distribution pattern for the Kenics mixer (binary mixture). Taken from Rauline et al. [25]

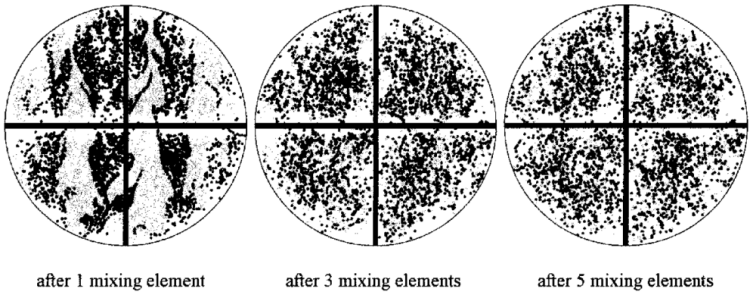

Figure 2.38 – Tracer distribution pattern for the SMX mixer (binary mixture). Taken from Rauline et al. [25]

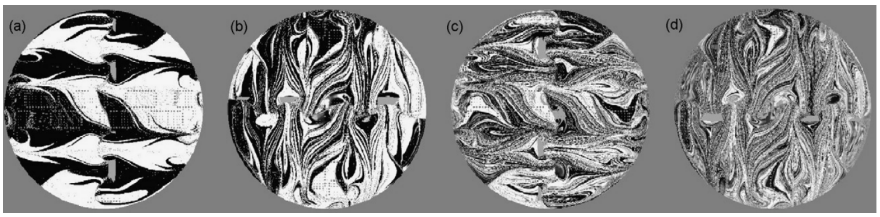

Figure 2.39 – CFD predictions of concentration distributions in cross-sections, generated using the trajectory mapping scheme, for original SMX mixing elements (ME) with (n=8, no gaps) (a) after 1 ME, (b) after 2 ME, (c) after 3 ME, and (d) after 4 ME. Taken from Hirschberg et al. (2009) [26].

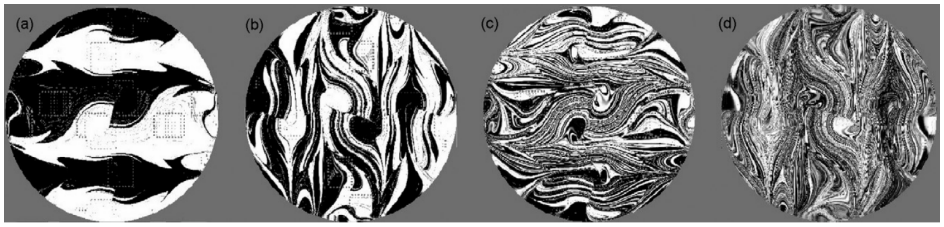

Figure 2.40 – CFD predictions of concentration distributions in cross-sections, generated using the trajectory mapping scheme, for SMX plus mixing elements (ME) (a) after 1 ME, (b) after 2 ME, (c) after 3 ME, and (d) after 4 ME. Taken from Hirschberg et al. (2009) [26].

Several authors investigated the performance of the Kenics static mixer. Among them, Kumar et al. 2008 [93] performed 3D CFD simulations and experiments for three different

Kenics static mixers over a wide range of Reynolds number, from 1 to 25,000. Furthermore, Kumar et al. (2008) [93] showed that the pressure drop is a function of the Reynolds number. They uncover that the ΔP per unit element in the Kenics increases with Re.

Hirschberg et al. 2009 [26] used CFD simulation to investigate a geometrical modification of the Sulzer SMX^{TM} static mixer, namely the new SMX plus. The latter is characterized by a reduced number of bars, and smaller gaps between the bars. These properties lead to a pressure drop reduction (about 50 %). Hirschberg et al. 2009 [26] proved that the mixing quality remains nearly unchanged with respect to the original SMX. These results were confirmed by LIF measurements and CFD simulations. Figure 2.39 and 2.40 depicts the CFD predictions of concentration distributions in several cross-sections of the mixers.

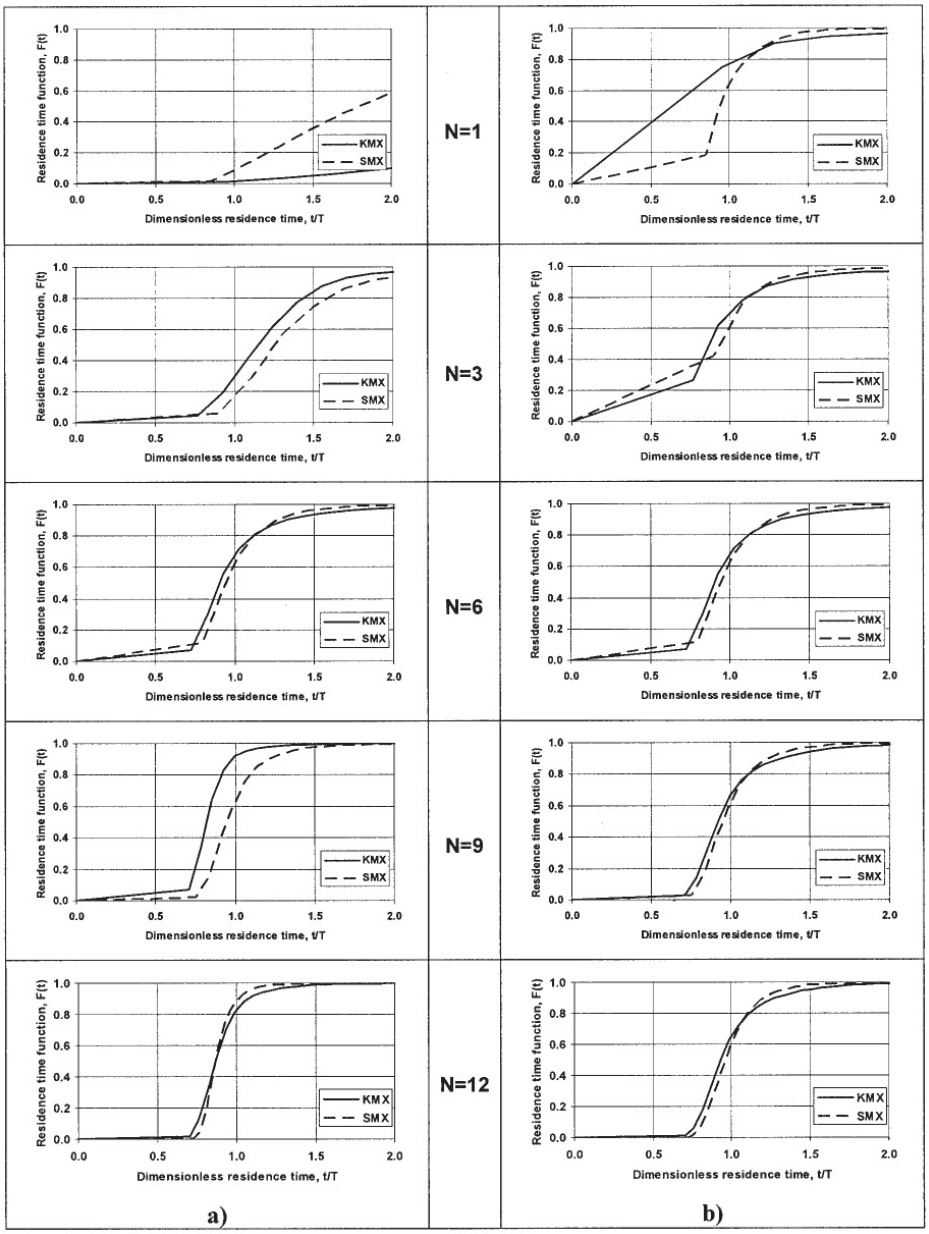

Figure 2.41 – Residence time distribution for off-centered (a) and centered (b) injection location (Heniche et al. 2005) [27].

Other authors studied the effect of the geometry on mixing, using CFD. In the work of

Heniche et al. [27], the performance of the KMX and the SMX static mixers were evaluated numerically and compared, using the finite element method. The pressure drop, stream function, mean shear rate, stretching efficiency, Lyapunov exponent, intensity of segregation, stretching of trajectories, and residence time were investigated for the two devices. Several differences between flat (SMX) and curved blades (KMX) were highlighted by Heniche et al. (2005) [27].

Furthermore, Heniche et al. (2005) [27] assessed a RTD model for injection of off-centred and centred particles in the KMX and SMX. The residence time function $F(t)$ curves versus the dimensionless time are shown in figure 2.41 for several mixer lengths. The KMX and the SMX present similar trends and generate narrower distributions when the number of elements N increases. The KMX mixer achieved almost plug-flow behaviour faster than the SMX for an off-centred injection. On the other hand, the SMX reached a plug-flow condition faster in the case of a centred injection [27]. They also observed that the blade curvature was associated with a slightly higher pressure drop than that of a flat blade. On the other hand, they observed that the curved blade is more efficient in terms of mixing than the flat blade design.

Liu et al. (2005) [28] studied the mechanism of drop breakup in standard SMX static mixers in the laminar flow regime through experimental observations and numerical simulations. They investigated the deformation and breakup of a single drop using the volume of fluid model. Figure 2.42 illustrates the system analysed by Liu et al. (2005) [28].

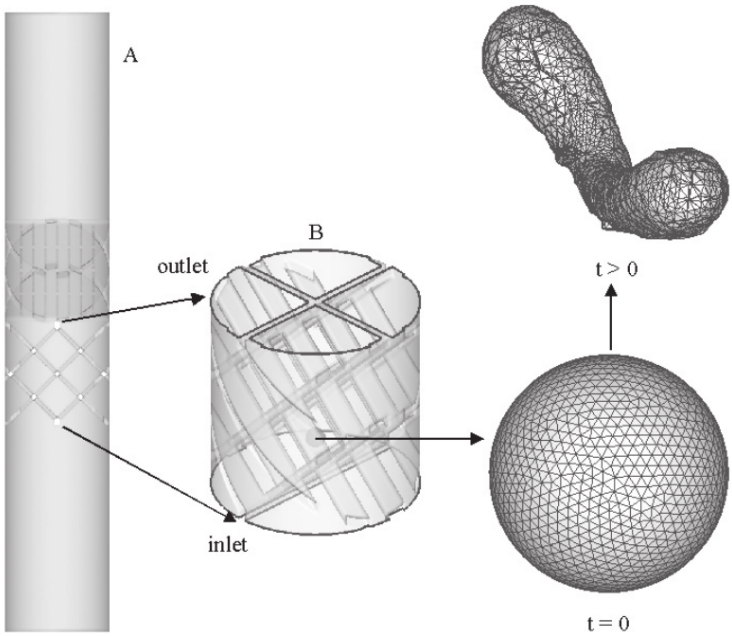

Figure 2.42 – Geometries used in simulations for drop breakup. First simulation in Geometry A for single phase flow gives the inlet and outlet boundary conditions in Geometry B. Second simulation in Geometry B tracks drop shape with VoF model. Taken from Liu et al. (2005) [28].

Liu et al. (2005) [28] found that drops deform and break-up after collision with the leading edges and cross-points of the SMX bars. Furthermore, they observed that drop collision with a bar cross-points is more effective for drop breakup [28]. This phenomenon is related to

the strain rate and thus to the critical capillary number. Liu et al. (2005) [28] affirmed that the drop breakup mechanism at the cross-points is however different from a simple 2D elongational flow. The strain rate computed in a cross-section of the mixer is reported in figure 2.43.

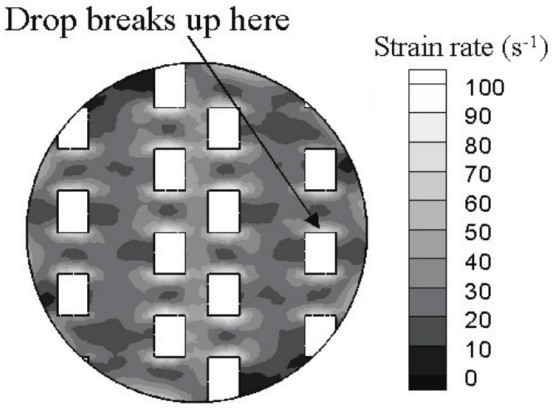

Figure 2.43 – Strain rate distribution on the cross-section C-C where a drop breaks up in a gap between crossbars. Taken from Liu et al. [28]

Zalc et al. (2002) [90] characterized Newtonian fluid mixing in a SMX static mixer at low and moderate Reynolds numbers. They performed a 3D computational analysis using unstructured tetrahedral grids. Their CFD model was validated against pressure drop values found in the literature. A qualitative and quantitative investigation of the effect of Reynolds number on flow in the SMX static mixer was carried out. One major result of Zalc et al. (2002) [90] research is that the flow is essentially independent of Reynolds number for $Re < 1$. Substantial deviations were observed at higher Reynolds numbers.

Two differently coloured fluids streams were injected in the SMX. The mixing performance of the mixer was then quantified by evaluating the striations in a cross-section. The relative standard deviation permitted Zalc et al. (2002) [90] to compute the mixing rate. Good agreement was obtained between the computational and experimental results. The relative standard deviation decreases with increasing the flow rate. This led Zalc et al. (2002) [90] to affirm that lower flow rates produce more efficient mixing with less energy consumption and thus to recommend the use of low flow rates in case of viscous fluids mixing.

2.4 Techniques for experimental analysis of biphasic dispersions

Several techniques were employed for the analysis of biphasic systems over the years. Among them, the shadowgraphy and the PIV are the most widespread. These experimental methodologies are non-invasive and non-destructive.

The following subsections 2.4.1 and 2.4.2 describe the main findings of these techniques in gas-liquid dispersions. It should be noted that, to our best knowledge, shadowgraphy and PIV were never applied to transparent SMX static mixers.

2.4.1 Bubble Shadowgraphy

When dealing with gas liquid flows, it is often advantageous to perform a shadowgraphy of the bubbles. This technique allows a complete examination of the system. This methodology was often employed to obtain estimations of gas hold-up, bubbles shapes, bubbles size, bubbles velocities etc.(Martin et al. (2017) [101]). The versatility of the shadowgraphy, combined with the relatively easy installation of the experimental set up, facilitated its deployment in many research fields over the last years.

As a recent example, Laupsien et al. (2017) [29] recorded the projected shadows of each bubble by using a camera and a LED panel installed behind a transparent column. As illustrated in figure 2.44, images coming from a shadowgraphy analysis are clear, once settled the camera options and found the correct position of the light. The quality and resolution of the images combined with the high contrast between the liquid phase and gas phase allow several post-treatments. Several authors used this technique in different biphasic systems such as Harleman et al. (2011) [102] , Sathe et al. (2010) [10] and (2013) [53], Li et al. (2012) [103], Zaruba et al. (2005) [50]. Among these references, some employed Matlab®. for the post-treatment of the frames, like Laupsien et al. (2017) [29].

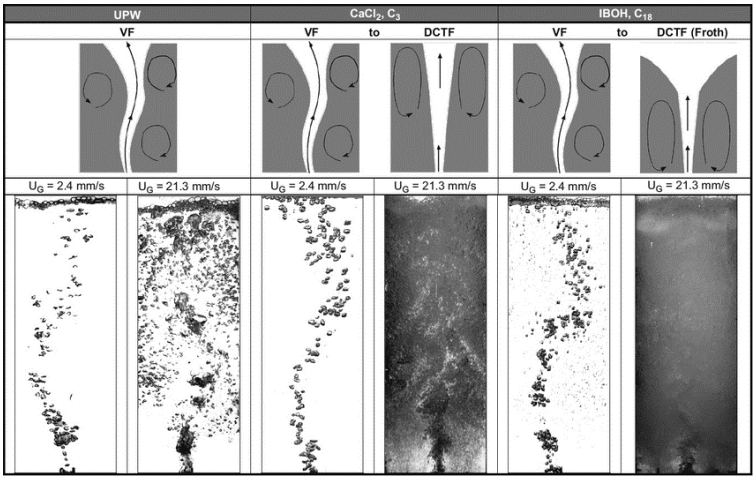

Figure 2.44 – Bubble Plume Oscillations in Viscous Fluids (Laupsien et al. 2017) [29].

The shadowgraphy technique can be used to understand the dispersed phase behaviour. This technique was widely adopted in the field of bubble column research. Researchers like Sathe et al. (2010) [10], Sathe et al. (2013) [53], Leitch and Baines (1989) [104], Zaruba et al. (2005) [50] applied such experimentations to various bubble columns.

However, other experimental techniques must be used to get information about the continuous phase. In the bibliography, it was noticed that the PIV experimentation is often used simultaneously with the shadowgraphy, to achieve an overall view of the flow inside the biphasic system [10, 53].

2.4.2 Velocity measurement technique : the PIV

The Particle Image Velocimetry (PIV) is an optical method, based on tracer tracking and image analysis techniques (Strubel et al. 2017 [105]). This methodology is used for the

determination of velocity fields (Aubin et al. (2004) [49]). In the 1980s, the PIV technique for the measurement of fluid velocities gained numerous applications (Senatore et al. 2013 [106]). The widespread applications of the PIV are mainly due to two advantages over other methods for the measurement of velocity : the PIV is non-intrusive and allows high resolution measurements over an extended spatial domain (Aubin et al. (2004) [49].

Several PIV techniques were developed over the years. For example, Chen and Fan (1992) [32] implemented a particular PIV method which was able to measure the instantaneous flow properties simultaneously with velocity vectors, like the hold-ups, and was also able to discriminate the flow properties among different phases. The fluid is seeded with solid tracer particles of small diameters. The particles are assumed to tightly follow the flow dynamics (Raffel et al. 2007 [30]). However, it is important to emphasize that the degree to which the tracer particles follow the fluid flow is strongly linked to their Stokes number. This dimensionless number allows the classification and characterization of the behaviour of suspending particles in fluids flow. The Stokes number is defined as the ratio of the characteristic time of the particle to the characteristic time of the fluid flow. It is defined as follows [30] :

$$Stk = \frac{t_0\, u_0}{l_0} \tag{2.57}$$

where u_0 is the velocity of the fluid flow away from any obstacle, t_0 is the Stokes relaxation time of the particle and l_0 is the obstacle characteristic dimension. A particle with a low Stokes number tends to follow the fluid flow, while a particle with a large value of Stokes number is dominated by its inertia, i.e. the particle tries to continue along its initial trajectory (Raffel et al. 2007 [30]).

The fluid is illuminated with a multi pulsing laser sheet so that particles become shiny and visible. Using a high-resolution camera and dedicated software, it is possible to calculate speed and direction (i.e. the velocity field) of the flow by tracking the motion of the seeding particles (Strubel et al. 2017 [105]). Figure 2.45 provides a graphical explanation of a typical PIV setup.

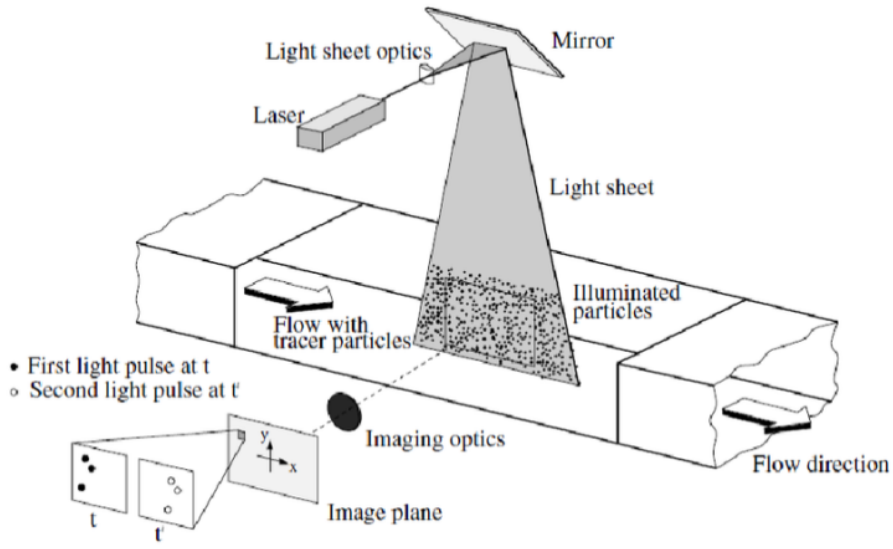

Figure 2.45 – PIV system. Taken from Raffel et al. (2007) [30].

Through a high-speed and high-resolution camera, a series of consecutive images can be recorded. These images faithfully rebuild and track the particles displacement during the PIV experiments (Chen, Fan 1992 [32]). The images post-treatment is realized by a specific software which, by doing an identification and classification of the particles in every image, can measure their displacement. By linking the spatial movement of the particles and the camera acquisition frequency, the software can compute the local velocities in all the zones where particles are located.

The bibliography appeared in the last years reveals that the PIV technique turns out to be an important way of measuring the velocity for several fluids systems. A significant amount of experiments was carried out and many systems were analysed. Among these measurements, some are particularly relevant for our study of gas liquid systems. In particular, bubble columns were treated successfully in several PIV experimental studies.

Liu, Zheng (2006) [31] examined a chain of bubbles rising in a stagnant liquid. By using red fluorescent polymer microspheres, with a density of 1050 kg/m^3 and a mean diameter of 7 micrometers, the liquid phase was seeded to perform the PIV. In their examinations, Liu, Zheng (2006) [31] also analysed the trajectories for several bubble diameters and different stagnant liquid phases. Figure 2.46 resumes the typical paths highlighted.

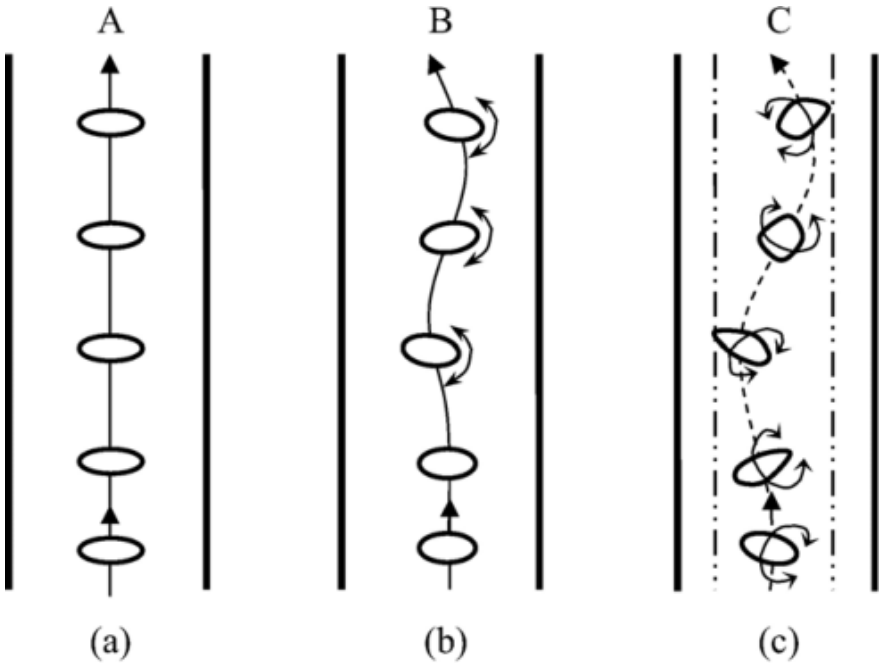

Figure 2.46 – Typical bubble rising trajectory in several liquids. (a) Straight line, (b) Zigzag and (c) Spiral. Taken from Liu, Zheng (2006) [31].

Bubbles can rise in the stagnant liquid with three types of trajectories : straight line (a), zigzag (b) and spiral (c). The bubble trajectory plays a key role in terms of flow field development. Different bubble paths induce different liquid flow structures and bubbles wake (Liu, Zheng 2006 [31]). The bubble rise velocity is also affected by the path.

Figure 2.47, taken from Liu, Zheng [31], highlights an instantaneous liquid velocity field for a bubble rising with rectilinear trajectory. This behaviour was observed for a solution of 72 wt.% glycerine in deionized water of viscosity 24.8 mPa s. The velocity field shows a

simple structure : liquid upflow in the centre of the square column and downflow in the side regions. The liquid is pushed ahead by the rising bubbles while the liquid behind them is sucked into the generated wake [31].

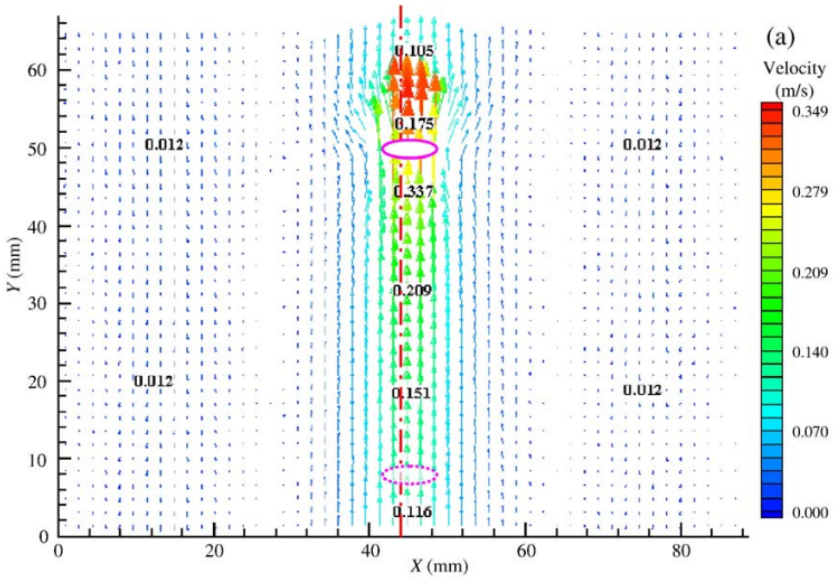

Figure 2.47 – Liquid velocity field induced by bubbles following a straight-line trajectory. Taken from Liu, Zheng (2006) [31].

The seeding particles can affect the liquid properties and change the terminal velocity or the shape of the bubbles. Some authors focused on this problem, like Lindken and Merzkirch (2002) [107]. They made some measurements on two systems, deionized water/clean air and deionized water seeded with tracer particles/clean air at 296 K.

In their experiments, by means of simultaneous shadowgraphy measurements, Lindken and Merzkirch [107] were able to estimate the bubble rise velocities, the bubble sizes along with the continuous phase velocities. The distribution of bubble rise velocity against equivalent bubble diameter obtained suggests no dependency on whether the water was seeded or not.

PIV experiments were implemented in stirred tanks and bubble columns by several authors like Gui et al. (2001) [108], Aubin et al. (2004) [49], Bilel Ben Amira et al. (2015) [109] and others already cited. Aubin et al. (2004) [49] proposed a series of experimental investigations of liquid phase hydrodynamics in aerated stirred tank.

Chen et al. (1999) [110] made several studies of bubble columns. In their investigation, the hydrodynamics of a cylindrical bubble column with a diameter of 10 cm was thoroughly analysed. Three techniques were employed : the computer-automated radioactive particle tracking (CARPT), particle image velocimetry (PIV), and computed tomography (CT) to test three superficial gas velocities, namely 2, 4, and 8 cm/s.

During their experiments, Chen et al. (1999) [110] obtained typical PIV time series as results. One of these is reported in figure 2.48. In this time series for the vertical liquid velocity, the large vortices structures are quite evident, i.e. periods of positive and negative axial velocity alternate [110].

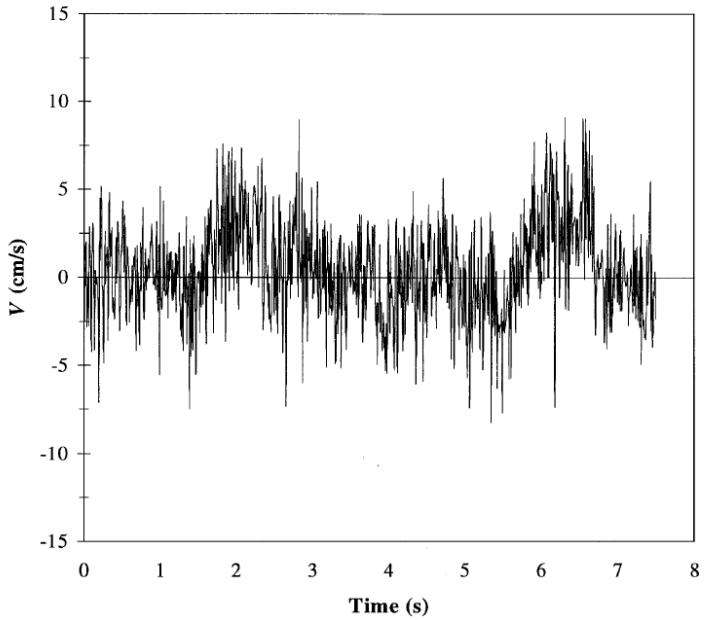

Figure 2.48 – Time-series of the axial velocity. Superficial gas velocity =4.0 cm/s. Taken from Chen (1992) [32].

2.5 Chapter summary

The main results of previous studies regarding gas liquid systems and static mixers were illustrated in the present chapter. The literature concerning the experimental means employed to analyse gas-liquid dispersion were reported as well.

This literature review highlighted the main gaps in the current knowledge. Researches on hydrodynamics inside static mixers are rather limited, particularly in the present case where the liquid is stationary or when the liquid velocity is negligible compared to the gas one.

Furthermore, dispersion, rupture and coalescence phenomena of gas bubbles in organic phases inside the Sulzer static mixer SMX^{TM} have not yet been studied.

Bibliography studies revealed that, to our best knowledge, shadowgraphy and PIV have never been applied to transparent SMX^{TM} static mixers. The deployment of these techniques could provide deeper insights into the dispersion mechanisms involved in the mixers.

Part I

Experiments

Chapter 3

The methodology

Chapter 3 introduces the experimental methodology employed in the present research. The data collected from various experiments were examined. The measurement methods adopted were the Backlight Shadowgraph Technique (BST), the Particle Image Velocimetry (PIV), the High frequency PIV (HFPIV) and oxygen absorption (estimation of k_La). The goal is to combine various approaches to enlarge the knowledge of the system under examination : the SMX static mixer. The experiments were done using a column holding up the SMX static mixer (see section 3.1.2).

Specific technical means were utilized for the PIV/HFPIV measurement. This is because these techniques were never applied to such complicated systems, to our best knowledge. In the following sections, the methodologies used to quantify the system proprieties will be deeply illustrated. The experimental apparatus will be detailed as well.

3D plastic printing of the SMX was used for all the experiments, except for some tests performed with a metallic SMX (see section 3.1.1). The main target was to measure the gas hold-up, the bubbles size, shape and velocity in several sections of the static mixer and to estimate the liquid flow fields as well as the mass transfer coefficient (k_La).

As reported in the chapter 1, experiments with a liquid flow were also carried out. These proved indispensable in order to validate the initial hypothesis that a slow liquid flow does not significantly affect the results. This hypothesis derives from the different velocity involved in the system. In fact, bubbles rise with a much larger velocity than that of a liquid in the laminar regime. Results with liquid circulation (co-current and counter current) will be further discussed in section 4.7.

3.1 Experimental set-up

Two main experimental campaigns were executed, one at Nancy in LRGP labs and one at IFPEN. They were aimed at characterizing the behaviour of gas dispersions in aqueous and organic systems in the SMX mixer. The experimental set-up consisted of SMX elements inserted into a glass column and immerged either into water or water + SDS (first experimental campaign), either into n-heptane (second experimental campaign). Gas bubbles were generated at the bottom of the glass column by gas injectors.

The gas flow rate was controlled by using an electronic valve linked to a control station. This flow rate regulation device is accurate and has a quick response time (see subsection 3.1.3). As will be explained in section 3.5, the mass transfer experiments required the use of two different gases as dispersed phase : nitrogen and air. The Reynolds number for the gas phase, defined as equation 2.8, varied from 1 to 16.

Two sizes of nozzle diameter were employed to extend the range of validity of the results for both employed liquids. Two different types of Particle Image Velocimetry techniques were employed to collect the liquid velocity fields, namely the HFPIV (High Frequency) and PIV (standard).

Five different SMX lengths were employed, with 1, 2, 5, 10 and 15 elements. The behaviour of the column without any mixing element inside was analysed as well. This "0" element length served as a reference for the comparison with SMX static mixers.

3.1.1 The transparent SMX mixers

The SMX^{TM} Sulzer was employed in all the experiments performed. As presented in section 2.2.2, the static mixers are constituted by an elementary unit which is repeated and rotated along the main axis. The number of mixer elements depends on the application context [38]. Moreover, the number of mixer elements has a considerable influence on its behaviour (Singh et al. 2009 [95]).

Figure 3.1 depicts the 10 elements mixer structure used during the experiments. Each element is rotated by 90 degrees with respect to the previous one. Moreover, the elements are made by a series of inclined blades to 45 degrees from the axis.

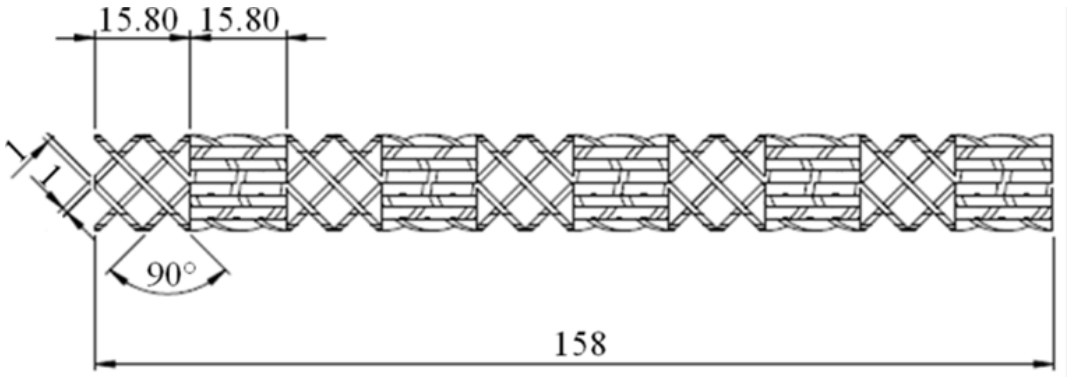

Figure 3.1 – Details of the 10 elements SMX static mixer. The length unit is mm. Taken from Scala et al. (2019) [9].

The width (resp. thickness) of a single crossbar is 1.98 mm (resp. 1 mm). The length and diameter of an element are both 15.8 mm. The ratio between diameter and length of an element is thus 1, which conforms to the standard SMX definition (Liu et al. 2006 [111] ; Singh et al. 2009 [95]). All the elements are identical.

All the mixers investigated in the present work were created through 3D printing of CAD files in Accura ClearVue^{TM} material. This material permitted us to obtain a fully transparent plastic SMX mixers.

The 1, 2, 5, 10, 15 elements devices have an overall length of 15.8, 31.6, 79, 158 and 237 mm respectively. The distance between the gas injector and the 1st mixing element was kept constant at 100 mm during all the tests. This space was largely enough for bubbles to reach their terminal rising velocity U_T.

3.1.2 Column

The optical techniques, namely PIV/HFPIV and Back-light shadowgraph, require a clear optical access to the system. This conducted us to use transparent materials. As mentioned before, two different columns were used, for aqueous or organic phase. The devices had approximately the same characteristics. The differences between the two columns are their length and their injection system mounting. These two structural differences are considered to be insignificant in terms of impact on the results.

Both cylindrical columns were made of glass. The columns were placed inside a box of squared section in order to reduce image distortion. This external jacket was filled with the same liquid as the column (water or heptane). Thanks to the above strategy, optical distortion was completely avoided. It is worth noting that the refractive indices of liquid phase, glass and plastic material of the mixers are close to each other. The mixer and the column are thus almost invisible from outside the cubic box. The degree of image distortion was checked by inserting a ruler inside the column and by verifying the length scale calibration of the camera lens.

Figure 3.2 depicts the column dedicated to the investigation of aqueous systems. The column employed for the experiments with heptane is illustrated in figure 3.3. The columns have a diameter of 16.2 mm and their heights are respectively 350 mm and 450 mm.

3.1.3 Fluids and flow regulators

As mentioned above, the SMX elements were inserted into a glass column and immerged into a liquid. During the first experimental campaign, aqueous solutions were investigated to obtain preliminary and basic results, mainly because of safety issues and easier experimental set-up. The aqueous solutions were also used to estimate the mass transfer. Most of the experiments with water were performed adding a small percentage of SDS (sodium dodecyl sulphate), namely 0.1% and 3%. This permitted us to decrease the surface tension σ between the water solution and the dispersed gas phase.

However, the primary target of this study is the investigation of organic fluids, and more precisely gasoline. Since normal heptane represents a good compromise between the gasoline properties resemblance, safety issues in the labs, the chemical inertness and the reproducibility of the experiments, it was chosen for the second experimental campaign

Nitrogen was used as a dispersed phase because it is a non-reactive stable compound. This guaranteed a higher number of re-uses of the same solution and safety with respect to the heptane. However, as illustrated in section 3.5, some experiments demanded the use of air instead of nitrogen, like, for instance, to carry out the mass transfer investigation. In this case, both gases, N_2 and O_2, were used. Table 3.1 sums up the fluids used in the experiments.

Air and nitrogen inlet pressures were settled to 2 bars for the whole experimental time

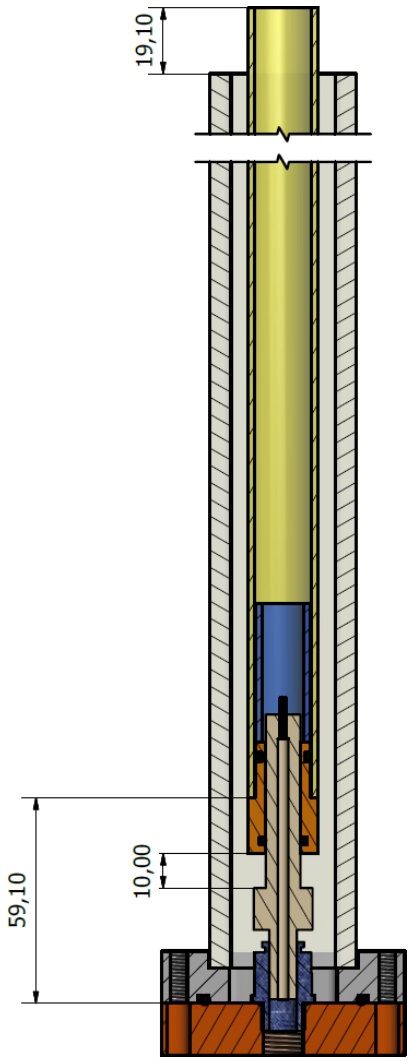

Figure 3.2 – Details of the column with double jacket used for the water + SDS systems.

Table 3.1 – Chemical properties of the products used in this research.

Substance	**Chemical formula**	**Density** $[kg\ m^{-3}]$	**Viscosity** $[Pa\ s]$	**Surface tension** $[N\ m^{-1}]$
Air (20°C, 1 atm)	N_2 and O_2	1.205	$1.82\ 10^{-5}$	-
Nitrogen (20°C, 1 atm)	N_2	1.165	$1.76\ 10^{-5}$	-
Liquid water	H_2O	998.2	$1.0\ 10^{-3}$	0.072
Liquid water + 0.1% SDS	$H_2O + SDS$	998.2	$1.0\ 10^{-3}$	0.050
Liquid water + 3% SDS	$H_2O + SDS$	998.6	$1.0\ 10^{-3}$	0.032
Liquid n-heptane	C_7H_{16}	683.8	$4.1\ 10^{-4}$	0.020

through a specific pressure regulator valve mounted on the gas line. By keeping constant the gas pressure, the effect of this parameter on the results were removed.

Figures 3.3, 3.7 and 3.11 show the equipment used in the experiments. As can be seen from the two flow diagrams (figures 3.7 and 3.11), a pressure regulator was mounted on the gas line. The pressure downstream of the flow controller was further monitored through a pressure controller. This operation is necessary in order to avoid pressure fluctuations due

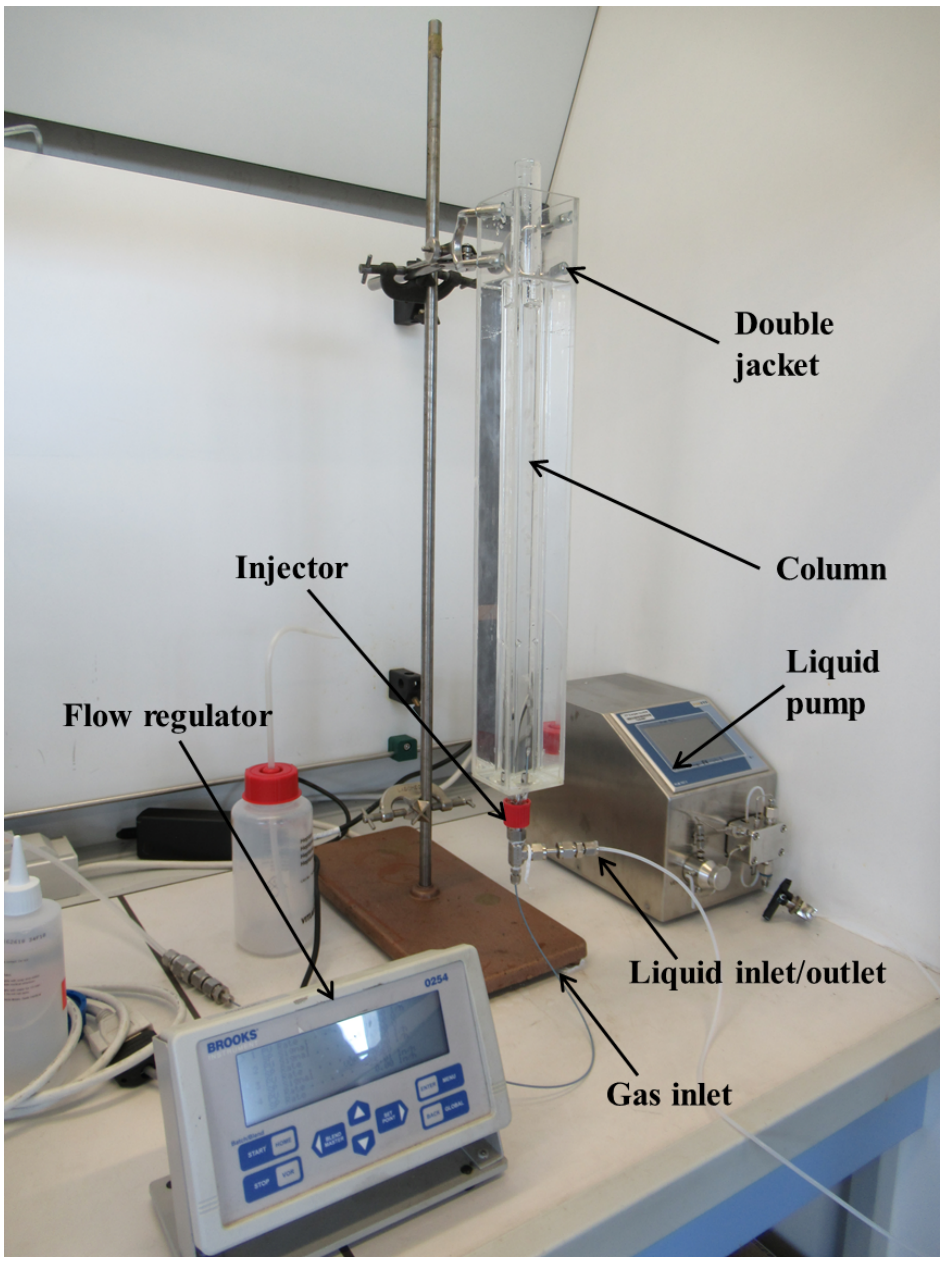

Figure 3.3 – Arrangement of equipment used in laboratory investigations with view of the column with double jacket used for the n-heptane investigation.

to the flow control apparatus.

The gas flow rate was controlled through an electronic valve connected to a flow regulator (see figure 3.3). The flow controller employed, namely the Brooks Instrument Flow Controller, is accurate as the maximum potential error during the flow regulations is lower than 2%.

The liquid flow was induced through a dosing pump (see figure 3.3). The device was a FLUSYS WADose PML-707. The latter belongs to the HPLMC (High Pressure Liquid Mass Controlled Pump) class and it is a very accurate liquid dosing and monitoring pump. The pump calibration was executed every day. The error associated to this flow regulation was less than 1%.

3.1.4 Injector

For each liquid (water and heptane), two different diameters of gas injectors were studied. Furthermore, two different injector geometries were also investigated : a flat orifice and a nozzle. The main difference between them is the bubble growth mechanism, as reported in chapter 2.

In the case of a flat orifice, the bubbles tend to be bigger for the same flow rate (see section 2.1.2). On the other hand, for a nozzle injector system smaller bubbles are generated because the fluid convection around the nozzle, especially below the bubble, enhances the detachment. Figures 3.4 and 3.5 illustrate both types of gas inlet. At the bottom of the images, it is possible to distinguish the injection apparatus.

Figure 3.4 portrays the flat orifice while figure 3.5 shows the nozzle. However, the main difference in terms of bubble size is due to the different fluids used. Indeed, as explained in subsection 3.1.3, the fundamental difference relies on the different surface tensions between gas and fluid (see table 3.1). Table 3.2 below shortly resumes the characteristics of injectors used.

Table 3.2 – Different injectors used in the present work.

Type	**Diameters [mm]**	**Liquid analysed**
Flat orifice (figure 3.4)	0.25 and 1	water/water + SDS
Nozzle (figure 3.5)	0.2 and 1	n-heptane

Figure 3.4 – Detailed view of the bubbles' generation with a flat orifice (diameter = 1 mm). Nitrogen/water system. Gas flow rate : 2.5 l/h.

Figure 3.5 – Detailed view of the bubbles' generation with a nozzle (diameter = 1 mm). Nitrogen/n-heptane system. Gas flow rate : 2.5 l/h.

3.1.5 Image Acquisition apparatus

Optical methods required a suitable images acquisition apparatus. In our works, the images were acquired through a high-speed and high-resolution camera, namely the FASTCAM SA-Z illustrated on figure 3.6. This camera has a 12-bit dynamic range, a resolution of $1\,024 \times 1\,024$ pixels and a frame rates up to 21 000 frames per second (fps). The FASTCAM camera is equipped with a highly light-sensitive image sensor (monochrome ISO 50 000).

Different lenses were used depending on the investigation objective. The focal length, the aperture and the closest focus-point were varied to achieve the highest quality images.

The camera manufacturer provides the camera control software Photron-FASTCAM®. This tool allows a broad control of the parameters, for instance, the triggering, the frame acquisition rates, the images sizes and resolutions, the exposition time and the shutter speed.

Figure 3.6 – FASTCAM SA-Z camera. Taken from Photron website.

3.2 Bubble characteristics

The shadowgraph technique was implemented to estimate the bubbles' characteristics. The technique, based on recording of the shadows created by bubbles rising in the liquid phase, is frequently used to investigate dispersed systems characterized by high contrast between the phases (Settle 2001 [112]). The images acquisition set-up used in the experiments, and reported in figure 3.7, is analogous to the one described by Laupsien et al. (2017) [29].

An EFFILUX LED panel was mounted behind the column, ensuring a homogeneous white lighting and providing a high illumination density (around 4000 lm). The distance between the panel and the column was 0.7 m, and was optimized to prevent any shadowing and reflection phenomena. Well-outlined shadows were created by the bubbles.

The light was collected on the opposite side of the column by a Photron SAZ camera (section 3.1.5), equipped with a $50mm\ f/2.8$ lens and operated 500 fps. The acquired images have a resolution of $256 \times 1\,024$ pixels, corresponding to 23×92 mm (about 11.1 pxl/mm). This allowed to visualize 5 elements with a satisfying resolution. In order to visualize all the elements, the experiments were repeated. The images were acquired during 20 s, and each experiment was repeated five times with five-minute intervals between them to improve the statistics. A detailed list of the tests performed is provided in table 3.3.

Table 3.3 – Operating conditions of Backlight shadowgraph technique measurements performed in this study.

N° of SMX elements	Nozzle diam. [mm]	Gas flow rate [l/h]	Liquid	Liquid flow rate [ml/h]
"0"[1], 1, 2, 5, 10, 15	0.2	2.5	H_20	0
"0"[1], 1, 2, 5, 10, 15	1	2.5	H_20	0
"0"[1], 1, 2, 5, 10, 15	0.2	2.5	H_20 + 0.1 % SDS	0
"0"[1], 1, 2, 5, 10, 15	1	2.5	H_20 + 0.1 % SDS	0
"0"[1], 1, 2, 5, 10, 15	0.2	2.5	H_20 + 3 % SDS	0
"0"[1], 1, 2, 5, 10, 15	1	2.5	H_20 + 3 % SDS	0
"0"[1], 1, 2, 5, 10, 15	0.2	5	H_20	0
"0"[1], 1, 2, 5, 10, 15	1	5	H_20	0
"0"[1], 1, 2, 5, 10, 15	0.2	5	H_20 + 0.1 % SDS	0
"0"[1], 1, 2, 5, 10, 15	1	5	H_20 + 0.1 % SDS	0
"0"[1], 1, 2, 5, 10, 15	0.2	5	H_20 + 3 % SDS	0
"0"[1], 1, 2, 5, 10, 15	1	5	H_20 + 3 % SDS	0
"0"[1], 1, 2, 5, 10, 15	0.2	7.5	H_20	0
"0"[1], 1, 2, 5, 10, 15	1	7.5	H_20	0
"0"[1], 1, 2, 5, 10, 15	0.2	7.5	H_20 + 0.1 % SDS	0
"0"[1], 1, 2, 5, 10, 15	1	7.5	H_20 + 0.1 % SDS	0
"0"[1], 1, 2, 5, 10, 15	0.2	7.5	H_20 + 3 % SDS	0
"0"[1], 1, 2, 5, 10, 15	1	7.5	H_20 + 3 % SDS	0
"0"[1], 1, 2, 5, 10, 15	0.2	10	H_20	0
"0"[1], 1, 2, 5, 10, 15	1	10	H_20	0
"0"[1], 1, 2, 5, 10, 15	0.2	10	H_20 + 0.1 % SDS	0
"0"[1], 1, 2, 5, 10, 15	1	10	H_20 + 0.1 % SDS	0
"0"[1], 1, 2, 5, 10, 15	0.2	10	H_20 + 3 % SDS	0
"0"[1], 1, 2, 5, 10, 15	1	10	H_20 + 3 % SDS	0
"0"[1], 1, 2, 5, 10, 15	0.25	1	C_7H_{16} (normal)	0
"0"[1], 1, 2, 5, 10, 15	0.25	1	C_7H_{16} (normal)	23, 114, 228, 342
"0"[1], 1, 2, 5, 10, 15	1	1	C_7H_{16} (normal)	0
"0"[1], 1, 2, 5, 10, 15	1	1	C_7H_{16} (normal)	23, 114, 228, 342
"0"[1], 1, 2, 5, 10, 15	0.25	2.5	C_7H_{16} (normal)	0
"0"[1], 1, 2, 5, 10, 15	0.25	2.5	C_7H_{16} (normal)	23, 114, 228, 342
"0"[1], 1, 2, 5, 10, 15	1	2.5	C_7H_{16} (normal)	0
"0"[1], 1, 2, 5, 10, 15	1	2.5	C_7H_{16} (normal)	23, 114, 228, 342
"0"[1], 1, 2, 5, 10, 15	0.25	5	C_7H_{16} (normal)	0
"0"[1], 1, 2, 5, 10, 15	0.25	5	C_7H_{16} (normal)	23, 114, 228, 342
"0"[1], 1, 2, 5, 10, 15	1	5	C_7H_{16} (normal)	0
"0"[1], 1, 2, 5, 10, 15	1	5	C_7H_{16} (normal)	23, 114, 228, 342

An algorithm for the post-treatment of the images was implemented in the Halcon® software. This algorithm is able to determine the velocities, formation frequency, positions and shapes of the bubbles. As the first step (and shared task) of the post-treatment, the

1. "0" indicates the use of the column without mixer.

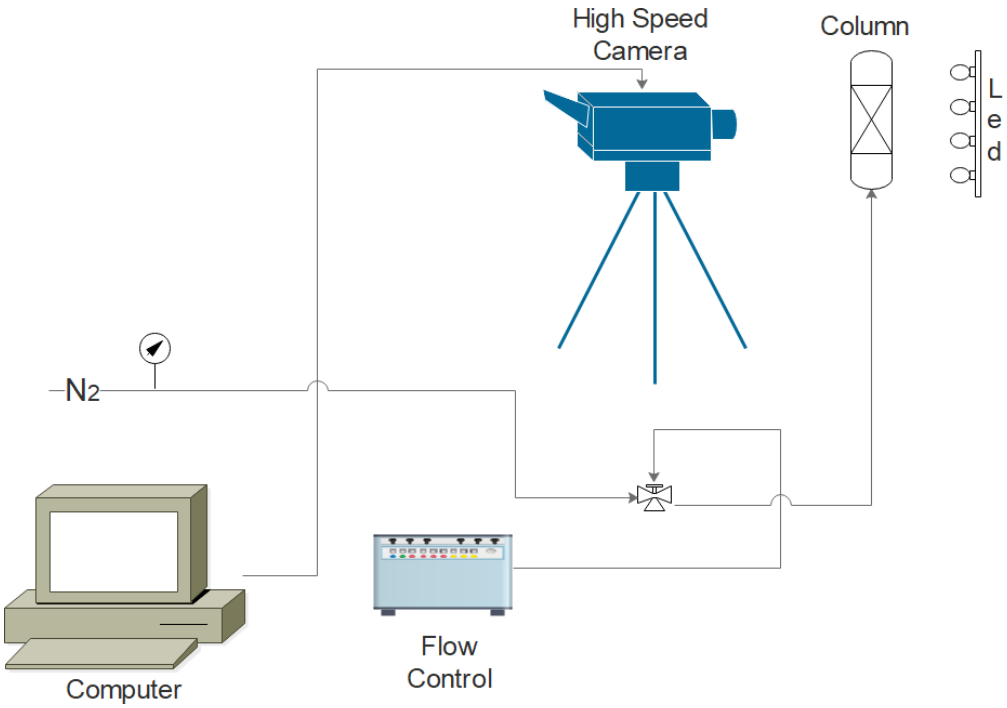

Figure 3.7 – Details of the experimental set-up used for the Back-light shadowgraph technique.

background of the images was isolated by comparing the common part of the acquisition sequence.

The background was then removed from each frame and the contrast between the liquid and bubbles was artificially increased. A threshold permitted us to separate the dispersed bubbles from the continuous liquid phase. Subsequently, a region number was assigned to each bubble. Further details on the modus operandi of the script used are given in the following subsections.

3.2.1 Bubbles' diameters and shapes

The Halcon®' operator `elliptic_axis` was chosen to estimate the bubbles' size and position. The operator `elliptic_axis` estimates the radii R_a and R_b and the orientation of the ellipse having the same aspect ratio of the input region (see MVTec Software GmbH website). The centre was estimated as well.

The number of events collected and examined, ranging from 70 000 to 100 000, was considered large enough to estimate the mean properties of the system (Buffo and Alopaeus 2016 [113]).

For the estimation of the bubbles' diameters, shapes and centres, the camera acquisition frequency was set to 500 fps. This acquisition frequency permitted an optimal mean bubble displacement between two consecutive frames, corresponding to 1 to 2 pixels. In fact, a minor displacement of bubbles would not ensure proper post-image processing. Smaller motions are in fact associated with greater errors in the localization of pixels.

The radii R_a and R_b calculation is based on the region moments. R_a and R_b are expressed

in pixels. In image processing, the image moment corresponds to a weighted average of the image pixels' intensities. A 2D region has 3 moments, namely M_{11}, M_{02} and M_{20}. Equations 3.1 and 3.2 describe the relation between the normalized moments and the radii Ra and Rb (see MVTec Software GmbH website). Figure 3.8 shows in detail how the post-treatment works and reports the radii R_a and R_b for a bubble.

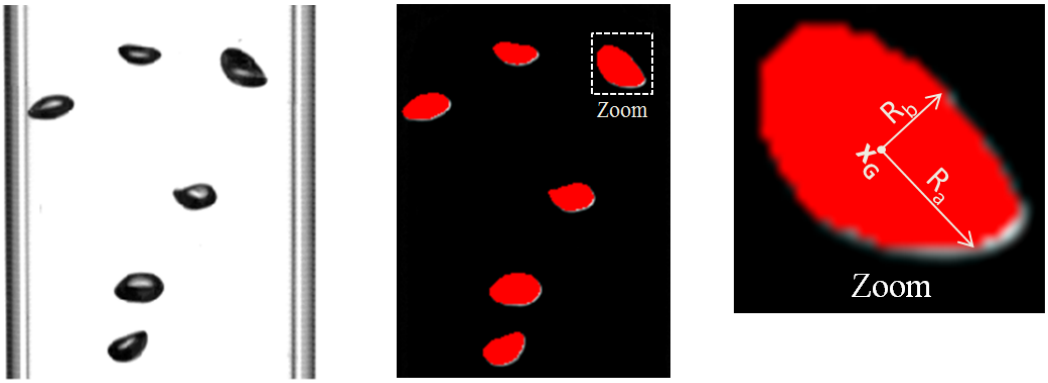

Figure 3.8 – Detailed view of the two radii R_a and R_b estimated through the Halcon®' operator `elliptic_axis`.

$$R_a = \frac{\sqrt{8(M_{20} + M_{02}) + \sqrt{(M_{20} + M_{02})^2 + 4M_{11}^2}}}{2} \tag{3.1}$$

$$R_b = \frac{\sqrt{8(M_{20} + M_{02}) - \sqrt{(M_{20} + M_{02})^2 + 4M_{11}^2}}}{2} \tag{3.2}$$

The acquired frames and the post-treatment implemented allowed us to have a 2D vision of the system. In order to obtain the bubble size on the third dimension, an assumption was necessary. The bubbles were hypothesized to have a spherical oblate shape. The missing size was thus assumed equal to the radius that had the highest absolute value.

The shape of the bubbles was evaluated by computing the sphericity ψ. This parameter indicates how closely the shape of the investigated object approaches that of a mathematically perfect sphere. The sphericity ranges from 0 to 1. The sphericity ψ of an object/particles is defined as the ratio of the surface area of a sphere having the same volume as the given object, to its surface area [114]. This definition is written as equation 3.3 :

$$\psi = \frac{\pi^{\frac{1}{3}}(6V_p)^{\frac{2}{3}}}{A_p} \tag{3.3}$$

In the former equation, V_p represents the volume of the object and A_p its surface. The sphericity of a perfect sphere is unity by definition. If r_V represents the equivalent radius of a sphere having a volume equal to V_p and if r_A designates the equivalent radius of a sphere having a surface equal to A_p, then the sphericity ψ is just the ratio of the square of these

equivalent radii :

$$\psi = \left(\frac{r_V}{r_A}\right)^2 \tag{3.4}$$

Furthermore, any object which is not a sphere will have sphericity less than 1. In case of an oblate spheroid of size $a \times b \times b$, equation 3.3 can be written as :

$$\psi = \frac{2\sqrt[3]{2ab^2}}{a + \frac{b^2}{\sqrt{a^2-b^2}} \ln\left(\frac{a+\sqrt{a^2-b^2}}{b}\right)} \tag{3.5}$$

3.2.2 Bubbles velocities

The Halcon®' operator `optical_flow_m` was chosen to estimate the bubbles' velocities. In more details, the `optical_flow_m` operator combined with the FDRIG algorithm was selected to compute the optical flow between two images (Brox et al. 2004 [115]). The optical flow represents the movement between two consecutive images and allows the estimation of pixels displacement velocities. The FDRIG algorithm is based on the minimization of the energy function (Brox et al. 2004 [115]).

The velocity of the bubbles ($\mathbf{U_b}$) was calculated by analysing its overall displacement between two frames. The ratio between the displacement ($\mathbf{d_2} - \mathbf{d_1}$) and the time elapsed between the frames ($t_2 - t_1$) is nothing but the rise velocity of the bubble, as stated in equation 3.6 hereafter :

$$\mathbf{U_b} = \frac{\mathbf{d_2} - \mathbf{d_1}}{t_2 - t_1} \tag{3.6}$$

3.2.3 Preferential paths

The preferential paths in the SMX and the bubble column were analysed as well. They represent zones or entire areas in which the probability to find a bubble is higher.

In order to explain the procedure we followed, we introduce here certain concepts. Images acquired with the shadowgraph technique are grey-scale. Each pixel of these images represents the intensity of light at that specific point. Pixel values are stored as 8-bit integers, which can vary from 0 to 255. 0 represents black whereas 255 represents white. Figure 3.9 depicts a classical grey-scale.

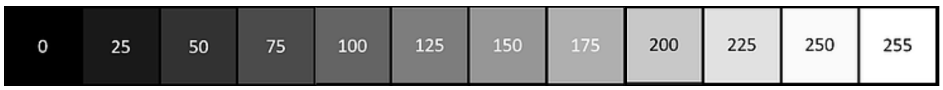

Figure 3.9 – Grey-scale with range of values.

Bubbles are delineated by their dark shadows. A pixel value inside a bubble is thus equal to 0. The continuous phase (water or heptane) is fully transparent. The pixel values corresponding to the liquid phase are white, and so with maximum pixel intensity 255.

Mean pixel values were obtained by averaging over time. More than 20 000 image frames were averaged to obtain reliable statistics. In Halcon®, the operator `intensity` was used

to calculate the mean and the standard deviation for a series of grey-scaled input images. This operator returns a single image containing the averaged value of the pixel at each point. In the resulting mean image, mean pixel values close to 0 (resp. 255) correspond thus to a region with a high (resp. poor) probability of finding a bubble.

3.3 Gas hold-up

The gas hold-up can be defined as the amount of gas kept within the column at a given time. It is one of the variables which characterizes how intense and long the contact between gas and liquid phase is. The gas hold-up is therefore related to the interfacial area between the phases. According to the nature of the system, this parameter can reach a stationary state or can vary periodically.

The analysis method employed is based on images acquisition and post-processing. Through the high-speed camera presented in section 3.1.5, a series of frames were acquired with a very low frequency, namely 5 Hz. This frequency was selected to obtain a sufficient Δt between two frames. A similar layout to that used for the shadowgraph technique was adopted (see figure 3.7).

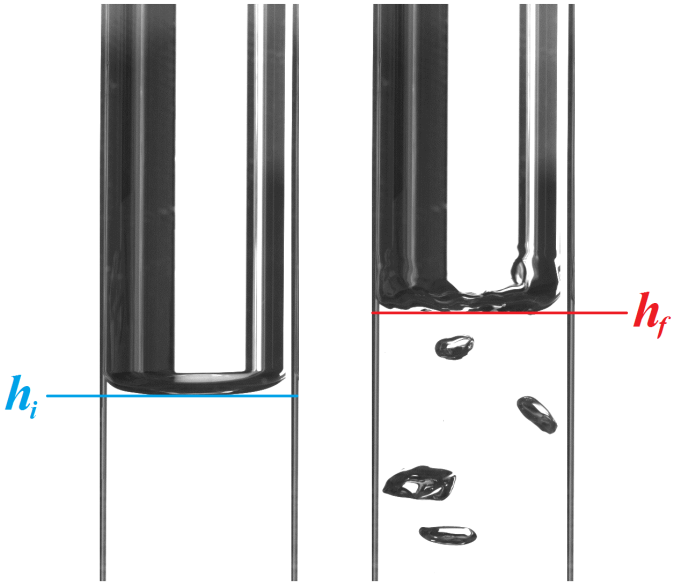

Figure 3.10 – Heptane level in the column without gas flowing (left) and with (right).

The first frame of the series was acquired without any gas flow in the column. This first image was used to achieve an initial state of the liquid level inside the column (h_i). Then, by injecting the gas and continuing the images acquisition, frames with a new liquid level were saved. The gas present within the column increases the overall volume. The volume difference is nothing but the gas hold-up. Figure 3.10 depicts the expansion of the liquid level in the column due to gas presence. Figure 3.10 shows a well delineated liquid meniscus, which was obtained thanks to the backlight led panel. The initial liquid level (h_i) and the expanded liquid level after gas injection (h_f) were measured by analysing the image sequences.

Measurement errors in locating the liquid head cannot be prevented because of its fluctuation. In fact, bubbles burst at the liquid surface and induced oscillations. To compensate these perturbations, several images were acquired to average the liquid level. In order to assess reliable values of hold-up, repeated calibration was performed to obtain scale factor from pixel to mm (about 11 pixel/mm).

The quality of images saved can be deemed more than acceptable to estimate very accurate mean values of hold-up. The increase of the liquid level due to the gas held in the liquid phase was measured by ImageJ ®, a software for the images' treatment.

At least 50 images were averaged to estimate the mean increment of liquid level. This number of frames was considered acceptable to estimate suitable mean values of the liquid level. The hold-up (ϵ_G) value revealed, in fact, to be unchanged by increasing the number of frames acquired.

Experiments were repeated four times with similar results. The values of each experiment were obtained with the following equation 3.7. The liquid volume inside the column (V_L) was measured and annotated before each test in order to double check the liquid volume values. The volume occupied by the SMX was subtracted from V_L.

$$\epsilon_G = \frac{V_G}{V_G + V_L} = \frac{(h_f - h_i)\left(\pi \frac{D_c^2}{4}\right)}{h_f \left(\pi \frac{D_c^2}{4}\right)} \tag{3.7}$$

Table 3.4 reports the operating conditions of the gas hold-up investigations.

3.4 Liquid velocity fields

In the present work, instantaneous velocity field measurements were achieved using a standard Particle Image Velocimetry (PIV) and a High Frequency Particle Image Velocimetry (HFPIV) system. Both of these techniques are non-intrusive (Link et al. 2008 [116]). PIV and HFPIV are based on the image processing of two consecutive frames acquired at a well-controlled time interval (Sathe et al. 2010 [10]).

The major and only difference between PIV and HFPIV is the frequency of data acquisition. In fact, the standard PIV operates with a considerably lower frequency of liquid flow acquisition.

The PIV is commonly employed to examine liquid flow or gas-liquid flow (Aubin et al. (2004) [49]). In our liquid velocity fields measurements, a method similar to that described in Funfschilling and Li (2001) [117] was used. The scheme employed is reported in figure 3.11.

The PIV images were acquired through the FASTCAM SA-Z high-speed and high-resolution camera described in section 3.1.5. As mentioned in section 3.1.2, the cylindrical column produces a lens effect totally cancelled out by the surrounding square jacket filled with n-heptane or water. The calibration, the distance between the camera lens and the column, and the relative position of both devices were controlled as well. To increase the quality

1. "0" indicates the use of the column without mixer.

Table 3.4 – Operating conditions of hold-up measurements performed in this study.

N° of SMX elements	Nozzle diam. [mm]	Gas flow rate [l/h]	Liquid	Liquid flow rate [ml/h]
"0"[1], 1, 2, 5, 10, 15	0.2	2.5	H_20	0
"0"[1], 1, 2, 5, 10, 15	1	2.5	H_20	0
"0"[1], 1, 2, 5, 10, 15	0.2	2.5	H_20 + 0.1 % SDS	0
"0"[1], 1, 2, 5, 10, 15	1	2.5	H_20 + 0.1 % SDS	0
"0"[1], 1, 2, 5, 10, 15	0.2	2.5	H_20 + 3 % SDS	0
"0"[1], 1, 2, 5, 10, 15	1	2.5	H_20 + 3 % SDS	0
"0"[1], 1, 2, 5, 10, 15	0.2	5	H_20	0
"0"[1], 1, 2, 5, 10, 15	1	5	H_20	0
"0"[1], 1, 2, 5, 10, 15	0.2	5	H_20 + 0.1 % SDS	0
"0"[1], 1, 2, 5, 10, 15	1	5	H_20 + 0.1 % SDS	0
"0"[1], 1, 2, 5, 10, 15	0.2	5	H_20 + 3 % SDS	0
"0"[1], 1, 2, 5, 10, 15	1	5	H_20 + 3 % SDS	0
"0"[1], 1, 2, 5, 10, 15	0.2	7.5	H_20	0
"0"[1], 1, 2, 5, 10, 15	1	7.5	H_20	0
"0"[1], 1, 2, 5, 10, 15	0.2	7.5	H_20 + 0.1 % SDS	0
"0"[1], 1, 2, 5, 10, 15	1	7.5	H_20 + 0.1 % SDS	0
"0"[1], 1, 2, 5, 10, 15	0.2	7.5	H_20 + 3 % SDS	0
"0"[1], 1, 2, 5, 10, 15	1	7.5	H_20 + 3 % SDS	0
"0"[1], 1, 2, 5, 10, 15	0.2	10	H_20	0
"0"[1], 1, 2, 5, 10, 15	1	10	H_20	0
"0"[1], 1, 2, 5, 10, 15	0.2	10	H_20 + 0.1 % SDS	0
"0"[1], 1, 2, 5, 10, 15	1	10	H_20 + 0.1 % SDS	0
"0"[1], 1, 2, 5, 10, 15	0.2	10	H_20 + 3 % SDS	0
"0"[1], 1, 2, 5, 10, 15	1	10	H_20 + 3 % SDS	0
"0"[1], 1, 2, 5, 10, 15	0.25	1	C_7H_{16} (normal)	0
"0"[1], 1, 2, 5, 10, 15	0.25	1	C_7H_{16} (normal)	23, 114, 228, 342
"0"[1], 1, 2, 5, 10, 15	1	1	C_7H_{16} (normal)	0
"0"[1], 1, 2, 5, 10, 15	1	1	C_7H_{16} (normal)	23, 114, 228, 342
"0"[1], 1, 2, 5, 10, 15	0.25	2.5	C_7H_{16} (normal)	0
"0"[1], 1, 2, 5, 10, 15	0.25	2.5	C_7H_{16} (normal)	23, 114, 228, 342
"0"[1], 1, 2, 5, 10, 15	1	2.5	C_7H_{16} (normal)	0
"0"[1], 1, 2, 5, 10, 15	1	2.5	C_7H_{16} (normal)	23, 114, 228, 342
"0"[1], 1, 2, 5, 10, 15	0.25	5	C_7H_{16} (normal)	0
"0"[1], 1, 2, 5, 10, 15	0.25	5	C_7H_{16} (normal)	23, 114, 228, 342
"0"[1], 1, 2, 5, 10, 15	1	5	C_7H_{16} (normal)	0
"0"[1], 1, 2, 5, 10, 15	1	5	C_7H_{16} (normal)	23, 114, 228, 342

and the resolution of acquisitions, the SMX mixers' elements were examined in groups of five. This decision represents a fair compromise between image quality and the number of elements visualized on each image.

In multiphase flows, the PIV shows certain limitations (Raffel et al. 1998 [118] ; Funfschilling and Li 2001 [117]). Among them, the major limitations encountered in this study

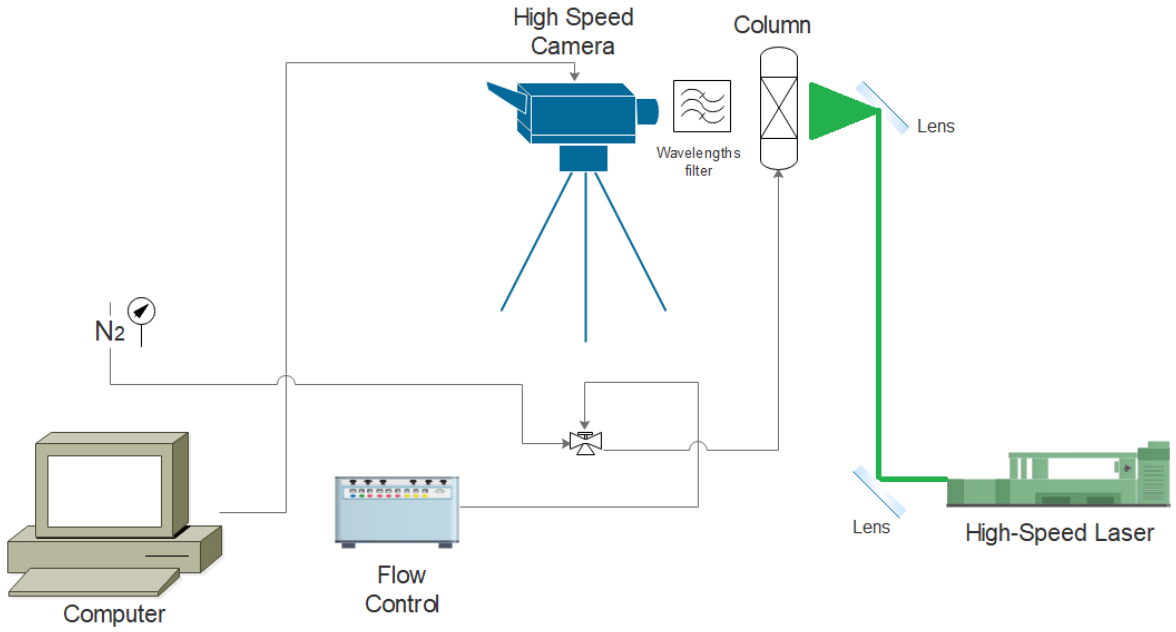

Figure 3.11 – Simplified representation of the PIV/HFPIV scheme used in the present research.

were the sedimentation of the seeding particles, and the shadows created by SMX and bubbles. When working with the heptane, the light diffraction on the gas-liquid interfaces, SMX and column walls were partially solved by employing suitable fluorescent seeding particles (see section 3.4.2).

The standard PIV was used for a preliminary study of the system with water-based solutions. This technique is known to be easier to deploy than the HFPIV. The time required for data acquisition and post-treatment is notably lower. The HFPIV, even if it is more complex, allows a higher quality and quantity of data.

The n-heptane was investigated more thoroughly. In fact, for each configuration, namely with different gas flow rates, mixer length and diameter of the injector, 7 500 flow fields were acquired in total and processed to obtain the averaged flow field. The 7 500 fields were collected through 5 different repetition tests, each corresponding to 1 500 flow fields. For each test, the solution containing the seeding particles was removed from the column and stirred for at least 2 minutes before reuse. The operating conditions of the PIV and HFPIV are reported in table 3.5.

3.4.1 Laser sheet

For the first experimental campaign, a Dantec Dynamics DualPower Laser at 532 nm was employed for the classic PIV investigation in aqueous system. This is a dual cavity flash-pumped Nd :YAG laser with a frequency of 15 Hz. The delay between the 2 laser pulses was varied between 2 ms and 8 ms. The energy per pulse oscillated between 65 and 200 200 MJ.

For the second experimental campaign, a high-speed Quantronix Hawk-Duo Nd :YAG at 532 nm was used in the HFPIV investigation in heptane. This is a dual oscillator head

1. "0" indicates the use of the column without mixer.

Table 3.5 – Operating conditions of standard Particle Image Velocimetry measurements performed in this study.

N° of SMX elements	Nozzle diam. [mm]	Gas flow rate [l/h]	Liquid	Liquid flow rate [ml/h]
"0"[1], 5, 10, 15	0.2	2.5	H_20	0
"0"[1], 5, 10, 15	1	2.5	H_20	0
"0"[1], 5, 10, 15	0.2	2.5	H_20 + 0.1 % SDS	0
"0"[1], 5, 10, 15	1	2.5	H_20 + 0.1 % SDS	0
"0"[1], 5, 10, 15	0.2	2.5	H_20 + 3 % SDS	0
"0"[1], 5, 10, 15	1	2.5	H_20 + 3 % SDS	0
"0"[1], 5, 10, 15	0.2	5	H_20	0
"0"[1], 5, 10, 15	1	5	H_20	0
"0"[1], 5, 10, 15	0.2	5	H_20 + 0.1 % SDS	0
"0"[1], 5, 10, 15	1	5	H_20 + 0.1 % SDS	0
"0"[1], 5, 10, 15	0.2	5	H_20 + 3 % SDS	0
"0"[1], 5, 10, 15	1	5	H_20 + 3 % SDS	0
"0"[1], 5, 10, 15	0.2	7.5	H_20	0
"0"[1], 5, 10, 15	1	7.5	H_20	0
"0"[1], 5, 10, 15	0.2	7.5	H_20 + 0.1 % SDS	0
"0"[1], 5, 10, 15	1	7.5	H_20 + 0.1 % SDS	0
"0"[1], 5, 10, 15	0.2	7.5	H_20 + 3 % SDS	0
"0"[1], 5, 10, 15	1	7.5	H_20 + 3 % SDS	0
"0"[1], 5, 10, 15	0.2	10	H_20	0
"0"[1], 5, 10, 15	1	10	H_20	0
"0"[1], 5, 10, 15	0.2	10	H_20 + 0.1 % SDS	0
"0"[1], 5, 10, 15	1	10	H_20 + 0.1 % SDS	0
"0"[1], 5, 10, 15	0.2	10	H_20 + 3 % SDS	0
"0"[1], 5, 10, 15	1	10	H_20 + 3 % SDS	0
"0"[1], 1, 2, 5, 10, 15	0.25	1	C_7H_{16} (normal)	0
"0"[1], 1, 2, 5, 10, 15	1	1	C_7H_{16} (normal)	0
"0"[1], 1, 2, 5, 10, 15	0.25	2.5	C_7H_{16} (normal)	0
"0"[1], 1, 2, 5, 10, 15	1	2.5	C_7H_{16} (normal)	0
"0"[1], 1, 2, 5, 10, 15	0.25	5	C_7H_{16} (normal)	0
"0"[1], 1, 2, 5, 10, 15	1	5	C_7H_{16} (normal)	0

with a high repetition rate and an average power of 120 W. Only one laser cavity was used. Two different frequencies were used to perform data acquisition. The instantaneous flow velocities were acquired at 100 Hz. The laser time pulse ranged from 2 ms to 8 ms (from 500 Hz to 125 Hz) with a view to achieve the optimal displacement of the particles between the two consecutive frames required for the velocity field computation. The laser and the camera were connected via TTL inputs/outputs with a high efficiency synchronizer.

For both techniques, the pulsed light was converted into a laser sheet by using a series of curved mirrors and lenses. The laser sheet was focused in the median section of the column, along the axial direction. The laser sheet can be considered two-dimensional because of its small thickness in the orthogonal direction. The plane position and thickness in both sides

of the jacket were checked daily and kept constant.

3.4.2 PIV seeding particles and filtering system

The choice of the appropriate particles is often critical in order to perform the PIV experiments (Strubel et al. 2017 [105]). In standard PIV, the light issued from Mie scattering on the particles illuminated by the laser sheet is collected by the camera. But the camera also collects the light coming from other sources of Mie scattering. In our experimental set-up, Mie scattering on the walls of the glass column, on the SMX elements and on the gas bubbles overwhelmed the light coming from the particles. Therefore, fluorescent particles were used. Since the fluorescent signal is at a higher wavelength than the excitation from the laser, it was possible to separate the Mie scattering on the particles from the Mie scattering on other surfaces by using a proper spectral filter in front on the lens of the camera.

Among all the fluorescent particles available, the `PS-FluoRed-Fi251` particles have the lowest density, namely 1050 kg/m^3. They revealed to be suitable with both water and n-heptane. All other properties are resumed in table 3.6.

Table 3.6 – Characteristics of the particles used in this investigation.

Seeding Particles	PS-FluoRed-Fi251
Mean Diameter [µm]	25.07
Standard Deviation [µm]	0.20
CV %	0.8
Solids Content [wt. %] :	2.5
Density [kg/m^3]	1050
Shape	Spherical

The particles used are fluorescently labelled polystyrene particles (PS-Fluo). The copolymerization process generates polymer particles with favourable properties such as high monodispersity (coefficient of variance CV $< 5\%$), spherical shape, low density and bright fluorescence as well as minimized dye leaching into the surrounding medium.

Furthermore, the `PS-FluoRed-Fi251` particles have the property to absorb the laser light with a wavelength of 532 nm and to re-emit with a wavelength of 607 nm. This specific property allowed us to use a filter to remove all of the reflected and scattered laser light from the static mixer, the column, and the bubbles. This filter allowed only the light with wavelength between 595 nm and 615 nm to reach the camera lens. This improved significantly the quality of the investigation. This filter has a null transmittance for wavelengths lower than 556 nm, as shown on figure 3.12.

The filter was mounted facing the camera lens as shown in figure 3.11 and figure 3.13. The filtered image presented on figure 3.14 exhibits the successful tracking of seeding particles. The SMX structure appears as black zones. Thanks to the zero-transmittance of the filter, the laser light scattered out of the static mixer was well filtered.

One of the major problems encountered with the former particles is their sedimentation velocity. When the particles are suspended in n-heptane, their sedimentation velocity

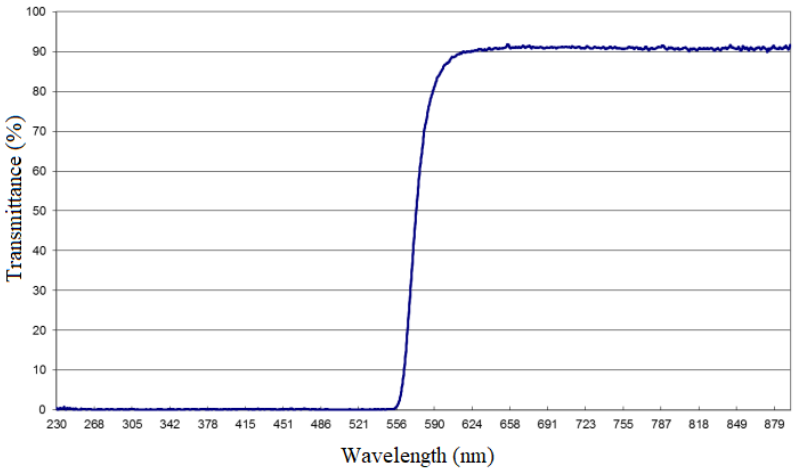

Figure 3.12 – Transmittance of the filtering system employed in PIV experiments.

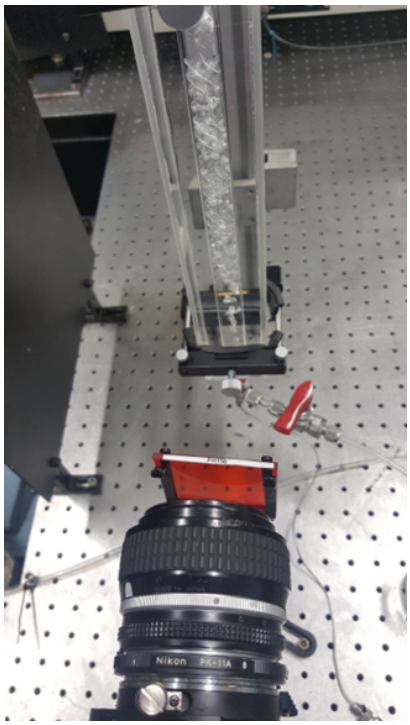

Figure 3.13 – Details of the PIV camera lens and filtering system used during the investigation.

Figure 3.14 – A typical PIV acquisition after filtration.

$u_{s,p}$ reaches about 0.3 mm/s. This velocity was estimated with the Stokes law (G. Stokes 1850 [119]) :

$$u_{s,p} = \frac{2}{9} \frac{\rho_p - \rho_L}{\mu} g R_p^2 \tag{3.8}$$

where g is the gravity acceleration, R_p is the radius of the spherical particle. ρ_p and ρ_L are respectively the density of the particles and the fluid (liquid). μ represents the fluid dynamic viscosity. The Stokes law was established for spherical particles at low Reynolds number, by writing an equilibrium between the gravity and drag forces. If $\rho_p > \rho_L$, the particle is falling downwards. If $\rho_p < \rho_L$, the particle is rising upwards.

In the case of `PS-FluoRed-Fi251` particles, the particles sedimentation velocity was confirmed by the PIV results (see also chapter 4). The corresponding Stokes' relaxation time is 89 µs for these seeding particles. It can be considered suitable enough for the time scale of PIV experiments. The sedimentation velocity calculated in aqueous system is significantly lower because of the similarity of water and particles densities. No sedimentation problems were identified in aqueous systems.

The sedimentation in heptane conducted us to remove the solution from the column at the end of each experiment. The solution containing the particles was then collected in a dedicated agitation system that ensured their homogeneity. This approach guaranteed reliable results and repeatability of experiments. The temperature was monitored and kept constant so that the luminous intensity associated with the particles was not affected.

There was a last issue which appeared as an additional problem : the dye migration from the particles surface into heptane. It was thus decided to change every day the heptane solution and to add new tracer. The tests confirmed a good quality of the signal seven hours after the particles were dispersed in the heptane. After that time interval, the signal became insufficient and the background noise coming from the dye extraction made difficult the data post-treatment.

3.4.3 Image acquisition and processing

The PIV images were acquired through the a high-speed FASTCAM SA-Z CMOS camera, equipped with a $50mm\ f/2.8$ lens. The resolution of the images was $256 \times 1\ 024$ pixels, corresponding to 23×92 mm (about 11.1 pxl/mm).

Data were collected and analysed by DaVis LaVision® (HFPIV) and Dantec Dynamic-Studio® (standard PIV) software. These software share similar bases and modus operandi. They subdivide the PIV images into small interrogation windows where the velocity of fluid is measured.

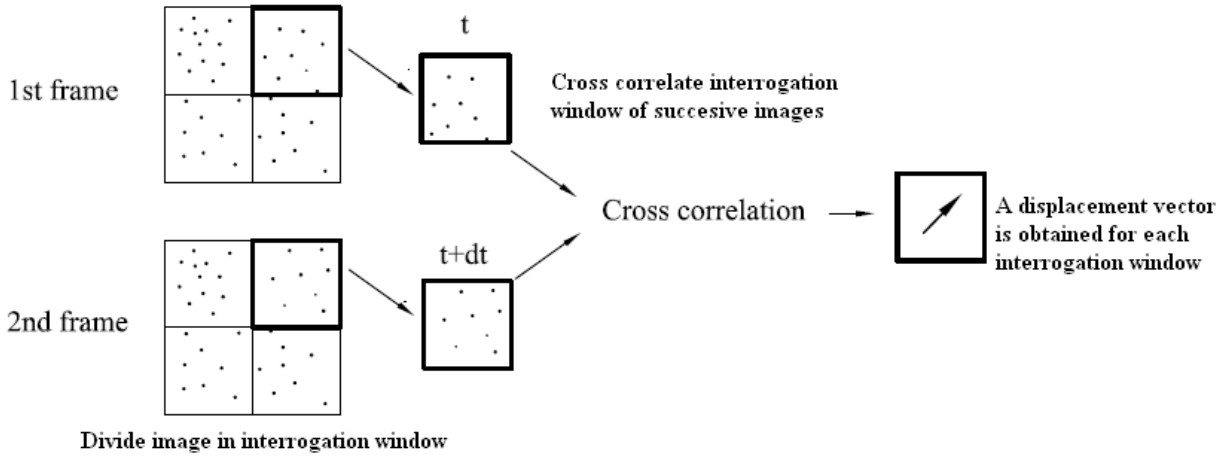

Figure 3.15 – Illustration of the basic principle of PIV. Taken from Mokhtar et al. (2017) [33].

Figure 3.15 describes the particles' motion between two consecutive frames (frame 1 acquired a t and frame 2 at $t + dt$). The displacement vector at time t, $d\mathbf{x}(t)$, was obtained

by searching for the maximum of cross-correlation between two consecutive frames. This displacement was a global value over all the particles present in the interrogation window. The velocity was then determined by :

$$\mathbf{u}(t) = \frac{d\mathbf{x}(t)}{dt} \tag{3.9}$$

The adaptive PIV scheme was selected in order to achieve the highest possible accuracy, robustness and spatial resolution (see LaVision website). This method allows the use of the multi-pass option. The latter permitted us to decrease progressively the interrogation window size. The window size ranged from 64×64 pixels to 8×8 pixels.

Noise was removed by applying a Gaussian filter. The Gaussian filter belongs to the image-blurring filter class. It uses a Gaussian function for calculating the transformation to apply to each frame pixel. The equation 3.10 hereafter expresses the Gaussian function in two dimensions :

$$G(x, y) = \frac{1}{2\,\pi\,\sigma_d^2}\; e^{-\frac{x^2+y^2}{2\,\sigma_d^2}} \tag{3.10}$$

where x represents the distance from the origin in the horizontal axis, y the distance from the origin in the vertical axis and σ_d is the standard deviation of the Gaussian distribution.

The post-treatment and image-filtering algorithms within Davis® and DynamicStudio® allowed proper phases discrimination. The bubbles were completely removed from the PIV raw images if they were located on the laser plane.

3.5 Mass transfer and k_La estimation

Mass transfer measurement is a key factor to assess the efficiency of static mixers in saturation or stripping of gases, as discussed in the bibliography study in section 2.3.7. However, an accurate estimation of the transfer coefficient can be delicate.

In the present research, we used an oxygen probe for aqueous solutions in order to assess the mass transfer efficiency of the mixer. The methodology we used was thus based on the oxygen transfer between air and an aqueous solution. Once the probe was fixed at the exit of the column, a stripping of the oxygen present in the water was done by flowing nitrogen into the column. The O_2 concentration read by the probe decreased until zero. A calibration was necessary at that point. Then, the column feed was changed from nitrogen to air. The O_2 concentration increased in time up to a saturation value. All experiments were executed with this same procedure.

Experiments were performed both with and without the SMX. As the probe was particularly thin (see section 3.5.1), perturbations brought by the probe were negligible at the gas outlet. Local accumulation of oxygen in proximity of the probe detection point were completely avoided. Different positions of the oxygen probe were also tested in the exit section of the column.

3.5.1 The oxygen probe

In the present study, a Unisense Oxygen probe OX-100 with a tip diameter between 90 µm and 110 µm was selected. This microsensor is shown in figure 3.16. The probe recorded the data with a frequency of 4 Hz. The signal resulting from this analysis was in picoAmpere pA. A normalization of the signal was necessary in order to homogenize the data resulting from different tests.

Figure 3.16 – Unisense oxygen microsensor employed to collect the oxygen concentration data. Picture taken from Unisense website.

The Unisense Oxygen Microsensor is a highly accurate and thin probe. Its response time is less than 2 seconds. Furthermore, this oxygen microsensor shown an insignificant oxygen consumption during the experiments. This Clark-type probe was employed to measure the partial pressure of the oxygen (P_{O_2})in the liquid phase in the several sections in the column.

The P_{O_2} measurement is based on oxygen diffusion through a silicone membrane to an oxygen reducing cathode. The reducing cathode is polarized against an internal Ag/AgCl anode. Moreover, the Unisense microsensor has a guard cathode that removes any oxygen in the electrolyte, thus minimizing zero-current and pre-polarization time. As stated before, the resulting sensor signal is in the picoAmpere (pA) range.

The probe signal was collected with a high quality picoammeter, namely the Unisense Microsensor Multimeter. This device is equipped with a signal amplifier. The complete acquisition system is depicted in figure 3.17. The Microsensor Multimeter is easy to operate with automatic sensor recognition for most Unisense microsensors. It allowed us to establish a direct communication to PC via USB connection, and also to export directly in `CSV` files the collected data.

Figure 3.17 – Unisense Microsensor Multimeter and Unisense microsensors. Picture taken from Unisense website.

3.5.2 Experimental techniques and models for k_La determination

Two different approaches can be adopted for measuring the oxygen transfer coefficient : the dynamic method and the steady-state method. More detailed descriptions of these methods are available in the literature (Godbole et al. 1984 [120], Dudley 1995 [121], Chaumat et al. 2005 [122], Dhaouadi et al. 2008 [123], Pinelli et al. 2010 [124], Kovats et al. 2017 [125]).

The mass transfer between the gas and the liquid phase is usually described by Lewis-Whitman theory. This model, based on the two films, describes the exchange of a gas compound from one phase to another. The mass transfer is caused by a concentration gradient.

The driving force of the mass transfer is usually concentrated at the interface, namely within the film of each phase. A more detailed view of the oxygen transfer from air bubbles to water is shown in figure 3.18. The oxygen concentration profile is plotted versus the interface distance. The two films, δ_L and δ_G, are highlighted as well.

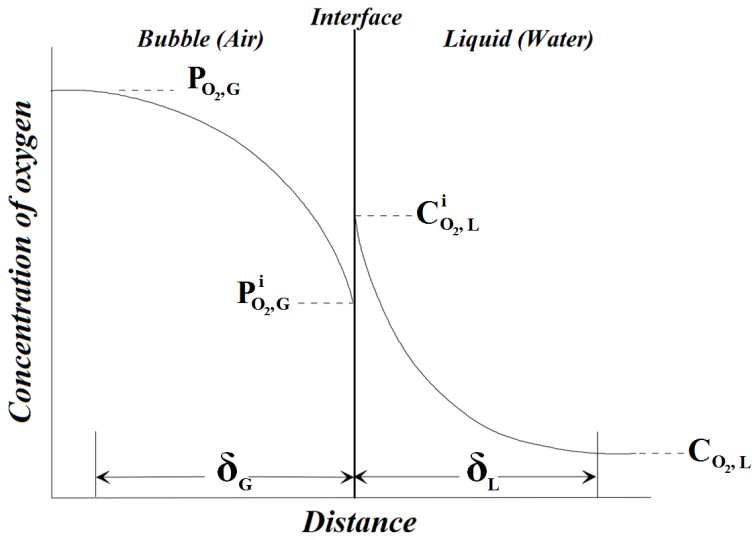

Figure 3.18 – Oxygen concentration evolution with respect to gas-liquid interface distance.

The gaseous phase the concentrations are expressed as partial pressure of the component (P_{O_2}) . The two interfacial flows representing the transfer of oxygen (J_{O_2}) from the gaseous phase to the liquid phase are reported in equation 3.11 and equation 3.12. $J_{O_2,G}$ represents the interfacial flux in the gas phase and $J_{O_2,L}$ is the interfacial flux in the liquid phase.

$$J_{O_2,G} = k_G(P_{O_2} - P^i_{O_2}) \tag{3.11}$$

$$J_{O_2,L} = k_L(C_{O_2} - C^i_{O_2}) \tag{3.12}$$

P_{O_2} and C_{O_2} are the partial pressure and the concentration of the oxygen respectively in the gas and in the liquid. Partial pressure at the interface ($P^i_{O_2}$) is related to concentration $C^i_{O_2}$ through the Henry law (see equation 2.1). k_G ($\frac{\mathrm{m}}{\mathrm{s}}$) and k_L $\left(\frac{\mathrm{mol/(s{\cdot}m^2)}}{\mathrm{(mol/m^3)}}\right)$ are respectively the mass transfer coefficient for the gas side and the liquid side.

When the oxygen contraction in the liquid phase reaches the equilibrium ($C^*_{O_2}$), equation 3.11 can be written as :

$$J_{O_2,G} = H_{O_2} k_G (C^*_{O_2} - C^i_{O_2,L}) \tag{3.13}$$

The oxygen concentration at the interface is difficult to measure. It is therefore convenient to introduce the overall mass transfer (K_L). If the oxygen flux is expressed in terms of the overall liquid driving force, the following equation is obtained :

$$J_{O_2,L} = K_L (C^*_{O_2} - C_{O_2,L}) \tag{3.14}$$

The two flux $J_{O_2,G}$ and $J_{O_2,L}$ are identical at the equilibrium. By manipulating equations 3.12, 3.13 and 3.14, we can relate the coefficients as follows.

$$\frac{1}{K_L} = \frac{1}{H_{O_2} k_G} + \frac{1}{k_L} \tag{3.15}$$

When H_{O_2} is high (low gas solubility) and $k_G >> k_L$, equation 3.15 becomes :

$$\frac{1}{K_L} = \frac{1}{H_{O_2} k_G} + \frac{1}{k_L} \approx \frac{1}{k_L} \tag{3.16}$$

This approximation is valid for water/air systems because of the low solubility of oxygen. The limiting step in this case is the diffusion of the O_2 into the liquid phase. The O_2 Transfer Tate (OTR) can be expressed as function of the flux and the specific surface area a.

$$OTR = J_{O_2,L} = K_L a (C^*_{O_2} - C_{O_2,L}) \approx k_L a (C^*_{O_2} - C_{O_2,L}) \tag{3.17}$$

The "gassing-in" dynamic method was adopted in this investigation to determine k_La values in the static mixer. It consists in a step change in the gas inlet from nitrogen (oxygen stripping) to air (oxygen adsorption). More details can be found in section 2.3.7. Table 3.7 reports the experimental conditions investigated with the "gassing-in" dynamic method.

Table 3.7 – Operating conditions of oxygen transfer measurements performed in this study.

N° of SMX elements	**Nozzle diam. [mm]**	**Gas flow rate [l/h]**	**Liquid**	**Liquid flow rate [ml/h]**
"0"[1], 5, 10	0.25	1	H_20	0
"0"[1], 5, 10	1	1	H_20	0
"0"[1], 5, 10	0.25	2.5	H_20	0
"0"[1], 5, 10	1	2.5	H_20	0
"0"[1], 5, 10	0.25	5	H_20	0
"0"[1], 5, 10	1	5	H_20	0

There are several models for the experimental data fitting, i.e. the perfectly mixer phase model, the plug flow model, the axial dispersion model and the no depletion model [124]. The

1. "0" indicates the use of the column without mixer.

perfect mixing model was adapted for both phases (gas and liquid). This model is considered as suitable for a first approximation (Márquez et al. 1994 [126], Pinelli et al. 2010 [124]). The perfectly mixer model is featured by constant k_La and, unless otherwise specified, constant and uniform hold-up.

The mass balance equations for the liquid and gas phase are reported below. For the liquid phase, the mass balance equation is written as [124] :

$$\frac{dC_{O_2,L}}{dt} = \frac{k_La}{1-\epsilon_G}\left(\frac{C^i_{O_2,G}}{H_{O_2}} - C_{O_2,L}\right) \tag{3.18}$$

where ϵ_G is the gas fraction, H_{O_2} represents a proportionality coefficient and $C^i_{O_2,G}$ is the oxygen concentration at the interface. The mass balance in the gas phase is reported in equation 3.19 [124] :

$$\frac{dC_{O_2,G}}{dt} = -\frac{Q_G\, C_{O_2,G}}{V_G} - \frac{k_La}{\epsilon_G}\left(\frac{C_{O_2,G}}{H_{O_2}} - C_{O_2,L}\right) \tag{3.19}$$

where Q_G is the volumetric gas flow rate, V_G represents the gas volume and $C_{O_2,G}$ is the oxygen concentration in the gas phase. In summary, k_La values were obtained with the dynamic method. The experimental oxygen-dissolved concentrations were fitted with an idealized model and the overall k_La value, that gives the best match, was retained. All experiments were performed at a constant temperature of 20°C.

3.6 Chapter Summary

The present chapter introduces the experimental methodology used : Backlight Shadowgraph Technique (BST), Particle Image Velocimetry (PIV), High frequency PIV (HFPIV) and oxygen absorption (estimation of k_La). The technical means and the methodologies used to quantify the system characteristics were deeply illustrated. Furthermore, this chapter reported the operating conditions of the main experimental techniques employed in the current study. Several parameters were varied to analyse their effect on the system, namely the number of mixing elements, the nozzle diameter, the gas and liquid flow rates.

Chapter 4

Results and discussion

The present chapter 4 is dedicated to the results obtained throughout the experimental investigations. An overview of the main problems in the different experiments performed was provided for each technique in dedicated sections of chapter 3. This chapter follows the same structure as chapter 3. The results concerning the bubbles' diameters, shapes, velocities and preferential paths, gas hold-up, liquid velocity fields and mass transfer are developed in the below sections. Only the most meaningful results were outlined here, with an emphasis on the 10 elements SMX and on the results obtained in the organic phase. Some of the results presented in this chapter were also the object of a publication by Scala et al. (2019) [9].

4.1 Bubbles' diameters and shapes

In this section, results concerning the normal heptane organic phase will be emphasized. Considerations on aqueous systems will be discussed to a lesser extent. The low surface tension between nitrogen and heptane leads to more breakage and coalescence events and makes the shadowgraph investigation more interesting.

The mean bubble diameter was estimated by applying the hypothesis that bubbles are ellipsoids (Grund et al. 1992 [127] ; Lage and Espósito 1999 [128] ; Bouaifi et al. 2001 [86] ; Kazakis et al. 2008 [129]). Based on this assumption, an equivalent bubble diameter can be estimated. This diameter is defined as the diameter of the sphere whose volume is equivalent to the ellipsoidal bubble volume (Lage and Espósito 1999 [128]).

The above hypothesis was later verified. The amount of gas contained throughout the system with and without static mixers was recomputed by summing up the volumes of all the bubbles. These integrated values were found comparable to the experimental values reported in the section 4.4. The maximal deviation observed is lower than 5%. This deviation could be attributed to the ellipsoidal assumption made about bubbles' shapes.

The satisfactory comparison between these two different methods reveals the accuracy of the images post-treatment algorithm implemented in Halcon® and Matlab®. The Halcon® treatment proved to be robust and efficient as it was able to detect more than 99% of the bubbles in the following operating conditions : heptane, $Q_G = 1\,\mathrm{l/h}$, $d_n = 1\,\mathrm{mm}$.

4.1.1 Bubbles' diameters in aqueous system

The SDS dissolved led to a significantly higher dispersion efficiency due to the lower surface tension between the phases. Figure 4.1 shows how the dispersion improves when the concentration of SDS increases.

In pure water, it was not possible to carry out experiments inside the SMX for high flow rates ($> 5\,\mathrm{l/h}$), because of insufficient light passing through the column and too many overlapping bubbles. The above can be observed in the second picture from the left in figure 4.1. A large amount of bubbles accumulated at the inlet of the SMX static mixer, as shown on the two leftmost images of figure 4.1. At higher flow rate (second image from left), a gas cushion of more than 10 mm was encountered at the inlet of the SMX. Although pure water examinations were not possible at high flow rates, an examination of the regions immediately before and after the SMX were still feasible due to the absence of bubbles accumulation in these regions.

When increasing the SDS concentration (rightmost images of figure 4.1), the amount of bubbles stuck on the SMX surface drastically decreases, thus making PIV and shadowgraph experiments feasible.

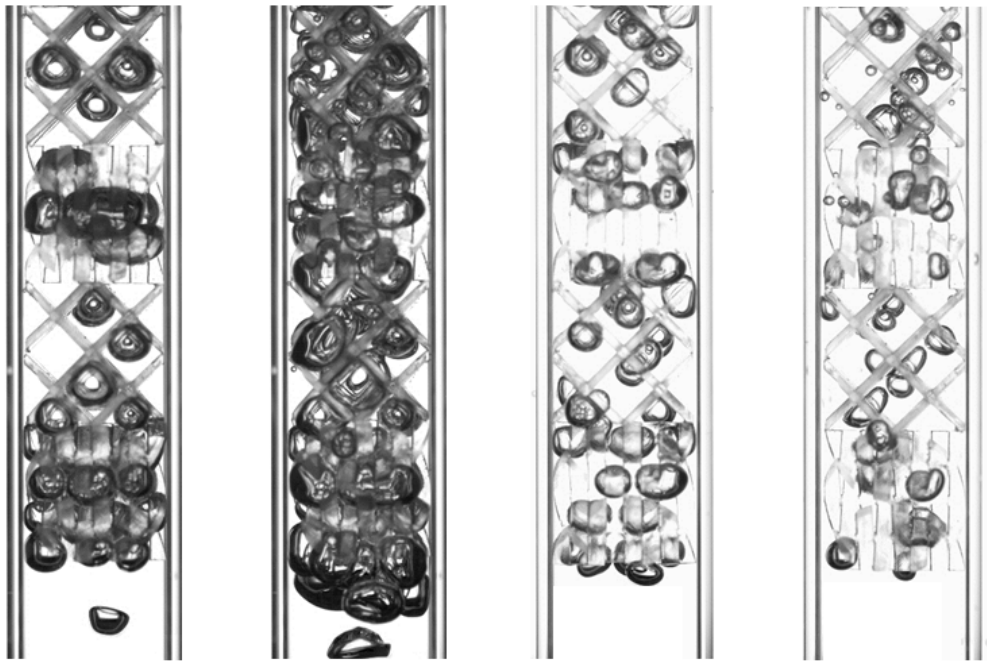

Figure 4.1 – Backlight images under different operating conditions. From left to right : Pure water with $d_n = 1\,\mathrm{mm}$ and $Q_G = 2.5\,\mathrm{l/h}$, Pure water with $d_n = 1\,\mathrm{mm}$ and $Q_G = 10\,\mathrm{l/h}$, Water + 0.1% of SDS with $d_n = 1\,\mathrm{mm}$ and $Q_G = 2.5\,\mathrm{l/h}$, and Water + 3% of SDS with $d_n = 1\,\mathrm{mm}$ and $Q_G = 2.5\,\mathrm{l/h}$

In aqueous systems, the analysis of diameters revealed a prevalence of coalescence phenomena inside the mixer. Using pure water, the mean equivalent diameter doubled between inlet and outlet. Adding 3% of SDS, the diameter between inlet and outlet remained almost unchanged. However, the distribution evolved considerably. A high quantity of small bubbles with diameters inferior to 1 mm was observed at the SMX outlet.

4.1.2 Bubbles' diameters in normal-heptane

A more extensive analysis than in water was undertaken in heptane. The following parameters were varied in the experiments :

- 6 SMX configurations : 0 (i.e. empty bubble column), 1, 2, 5, 10 and 15 SMX elements ;
- 2 gas flow rates : 1 and 2.5 l/h ;
- 2 nozzle diameters : 0.25 and 1 mm.

Note that it was not possible to predict bubbles' characteristics for higher gas flow rates (5 l/h) due to overlaps of bubbles that prevented estimating their diameters.

At first, the bubbles' shapes and velocities in the empty column were compared to those measured before the SMX inlet. No significant difference was identified. This observation proved that the mixer does not affect the bubble shapes and velocities in its upstream region. This observation remained valid at positions further than two cylinder diameters upstream the SMX.

Figures 4.2, 4.3, 4.4 and 4.5 display the Probability Density Function (PDF) of the bubbles' diameter at $Q_G = 2.5$ l/h for both nozzle diameters, in the simple column without mixer (see figure 4.2) and at the outlet of SMX of different lengths (see figures 4.3, 4.4 and 4.5).

From the plot without mixer of figure 4.2, it can be seen that the distribution obtained using the bigger nozzle is narrower around the Sauter diameter. The distribution resulting from $d_n = 0.25$ mm and $Q_G = 2.5$ l/h presents a different trend, with a secondary peak corresponding to small bubbles ($d_e \simeq 0.6$ mm). This is explained by a different bubbles' detachment regime from the small injector (more details can be found in section 2.1.2).

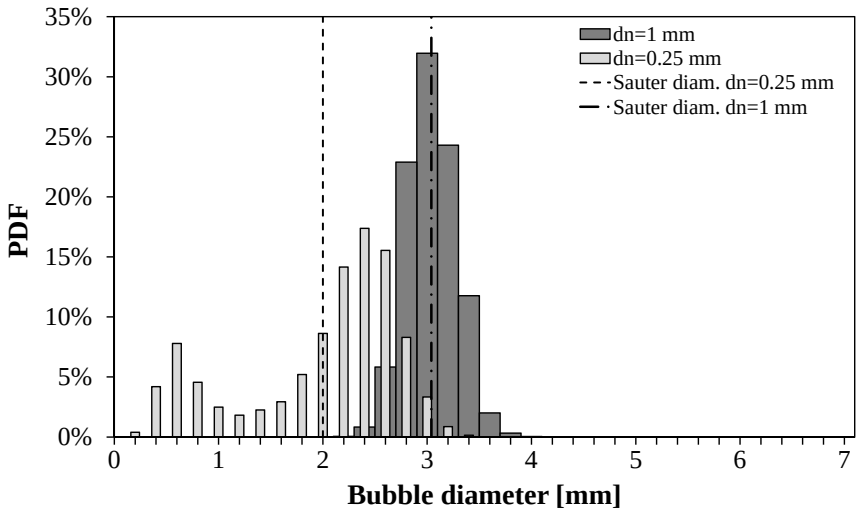

Figure 4.2 – Equivalent diameter distributions measured in empty column. $Q_G = 2.5$ l/h.

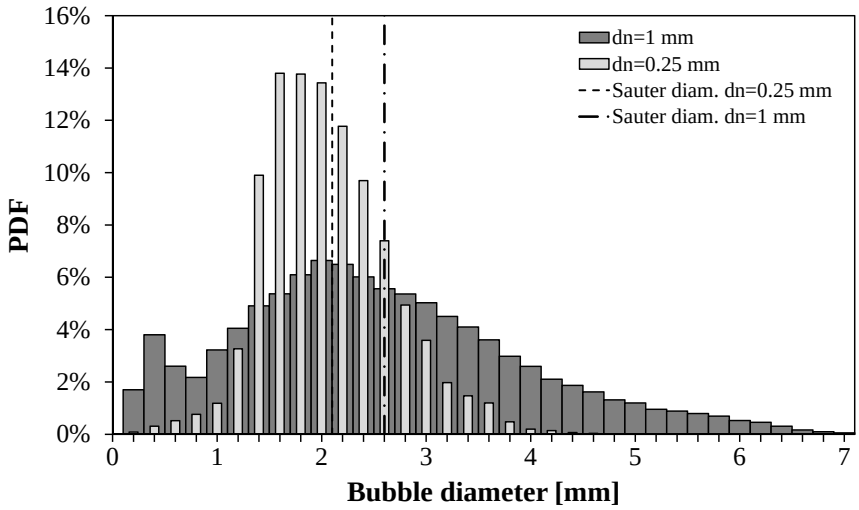

Figure 4.3 – Equivalent diameter distributions measured at the 5 SMX elements exit. $Q_G = 2.5\,\mathrm{l/h}$.

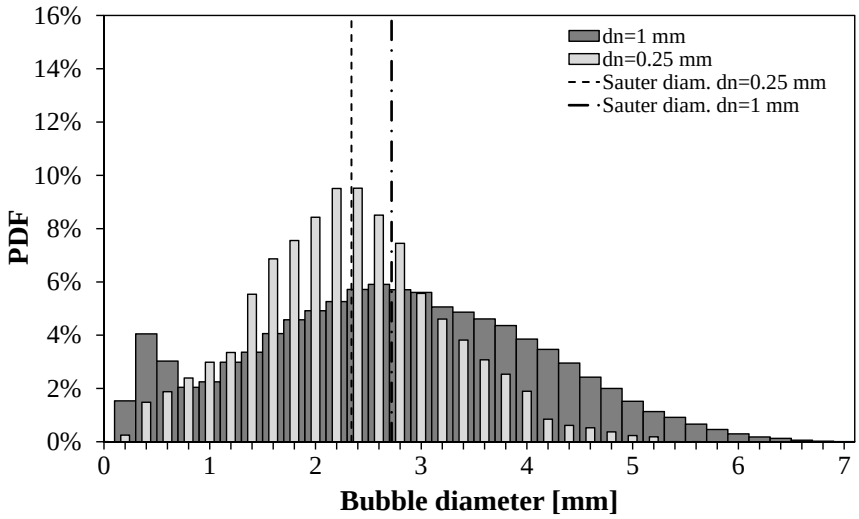

Figure 4.4 – Equivalent diameter distributions measured at the 10 SMX elements exit. $Q_G = 2.5\,\mathrm{l/h}$.

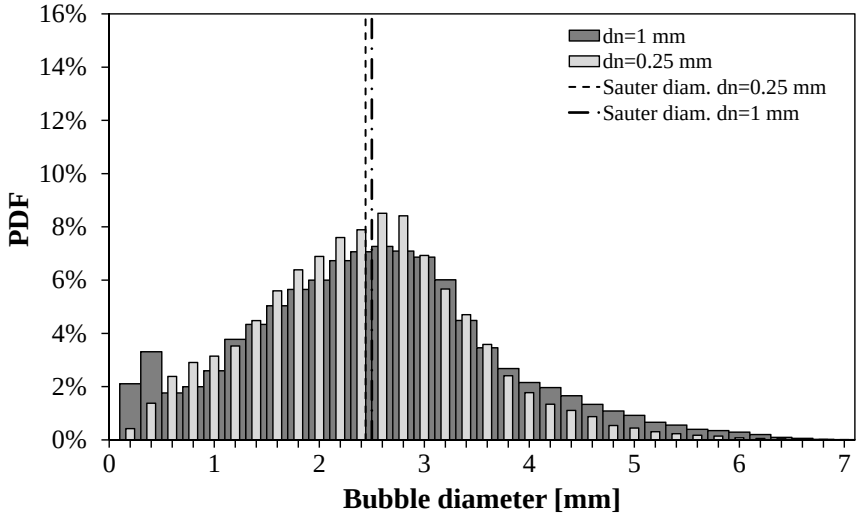

Figure 4.5 – Equivalent diameter distributions measured at the 15 SMX elements exit. $Q_G = 2.5\,\mathrm{l/h}$.

As shown in figures 4.3, 4.4 and 4.5, the probability density function (PDF) of bubbles' diameter changed considerably at the three mixer exit, when compared to figure 4.2. All distributions are wider. The percentages of small bubbles ($d_e < 1.5\,\text{mm}$) as well as large bubbles ($d_e > 4\,\text{mm}$) clearly increased, in particular for the longest SMX.

On figures 4.3, 4.4 and 4.5, the smallest bubbles generated by the smaller nozzle with $d_n = 0.25\,\text{mm}$, which were visible through the secondary peak in the left of figure 4.2, tended to coalesce when passing through the mixers. The breakup phenomena leading to small bubbles were thus reduced with $d_n = 0.25\,\text{mm}$.

The most striking changes were observed for the bigger nozzle. The probability density function (PDF) resulting from the 1 mm nozzle reported for the 5 elements in figure 4.3 shows a significant primacy of coalescence phenomena. A peculiar trend should be noted with the 1 mm nozzle, as a peak is detected in proximity of 0.5 mm. These small bubbles were generated mainly during the impact with the SMX first element. In fact, the bubbles have bigger diameters before entering the mixer (d_{32}=3.05 mm) and hence higher velocities. This translates into a high break-up probability. The Sauter diameters d_{32} detected at the exit of the 5 elements are clearly dependent on the injector size.

Figure 4.4 provides the bubble size distributions measured at the outlet of 10 SMX elements. The distributions present some changes for both nozzles when compared with 5 elements on figure 4.3. The histogram for the 0.25 mm nozzle is more spread, which signifies that more bubbles broke-up and/or coalesced. However, concerning the 1 mm nozzle histogram, the changes are less obvious. Besides, the Sauter diameters are almost comparable.

The data in figure 4.5 show the PDF of the equivalent diameter observed after 15 elements. The size distributions for the 0.25 mm and 1 mm nozzles are now similar to each other. These results tend to prove that a dynamical equilibrium is reached inside the 15 elements mixer. This equilibrium stems from the dynamic competition between the coalescence and break-up of bubbles involved in the mixer. The Sauter diameters d_{32} depend much less on the nozzle, and vary around 2.5 mm.

All the above observations revealed that the nozzle diameter governed the bubbles sizes. This trend was more evident on the measurements without the static mixer (see figure 4.2). The gap between the injectors is even more marked for low nitrogen flow rates. To complete this discussion, figure 4.6 provides further understanding of the effect of the nozzle diameter at $Q_G = 1\,\text{l/h}$. It can easily be noted that the overall amount of bubbles is higher in the image on the left of figure 4.6. That is because, when reducing the nozzle diameter for a given gas flow rate, smaller bubbles are released at a higher frequency.

However, the presence of an SMX of increasing length dampens the differences caused by the injector size. By increasing the SMX length at $Q_G = 2.5\,\text{l/h}$, the mean Sauter diameters for the two nozzle sizes tend to reach the same value at the SMX exit as shown from figure 4.3, through 4.4 up to 4.5.

Figures 4.7, 4.8 and 4.9 depict the equivalent diameter distribution for the $d_n = 1\,\text{mm}$ nozzle and for gas flow rate $Q_G = 1\,\text{l/h}$ plotted against $Q_G = 2.5\,\text{l/h}$ previously shown in figures 4.2, 4.3 and 4.4. The distributions at $Q_G = 1\,\text{l/h}$ differ from those shown above. A lower percentage of bubble breakup was observed. In addition, less coalescence was detected. The lower frequency of bubble formation leads to an inferior amount of bubbles in the system, and so to a lower probability of collisions, which in turn conducts to less coalescence events.

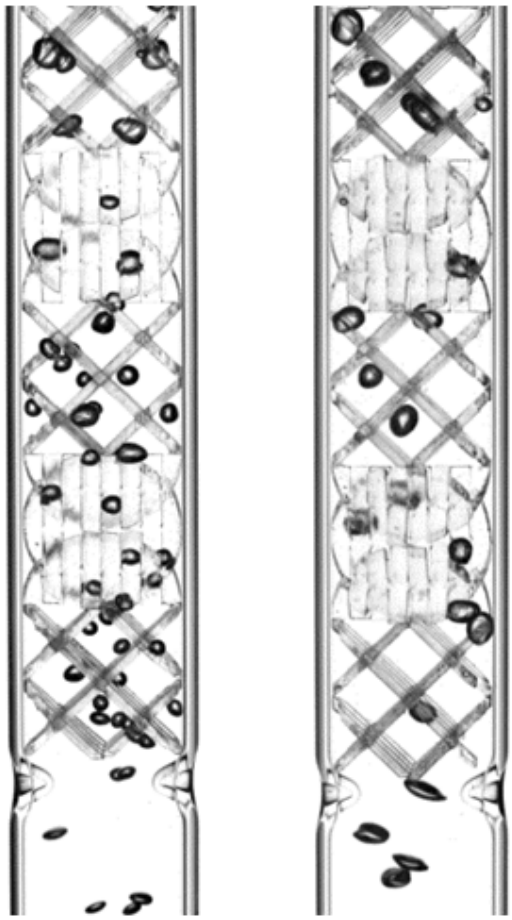

Figure 4.6 – Comparison between two nozzles diameters : 0.25 mm (left) and 1 mm (right). $Q_G = 1\,\mathrm{l/h}$.

The bubbles' formation frequency was also calculated by monitoring the nozzle area. The major results are gathered in table 4.1. It is worth noting that the presence of the static mixer inside the column does not affect the bubbles' formation frequency. The formation frequency of the bubbles and the flow rate permitted us to calculate bubbles' mean diameters. The diameters estimated by the bubbles' shadows are reported in the last column of table 4.1. The maximum deviation is less than 13%.

Table 4.1 – Bubbles characteristics obtained by post-treatment of shadowgraph images.

Nozzle diameter [mm]	**Flow rate [l/h]**	**Frequency formation [bubbles/s]**	**Calculated diameters [mm]**	**Shadows estimated diameters [mm]**
0.25	1	68	1.98	1.91
0.25	2.5	89	2.45	2.17
1	1	25	2.79	2.70
1	2.5	45	3.09	3.05

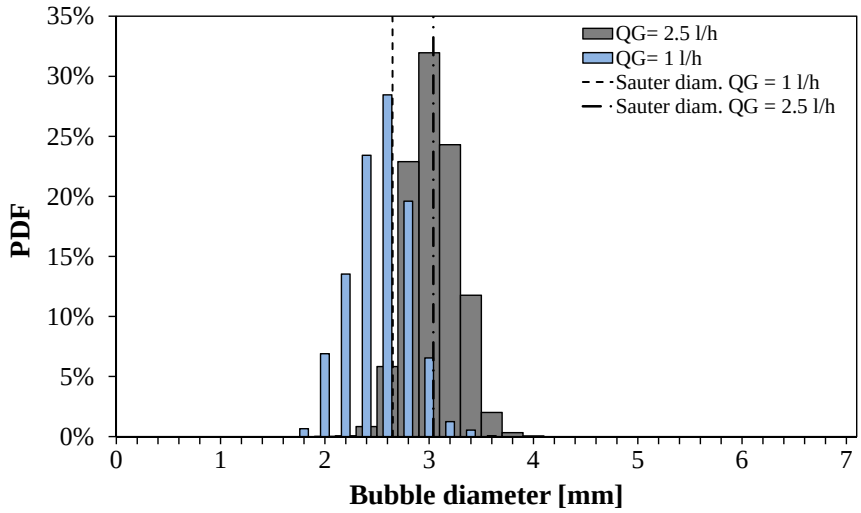

Figure 4.7 – Equivalent diameter distribution measured in the bubble column. $Q_G = 1\,\mathrm{l/h}$, $d_n = 1\,\mathrm{mm}$.

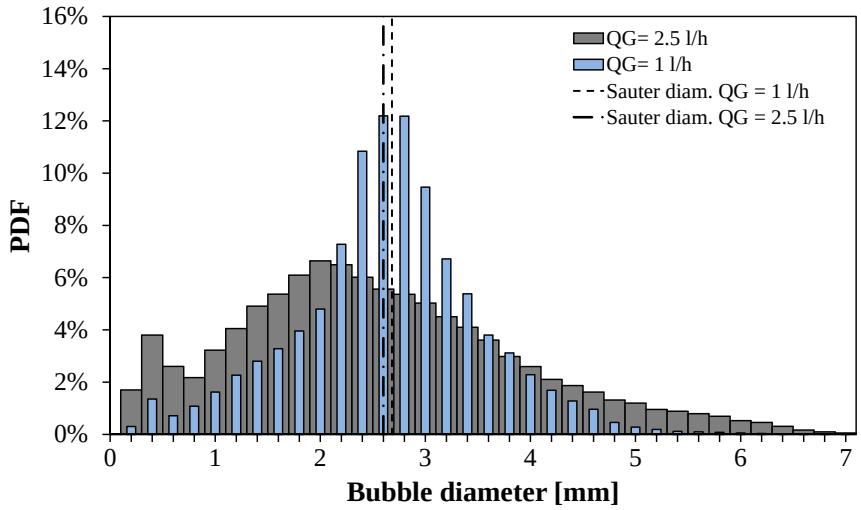

Figure 4.8 – Equivalent diameter distribution measured at the outlet of 5 elements. $Q_G = 1\,\mathrm{l/h}$, $d_n = 1\,\mathrm{mm}$.

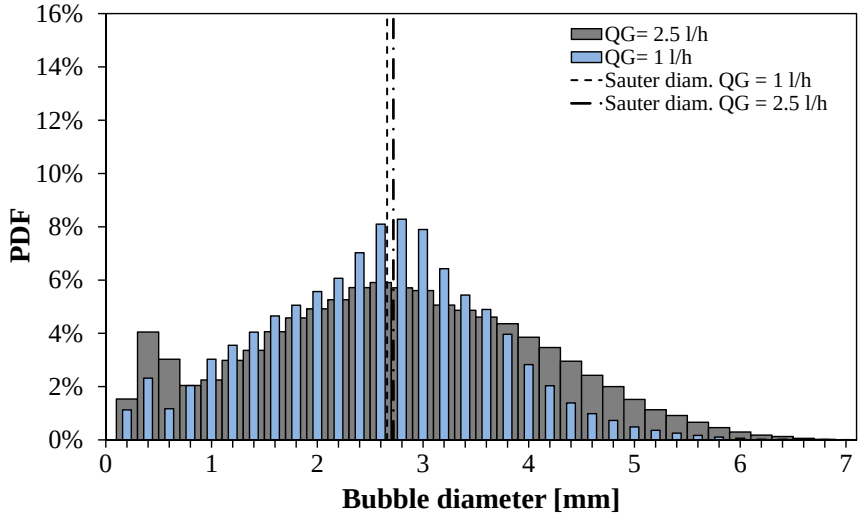

Figure 4.9 – Equivalent diameter distribution measured at the outlet of 10 elements. $Q_G = 1\,\mathrm{l/h}$, $d_n = 1\,\mathrm{mm}$.

4.2 Bubble velocities

The average bubble velocity inside the empty column and the mixer is an important parameter that determines the gas residence time in the liquid. The bubble velocities were evaluated through the shadowgraph by tracking the bubbles' position in time every 0.02 s. This time interval was necessary in order to limit errors in the post-treatment process. As in section 4.1.2, measuring velocities for higher gas flow rates (> 5 l/h) was not possible due to too many overlapping bubbles.

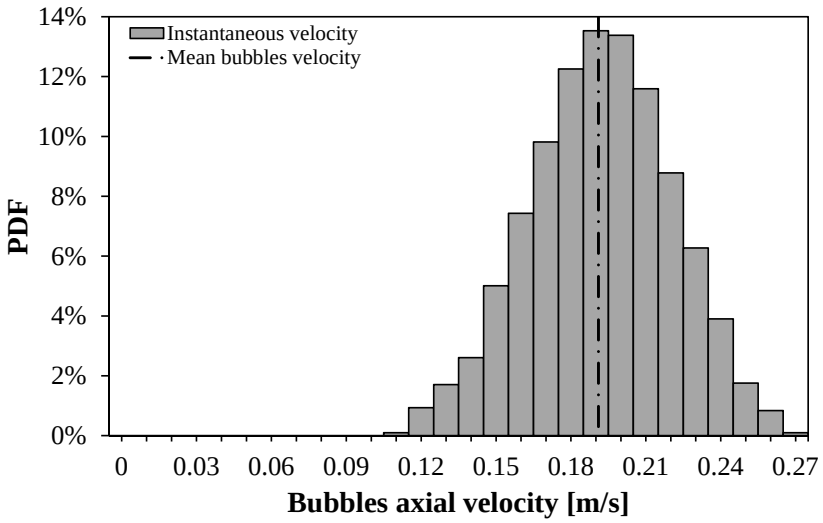

Figure 4.10 – Vertical velocity components (u_y) distribution in the empty bubble column in n-heptane. $Q_G = 1$ l/h, $d_n = 1$ mm.

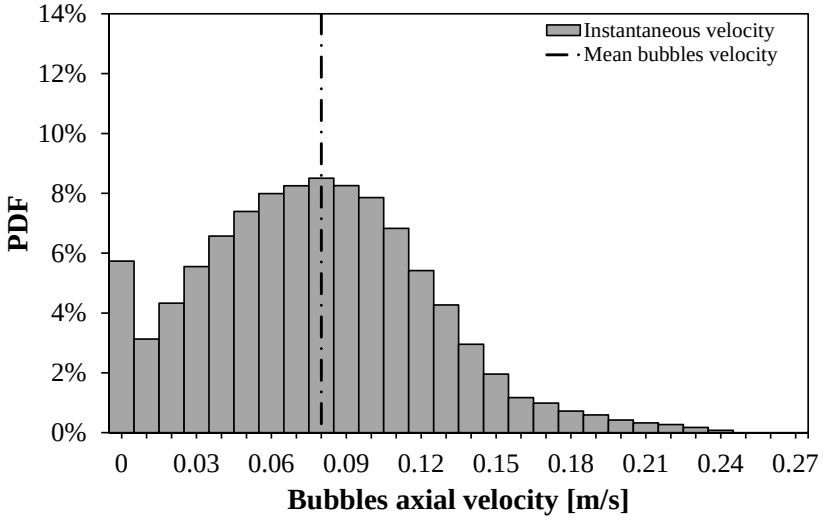

Figure 4.11 – Vertical velocity components (u_y) distribution in the 10 SMX elements in n-heptane. $Q_G = 1$ l/h, $d_n = 1$ mm.

As an example, the histograms showing the Probability Density Function (PDF) of the vertical velocity component u_y and its mean value resulting from the empty column and the 10 SMX elements in n-heptane are reported respectively on figure 4.10 and figure 4.11. For the column without SMX, the PDF follows a normal distribution. The wide distribution may be due to the oscillation of both bubble shapes and trajectories. In fact, the zigzag and spiral rising causes shape deformation and velocity instability. In fact, it is widely documented that

the continuous changes of the bubble shape significantly affect the rising velocity (Saffman 1956 [130] ; Mougin and Magnaudet 2001 [131] ; Tripathi et al. 2015 [132]).

The bubbles' velocities evolved considerably when the SMX was employed. As outlined in figure 4.11, the histogram of the Probability Density Function (PDF) of vertical velocity components is significantly altered, with velocities inside the mixer scattered over the range 0 - 0.24 m/s. The mean axial velocity detected inside the SMX is about 0.08 m/s. A similar value was found for the horizontal component of the velocity in all of the elements facing the camera. The mean velocity in the first element (0.12 m/s) is relatively higher than the others. Furthermore, no relevant changes of bubbles' mean velocity were observed inside the mixer after the third element.

A considerable amount of bubbles displays negligible velocity ($u_y < 0.01\,\mathrm{m/s}$. These null values were mainly detected in the vicinity of the SMX crossbars. There are several possible explanations for this behaviour. Firstly, the gap between the bars might be smaller than the bubble diameter, acting therefore as an obstacle. Furthermore, the space available decreases in some specific regions such as those at the junctions between two consecutive elements. The energy required for the bubbles' deformation significantly affects their velocities.

A comparison between the measured velocity of the bubbles and those estimated by an empirical correlation was done. Various correlations for bubble rising velocity under different operating conditions are available in the literature (Harmathy 1960 [133] ; Mendelson 1967 [134] ; Wallis 1974 [135] ; Tomiyama et al. 1998 [136] ; Raymond and Rosant 2000 [137] ; Tomiyama 2002 [138, 139]). Tomiyama (2002) [138] proposed a correlation that allows the calculation of the terminal velocity for a distorted oblate spheroidal bubble :

$$U_T = \frac{\sin^{-1}\sqrt{1-E^2} - E\sqrt{1-E^2}}{1-E^2}\sqrt{\frac{(\rho_L-\rho_G)\,g\,d_b}{2\,\rho_L}\frac{E^{2/3}}{1-E^{\,2}} + \frac{8\,\sigma}{\rho_L\,d_b}\,E^{4/3}} \tag{4.1}$$

In this correlation, only valid for oblate spheroids, the terminal velocity U_T depends on the bubble diameter d_b, the fluid properties and the aspect ratio E less than 1. The aspect ratio is defined as the ratio of the polar to equatorial lengths. The bubbles' aspect ratio was estimated in order to evaluate the terminal velocity for our experiments. The post-processing of the shadowgraph acquisitions revealed that the value of mean vertical velocity U_T in the empty column is about 0.19 m/s for the 1 mm nozzle. This value is close to 0.195 m/s when estimated by the above empirical correlation. Switching from the 1 mm to the 0.25 mm nozzle, the bubbles mean axial velocity U_T decreased to 0.173 m/s, relatively close to 0.176 m/s from the correlation of Tomiyama (2002) [138].

As aforementioned, the rising (axial) velocity u_y of bubbles allowed the estimation of their mean residence time. The minimum distance travelled by a bubble was measured by assuming its passage on the shortest path possible, namely moving with a straight path along the axial direction. The bubbles' velocities and their rising path length allowed us to determine the mean residence time under various operating conditions. The findings suggest that the mixer enhances at least twice the mean residence time. For example, the length of the 10 SMX elements L_{SMX} is 0.158 m. If we consider the average axial velocity u_y of the bubbles inside the mixer, i.e. 0.08 m/s, the average residence time is $\tau = L_{SMX}/u_y$, which is about 2 s. On the other hand, for the same section in the bubble column but without SMX (0.158 m), the residence time is about 0.85 s since $u_y = 0.19\,\mathrm{m/s}$.

4.3 Preferential paths

Preferential paths were assessed for heptane only. A statistical analysis of the probability to find bubbles throughout the column was performed by processing the instantaneous images. The results obtained in the column without SMX revealed that the probability of finding a bubble in the central zone of the column is higher than near the walls. These results are consistent with those of other authors (Saffman 1956 [130] ; Clift et al. 1978 [140] ; Lunde and Perkins 1998 [141]). We performed an identical analysis for the 5, 10 and 15 SMX elements. Figure 4.12 and figure 4.13 depict the preferential paths observed in the bubble column.

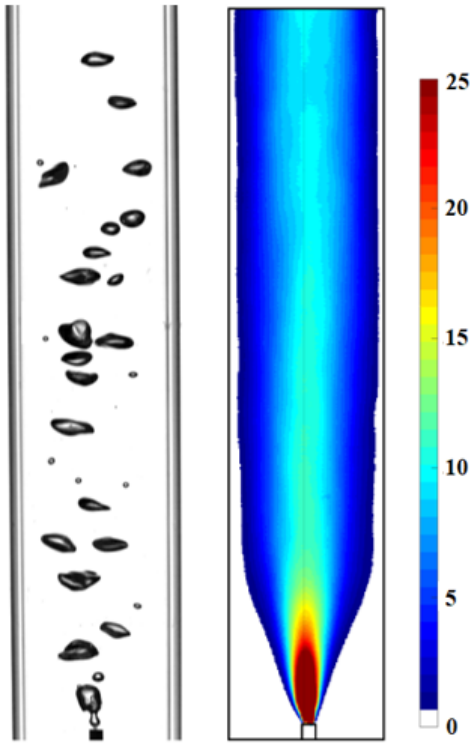

Figure 4.12 – Shadowgraph acquisition example and bubble occurrence probability detected in the bubble column fed by $d_n = 0.25\,\text{mm}$.

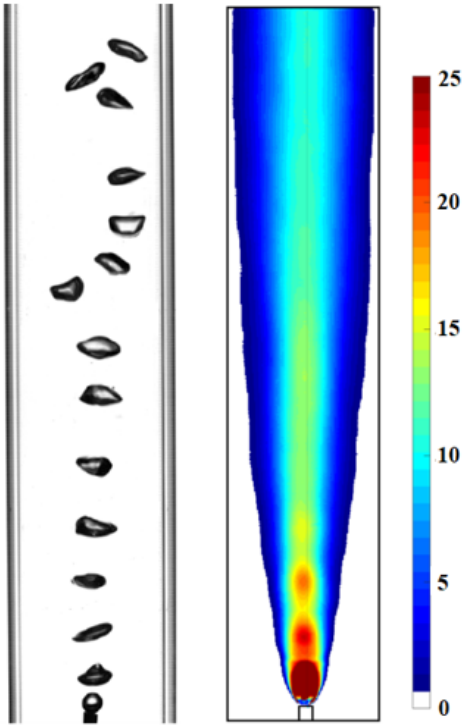

Figure 4.13 – Shadowgraph acquisition example and bubble occurrence probability detected in the bubble column fed by $d_n = 1\,\text{mm}$.

Figure 4.14 show the bubble occurrence probability in static mixers of different lengths. A particular behaviour of the system was observed : the bubbles come out of the mixer by following the orientation of the bars. For instance, at the output of the 1-element SMX, the probability of finding a bubble is higher on the sides of the column. This behaviour was indeed observed in all mixers with an odd number of elements. Compared to the bubble column, the mean probability of finding bubbles inside the mixing device is higher.

Since the 15 SMX elements led to similar data, figures 4.15 and 4.16 show only the results obtained with 10 elements. Here again, the instantaneous and mean probabilities of finding bubbles inside the mixer were increased. The static mixer decreased the bubbles velocities and therefore increased their residence time (see section 4.2). Another observation

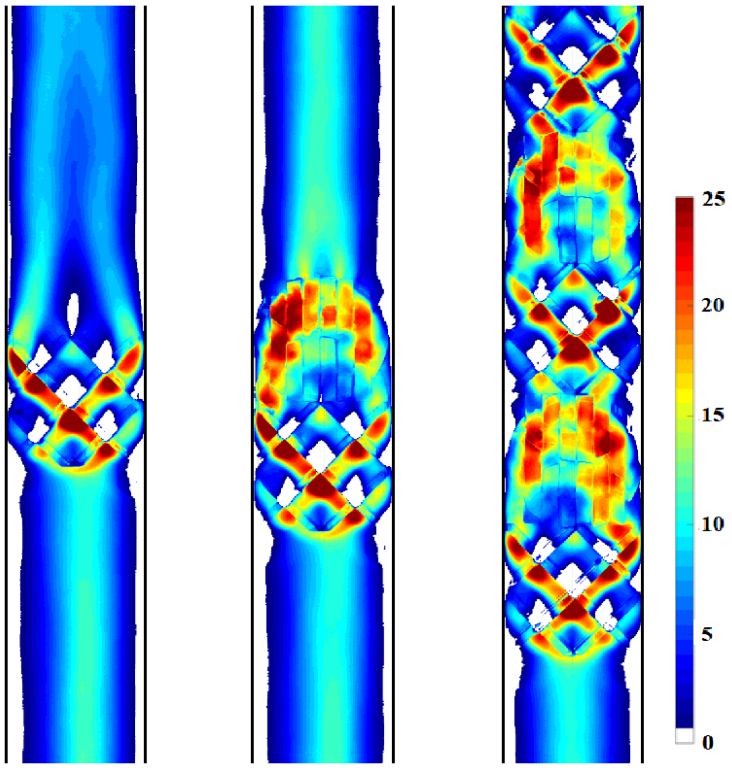

Figure 4.14 – Bubble occurrence probability detected in the several SMX mixers. From left to right : 1 element, 2 elements and 5 elements. Operating conditions : $d_n = 1\,\text{mm}$ and $Q_G = 2.5\,\text{l/h}$.

emerged from the images of figures 4.12, 4.13, 4.14, 4.15 and 4.16 : bubbles rise in the SMX by following preferential paths. These preferential paths are located close to the mixer's inclined bars. Furthermore, zones with a null probability (lower than 0.5%) of finding bubbles can be distinguished. These regions appear in white on the images. Down-flows were confirmed in these zones by the PIV technique.

4.4 Gas hold-up

Gas hold-up experiments were conducted using both the plastic SMX mixers and the empty bubble column. Increments of the liquid level were measured once nitrogen bubbles were generated in the system. The volume of gas V_G and liquid V_L were then estimated. More details on the technique used can be found in section 3.3.

4.4.1 Nitrogen hold-up in aqueous system

The following parameters were varied in the gas hold-up experiments in water :

- 6 SMX configurations : 0 (i.e. empty bubble column), 1, 2, 5, 10 and 15 SMX elements ;
- 3 SDS concentrations : 0%, 0.1%, and 3% (More details about the fluids properties are reported in table 3.1) ;
- 4 gas flow rates : 2.5 l/h, 5 l/h, 7.5 l/h and 10 l/h ;

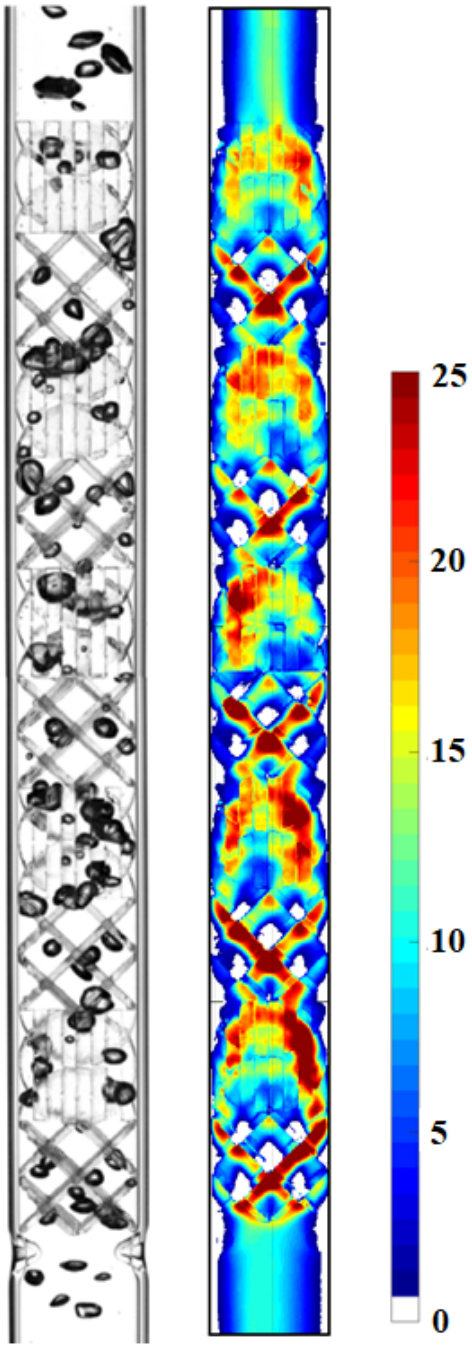

Figure 4.15 – Shadowgraph acquisition example and bubble occurrence probability detected in the 10 SMX elements fed by $d_n = 0.25\,\text{mm}$.

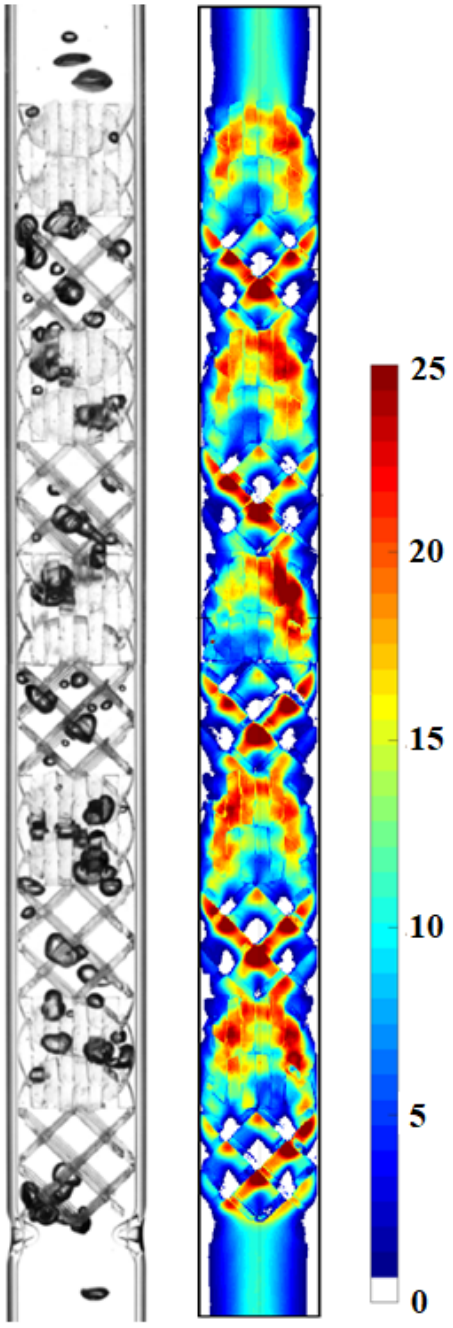

Figure 4.16 – Shadowgraph acquisitions and respective bubble occurrence probability detected in the 10 SMX elements fed by $d_n = 1\,\text{mm}$.

- 2 nozzle diameters : 0.2 mm and 1 mm.

Some of the results are presented in figures 4.17 and 4.18. Error bars are reported in both figures. These plots show that there is an important quantity of gas retained in the solution. The effect of each parameter will be discussed below. It must be noted that the behaviour of aqueous systems led to challenging conditions. The bubble coalescence phenomena caused the formation of large bubbles from the first elements of the mixer. Furthermore, the surface tension did not favour break-up of the bubbles. Therefore, a high percentage of bubbles stuck

on the SMX surface was observed. At last, when SDS was added, foam was present at the meniscus. All these features of the system made the collect of the gas hold-up values (ϵ_G) complicated.

Figure 4.17 and figure 4.18 show that the presence of the static mixer has a significant influence on the hold-up values. The hold-up ϵ_G in the SMX static mixer is about two times higher than that in a simple column. The trends found suggest that static mixers are more performing with pure water (see figure 4.18). However, a more detailed analysis highlights that the higher hold-up reached in pure water is mainly due to the amount of bubbles that remain stuck on the static mixer surface, or to be more precise, on the cross-bars of the mixer structure.

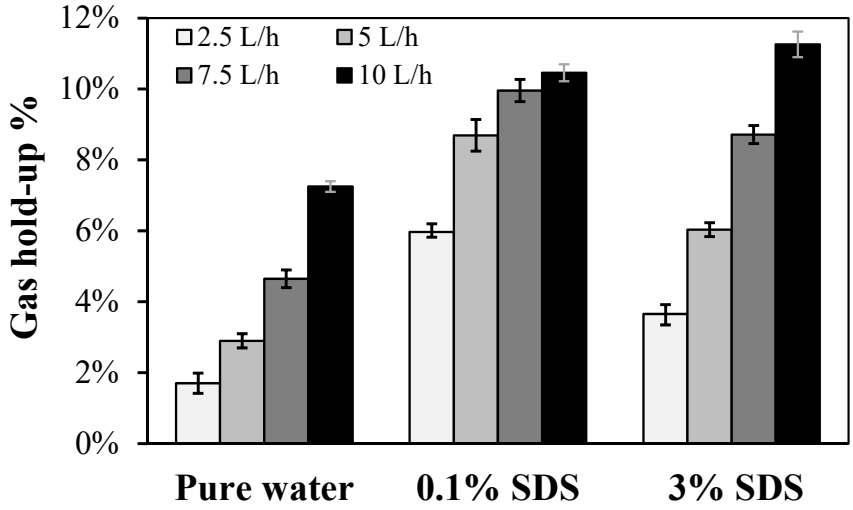

Figure 4.17 – Gas hold-up values for different concentrations of SDS measured in the bubble column (without SMX). $d_n = 0.2\,\text{mm}$.

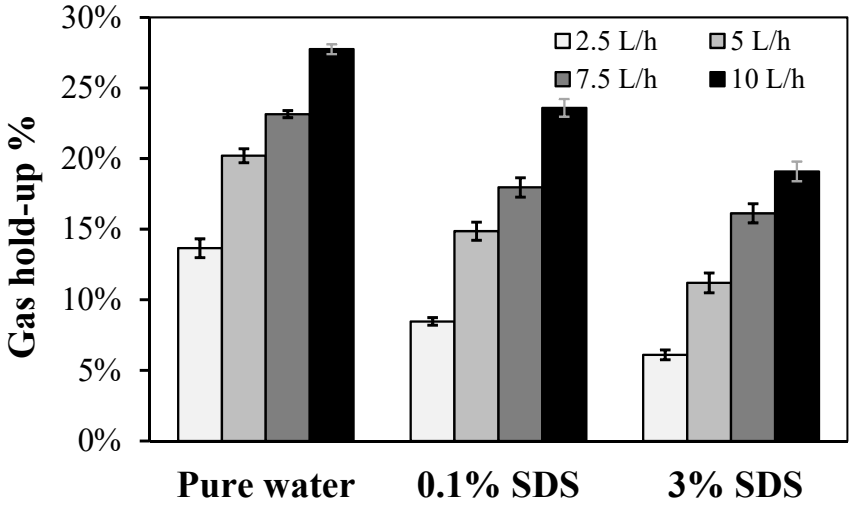

Figure 4.18 – Gas hold-up values for different concentrations of SDS observed in the column housing the 10 elements device. $d_n = 0.2\,\text{mm}$.

For all cases analysed, an increase in the gas flow rate positively affected the gas hold-up. The effect of the SDS, and therefore of the surface tension, was also analysed. The

data collected employing the SDS solutions was partially affected by foam formation. This problem affected all experiments where the surfactant agent was added. The foam entrained a certain amount of liquid (about 1% during each test). Furthermore, it made less sharp and delineated the liquid surface. The liquid level in the column was re-established before each test by stopping the gas flow and adding some SDS solution. The foam phenomenon is most intensive for the 3% SDS solution regardless the flow rate. For the 0.1% SDS solution, the foam formation can be almost neglected for a flow rate lower than 5 l/h. By increasing the flow rate over 7.5 l/h, an important quantity of foam was observed.

In the bubble column (see figure 4.17), the gas dispersion within pure water exhibits a lower hold-up than the one observed for the SDS solutions, regardless of the flow rate. In fact, a lower surface tension leads to the formation of smaller bubble diameters, which means a lower mean velocity and therefore higher residence time.

By adding the SDS, the amount of bubbles trapped on the surface of the mixer decreased. However, small bubbles are still blocked on the surface of the static mixer even when 0.1% SDS is added. The amount of bubbles that remain trapped becomes negligible with the solution containing 3% of SDS. The above observation explains the results found on figure 4.18 : pure water solutions reached higher hold-up values because of a larger amount of bubbles stuck on the surface of the SMX mixer.

4.4.2 Nitrogen hold-up in normal-heptane

The physical properties of the n-heptane, more precisely viscosity and surface tension, strongly affect the overall system behaviour and thus the gas hold-up ϵ_G compared to water.

For the gas hold-up experiments with n-heptane, the following parameters were varied :

- 6 SMX configurations : 0 (i.e. empty bubble column), 1, 2, 5, 10 and 15 SMX elements ;
- 3 gas flow rates : 1 l/h, 2.5 l/h and 5 l/h) ;
- 2 nozzle diameters : 0.25 mm and 1 mm.

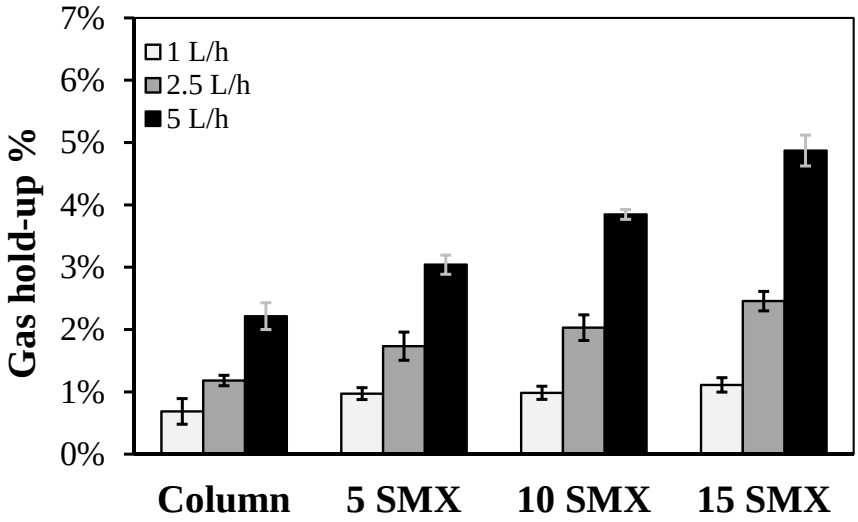

Figure 4.19 – Gas hold-up values in n-heptane for the 0.25 mm nozzle injector.

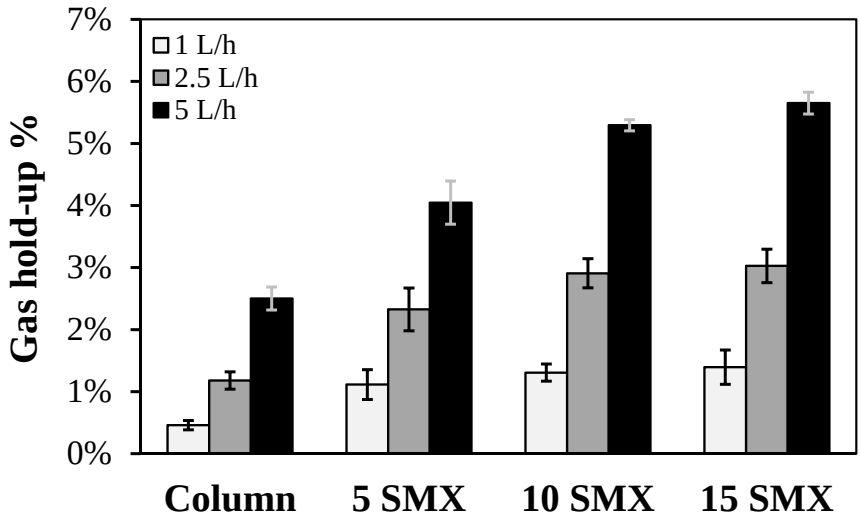

Figure 4.20 – Gas hold-up values in n-heptane for the 1 mm nozzle injector.

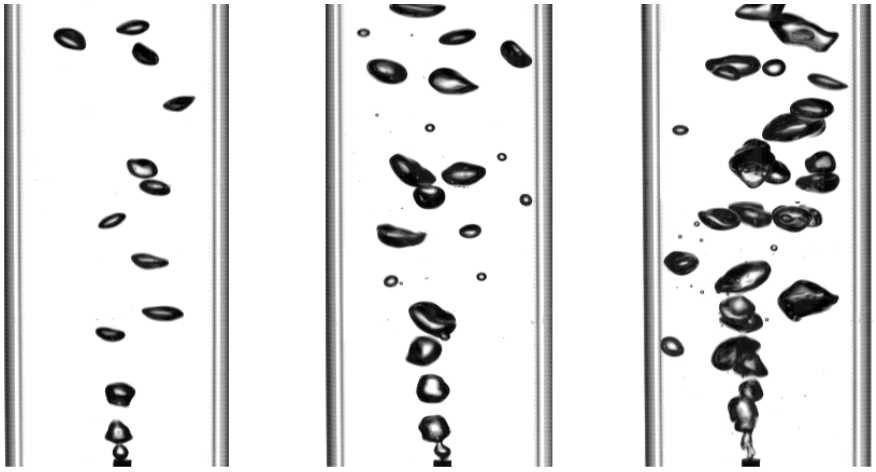

Figure 4.21 – Different formation regime of the bubbles for several nitrogen flow rates (respectively from left to right 1 l/h, 2.5 l/h and 5 l/h). $d_n = 0.25$ mm.

Figures 4.19 and 4.20 present the results obtained with n-heptane. Error bars show the standard deviations and depict the variability among the performed experiments. The hold-up increases with the gas flow rate in all cases, which is the first expected result. The comparison of the hold-up values with and without static mixer shows a substantial increase caused by the presence of the mixing device. It is interesting to note that in all of the eighteen cases with the SMX, the hold-up is increased with respect to the simple bubble column. Looking at all the SMX cases examined, it can be noticed that the gas hold-up increases with the number of elements.

The hold-up values resulting from the smallest nozzle with $d_n = 0.25\,\text{mm}$ and lowest gas flow-rate ($Q_G = 1\,\text{l/h}$) appear to be almost constant. A possible explanation for this particular behaviour might arise from bubbles' sizes in these conditions. The small bubbles generated can potentially rise into the mixer more swiftly, without interacting with each other, except in the very first elements of the device. Coalescence and breakup phenomena are restricted under these circumstances.

The values of hold-up detected for the 0.25 mm nozzle (see figure 4.19) suggest that this

smaller injector leads to smaller bubbles, then lower terminal velocities, higher residence time and then a higher hold-up of nitrogen. This was found to be true except for the higher gas flow rate ($Q_G = 5$ l/h). This uncommon behaviour is mainly due to a transition of the bubbles' formation regime towards a jet regime. This change in the formation regime is visible in figure 4.21.

The larger nozzle diameter appears to increase the gas hold-up significantly with respect to the smaller nozzle, for all gas flow rates as can be seen from figure 4.20. Besides, the effect of the nozzle size on the gas hold-up cannot be neglected even by employing 15 elements. Nevertheless, an equilibrium between coalescence and breakup phenomena cannot be excluded particularly in the last elements of the mixer. These observations are further discussed in section 4.1.

4.5 Liquid velocity fields

This section presents and analyses liquid velocities obtained by the PIV in water and the HFPIV in n-heptane.

4.5.1 Liquid velocities fields in aqueous system

In aqueous systems, the analysis of data obtained from the column without mixer led to expected results : a central up-flow was detected near the nitrogen bubbles rising through the stagnant liquid, while a down-flow was observed close to the column walls due to the mass balance. The seeding particles have a density close to the water. This implies that their sedimentation velocity is rather low, namely less than 80 µm/s.

The PIV technology performed well for all experiments run without the static mixer, with or without SDS. As an example, figure 4.22 illustrates some PIV instantaneous velocity fields. The first picture displays the portion of the column examined. It corresponds to a raw PIV image. On its bottom, the flat orifice gas injection can be seen. The image in the middle comes from the overlapping of the PIV vector field with the raw camera acquisition. On the right, a colour map visualization of the velocities field is illustrated.

Velocities around 0.20 m/s were detected around the bubbles in the column without mixer and in pure water. This value is in accordance with the estimation provided by the correlation reported by equation 4.1 in section 4.2. By adding SDS to the solution, the bubbles' sizes and velocities decrease progressively. By employing the 0.2 mm injector, the bubbles' diameter reduction was sufficiently important to promote an almost straight ascendant path along the axis of the column.

As aforementioned, the SDS surfactant proved to be essential to properly investigate the static mixers. However, the formation of foam and the persistence of some bubbles attached to the elements' surface led to difficulties in collecting data inside the mixer. The largest amount of foam was generated when employing 3% SDS. The highest quantity of bubbles trapped on the mixer surface was observed with 0.1% SDS. The presence of these static bubbles increased the amount of gas hold-up in the column (see also section 4.4.1). Another drawback of these static bubbles was the growth of shadow zones inside the mixer. The laser sheet had therefore difficulties to penetrate through the system. Also, a non-negligible

amount of seeding particles was dragged away by the foam.

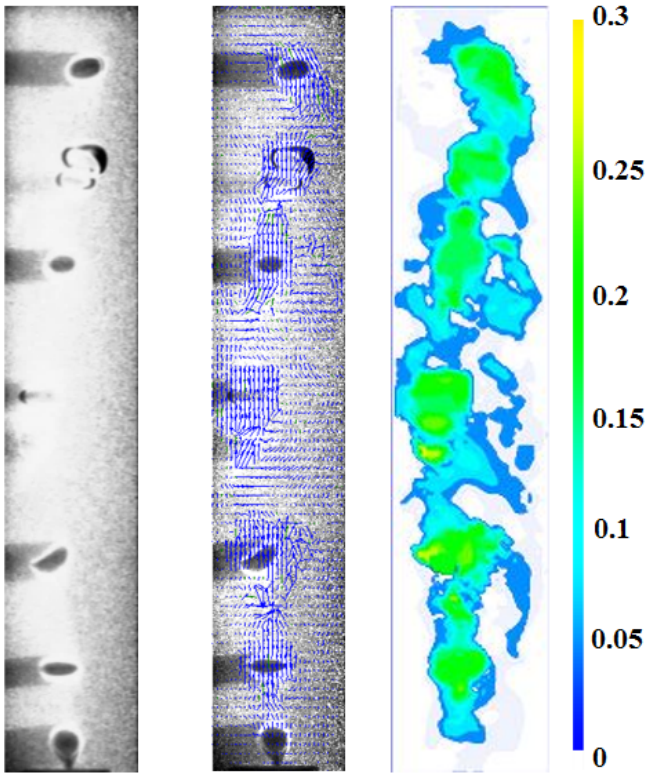

Figure 4.22 – Detailed view of the gas inlet in the bubble column. From left to right : raw PIV instantaneous acquisition, overlap with the vectors field and velocity magnitude scalar map. 0.1% SDS ($\sigma = 50.3\,\mathrm{mN/m}$), $Q_G = 2.5\,\mathrm{l/h}$, $d_n = 1\,\mathrm{mm}$.

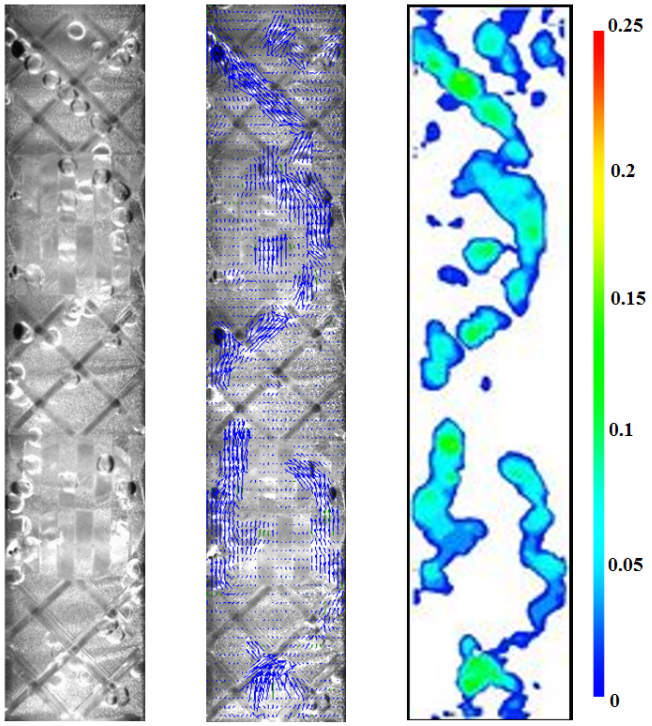

Figure 4.23 – First 5 of the 10 SMX elements. From left to right : raw PIV instantaneous acquisition, overlap with the vectors field and velocity magnitude scalar map. 3% SDS ($\sigma = 32\,\mathrm{mN/m}$), $Q_G = 2.5\,\mathrm{l/h}$, $d_n = 0.2\,\mathrm{mm}$.

In pure water, large coalescence of bubbles and high hold-up complicated the PIV experiments. The PIV images revealed that the bubbles tended to merge immediately before the mixer and then rose as one large bubble. These large bubbles created large shadows when traversed by the laser sheet.

The best configuration for the PIV was undoubtedly achieved using 0.2 mm flat nozzle and 3% SDS solution. The surface tension is then reduced, which has the effect of creating smaller bubbles. Sample results in this configuration are shown in figure 4.23. The images on figure 4.23 reveal a typical flow field observed in the SMX static mixer for 3% of SDS. The small bubbles move as a chain, each bubble follows the wake created by the previous ones. This implies the formation of preferential paths in the SMX static mixer whose existence was confirmed by both PIV and shadowgraph. Far from a bubble, a weak down-flow was noted.

4.5.2 Liquid velocities fields in n-heptane

The HFPIV technique was employed to examine the velocity fields in normal-heptane. As for water, the two configurations of empty column and column with SMX were investigated. As reported in section 3.4, 7 500 frames were acquired to enhance the accuracy of the results. The introduction of a lower gas flow rate than those used in the aqueous solutions, here 1 l/h, permitted a better isolation of the bubbles, with less shadowed areas. Flow patterns became too complicated to interpret for larger gas flow rates due to the presence of numerous bubbles.

The DaVis-LaVision® software was used for pre-processing the raw PIV images. It permitted a sophisticated treatment capable to remove the bubbles interference and to enhance the light emitted by the particles, namely by filtering and normalizing the pixels intensity. This approach allowed us to partially solve the problem related to laser light scattering on the bubbles' interfaces.

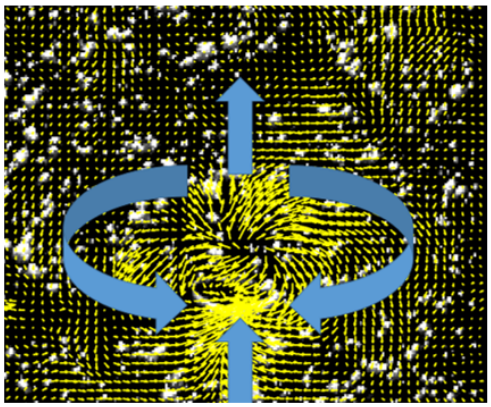

Figure 4.24 – Detailed view of the velocity field detected in normal-heptane around a bubble. Results obtained with $d_n = 1\,\text{mm}$ and $Q_G = 1\,\text{l/h}$.

Figure 4.24 shows an example of the flow around a bubble that rises exactly in the plane of the laser. The velocity field collected was well delineated : an up-flow was detected upstream and downstream the bubble rising, while a down-flow was measured in the side regions. Figure 4.25 illustrates an instantaneous velocity field and its time average obtained by the PIV performed in the column without the SMX. The gas injecting system was located below the bottom of this image. The bubbles and the liquid velocity flow field are shown

overlapped in the l.h.s. of figure 4.25. Bubbles that are not crossed by the laser plane do not perturb the PIV measurement. In the case of figure 4.25, the two bubbles at the bottom were located behind the laser plane. On the r.h.s. of figure 4.25, the average velocity field of the same region is illustrated. As with water, data obtained from the empty column led to the expected results of a mean up-flow in the axial region due to bubbles rising, and of a mean down-flow near the column wall.

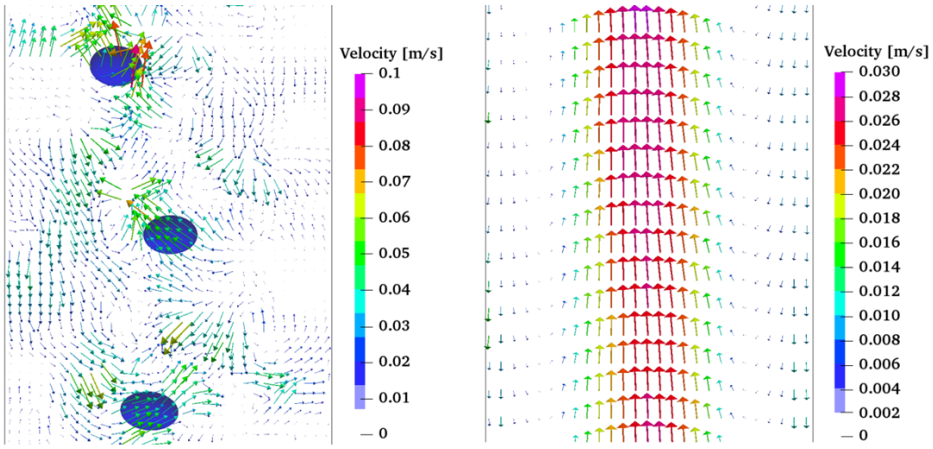

Figure 4.25 – PIV results in the empty column : instantaneous vector field coloured by velocity magnitude (l.h.s.) and averaged vector field in the same column section (r.h.s.). Results obtained with $d_n = 1\,\text{mm}$ and $Q_G = 1\,\text{l/h}$.

The PIV results are completely different when the SMX mixers are used. For example, figure 4.26 illustrates an instantaneous velocity field measured inside the first SMX element. The liquid motion due to a bubble passage can be identified by looking scrupulously at the picture on the right of figure 4.26, where the bubbles' shapes are reported as well. For instance, an up-flow was observed in proximity of the three rightmost bubbles. Some velocity fields, however, may not match the expected mid cutting plane pattern through a bubble as in the case of the leftmost bubbles. This is due to the fact that the cutting plane of figure 4.26 is shifted along the third direction with respect to the bubbles' mid centreline plane.

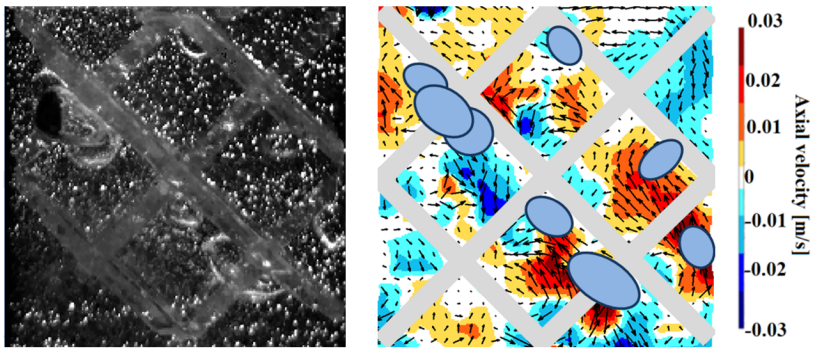

Figure 4.26 – Raw PIV image and instantaneous flow field in the first SMX element (coloured by axial component of velocity). $d_n = 0.25\,\text{mm}$, $Q_G = 1\,\text{l/h}$.

The main liquid flows were located in the zone of bubbles' passage. Entrainment up-flows were observed in the bubbles' proximity, in front of a bubble and in its wake, when looking in a median cutting plane of the bubble. Down-flows were encountered in the lateral sides of the bubbles' paths. Inside the mixer, a reduction of the velocities was observed,

due to lower bubbles velocities inside the mixer. The bubbles velocities are approximately 2 to 3 times smaller inside the mixer compared to the empty column. Moreover, PIV results suggest that the bubbles rise in the wake left by the previous ones. This behaviour implies some preferential paths in the SMX static mixer.

The high acquisition frequency allowed to detect rapid phenomena like bubble deformation and break-up. On the other hand, the findings in this study are subject to some limitations. Firstly, the PIV technique is only 2D planar. Furthermore, it was not possible to collect data in the regions close to the SMX elements' bars and in the regions characterized by high values of gas hold-up. In fact, the quality of PIV results decreased with the amount of bubbles. The presence of bubbles created black zones and shadows. Besides, the gas-liquid interfaces reflected the laser, making the tracking of seeding particles difficult. In these areas, it was often not possible to measure the flow field. This is a well-known problem of the PIV measurements in multiphase flows (Funfschilling and Li 2001 [117]).

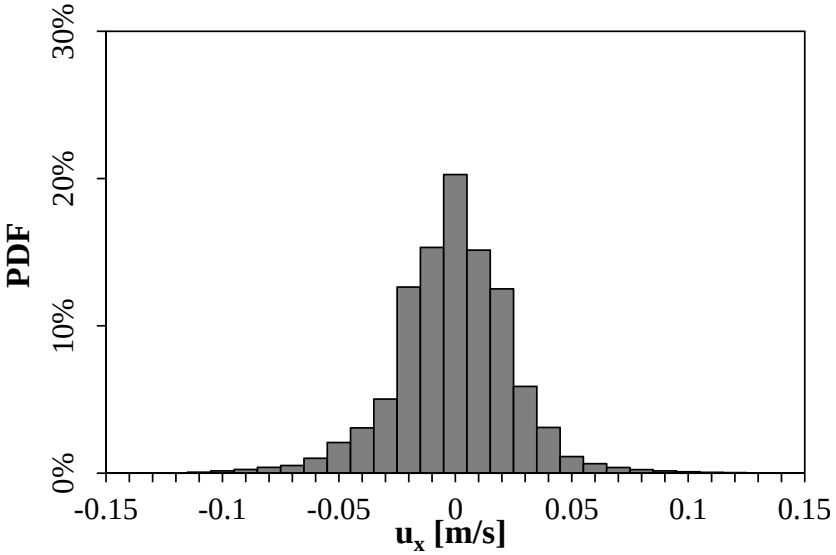

Figure 4.27 – Liquid u_x velocities distributions detected by PIV in the column without SMX. $d_n = 0.25\,\text{mm}$, $Q_G = 2.5\,\text{l/h}$.

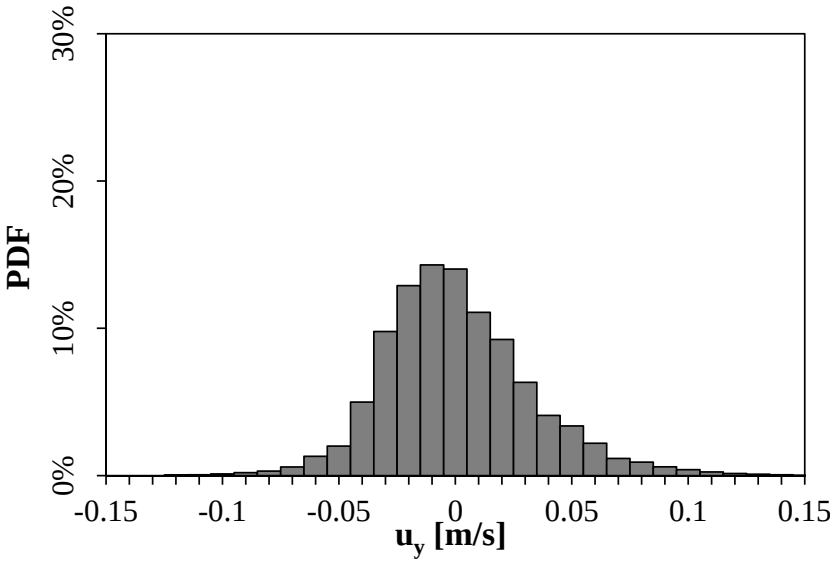

Figure 4.28 – Liquid u_y velocities distributions detected by PIV in the column without SMX. $d_n = 0.25\,\text{mm}$, $Q_G = 2.5\,\text{l/h}$.

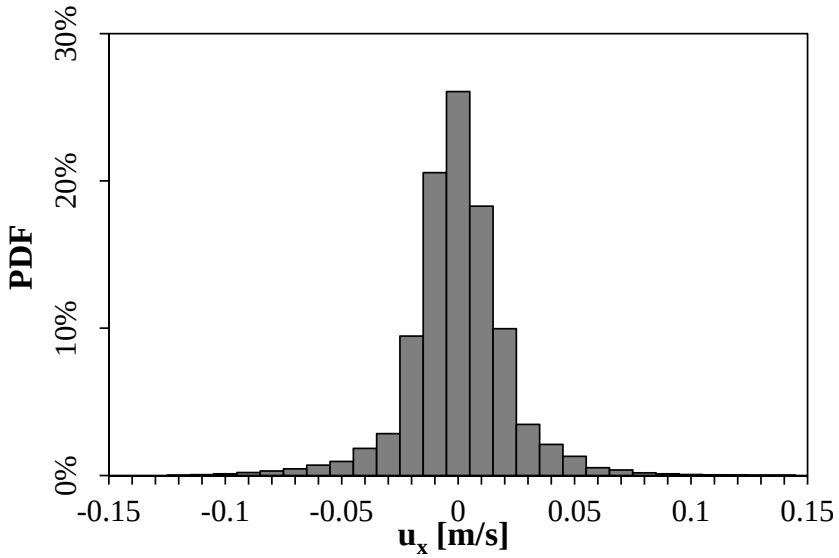

Figure 4.29 – Liquid u_x velocities distributions detected by PIV in the column with 10 SMX elements. $d_n = 0.25\,\text{mm}$, $Q_G = 2.5\,\text{l/h}$.

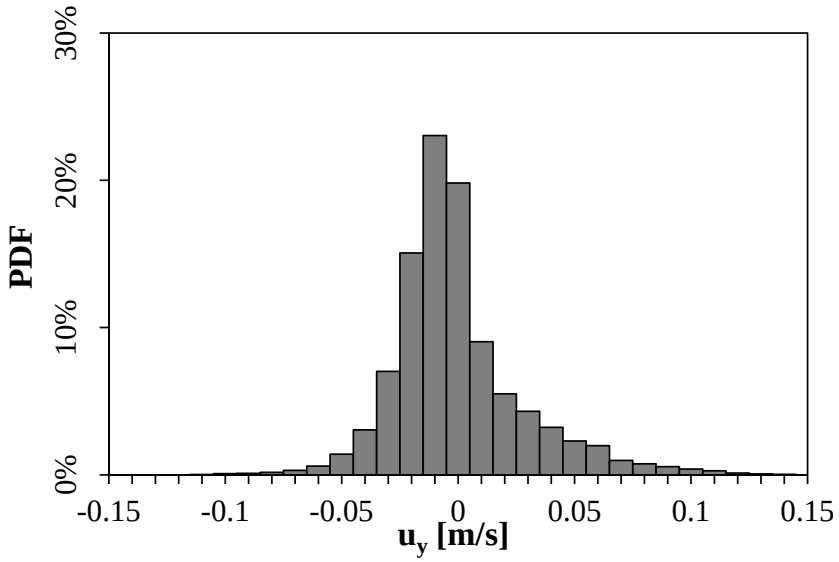

Figure 4.30 – Liquid u_y velocities distributions detected by PIV in the column with 10 SMX elements. $d_n = 0.25\,\text{mm}$, $Q_G = 2.5\,\text{l/h}$.

The results from the empty column and the SMX mixer were further compared in order to reveal the effect of the mixing device. The horizontal u_x and vertical u_y liquid velocities probability distributions found for $Q_G = 2.5\,\text{l/h}$ in the bubble column are reported in figures 4.27 and 4.28. Note that the particles sedimentation velocity was subtracted from the vertical component u_y. As expected, velocities in the empty bubble column were found to be inherently related to the bubble rising velocities (see equation 4.1 in section 4.2), with maxima of approximately 0.20 m/s. Velocities higher than 0.15 m/s and lower than -0.15 m/s were neglected in the histograms of figures 4.27 and 4.28, as they represent less than 0.1 % (resp. 0.05 %) for the empty column (resp. for SMX).

The histogram of u_x is rather symmetric and dominated by low values (see figure 4.27). The histogram of vertical velocity u_y (see figure 4.28) is non-symmetric. Larger values are obtained in the positive range ($u_y > 0$) than in the negative range. This corresponds to the axial entrainment up-flow due to the rising bubbles, with higher values. In the negative

range, the u_y histogram is more dominated by low values originating from down-flow near the column cylindrical walls. Due to mass conservation over cross axis sections, the down-flow absolute values are obviously smaller than axial up-flow values.

The vertical liquid velocities decreased significantly in favour of horizontal velocities in the 10 element SMX mixer, as shown in figures 4.29 and 4.30. The maximum magnitude of the liquid velocities detected inside the static mixer were between $\pm 0.10\,\mathrm{m/s}$ ($Q_G = 1\,\mathrm{l/h}$, not plotted here) and $\pm 0.15\,\mathrm{m/s}$ ($Q_G = 2.5\,\mathrm{l/h}$). The percentages of high velocities were much lower when the mixer was used. For the same reasons as in the column without SMX, the histogram of u_x is rather symmetric while the histogram of u_y is non-symmetric.

When comparing figures 4.27 and 4.28 with figures 4.29 and 4.30, it was noted that the axial component was more affected by the presence of the mixer. The standard deviation changed by 18.3 % for the horizontal components of the velocity histogram and by 26.5 % for the vertical. All distributions present a maximum around zero velocity due to the stagnant liquid operating conditions, but the SMX distributions are more dominated by small velocities. It can thus be stated that the presence of the SMX decreases both components of the velocity however in an unequal measure. This can be explained partly by the particular geometry of the SMX but also by the slower velocities observed inside the mixers. The 45° bars divert the bubbles' paths, thus causing changes in the velocities of the liquid phase.

The volumetric flow rate Q_V computed as equation 4.2 below was verified to be null in several cross sections of the column.

$$Q_V = \iint_S (\mathbf{u}\ \mathbf{n})\, dS \tag{4.2}$$

4.6 Mass transfer

The oxygen transfer performance in the SMX static mixer with air/water mixture was assessed by measuring the oxygen concentration. Since the actual interfacial area (a) for mass transfer in the SMX is not perfectly known, the product of the mass transfer coefficient to the interfacial area ($k_L a$) was determined. A typical result of such analysis for the bubble column and the static mixer is shown in figure 4.31. The mass transfer is enhanced by the presence of the static mixer. The oxygen concentration values measured in the liquid phase are higher after the same elapsed time.

The mass transfer coefficient $k_L a$ is estimated using the two mass balance equations (cf. equations 3.18 and 3.19). Integrating the differential balances yields the following result :

$$-\ln\left(\frac{1-C}{C^*}\right) = k_L a\ t + k_0 \tag{4.3}$$

The $k_L a$ is usually obtained by expressing results on a semi-log graph using data between 20% and 80% of the maximum oxygen concentration. This methodology was presented by Niewon (2015) [12]. The graph of figure 4.32 shows a typical example of experimental points. Only a few points (1 out of 20) were reported in figure 4.32 to clarify the representation. The linear fitting is displayed in the same graph. The coefficient of determination R^2 is almost unity, which indicates an excellent degree of point alignment and optimal data interpolation.

The overall mass transfer coefficient k_La is nothing more than the slope of the line shown in figure 4.32.

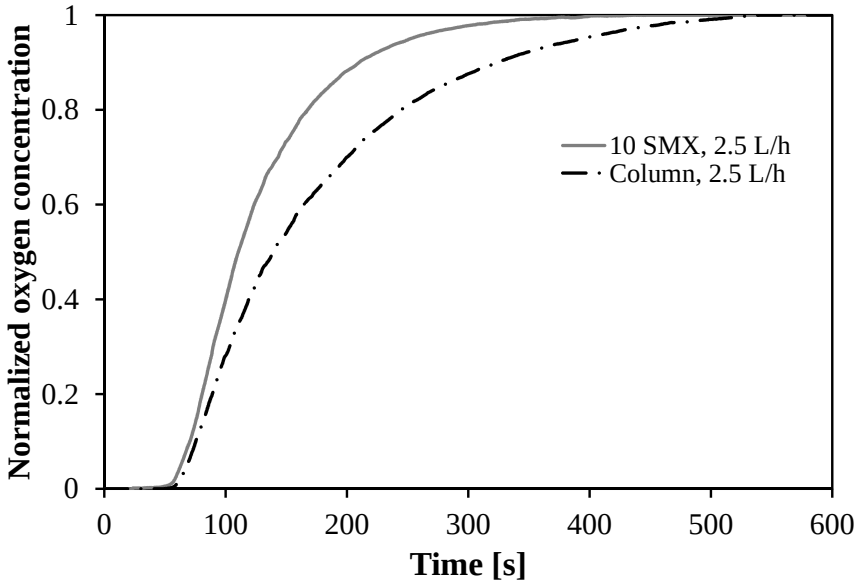

Figure 4.31 – Variation of the normalized oxygen concentration in time obtained from the bubble column with and without the static mixer. $d_n = 1\,\text{mm}$, $Q_G = 2.5\,\text{l/h}$.

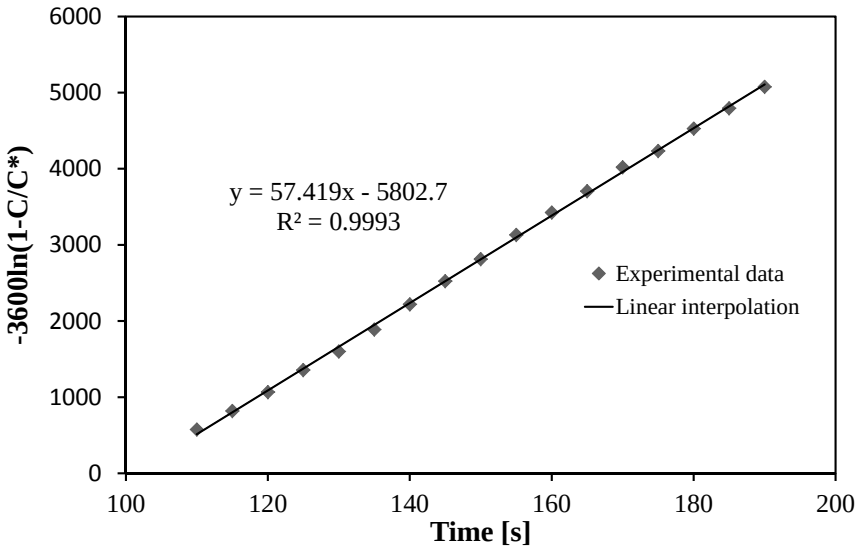

Figure 4.32 – Time evolution of $-3600\,\ln(\frac{1-C}{C^*})$ for the 10 SMX elements outlet. Raw points (1 out of 20) and fitting line (linear interpolation). $d_n = 1\,\text{mm}$, $Q_G = 2.5\,\text{l/h}$.

By increasing the gas flow rate Q_G, the mass transfer in the aqueous solution becomes more and more intense, due to enhanced bubbling. This behaviour is depicted by figure 4.33 where only the linear fittings are shown. Figure 4.33 shows the improvements made to the mass transfer by the static mixer. The comparison between the lines demonstrates a slope (and therefore k_La) that is twice bigger. It can therefore be deduced that the overall mass transfer in the mixer is about twice as in the bubble column. Table 4.2 summarises the main values of the volumetric mass transfer coefficient k_La obtained. By increasing the gas flow rate, the k_La is positively affected. The material nature of the mixer has also an effect on

k_La. The use of a metallic mixer improves the dispersion and thus also the mass transfer. This behaviour can be attributed to different wetting properties between the liquid and the mixer surface.

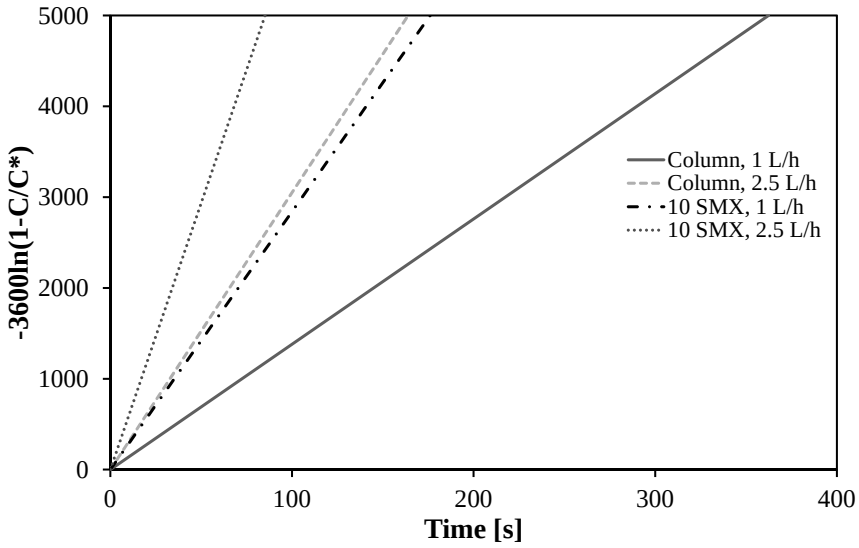

Figure 4.33 – Fitting lines of the time evolution of $-3600\ \ln(\frac{1-C}{C^*})$ for several operating conditions. $d_n = 1\,\text{mm}$.

Table 4.2 – Volumetric mass transfer coefficient (k_La) estimated in the several operating conditions. $d_n = 1$ mm.

Case	**Flow rate [l/h]**	k_La **[h^{-1}]**
Bubble column	1	13.8
Bubble column	2.5	30.5
Bubble column	5	53.2
10 elements SMX	1	28.4
10 elements SMX	2.5	58.7
10 elements SMX	5	100.5
10 elements SMX (met.)	1	45.7
10 elements SMX (met.)	2.5	67.3

4.7 Effect of liquid circulation

The effect of a liquid flow on the bubble shape, velocity, diameter and gas hold-up was evaluated. Different configurations were examined to extend the validity of the results. The tests were performed with a heptane flow in two directions, i.e. in co-current and counter-current with respect to the gas. The liquid velocities were set by selecting the Reynolds number. Li et al. (1997) [22] demonstrated that to maintain a laminar flow in the static mixer, the liquid Reynolds number should not exceed 15 [22]. Four different cases were thus investigated with Reynolds numbers equal to 1, 5, 10 and 15. Table 4.3 details the operating conditions of the performed tests.

Table 4.3 – Operating conditions of experiments with a liquid recirculation (in co-current and counter-current liquid flow).

Reynolds number	**1**	**5**	**10**	**15**
Liq. velocity in SMX [m/s]	0.0000375	0.000188	0.000375	0.000563
Liq. volumetric flow rate [m^3/s]	6.33 10^{-9}	3.17 10^{-8}	6.33 10^{-8}	9.5 10^{-8}
Liq. volumetric flow rate [l/h]	0.0228	0.114	0.228	0.342

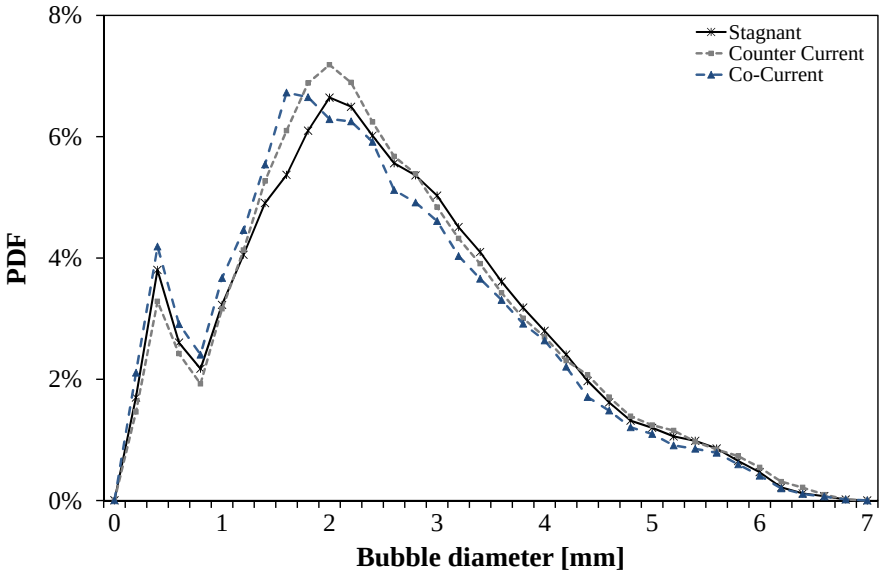

Figure 4.34 – Equivalent diameter distribution measured at the 5 elements outlet. Q_G = 2.5 l/h, $d_n = 0.2$ mm.

Experimental results demonstrated that there were no significant differences in bubble shape, velocity and diameter when the liquid was flowing in laminar regime (Re $<$ 15). As an example, the results of a test performed in the 5 SMX elements with a gas flow rate of 2.5 l/h and a liquid flow rate of $\pm$0.228 l/h (co-current and counter-current) are reported in figure 4.34. The effect of the liquid flow appears to be negligible on the bubbles size distributions in both configurations. The diameter distribution at the outlet of the 5 elements remained almost unchanged. The mean Sauter diameter varied by about 1.5%. The mean rising velocity differed by 2%. These differences are within the error range of the experiments.

The liquid velocities induced by a bubble passage, which are of the order of 0.15 m/s, are much higher than the velocities induced by the liquid flow, which are about 4×10^{-4} m/s as detailed in table 4.3.

As the effect of liquid circulation is negligible at low Reynolds, the present tests validate the approach of focusing this thesis only to stagnant liquid.

4.8 Chapter Summary

This chapter illustrated the main results obtained throughout the experimental investigations. An overview of the main problems in the different experiments performed was provided as well. The most meaningful results about bubbles' diameters, shapes, velocities and preferential paths, gas hold-up, liquid velocity fields and mass transfer were developed in the dedicated sections.

The investigation performed revealed that the SMX^{TM} substantially increased the gas hold-up and the residence time of bubbles for all operating conditions. Furthermore, coalescence and breakup phenomena were observed at high hold-up values. Preferential paths were observed inside the mixer. These could potentially affect the mass transfer efficiency throughout the device. The static mixer exhibited an efficient redistribution of bubble sizes.

The effect of a mean liquid flow on the bubble shape, velocity, diameter and gas hold-up was quantified. The tests performed with heptane revealed that the effect of the liquid flow appeared to be negligible if liquid Reynolds number is lower than 15.

Part II

CFD

Chapter 5

Numerical methods

This chapter details the mathematical, physical and numerical models used in the present investigation. OpenFOAM® was selected to carry out the simulations. The Computational Fluid Dynamics (CFD) toolbox OpenFOAM® offers many models for the resolution of multiphase problems. The main solvers we used are presented here.

5.1 Generalities on OpenFOAM

OpenFOAM® stands for "*Open-source Field Operation And Manipulation*". It is a free and open source C++ library for the development of customized numerical solvers, including pre-/post-processing utilities. It is mainly used for the solution of continuum mechanics problems (CFD) [142].

OpenFOAM® was originally called FOAM. It was a CFD software initially created at Imperial College in 1989 by Henry Weller, developed with Hrvoje Jasak as the other main

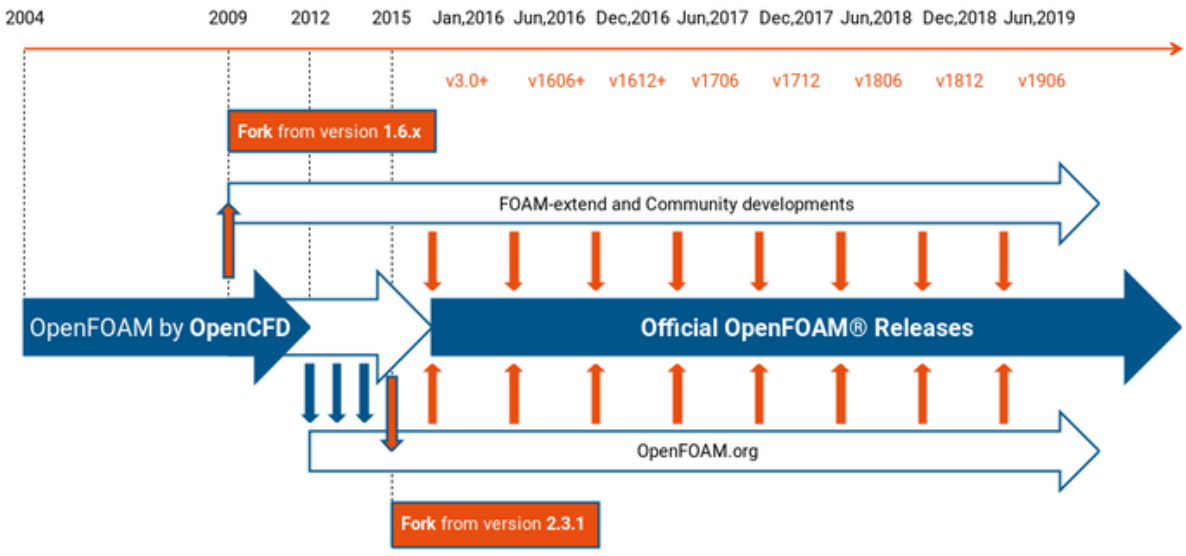

Figure 5.1 – OpenFOAM fork release history and the birth of the different versions available today. Take from Wikipedia [34]

developer. In the early 2000s, Weller and Jasak founded Nabla Ltd to commercialize the software. Then, Nabla Ltd ceased operation and released in 2004 FOAM as open source software under the name "*OpenFOAM*". In 2004, Weller funded OpenCFD, which developed primarily OpenFOAM releases. Jasak funded Wikki (see www.wikki.co.uk), which released and developed foam-extend, a fork of the OpenFOAM software. Figure 5.1 shows the history of the different forks of OpenFOAM. In 2011, OpenCFD was bought by SGI Corporation. The OpenFOAM Foundation was created at that time (openfoam.org). In 2012, SGI sold OpenCFD to ESI Group. In 2014, Henry Weller and Chris Greenshields left ESI Group and founded the company CFD Direct (cfd.direct). ESI Group created more recently a fork of the foundation version called OpenFOAM+ (openfoam.com), turned towards the industry. OpenCFD owns the OpenFOAM® trademark and grants use of the trademark to ESI Group and to the Foundation.

Nowadays, although there are several forks and versions of OpenFOAM, three main variants of the software can be identified. They are all released as free and open-source software under the GNU General Public License :

- The OpenFOAM Foundation version (openfoam.org). The OpenFOAM Foundation is the holder of the OpenFOAM® code and documentation copyright.

- The foam-extend version (foam-extend.org), released and maintained since 2009 by a large community and Wikki.

- The ESI-OpenCFD OpenFOAM+ version (openfoam.com). ESI-OpenCFD maintains and releases a new version every 6 months (in June and December).

In addition to the main versions listed above, there are other variants of OpenFOAM® maintained and released for specific applications. For instance, blueCFD®-Core, SIMSCALE®, CAELUS, and iconCFD® [34]. To date, a large portion of OpenFOAM® users are pushing for a single version containing and grouping all the functionalities of the different flavours available [142]. A Steering Committee was created to this target.

OpenFOAM® counts a wide user base across several areas of engineering and science, from both commercial and academic organisations. All above versions have a large range of features to solve problems involving complex fluid flows, chemical reactions, combustion, particulate flows, turbulence and heat transfer, solid mechanics and electromagnetic, and also finance.

For the present research, the version ESI-OpenCFD OpenFOAM+ was selected. This choice was dictated by the larger quantity of solvers and post-treatment tools present in the OpenFOAM+® release and missing in the others. In particular, the VoF solver `interIsoFoam`, which uses the method *isoAdvector* with *isoAlpha* (see section 5.5.1) is only available in OpenFOAM+ [11] since version v1706. The developments and contributions from users and community are constantly included in the release. Before each release, the version is tested by ESI-OpenCFD's development team, their development partners and selected customers. Besides, ESI-OpenCFD aims at creating the *"One OpenFOAM"* by integrating all the developments of the three main versions of the software.

5.2 Two-phase flow modelling

Multiphase flows are often encountered in a wide variety of configurations, in science, engineering or industry. In the chemical industry, various scales of gas-liquid, gas-solid, liquid-solid flows are encountered ranging from large bubble columns, packed-bed catalytic reactors, plate columns, agitated vessels, aerators, jets, micro-reactors or static mixers like in the present study. Several computational models were developed to investigate the hydrodynamic of the equipment listed above and of multiphase systems (Marchisio and Fox (2013) [143]). For instance : Eulerian-Eulerian [144–149], CFD-PBM [150–156], CFD-DEM (E-L) [157–162] and interface-capturing [35, 36, 163–166] .

In some cases, modelling biphasic gas-liquid systems requires an accurate reconstruction of the interface between phases. The literature on the subject is abundant as well as the number of methods. Figure 5.2 taken from Mirjalili et al. (2017) [35] shows a classification of the different interface capturing methods.

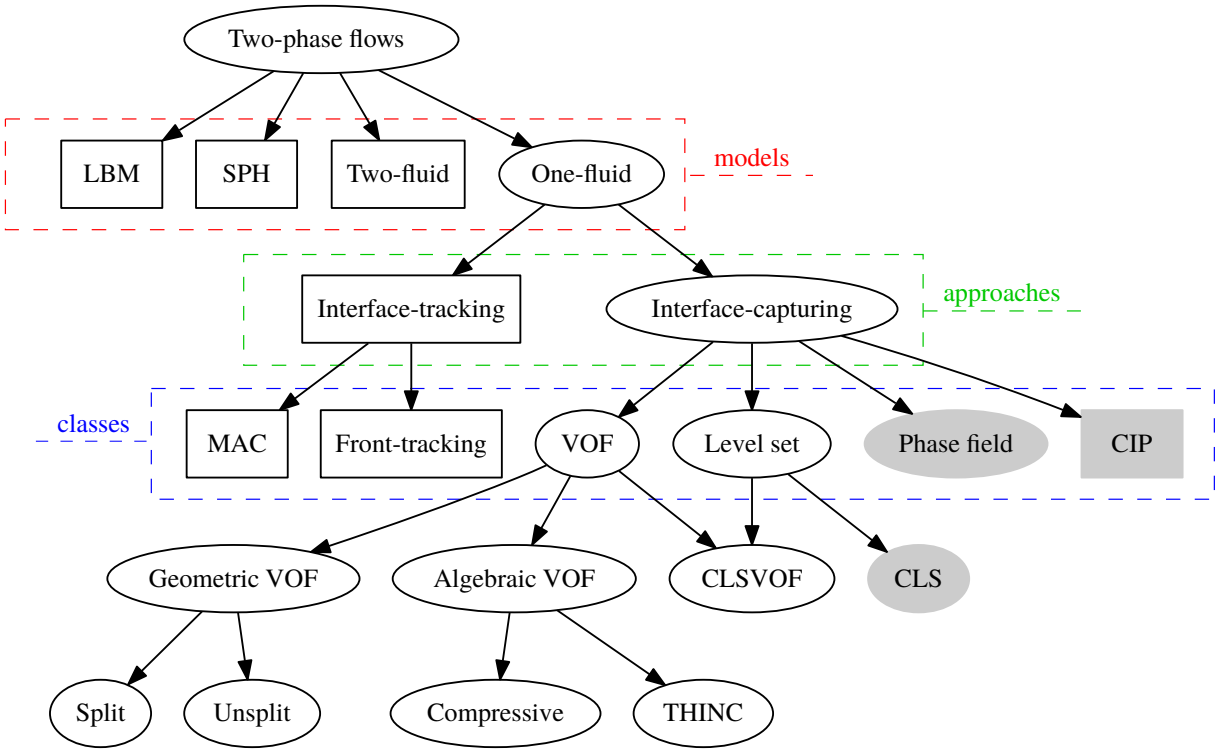

Figure 5.2 – Classification of methods for two-phase flows. Taken from Mirjalili et al. (2017) [35].

Thanks to the increase of computing resources, highly resolved simulations gain more and more interest to analyse in detail the physics of such multiphase flows. Many numerical methods emerged to simulate gas-liquid flows. Among these, implicit interface capturing approaches like level set (LS) [167] and volume of fluid (VoF) [163] proven to be efficient in simulating multiphase flows. Both level set (LS) and volume of fluid (VoF) methods belong to the so called one fluid interface-capturing methods [35, 168].

In the LS method, the interface is implicitly given by the zero level of a function Φ which is solution to the interface advection equation (Cottet and Maitre 2016 [166]). The main advantages of LS methods are their accurate computation of normal vector and curvature of the interface [166], and their simplicity in particular for extensions to adaptive mesh refinement (AMR). The LS method only relies on the discretization of an advection equation. Furthermore, this method is able to follow complex topology changes of the interfaces [166]. The LS method, introduced by Osher and Sethian (1988) [167], was then improved by Takahira et al. (2004) [169]. One of the common difficulties in level set approach is how to keep the interface thickness finite and to preserve the mass conservation. Although many improvements exist to fix the mass conservation problem, the error cannot be totally eliminated.

The VoF models a two-phase system through the resolution of momentum and volume fraction equations. VoF is often used for unsteady systems. It should be noted that the VoF can also be adopted for steady-state systems, but only if the solution does not depend on the initial conditions. The basic assumption of the model is that the two or more phases are not interpenetrating. This suggests that the VoF is not suitable for the modelling of miscible substances systems like a mix of gas phases. The VoF method presents some disadvantages, including the difficulty of capturing the geometric properties (interface normal and curvature). This is mainly due to the fact that the spatial derivatives are not continuous near the interface [170]. Inaccurate calculations of geometric properties lead to non-physical velocities in proximity of the interface, called spurious currents, which are due to an imbalance of surface tension force [170].

In recent decades, many authors presented an innovative approach to achieve mass conservation by coupling the LS with the VoF. This method, called coupled level set and volume of fluid (CLSVOF), was first introduced by Bourlioux (1995) [164] and further developed by Sussman and Puckett (2000) [171], Son and Hur (2002) [172], Nichita et al. (2010) [168] and Chakraborty et al. (2013) [170]. The CLSVOF method was developed to overcome the disadvantages of LS and VoF methods and to combine their advantages. In the CLSVOF, the LS function Φ is used to compute the surface tension contribution to the momentum equation (see equation 5.1) using the Brackbill method [173], while the VoF function is adopted to capture the interface and ensure mass conversation [168, 170].

In the present study, OpenFOAM® VoF solvers were used. As explained in section 5.1, the OpenFOAM® library and solvers benefit from a full access to the sources, an ease of implementation and modification of models, a large community and a null license cost. The important resources necessary to compute large VoF simulations like in this study would have been impossible with proprietary software.

5.3 VoF models and solvers

We consider here an unsteady, laminar, isothermal, Newtonian and incompressible two-phase flow. The flow is supposed without mass transfer across the gas-liquid interface. The governing equations of the VoF model are the continuity (equation 5.1) and momentum (equation 5.2) equations.

$$\frac{\partial \rho}{\partial t} + \nabla \cdot (\rho \mathbf{u}) = 0 \tag{5.1}$$

The momentum equations for mixture are written as :

$$\frac{\partial(\rho \mathbf{u})}{\partial t} + \nabla \cdot (\rho \mathbf{u}\mathbf{u}) = \nabla \cdot \tau - \nabla p + \rho \mathbf{g} + \mathbf{F}_\sigma \tag{5.2}$$

For incompressible flows, equation 5.1 is written as a divergence free condition :

$$\nabla \cdot \mathbf{u} = 0 \tag{5.3}$$

where p, ρ, μ are respectively the pressure, density and viscosity. Bold symbols are vectors. $\mathbf{u}$ denotes the velocity. $\mathbf{g}$ is the gravity. $\mathbf{F}_\sigma$ represents the surface tension force per unit of volume, which is expressed as a source term in the momentum equation. The product $\mathbf{uu}$ in equation 5.2 designs the outer product of $\mathbf{u}$, which is the tensor $\mathbf{u}\mathbf{u}^T$. For incompressible flows, the deviatoric stress tensor τ is expressed as :

$$\tau = \mu \left(\nabla \mathbf{u} + (\nabla \mathbf{u})^T\right) \tag{5.4}$$

A single 5.2 equation is solved for the two phases. In other words, the velocity field and the pressure field are shared among the phases. As OpenFOAM® is based on a finite volume algorithm, fields represent volume-averaged values, where the elementary volume is the volume of a grid cell.

In the VoF method, the continuity equation is converted into an advection equation for the volume fraction field α, representing for each cell the fraction of its volume which is occupied by one of the two fluids. Quantities can then be defined as volume fraction weighted sums. If α denotes the first phase volume fraction, ρ_1 the first phase density, ρ_2 the second phase density, then the density is defined as :

$$\rho = \alpha \rho_1 + (1 - \alpha)\rho_2 \tag{5.5}$$

Other quantities like viscosity or velocity can be defined similarly. A correct resolution of the two-phase system relies on a proper resolution and definition of the volume fraction field.

Hirt et al. (1981) [174] first introduced the Volume of Fluid (VoF) method and the volume fraction field α. Equation 5.6 can be seen as the conservation of the mixture components along the path of a fluid parcel :

$$\frac{\partial \alpha}{\partial t} + \mathbf{u} \cdot \nabla \alpha = 0 \tag{5.6}$$

We consider a system of two phases. For each cell of the domain, the volume fraction of a generic component p (α_p) can take three different values :

- The cell is completely full of component p :

$$\alpha_p = 1 \tag{5.7}$$

- The cell is full of the other component :

$$\alpha_p = 0 \tag{5.8}$$

- Both components are present in the cell. The cell belongs to the interface :

$$0 < \alpha_p < 1 \tag{5.9}$$

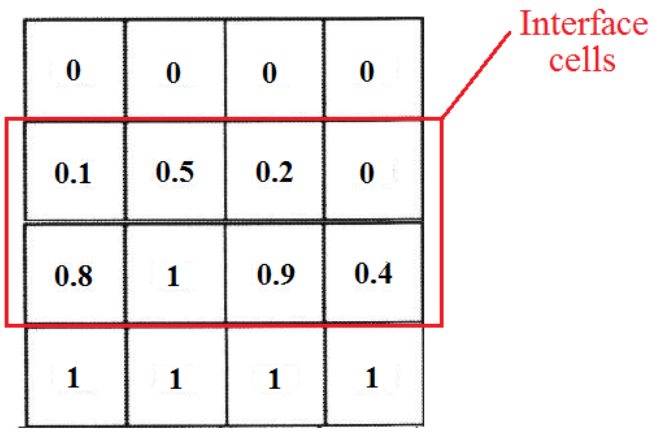

Figure 5.3 – Tracking of the interface in the VoF model.

Figure 5.3 contains an illustration of the above description. It is obvious from figure 5.3 that a finer discretization generates a more accurate reconstruction of the interface. Furthermore, it is not possible to model a dispersed phase which has a smaller volume than a cell volume. These observations will be further discussed in the first section of chapter 7, where the influence of the mesh and the choice of the spatial discretization step are addressed.

The non-linear advection reported in equation 5.6 represents a challenge in terms of spatial and temporal discretization. Furthermore, special care must be taken in the numerics to prevent smearing of the α-field and at the same time keeping it bounded ($0 \leq \alpha \leq 1$) [175].

Calculating the volume fraction distribution and advection accurately is a critical aspect of VoF methods. It requires to perform a proper evaluation of surface curvature, which is needed for the determination of surface tension force and pressure gradient across the interface [176]. A large variety of VoF schemes were developed over the last decades. These schemes can be grouped in two main categories : Algebraic Schemes and Geometric Schemes.

5.4 Algebraic Schemes (MULES)

In the `interFoam` solver, sharpness is obtained by introducing an artificial interface compression term in the α-equation (Weller et al. 2008 [165]), and boundedness is ensured by employing the MULES limiter (Multidimensional Universal Limiter with Explicit Solution). More details can be found in Deshpande et al. (2012) [177]. In the following, the `interFoam` solver will be used as a reference solver for comparisons (mainly in chapter 6). It will also be named as MULES which belongs to the algebraic schemes' category.

The artificial compression term added in equation 5.10 dumps the effect of numerical diffusion :

$$\frac{\partial \alpha}{\partial t} = \nabla \cdot (\mathbf{u}\,\alpha) + \nabla \cdot (\alpha\,(1-\alpha)\,\mathbf{u}_r) = 0 \tag{5.10}$$

where the term $\alpha(1-\alpha)\mathbf{u}_r$ acts only in the interfacial region ($0 < \alpha < 1$). The term $\mathbf{u}_r$ appearing in equation 5.10 expands as follows :

$$\mathbf{u}_r = c_r \left|\mathbf{u}\right| \frac{\nabla\alpha}{\left|\nabla\alpha\right|} \tag{5.11}$$

where the constant c_r has a recommended value in the range $1 \leq c_r \leq 4$ in order to ensure a sharp interface and limit the α function field to values between 0 and 1.

The solver `interFoam` was widely used and validated by several authors, Marschall et al. (2012) [178], Raeini et al. (2012) [179], Hoang et al. (2013) [180] and Bilger et al. (2017) [181]. Under some conditions the MULES method may fail in keeping the interface sufficiently sharp. Furthermore, the heuristic nature of the added compression term can lead to inaccurate interface advection and undesirable features such as non-physical ripples on the interface (Roenby et al. 2017 [182] and 2018 [183]).

5.5 Geometric Reconstruction Schemes

There are many geometric reconstruction VoF methods that present and develop different concepts. Noh et al. (1976) [184] were the pioneers in this field. They proposed the Simple Line Interface Calculation (SLIC). This method was mainly based on the approach developed by Debar (1974) [185]. Nowadays, SLIC methods are rarely used, despite the recent efforts made to improve the efficiency in the interface reconstruction of the method. Xiao et al. (2005) [186] and then Yokoi et al. (2007) [187] proposed substantial changes to the SLIC methods. They introduced respectively the Tangent of Hyperbola for Interface Capturing (THINC) and the Weighed Line Interface Calculation (WLIC) methods. While SLIC belongs to first order methods, Pilloid et al. (1992) [188] and (2004) [189] proposed a second order method named Piecewise Linear Interface Calculation (PLIC). The PLIC reconstruct methods assumes that the interface between two fluids can be approximated by a line (for 2D systems) or by a plane (for 3D systems).

In recent years, many efforts were made to increase the speed of geometric reconstruction VoF methods and to allow their use on unstructured meshes. Among the novelties that emerged stand out the solvers `interIsoFoam` and `interFlow` developed by Roenby et al.(2016) [36] and Scheufler and Roenby (2019) [37], respectively.

5.5.1 isoAdvector with iso-Alpha

Recently, Roenby et al.(2016) [36] presented an innovative geometric VoF method called *isoAdvector* with *isoAlpha*. The algorithm was implemented in the `interIsoFoam` solver and is available in OpenFOAM® + since version *v1706*.

Except for the interface advection step, the `interIsoFoam` (*isoAdvector*) solver is identical to the `interFoam` (MULES) solver. They both solve the governing equations in a segregated manner using the PIMPLE algorithm (a combination of the SIMPLE and PISO algorithms) for pressure-velocity coupling. Strictly speaking, *isoAdvector* and MULES also differ in the way `rhoPhi` (used in the momentum convection term) is calculated, which is described in Roenby et al. (2018) [183]. Furthermore, with recent improvements, the *isoAdvector* method

was made consistently second order for all mesh types (See Scheufler and Roenby (2019) [37] and section 5.5.2 after).

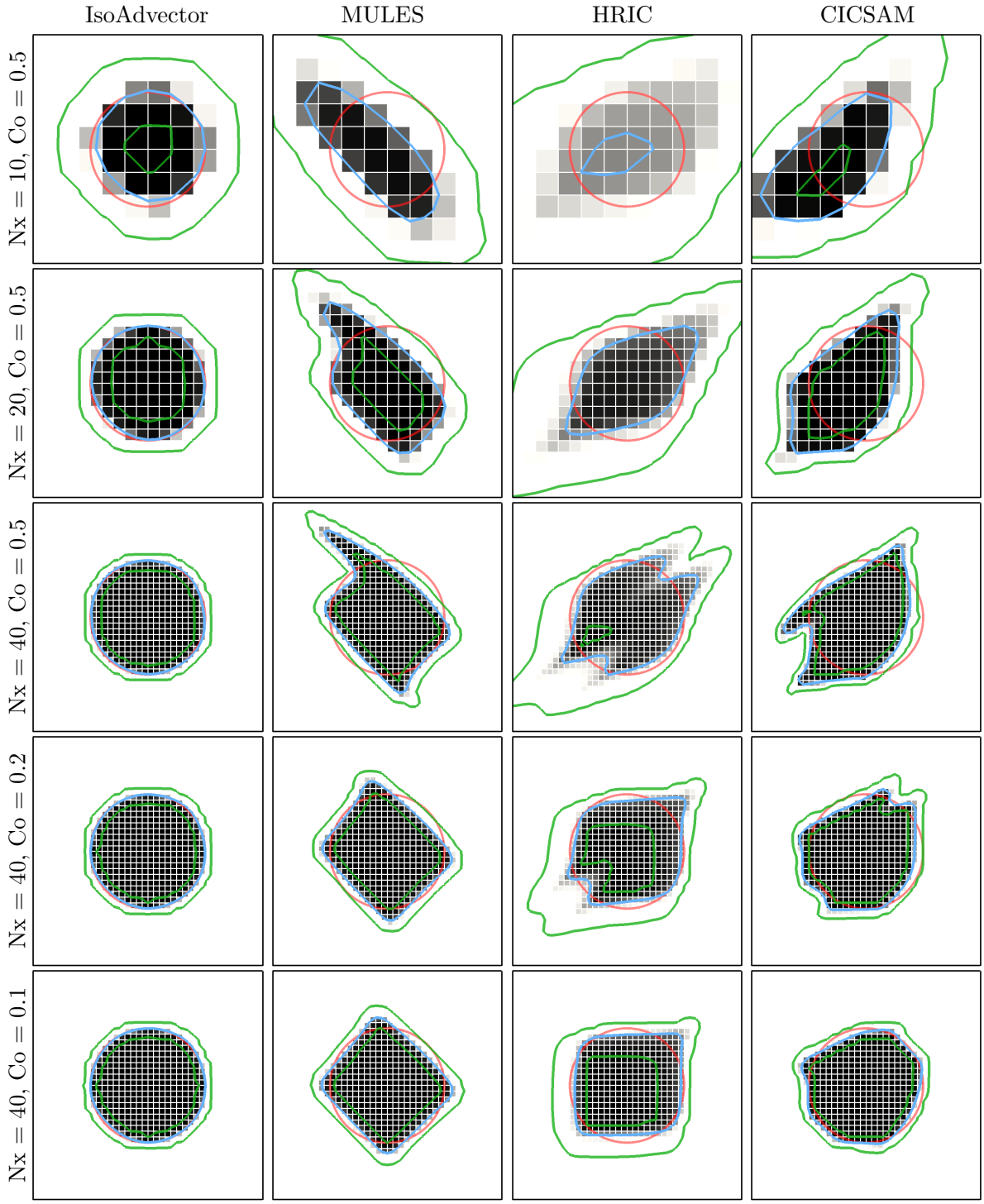

Figure 5.4 – Disk in uniform flow $U = (1, 0.5)$ at time $t = 4$ on a square mesh. Volume fractions shown in grey scale. Exact solution shown with red circles. $\alpha = 0.5$ contour shown in blue, and $\alpha = 0.01$ and $\alpha = 0.99$ contours shown in green. From Roenby et al.(2016) [36].

The *isoAdvector* with *isoAlpha* method implements new ideas in both the interface reconstruction step and the interface advection step. The reconstruction step uses efficient isosurface calculations to compute the interface location in a grid cell. The interface advection step uses a novel division of a physical time step into sub-time steps. In these sub-steps,

the volume fraction flux through a cell face is calculated analytically under the assumption that the interface is moving steadily across the face during the time interval. In the development of this procedure, no assumptions are made on the shape of a cell face, which makes the advection step applicable on arbitrary meshes [36].

Roenby et al.(2016) [36] tested *isoAdvector* with a variety of pure advection cases yielding very good results in terms of volume conservation, interface sharpness, boundedness and shape preservation. For instance, figure 5.4 shows the final volume fraction obtained with *isoAdvector*, MULES, HRIC, and CICSAM with five different combinations of mesh and time resolution.

They investigated the effect of refining the mesh resolution with fixed Courant number, namely CFL = 0.5 (first 3 rows). Then, Roenby et al.(2016) [36] used a finer mesh to evaluate the effect of a change in CFL. The number of Courant ranged from 0.1 to 0.5 (last 2 rows).

The first visual impression from figure 5.4 is that *isoAdvector* is superior at preserving the shape on all the cases. Roenby et al.(2016) [36] affirmed that MULES reported a tendency to align the interface at 45 degree with the mesh faces. Therefore, the MULES solution converged to a tilted square shape. The authors also showed that the HRIC scheme had a tendency to align the interface with the mesh faces. Finally, they stated that CICSAM method does not perform well in terms of shape preservation.

Roenby et al.(2016) [36] affirmed that, among the four methods examined, *isoAdvector* was the only scheme with volume preservation down to machine precision. Furthermore, *isoAdvector* kept the volume fraction data perfectly bounded [36].

They revealed that volume fraction thickness produced by *isoAdvector* was very close to the thickness of the exact analytical solution. On the other hand, the MULES interface thickness was 30-50% larger than the one of the exact solution [36]. HRIC performed rather bad in terms of interface sharpness. An important smearing of the interface can be clearly observed from figure 5.4. CICSAM kept the interface sharp for all runs. The latter was the best performing of the reference schemes investigated by Roenby et al.(2016) [36].

5.5.2 isoAdvector with PLIC-RDF

Scheufler and Roenby (2019) [37] presented an iterative residual based interface reconstruction procedure utilizing a reconstructed distance function (RDF) to estimate the local interface position and orientation from the raw volume fraction data. This new algorithm was developed in two variants based respectively on RDF isosurface reconstruction and on piecewise linear interface construction (PLIC) [37]. The latter reconstruction method, called plic-RDF, was evaluated in the present work.

Scheufler and Roenby (2019) [37] showed that their new method exhibits second-order convergence with mesh refinement in the interface position and orientation on both 2D and 3D structured and unstructured meshes. Especially on unstructured meshes and for the local interface orientation Scheufler and Roenby (2019) [37] significantly improved convergence properties compared to the reconstruction method presented by Roenby et al.(2016) [36], which was mainly based on isosurfaces of the volume fraction (see section 5.5.1).

1. Courant-Friedrichs-Lewy (or CFL)

Scheufler and Roenby (2019) [37] also presented a more advanced residual calculation. This method takes into account an estimate of the local radius of curvature relative to cell size. Figure 5.5 compares the performance of two geometric models introduced by Roenby et al.(2016) [36] (*isoAlpha*) and Scheufler and Roenby (2019) [37] (*plicRDF*), respectively.

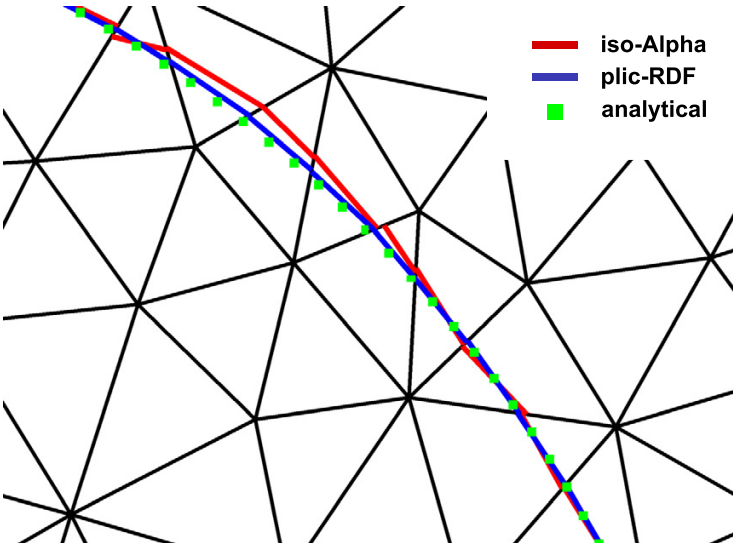

Figure 5.5 – Details of the interface reconstructed with the two geometric methods : *plicRDF* and *isoAlpha*. Taken from Scheufler and Roenby (2019) [37].

Furthermore, Scheufler and Roenby (2019) [37] implemented an initialization option that interpolates interface orientation from the previous time step. They affirmed that this new option leads to an improved and more accurate initial guess, which therefore reduces the number of iterations needed to reach convergence [37]. The *plic-RDF* algorithm uses the gradient calculation in the first time step of interface advection simulations. Thanks to this innovating approach, the volume fraction gradient usage was drastically reduced. It should be pointed out that this method is known to provide an erroneous initial guess on fine meshes.

In the present research, the reconstruction method *plic* with 5 iterations from Scheufler and Roenby (2019) [37] was used. Additionally, the *RDF* method was chosen to compute curvature instead of the volume fraction method (approach proposed by Cummins et al. 2005 [190] and Sun et al. 2010 [191]). In the following of this work, corresponding results will be referred as *isoAdvector plicRDF-5* or simply *plicRDF-5*. Besides, following the nomenclature in Scheufler and Roenby (2019) [37], we will refer to the original reconstruction algorithm of Roenby [36] as *isoAdvector isoAlpha* or simply *isoAlpha*.

5.6 Surface tension modelling

The molecules sitting at a free interface against vacuum or gas, present weaker binding than molecules in the bulk. The missing (negative) binding energy can therefore be viewed as a positive energy added to the surface. This energy, necessary to ensure the equilibrium of the interface, is called surface tension. More details about this force can be found in chapter 2.

The effects of surface tension might be neglected in the following conditions :

- $Re \ll 1$ and $Ca \gg 1$
- $Re \gg 1$ and $We \gg 1$

Reynolds, capillary and Weber numbers are respectively calculated with equations 2.39, 2.9 and 2.29. In the present case of static mixers, the values taken by these numbers cannot allow us to neglect the effect of surface tension.

The term $\mathbf{F}_\sigma$ that appears on the right-hand side of the equation 5.2 corresponds to the surface tension force. This term is modelled as a volume force acting on fluid near the surface. $\mathbf{F}_\sigma$ vanishes in the cells distant from the interface, either full gas cells ($\alpha = 0$) or full liquid cells ($\alpha = 1$).

Brackbill et al. (1992) [173] introduced one of the earliest model for the surface tension, namely the Continuum Surface Force (CSF). The CSF model produces a smooth transition in pressure at the interface due to its ability to distribute the interfacial forces over the volume (Engberg et al. 2014 [192]). Because of its simplicity and robustness, the CSF model is the most widely-deployed interfacial force model (Wang et al. 2014 [193]). The recent study of Wang et al. 2014 [193] also focused on the reduction of spurious currents, known as parasitic currents, generated near the interface with the CSF method.

Over the years, many methods aiming at modelling the surface tension force $\mathbf{F}_\sigma$ were developed. For instance, Lafaurie et al. (1994) [194] presented the Continuum Surface Stress (CSS). More recently, Liu et al. (2000) [195] and Kang et al. (2000) [196] introduced the Ghost Fluid Method (GFM). The CSS method presents some advantages over the CSF method for computational resolutions, especially when the surface tension is not constant. When the surface tension is constant, the CSF and CSS methods are almost equivalent. However, both methods introduce parasitic currents at the interface. These non-physical currents are mainly due to the imbalance of the pressure gradient and the surface tension force (Wang et al. 2014 [193]).

In OpenFOAM®, the surface tension force $\mathbf{F}_\sigma$ is often modelled as Continuum Surface Force (CSF) [142] :

$$\mathbf{F}_\sigma = \sigma \, \kappa \, \nabla \alpha \tag{5.12}$$

where σ represents the surface tension (constant) and κ is the curvature. The surface curvature κ is computed from the local gradient of surface normal $\mathbf{n}$, which is itself obtained from the gradient of volume fraction ([173], [142]) :

$$\kappa = -\nabla \cdot \mathbf{n} = -\nabla \cdot \left(\frac{\nabla \alpha}{|\nabla \alpha|} \right) \tag{5.13}$$

5.7 Stability condition

The space and time discretization algorithms for solving momentum and volume fraction equations will not be detailed here. The reader is referred to the user guide of OpenFOAM® [11] or to reference papers concerning the VoF solvers [36, 37, 177]. However, time discretization will be briefly discussed in this section, with the objective of presenting time schemes stability issues. The time schemes we used were either the first order Euler

scheme or the second order Crank-Nicolson scheme. Both schemes present stability conditions.

Let's denote Δt the time step. Δt should respect the Courant-Friedrichs-Lewy (CFL) condition :

$$CFL = \frac{\Delta t \ |U|}{\Delta h} < CFL_{\max} \tag{5.14}$$

where U is the fluid velocity in a considered grid cell and Δh the local spatial discretization (or grid size). For transport problems, the CFL number represents how many mesh cells a fluid particle passes through in a period of time. In other words, the fraction of cell that the flow will cross due to advection effect [197]. For explicit time-stepping schemes (e.g. Runge-Kutta), the CFL number must remain below the stability limit for the actual scheme to converge. The stability condition ($CFL < CFL_{\max}$) is established through a theoretical analysis for 1D pure convection on an ideal square grid. For example, a CFL minor than 1 ensures the stability of the Euler explicit scheme. For implicit and semi-implicit time schemes, the CFL limit does no longer constitute a stability limit. However, in a general computation, the grid is not uniformly hexahedral, which can lead to more restrictive stability conditions. For VoF applications, many authors recommended to choose a time step that leads to a Courant number of less than 0.3, even for implicit time schemes [36, 198, 199].

A wide range of physical phenomena can govern the system equations. Therefore, other stability criteria need to be introduced. The following expressions are used for the calculation of the time step for different physical models :

- Time step restriction due to convection (Lalanne et al. 2015 [200]) :

$$\Delta t_{conv \ \max} = \frac{\Delta h}{|U|} \tag{5.15}$$

- Time step restriction due to surface tension force (Brackbill et al. 1992 [173]) :

$$\Delta t_{\sigma \ \max} = \sqrt{\frac{(\rho_L + \rho_g)\Delta h^3}{4\pi\sigma}} \tag{5.16}$$

- Time step restriction due to gravity force (Deconinck and Dick 2006 [201]) :

$$\Delta t_{g \ \max} = \sqrt{\frac{\Delta z}{g_z}} \tag{5.17}$$

- Time step restriction due to viscous forces (Lalanne et al. (2015) [200]) :

$$\Delta t_{\mu \ \max} = \frac{\rho_L \ \Delta h^2}{2\mu_L} \tag{5.18}$$

In equation 5.17, Δz represents the discretization size along the gravity direction (here g_z). In equations 5.16 to 5.18, Δh is the local spatial discretization computed as :

$$\Delta h = \min(\Delta x, \Delta y, \Delta z) \tag{5.19}$$

Time-step restrictions due to surface tension force (equation 5.16) are usually the most restrictive [202]. The surface tension term is explicitly discretized in OpenFOAM®. In ad-

dition, time step restriction due to surface tension force facilitate the containment of the amplification of capillary waves along the interface (Galusinski et al. 2008 [203]), thus reducing spurious currents. The above reasons explain why most methods based on CSF formulation adopt the surface tension-induced stability condition reported by Brackbill. et al. (1992) [173], Galusinski et al. (2008) [203] and Denner et al. (2015) [202]. Galusinski et al. (2008) [203] improved the stability condition on the time step reported in equation 5.16. They introduced a new equation that takes into account all fluid characteristics (density and viscosity) :

$$\Delta t_{\sigma\ \max} = 4\,\frac{\mu}{\sigma}\,\Delta h \tag{5.20}$$

Finally, the global time step can be computed with this equation (Lalanne et al. 2015 [200]) :

$$\frac{1}{\Delta t} = \frac{1}{\Delta t_{conv\ \max}} + \frac{1}{\Delta t_{\sigma\ \max}} + \frac{1}{\Delta t_{g\ \max}} + \frac{1}{\Delta t_{\mu\ \max}} \tag{5.21}$$

The Δt can also be calculated with a more restrictive formulation :

$$\Delta t = \min\left(\Delta t_{conv\ \max},\, \Delta t_{\sigma\ \max},\, \Delta t_{g\ \max},\, \Delta t_{\mu\ \max}\right) \tag{5.22}$$

5.8 The bubbleTracker functionObject

The analysis of results is a fundamental aspect of CFD simulations. The output quantities of interest should be known before the simulation, in order to isolate and extract them in the most appropriate manner. Different approaches can be used for this purpose, for instance the conventional post-processing and run-time processing. Three different methods of data post-processing are available in OpenFOAM® :

- The solver is configured to include run-time processing (inlined into `controlDict`) ;
- The `postProcess` utility provides conventional post-processing of data written during the simulation ;
- The solver is run using the `-postProcess` option. This option only executes post-processing and is rather similar to the previous option.

The conventional post-processing are tools that permit us to analyse data after the simulation has completed. Run-time processing using inline code offers larger flexibility. It enables us to access all the data present in the database of the run, rather than just the data saved during the simulation. This method also allows the users to monitor data in real-time during the run. In addition, results are available on-the-fly before the end of the computations. For all these reasons, run-time processing was adopted in the present work.

Several post-processing tools are already implemented in the `functionObjects` framework and provided with OpenFOAM®. It should be noted that all the `functionObjects` available can be listed by running a solver with the `-listFunctionObjects` option, e.g. :

```
$> interIsoFoam -listFunctionObjects
```

Among the existing features implemented, we can mention the `functionObjects forces` that calculates the forces and moments by integrating the pressure and skin-friction forces

over a given patch, the `functionObjects fieldAverage` and `fieldMinMax` that calculate average quantities of volumetric and surface fields and the value and location of scalar minimum and maximum of a field, the `functionObjects scalarTransport` that will add a passive scalar transport and diffusion equation to the solver, the `functionObjects probes` that can record physical variables time signals at given probe locations, and some other various `functionObjects` for computing volume or surface integrals, y^+, Q criterion, sampling along lines and surfaces, etc. However, a `functionObjects` that extracts data similar to those obtained from our experiments is not yet implemented. This motivated the development of a home-made `functionObjects` called `bubbleTracker` that is able to isolate the bubbles present in the domain and to calculate their characteristics. A call to `bubbleTracker` was then added in the `controlDict` file.

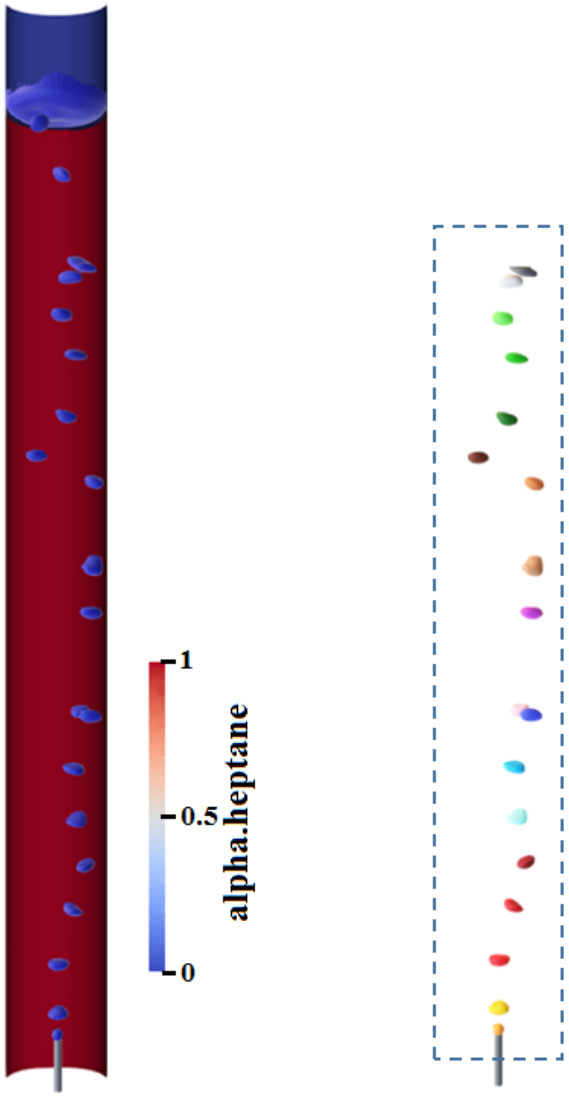

Figure 5.6 – `alpha.heptane` (l.h.s.) and `VoFColor` (r.h.s.) fields in the bubble column.

The `bubbleTracker` function generates and stores a `scalarField` called `VoFColor` based on the volume fraction field. This field is composed by integers representing the bubbles ID. Cells belonging to the same bubble receive an identical ID number. Then, each bubble detected is individually post-processed in order to obtain its characteristics. The bubble properties are saved in ASCII files during the computation. This in-lined processing tool allowed

us to drastically reduce the disk space required by storing only the wanted information. Figure 5.6 shows the bubbles segregation computed by the `bubbleTracker functionObjects`. Furthermore, a bounding box selection was added in order to limit the bubble detection to a user defined region. This box is highlighted in figure 5.6 with a dotted blue line.

Post-processing quantities of interest are described in details in chapter 4. These are the position of the bubble centroid, the bubble rise velocity, the bubble sphericity, area and volume. The overall gas hold-up and the total surface area of the gas-liquid interface can then be estimated by integrating over the number of detected bubbles. The volume of a single bubble V_b is computed by an integral of the gas volume fraction over the entire domain Ω as :

$$V_b = \int_\Omega (1-\alpha)\,\delta_b\,dv \tag{5.23}$$

where δ_b is a Dirac function computed from `VoFColor` that takes the value 1 for cells belonging to bubble number b and 0 elsewhere.

The centroid of mass $\mathbf{x}_G$ is computed through :

$$\mathbf{x}_G = \frac{1}{V_b}\int_\Omega (1-\alpha)\,\mathbf{x}\,\delta_b\,dv \tag{5.24}$$

where $\mathbf{x}$ denotes the cell centre coordinates. Similarly, the bubble velocity is calculated with :

$$\mathbf{U}_b = \frac{1}{V_b}\int_\Omega (1-\alpha)\,\mathbf{u}\,\delta_b\,dv \tag{5.25}$$

where $\mathbf{u}$ denotes the velocity, which is stored at cell centres in OpenFOAM®. The bubble area A_b is determined by using the method `area` of the C++ class `sampledIsoSurfaceCell` to compute the isosurface $\alpha = 0.5$.

In 2D, the sphericity of the bubble is called "circularity". The circularity $\mathcal{C}$ is defined as the ratio of the equivalent radius of the bubble based on its volume r_V over the equivalent radius of the bubble based on its surface r_A :

$$\mathcal{C} = \frac{r_V}{r_A} = \frac{\sqrt{V_b/(\pi\Delta_z)}}{A_b/(2\pi\Delta_z)} \tag{5.26}$$

where Δ_z denotes the size of the grid cells in the non-significant direction z. The circularity $\mathcal{C}$ takes the value 1 if a bubble is a perfect circle in 2D and decreases as the bubble deforms. On the other hand, in 3D, the sphericity ψ of a bubble is calculated by the square of radii ratio previously defined :

$$\psi = \left(\frac{r_V}{r_A}\right)^2 = \frac{(3/(4\pi)\,V_b)^{2/3}}{A_b/(4\pi)} \tag{5.27}$$

5.9 Chapter Summary

This chapter details the mathematical, physical and numerical models of OpenFOAM® solvers used in the present study. This open source software was selected to perform the Computational Fluid Dynamics (CFD) simulations of SMX static mixers. The main multi-

phase models available were reported and described. The VoF solvers were then selected for the present investigation.

The version ESI-OpenCFD OpenFOAM+ was employed in the present work. This choice was dictated by the larger quantity of solvers and post-treatment tools present in the OpenFOAM+® release. For instance, the VoF solver `interIsoFoam`, which uses the method *isoAdvector* with *isoAlpha* (see section 5.5.1) is only available in OpenFOAM+ [11] since version v1706.

Chapter 6

Assessment of VoF solvers on elementary cases

Before running into complex geometries, elementary quantitative benchmark configurations are essential for validation and comparison of interfacial flow solvers. This chapter is dedicated to two test cases. The first one is a single rising bubble benchmark. The second one, derived from the first, is a test case used for the quantification of spurious currents appearing in VoF solvers. Some of the results presented in this chapter were also the object of a publication by Gamet et al. (2019) [204].

6.1 Single rising bubble benchmark

Hysing et al. (2009) [205] proposed a 2D benchmark consisting in a single rising bubble in a quiescent liquid. Two different cases are described in Hysing et al. (2009) [205], corresponding to different density or viscosity ratios and to different surface tension. More recently, Adelsberger et al. (2014) [206] published a 3D equivalent of the same benchmark. For both these benchmarks, result data were made available online by the authors.

The first objective of this test case was to assess the performance and validate the VoF solvers in OpenFOAM® against a widely documented case of the literature. The OpenFOAM® numerical methods exposed in section 5.3, namely MULES, isoAlpha and plicRDF-5 were thus be compared together against the reference data in this case of a single rising bubble.

The second objective of this benchmark was to perform a grid sensitivity study in order to find the optimal number of cells across a diameter of bubble which gives a convergence of all results. The question of sufficient grid resolution for the case of single rising bubble in stagnant liquid was debated in previous works. Most works in the literature, such as Dijkhuizen et al. (2005) [207], Svihla et al. (2006) [208], Hua et al. (2008) [209], Amaya-Bower et al. (2010) [210], Andersson et al. (2011) [211], Aoron et al. (2015) [212], Badreddine et al ; (2015) [213], pointed out that about 20 cells per bubble diameter were needed in order to obtain satisfactory resolution. This point will be discussed in section 6.1.2 below.

6.1.1 Definition of test case

The test case number 2 as described by Hysing et al.(2009) [205] was used here. We used only this second test case as it was judged more representative of SMX cases and final industrial applications.

The 2D case set-up is reported in figure 6.1. First phase (liquid) properties are $\rho_1 = 1000\,\mathrm{kg\,m^{-3}}$, $\mu_1 = 10\,\mathrm{kg\,m^{-1}\,s^{-1}}$, while second phase (gas) takes $\rho_2 = 1\,\mathrm{kg\,m^{-3}}$, $\mu_2 = 0.1\,\mathrm{kg\,m^{-1}\,s^{-1}}$ as physical parameters. The surface tension is $\sigma = 1.96\,\mathrm{N\,m^{-1}}$. Gravity is taken as $g = 0.98\,\mathrm{m\,s^{-2}}$. Extension of this test case to 3D is straightforward [206]. Note however that Adelsberger et al. (2014) [206] replaced the side walls boundary conditions by no-slip walls, instead of slip walls like in Hysing et al.(2009) [205].

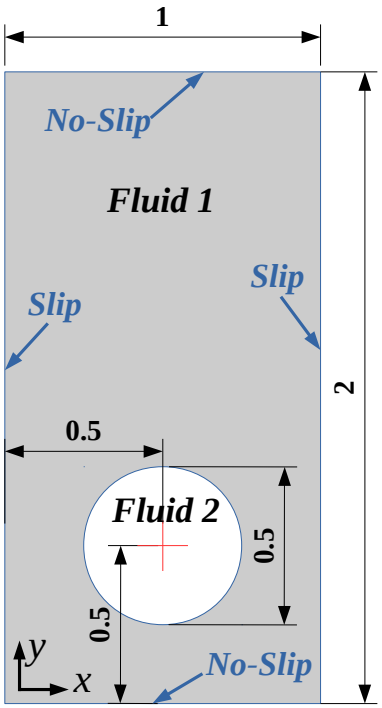

Figure 6.1 – Configuration and boundary conditions for 2D bubble benchmark.

Uniform Cartesian grids (cubic hexahedra) or triangular grids (triangular prisms in 2D or tetrahedra in 3D) were used for all simulations. Several grid resolutions were used ranging from 20 to 320 (640 in 2D) cells along the x direction, with the cell size halved along all computed spatial directions in each refinement. Hexahedral uniform grids were generated with the utility `blockMesh`, while prismatic/tetrahedral grids were created with Pointwise® using mean edge size identical to the Cartesian grids.

For the 2D cases, the grids are in the plane xy on a 1×2 m domain. The number of cells in the y direction is the double of that in the x direction. The bubble rises along the positive y direction. As OpenFOAM® computations are always three dimensional, there is one single cell in the z direction, which was taken of the same size as along x or y. For the 3D cases, the number of cells and the domain's length in the x and z directions are identical. The bubble was initialized as a cylinder (2D) or as a sphere (3D) using the `setAlphaField` utility.

The Crank-Nicolson second order time scheme with blending coefficient 0.9 was used for

all computations. The convective term was treated with `Gauss limitedlinearV 1`, and, in the MULES simulations, `Gauss vanLeer` was used for the α convection (See OpenFOAM® User's guide [11] for more details on numerical schemes).

The `Gauss linear` scheme was used for gradient terms on hexahedral grids while `pointCellsLeastSquares` was used for prismatic/tetrahedral meshes [11]. The GAMG implicit solver [11] was used for pressure terms, while the smooth solver was used for the velocity. Constant time steps were used, starting at $\Delta t = 0.002$ s for the coarsest level and reduced for finer grids to keep the maximum CFL number below 0.05. Such small time steps combined with the Crank-Nicolson second order scheme ensure that discretization errors due to time scheme are kept to a very low level.

The PIMPLE algorithm [11] was operated with `nOuterCorrectors` set to 3 and with 3 PISO correctors (`nCorrectors` set to 3). Setting `momentumPredictor` to `true` was necessary for accuracy with isoAdvector. The number of non-orthogonal correctors (`nNonOrthogonalCorrectors`) was set to 1 on prismatic/tetrahedral grids, 0 on hexahedral grids. Computations were run up to physical time $t = 3$ s in 2D and to $t = 3.5$ s in 3D.

6.1.2 Results and discussion

Figure 6.2 shows results for the rising velocity for MULES, isoAdvector with isoAlpha and plicRDF-5 on 2D hexahedral grids compared to the highest resolution reference data available in the literature [205]. The number of cells per diameter is simply the half of the number of cells along the x direction. From one level of grid refinement to the next finer one, the expected computational cost increase is $2^{n_d} \times 2$, where n_d is the number of dimensions (2 or 3) and the additional factor 2 corresponds to a necessary division by 2 of the time step in order to preserve a constant CFL when increasing the grid level. This makes a factor 8 in 2D and a factor 16 in 3D. In practice, this law was mostly verified for the low resolution grids. Performance issues when using full computational nodes versus partial nodes might be at the origin of differences on larger cases.

On figure 6.2, we first note that grid convergence is reached by all three OpenFOAM® solvers. MULES and plicRDF-5 results are rather similar, while isoAlpha results converge to a slightly different solution. All of the VoF solvers show velocity curves that tend to converge to the literature results when the grid resolution increases.

Figure 6.3 shows results on triangular grids. At higher grid resolutions, we clearly notice that neither MULES nor isoAlpha reach a grid convergence, showing overestimated bubble velocities (see red curves). This behaviour can be explained by an increase of spurious currents at highest grid resolutions for these methods. The integral procedure to compute bubble velocity of equation 5.25 inherently accounts for spurious currents in the solution. Spurious currents will be discussed in more detail hereafter in section 6.2 in the objective to quantify their effect on the solution.

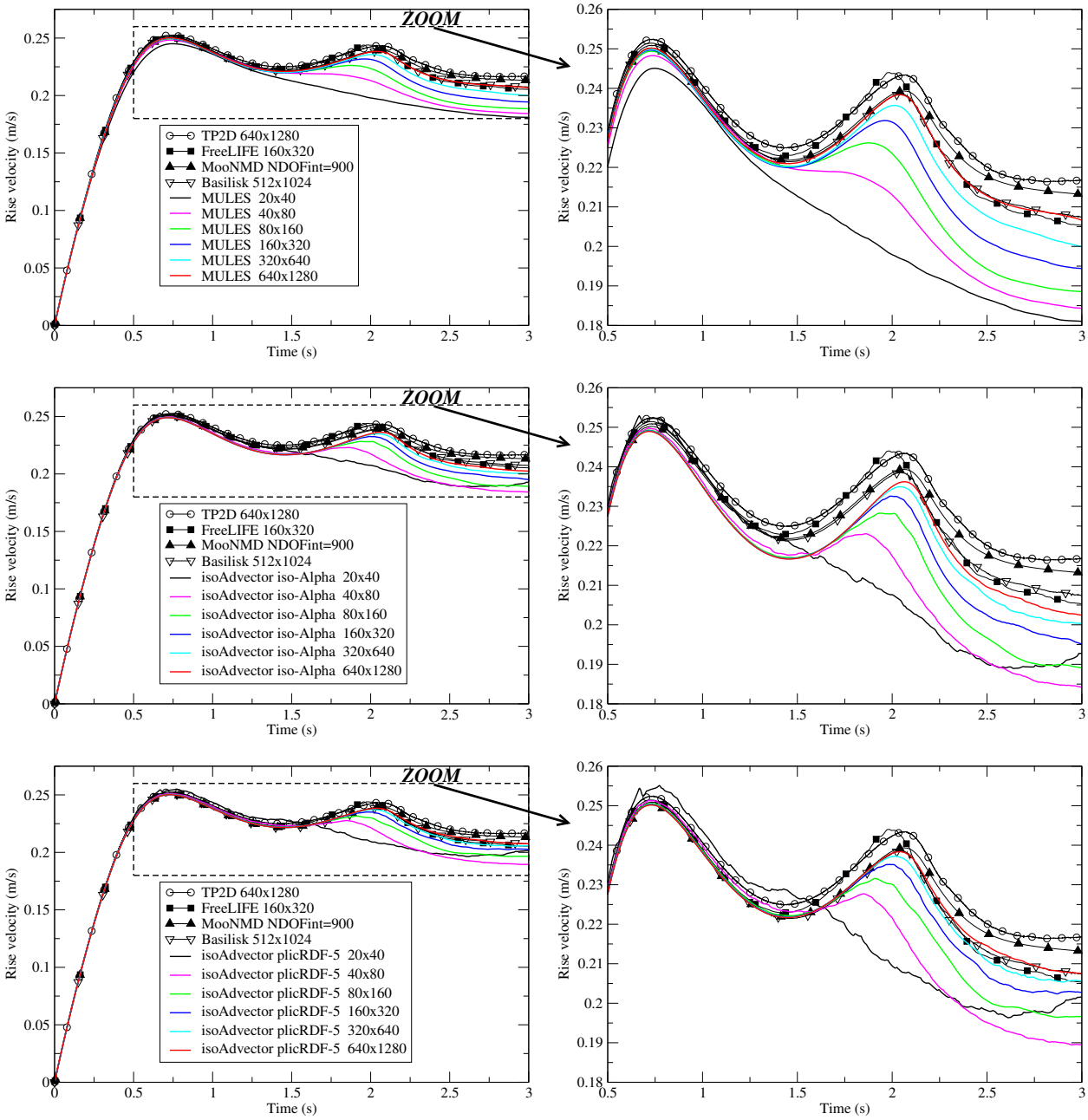

Figure 6.2 – Time evolution of rise velocity on 2D hexahedral grids for solvers MULES (top), isoAdvector with isoAlpha (middle) and plicRDF-5 (bottom) reconstruction schemes.

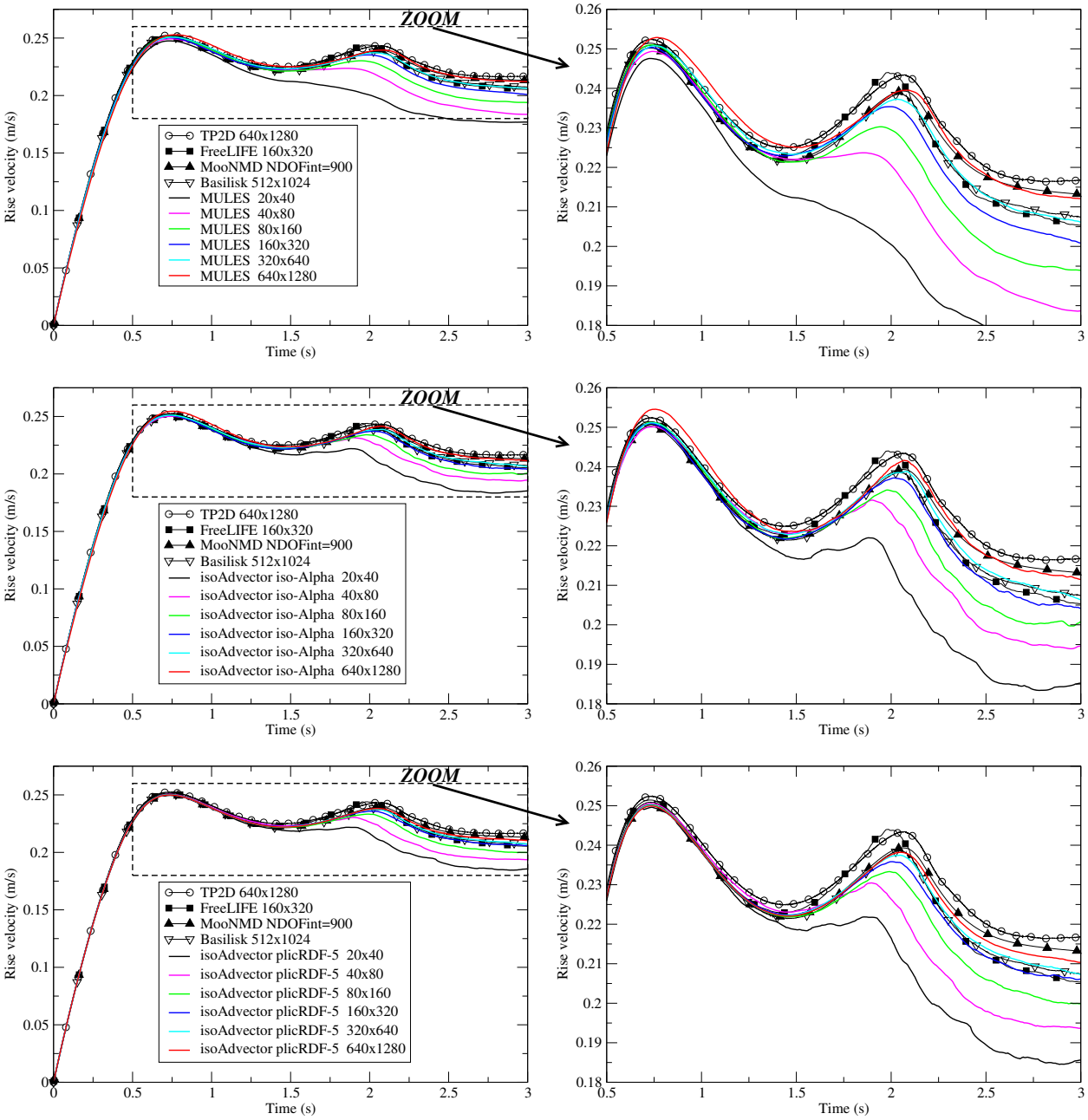

Figure 6.3 – Time evolution of rise velocity on 2D triangular grids for solvers MULES (top), isoAdvector with isoAlpha (middle) and plicRDF5 (bottom) reconstruction schemes.

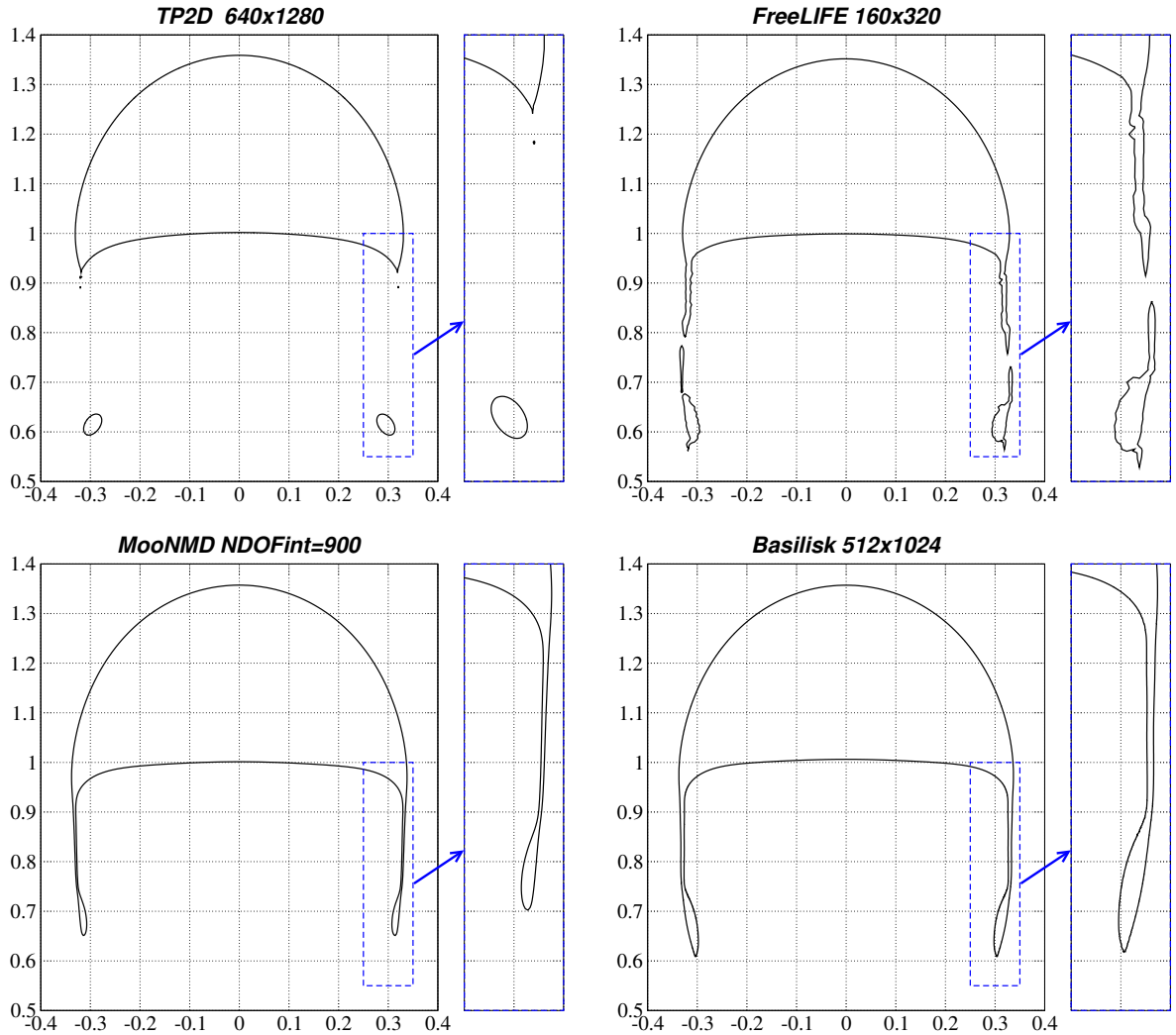

Figure 6.4 – Bubble shape at time t=3 for TP2D, FreeLIFE, MoonNMD and Basilisk solvers.

Figure 6.4 shows the bubble shape at time $t = 3$ obtained by reference solvers in the literature for the 2D case. It can first be noted that every code gives a different solution, particularly in the trains of detached bubbles. As a matter of fact, the test case number 2 of the benchmark of Hysing et al. (2009) [205] is more challenging to simulate than test case 1.

Figures 6.5, 6.6 and 6.7 compare the bubble shapes for respectively MULES, isoAlpha and plicRDF-5, for two grid resolutions, either on hexahedral or prismatic meshes. All bubble shapes for all solvers are rather coherent in terms of global positions of the main leading and trailing fronts. For each solver of figures 6.5, 6.6 and 6.7, the trains of detached bubbles are different between hexahedral and prismatic grids. The OpenFOAM® finest grids results are close to MooNMD and Basilik shapes, as plotted in figure 6.4.

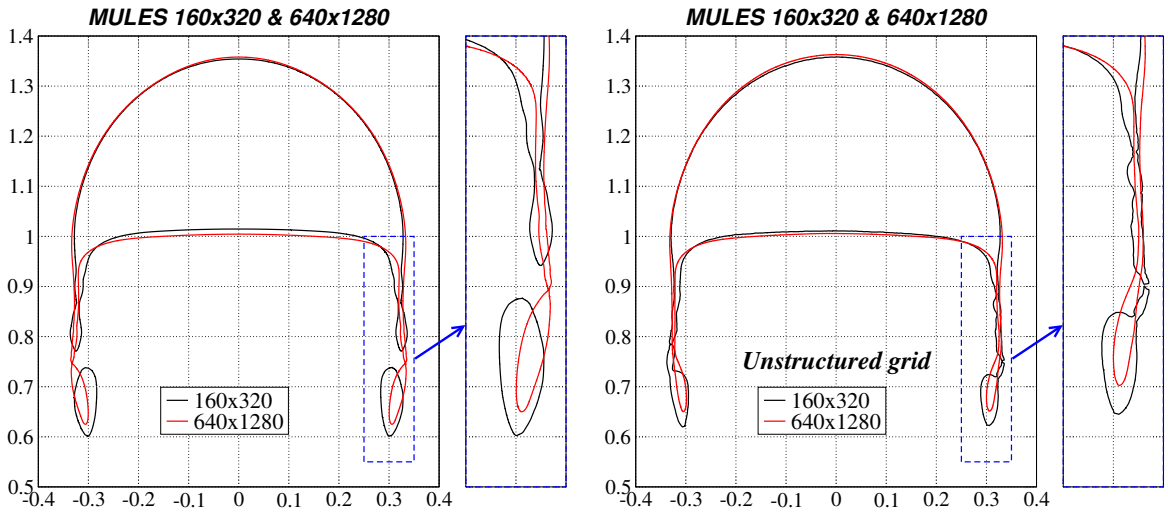

Figure 6.5 – Bubble shape at time t=3 for MULES. Left : square grids, Right : triangular.

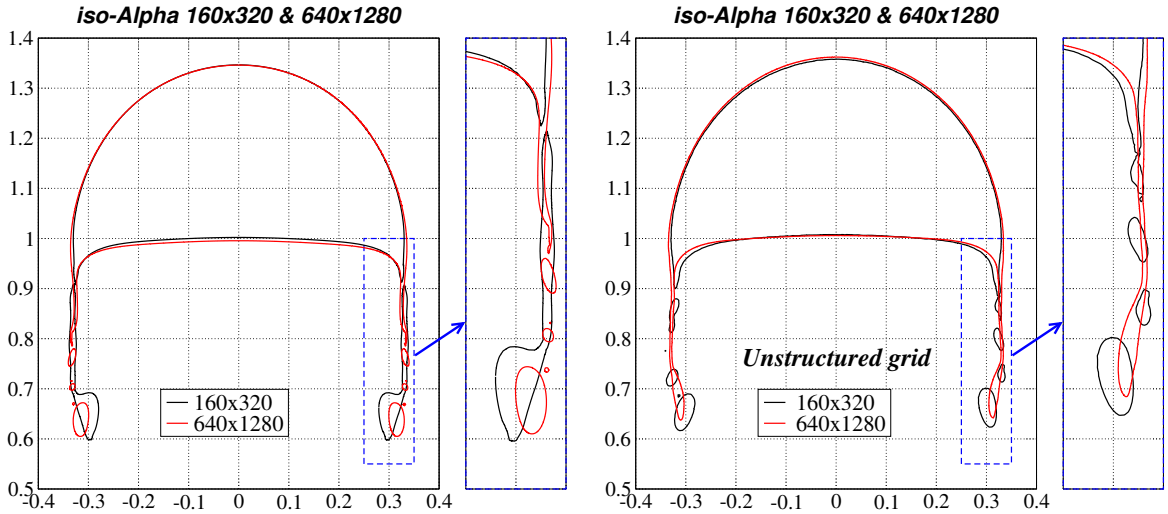

Figure 6.6 – Bubble shape at time t=3 for isoAdvector isoAlpha. Left : square grids, Right : triangular.

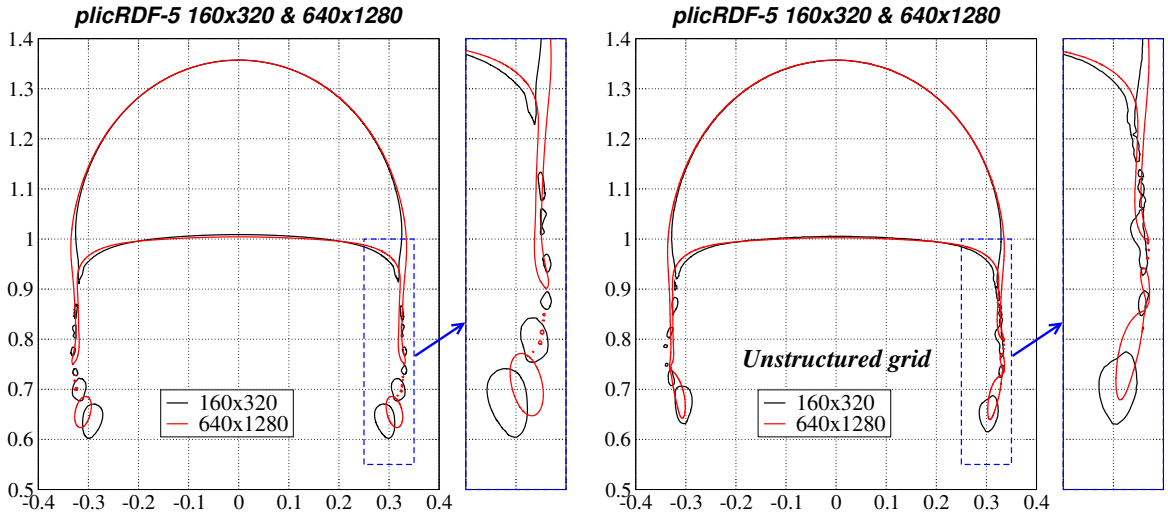

Figure 6.7 – Bubble shape at time t=3 for isoAdvector plicRDF-5. Left : square grids, Right : triangular.

Circularity in 2D is shown on figures 6.8 and 6.9, at respective grid resolutions 160×320 and $640 \times 1\ 280$. OpenFOAM® solvers compare well to reference data, except with the TP2D solver which experiences a different bubble tail structure (see also top left plot in figure 6.4). The difference between square (continuous lines) and triangular (dashed lines) grids on MULES, isoAlpha or plicRDF-5 circularities is more visible for time $t > 2$ up to the end of the simulation. This is mainly due to the difference in the bubble tail, discussed hereafter.

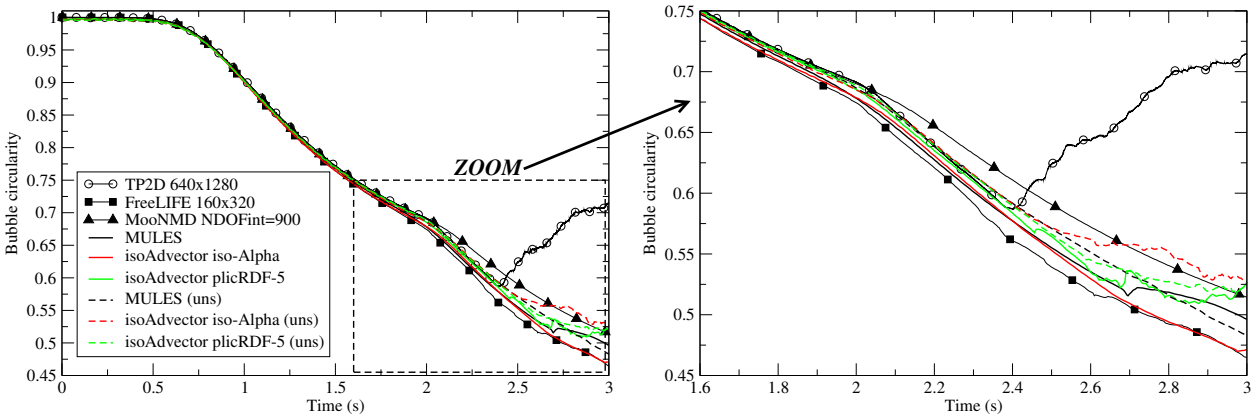

Figure 6.8 – Bubble circularity at resolution 160×320. Comparison of MULES, isoAdvector isoAlpha and plicRDF-5 with reference data for both Cartesian and triangular grids.

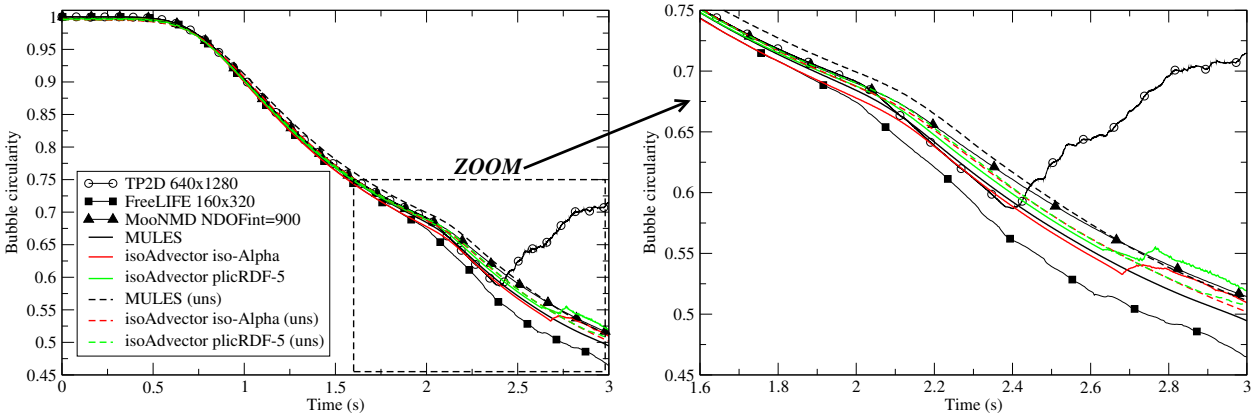

Figure 6.9 – Bubble circularity at resolution 640×1280. Comparison of MULES, isoAdvector isoAlpha and plicRDF-5 with reference data for both Cartesian and triangular grids.

For completeness about the bubble shape at time $t = 3$, we show in figures 6.10, 6.11 and 6.12 a comparison of the bubble shape on increasing size 2D triangular grids with respect to the finest 2D Cartesian grid shape made with the same solver.

MULES and plicRDF-5 show a correct grid convergence. At the finest levels (320×640 and $640 \times 1\ 280$), square and triangular grids are almost identical, particularly in their main fronts. One should however notice a small discrepancy in the upper front for the MULES solver at $640 \times 1\ 280$ (see figure 6.10). For the isoAlpha solver, the difference between square and triangular grids remains for all levels, and even increases slightly at the highest resolution.

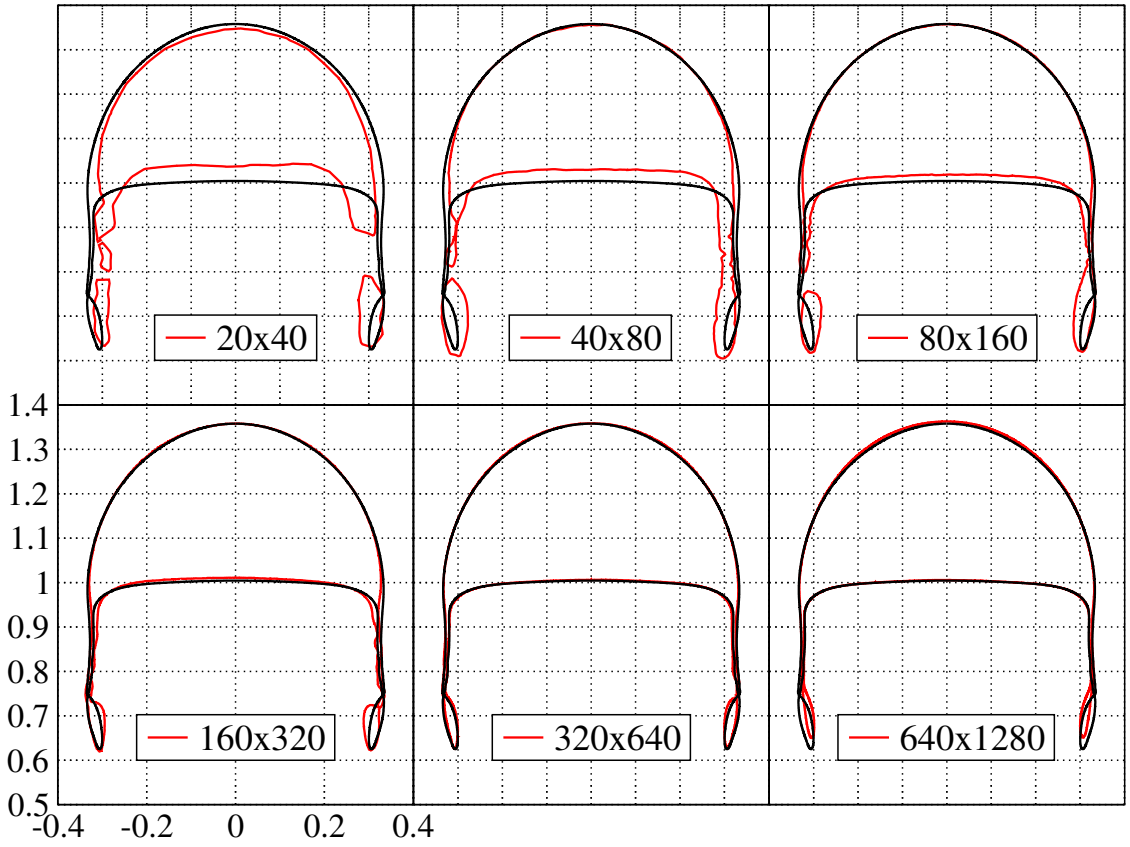

Figure 6.10 – Comparison of bubble shape obtained on different resolution triangular grids (red) against the finest Cartesian grid at 640x1280 (black). Plots for MULES at time $t = 3$.

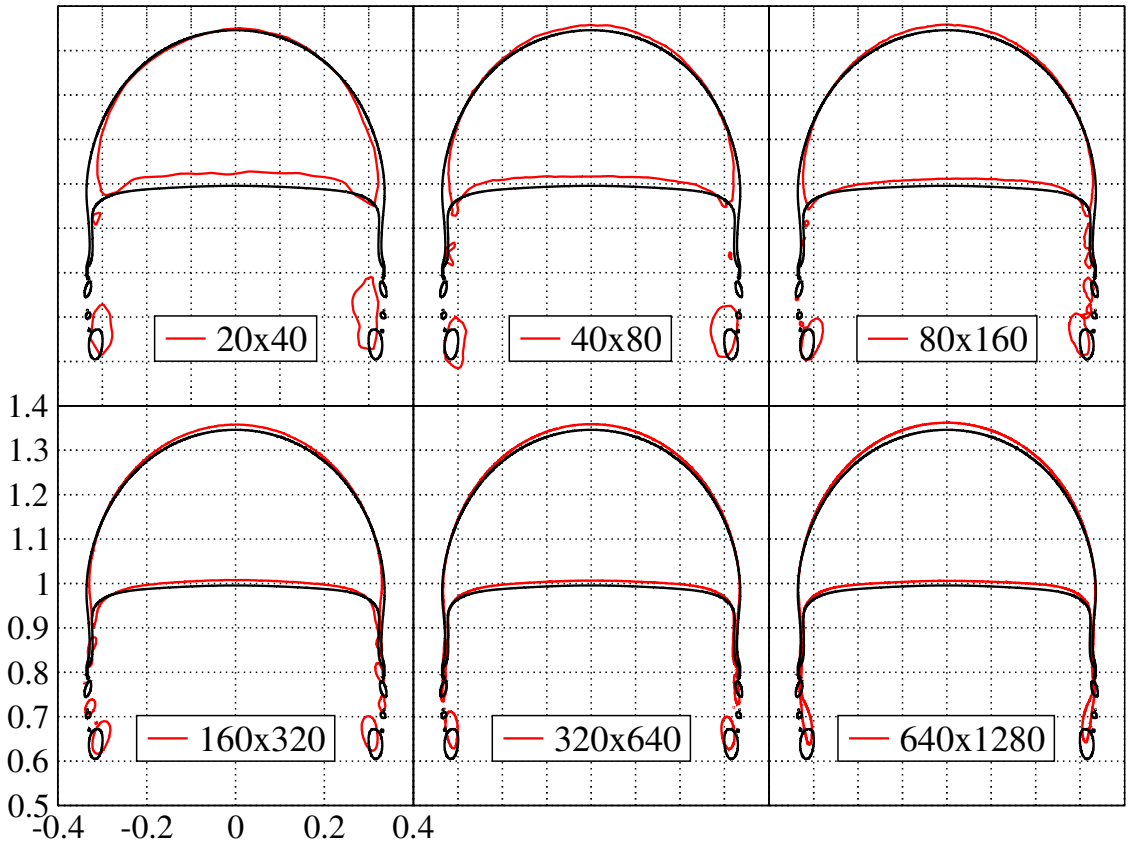

Figure 6.11 – Comparison of bubble shape obtained on different resolution triangular grids (red) against the finest Cartesian grid at 640x1280 (black). Plots for isoAdvector isoAlpha at time $t = 3$.

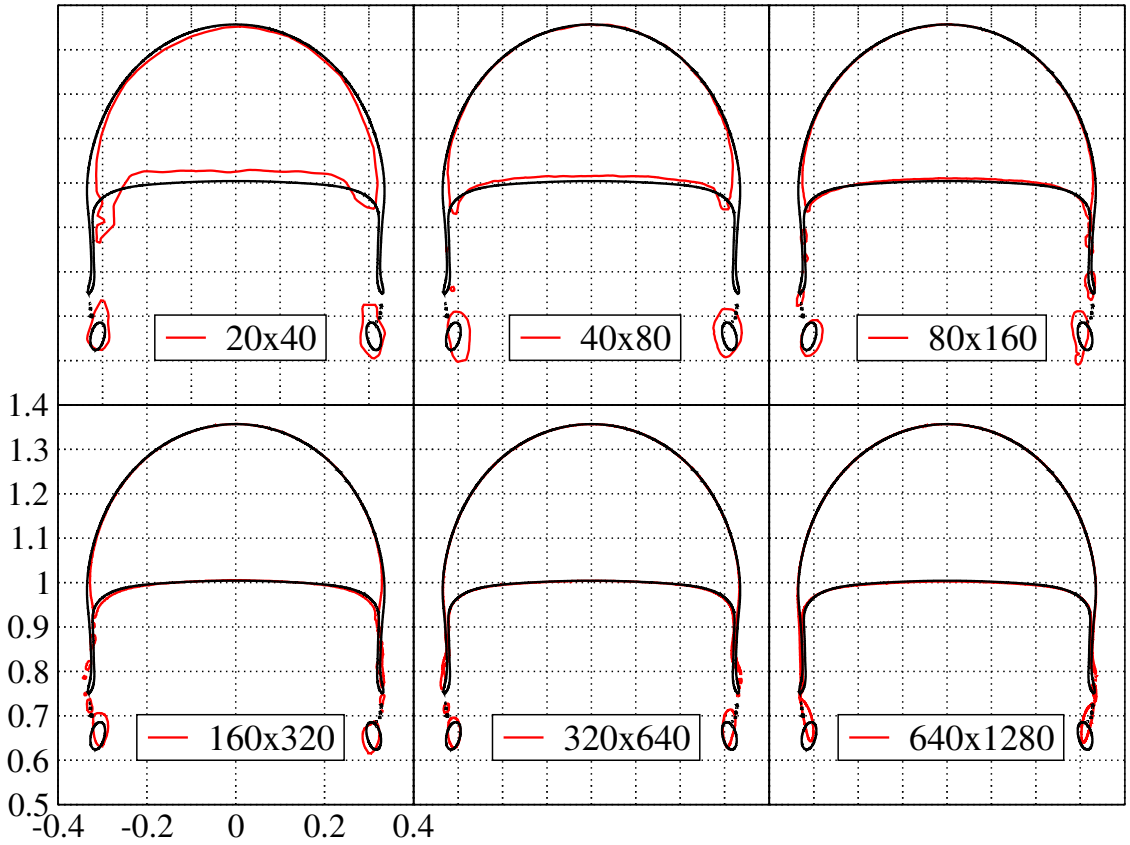

Figure 6.12 – Comparison of bubble shape obtained on different resolution triangular grids (red) against the finest Cartesian grid at 640x1280 (black). Plots for isoAdvector plicRDF-5 at time $t = 3$.

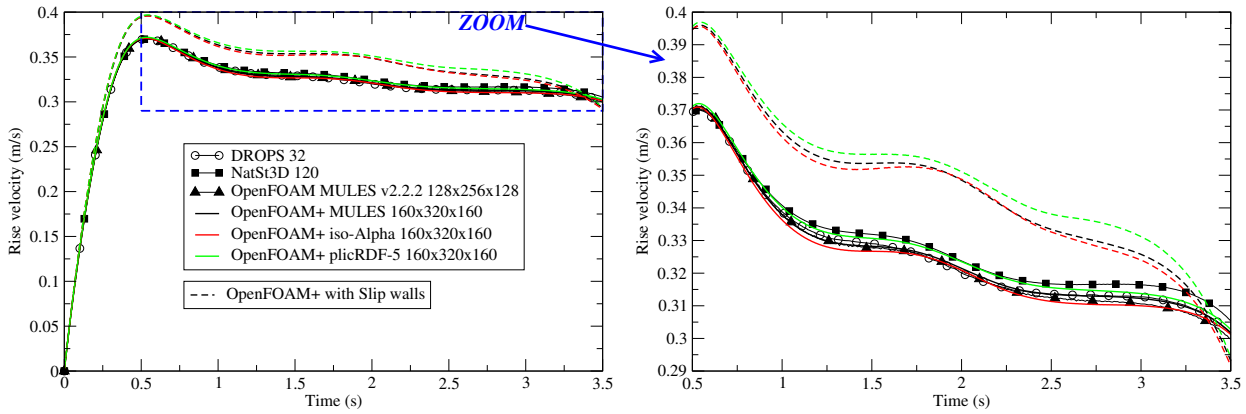

Figure 6.13 – Time evolution of the rise velocity for all solvers on 80x160x80 grids.

3D results show the same trend as those reported in the literature if the mesh is sufficiently refined. For example, figure 6.13 reports the bubble velocity for different solvers on $160 \times 320 \times 160$ grids. DROPS, NatSt3D and OpenFOAM 2.2.2 results are taken from Adelsberger et al. (2014) [206]. We recall that these authors replaced the side walls boundary conditions by no-slip walls, instead of slip walls like in Hysing et al.(2009). The effect of using slip walls is clearly visible in figure 6.13. Unsurprisingly, slip walls conduct to a higher bubble velocity.

Figures 6.14, 6.15 and 6.16 show the rising velocity for respectively the MULES, isoAdvector iso-Alpha and PLIC-RDF5 solvers in 3D. The isoAdvector solvers show a clear improvement on tetrahedral grids, with less difference between hexa and tetra of the same resolution. This error is even more reduced with the PLIC-RDF5 solver, as shown in figure 6.16.

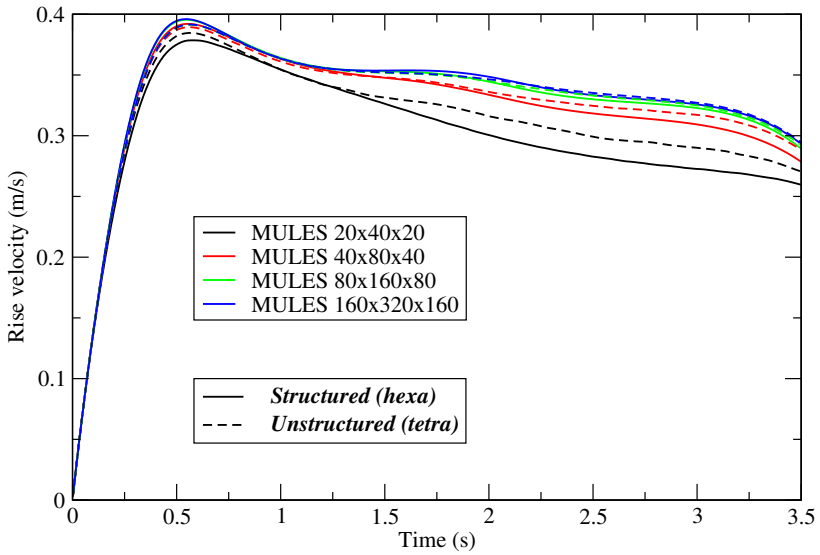

Figure 6.14 – Time evolution of rise velocity for MULES.

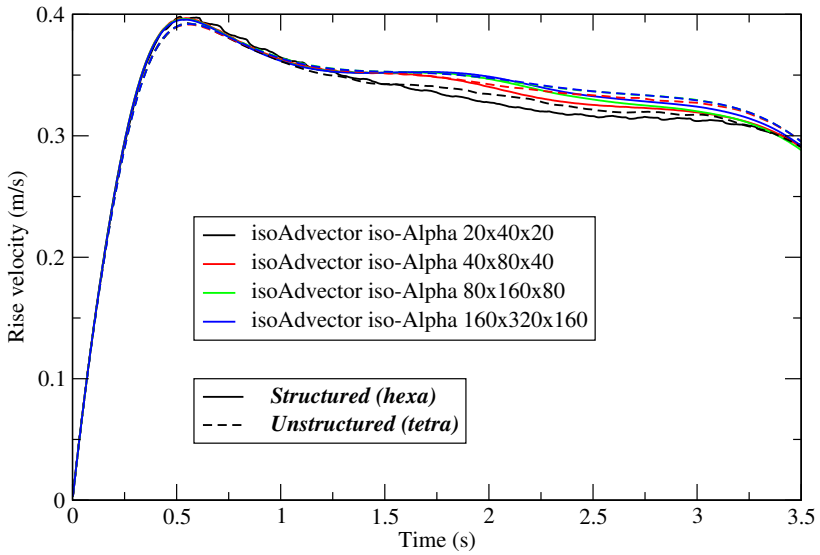

Figure 6.15 – Time evolution of rise velocity for isoAdvector iso-Alpha.

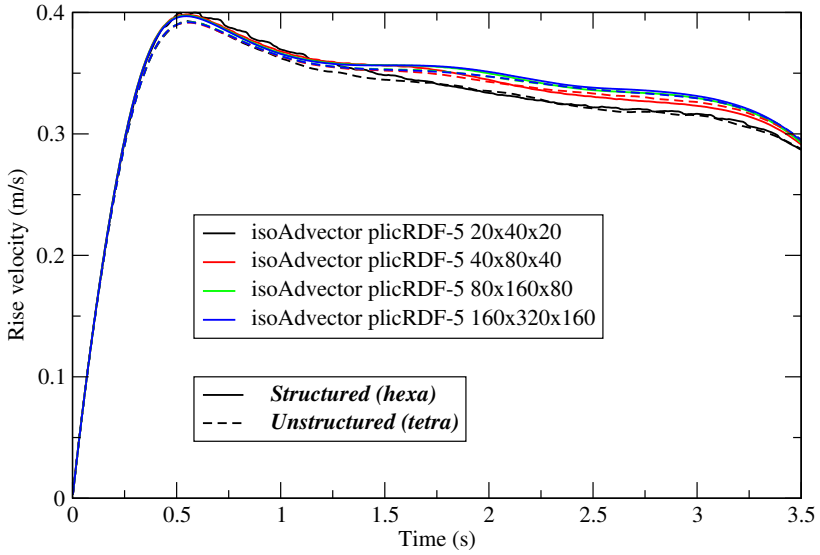

Figure 6.16 – Time evolution of rise velocity for isoAdvector PLIC-RDF5.

Figures 6.17 and 6.18 show the bubble shape at time $t = 3.5$ obtained by the OpenFOAM® solvers for two grid resolutions, either on hexahedral or tetrahedral meshes. As for the 2D results, it can first be noted that every solver gives a different solution, particularly in the trains of detached bubbles. For tetrahedral grids, the main fronts are coherent between the solvers and slightly shifted along the rising direction with respect to hexahedral grids. The positions of the main fronts are equivalent between the two grid resolutions, as both grids respect the minimal resolution criteria discussed hereafter. When increasing the grid resolution, the trains of detached bubbles are modified. This tends to prove that these detachments are highly sensitive to grid size, and probably to the surface tension force calculation.

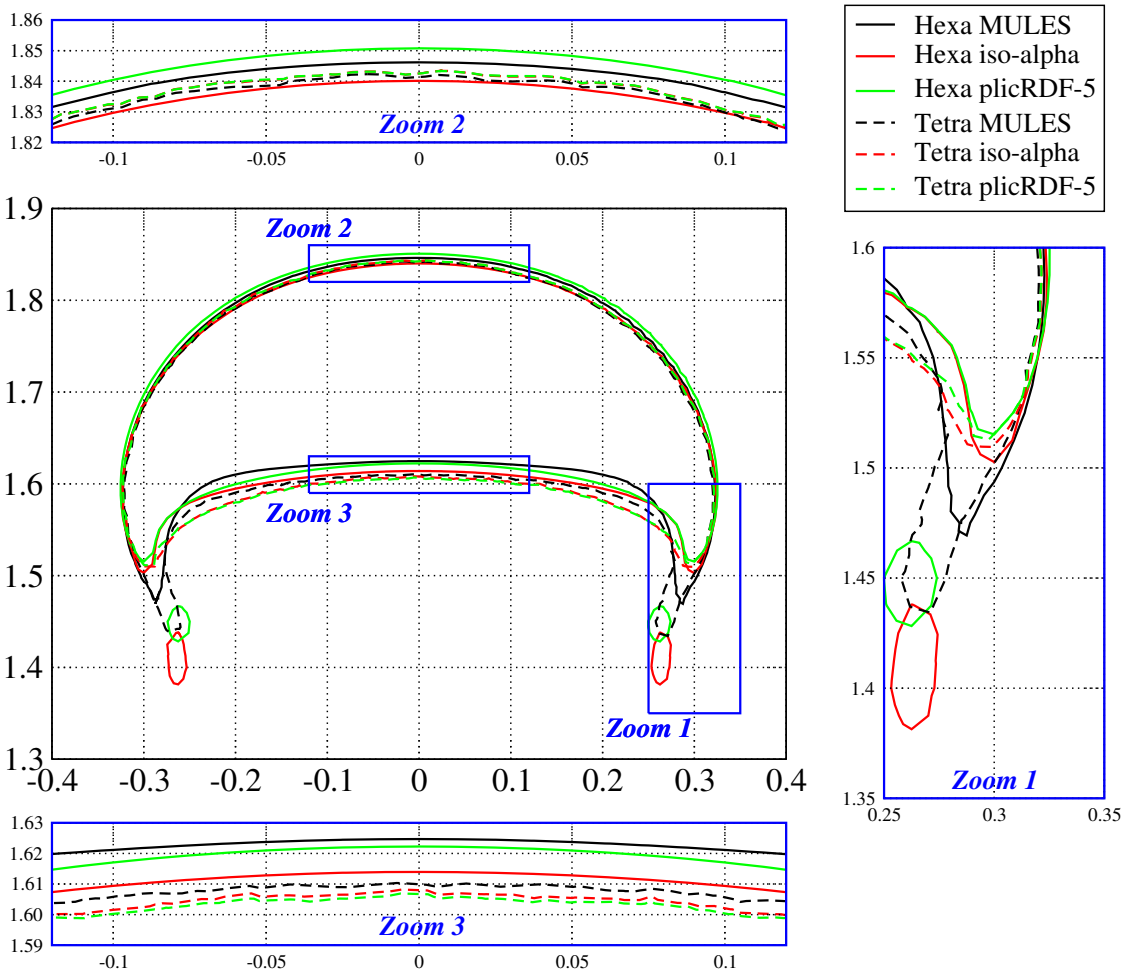

Figure 6.17 – Comparison of bubble shape at time t = 3.5 for all solvers on $80 \times 160 \times 80$ grids.

Considering the 2D and 3D results provided by this analysis, it was found that using the medium coarse grid in this study, corresponding to 40 cells per diameter, would provide reasonable accuracy and avoid high computational cost. This result states that roughly twice the resolution of the previous study of Amaya-Bower et al (2010) [210] is required for the current solvers.

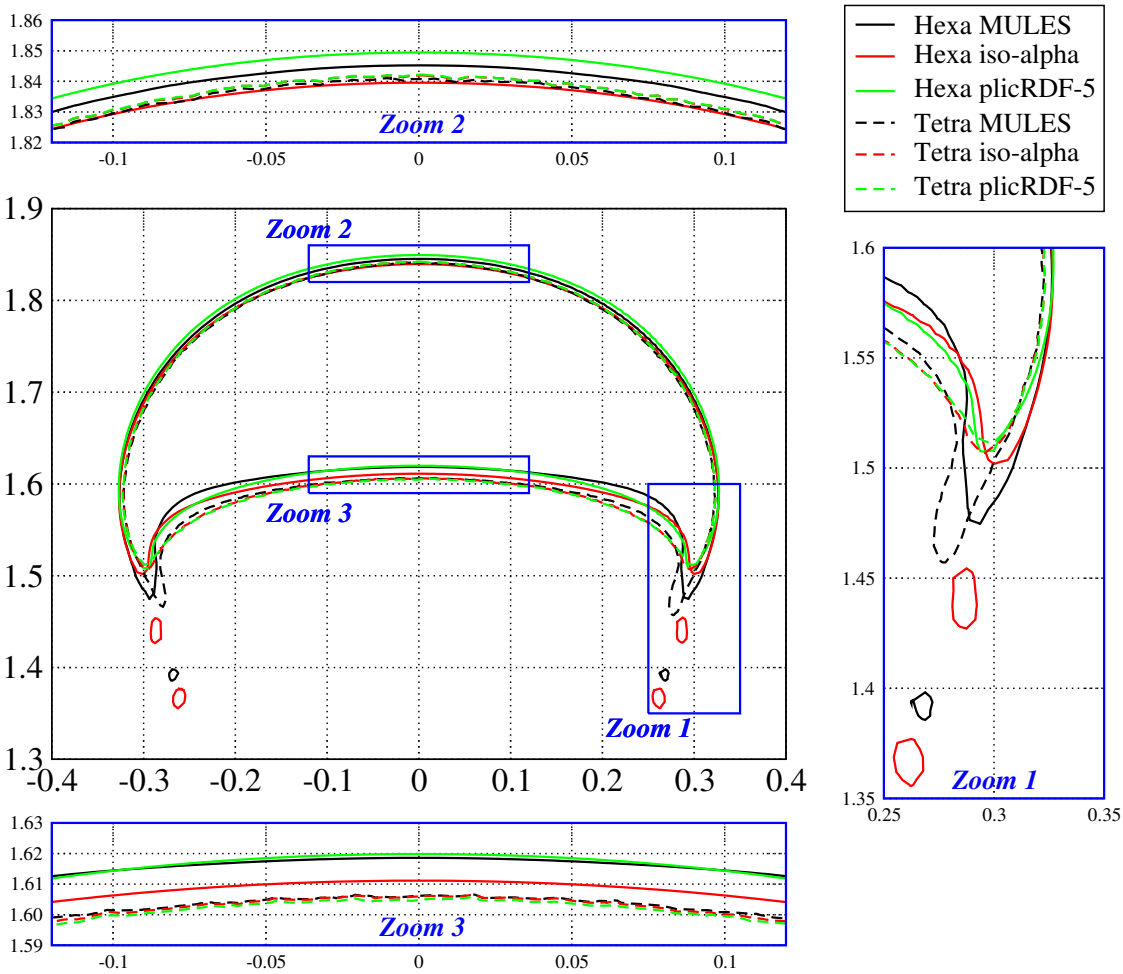

Figure 6.18 – Comparison of bubble shape at time t = 3.5 for all solvers on $160 \times 320 \times 160$ grids.

6.2 Static bubble for spurious currents quantification

Several authors investigated the magnitude of errors in numerical calculations. For instance, Popinet et al. (1999) [214], Herrmann (2008) [215], Albadawi et al. (2013) [216], Abadie et al. (2015) [217] estimated the magnitude of spurious currents generated by errors in the calculation of the curvature after advection in VoF and LS methods.

In an attempt to quantify the spurious currents generated by the OpenFOAM® VoF methods studied here, this section uses a zero-gravity single bubble test case, derived from section 6.1. This elementary case provides a base of comparison of the OpenFOAM® numerical methods with each other.

In a static configuration such as the circular bubble studied in this section, the Navier-Stokes momentum equations 5.2 are reduced to a balance between pressure gradient and surface tension force. Spurious currents can occur from a numerical imbalance between the discretization of these two terms. This numerical imbalance creates a source term in the vorticity production equation, which in turn generates velocities, which themselves will modify the curvature of the gas-liquid interface and produce errors in the surface tension computation, etc.

6.2.1 Definition of test case

We derived a zero-gravity test case from the definition of the single rising bubble, stated in paragraph 6.1.1. The domain is now 1×1 m and the gravity is set to 0. All other physical and numerical parameters are kept identical. This test case is ideally not supposed to generate any velocity field. The case is illustrated in figure 6.19.

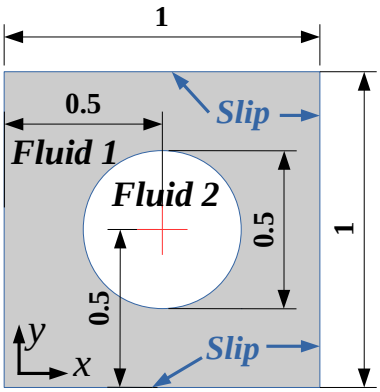

Figure 6.19 – Configuration and boundary conditions for 2D spurious currents test case.

6.2.2 Results and discussion

Figure 6.20 shows a qualitative view of the spurious currents generated by the different OpenFOAM® solvers used here. Note that plicRDF-5 vectors were scaled by a factor 80 with respect to other solvers to make them visible.

In order to quantify these generated spurious velocities, we monitored the maximum of velocity magnitude $U_{\max}$ over the computational domain. $U_{\max}$ is measured at each time step. We can introduce the velocity scale $u_\sigma = \sigma/\mu_1$. Spurious currents magnitude can then be non-dimensionalized in terms of a capillary number as $Ca_{\max} = (\mu_1 U_{\max})/\sigma = U_{\max}/u_\sigma$. Time can be normalized by scaling with $t_0 = D_0/u_\sigma$ where D_0 is the initial diameter of the bubble.

The resulting maximum capillary number is plotted on figures 6.21 and 6.22, for, respectively, hexahedral and triangular 2D grids. The same scales were used on both plots. The noticeable point is that plicRDF-5 generates spurious vectors on hexahedral grids by almost two orders of magnitude smaller than other solvers, as shown on figure 6.21.

On hexahedral grids, MULES and isoAlpha velocity errors are not always lower for higher grid resolutions. On the other side, plicRDF-5 obtained reduced errors for higher grid resolutions. Compared to hexahedral grids, triangular grids generate more errors for all solvers (see figure 6.22). On triangular grids, plicRDF-5 generates spurious vectors by more than one order of magnitude smaller than other solvers.

Spurious velocities can have an influence on the shape of the bubble. In the present case with zero gravity, the bubble should remain perfectly 2D cylindrical. The graph of figure 6.23 (resp. 6.24) shows the relative error on the radius in percent on hexahedral (resp. triangular) grids of increasing sizes. $r_0 = D_0/2$ denotes the bubble radius at time $t = 0$.

For hexahedral grids, MULES and isoAlpha show maximal errors along the coordinate

axes directions (at 0, ±90 or ±180 degrees) and also along grid median directions at 45 degrees. isoAlpha shows an increasing error when the grid resolution increases. plicRDF-5 errors are smaller, particularly along the coordinate axes directions.

For triangular grids, errors displayed on figure 6.24 no longer show preferential directions. They are also larger than on figure 6.23. Like for hexahedral grids, plicRDF-5 errors are also reduced with respect to other OpenFOAM® solvers.

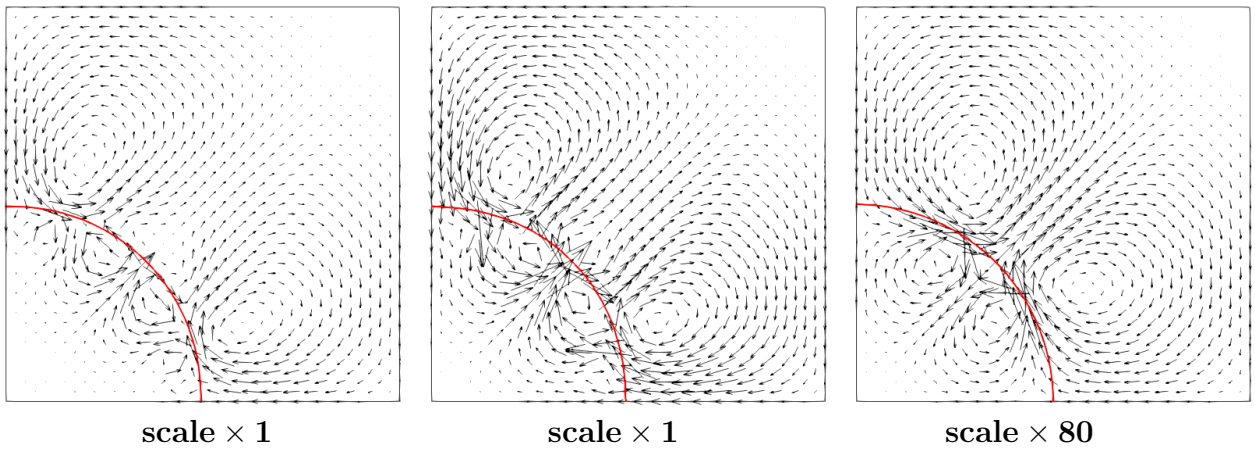

Figure 6.20 – Bubble under 0 gravity : visualization of spurious currents at time $t = 1.5$ in top right quarter on a 80x160 hexahedral grid. Left : MULES. Middle : isoAlpha. Right : plicRDF-5. Vectors on the r.h.s. plicRDF-5 image are scaled by a factor 80 with respect to MULES or isoAlpha. The red line materializes the isoline $\alpha = 0.5$.

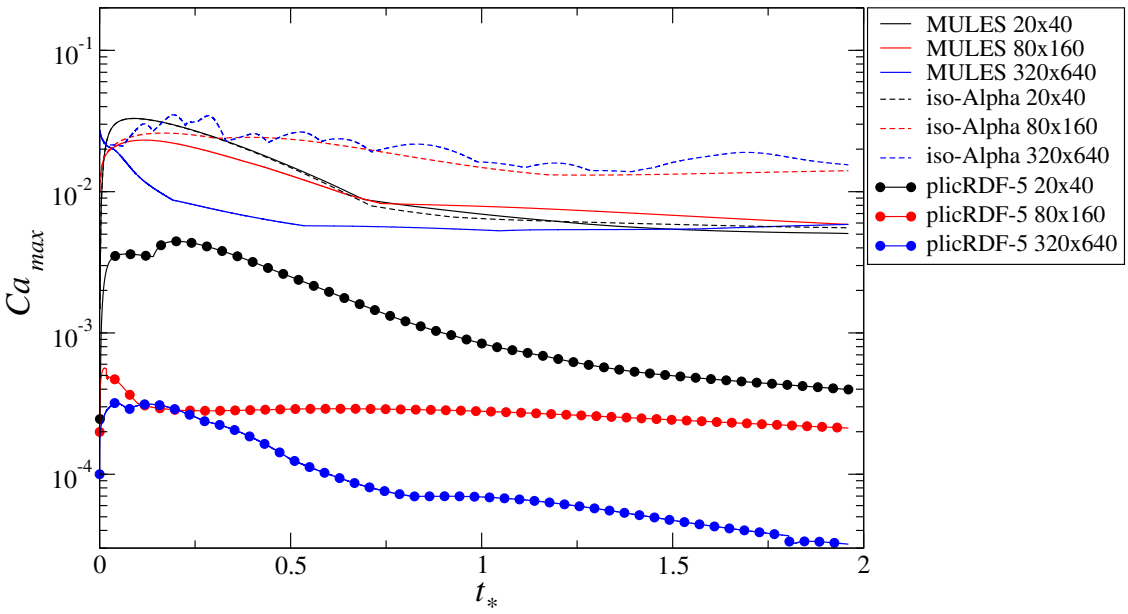

Figure 6.21 – Bubble under 0 gravity : Maximum capillary number over the computational domain for hexahedral grids versus non-dimensional time.

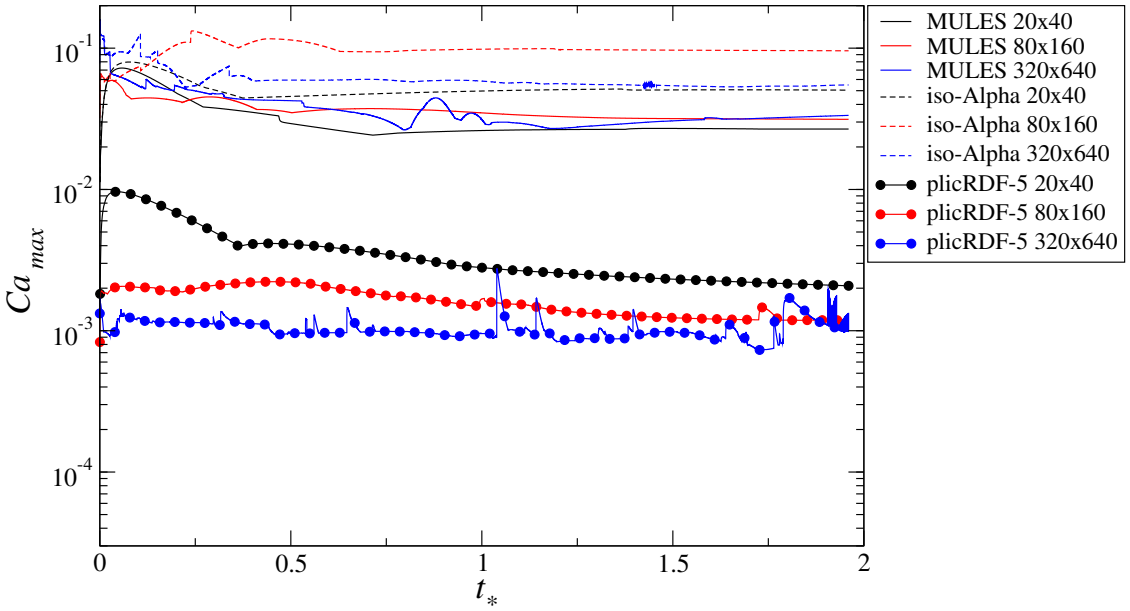

Figure 6.22 – Bubble under 0 gravity : Maximum capillary number over the computational domain for triangular grids versus non-dimensional time.

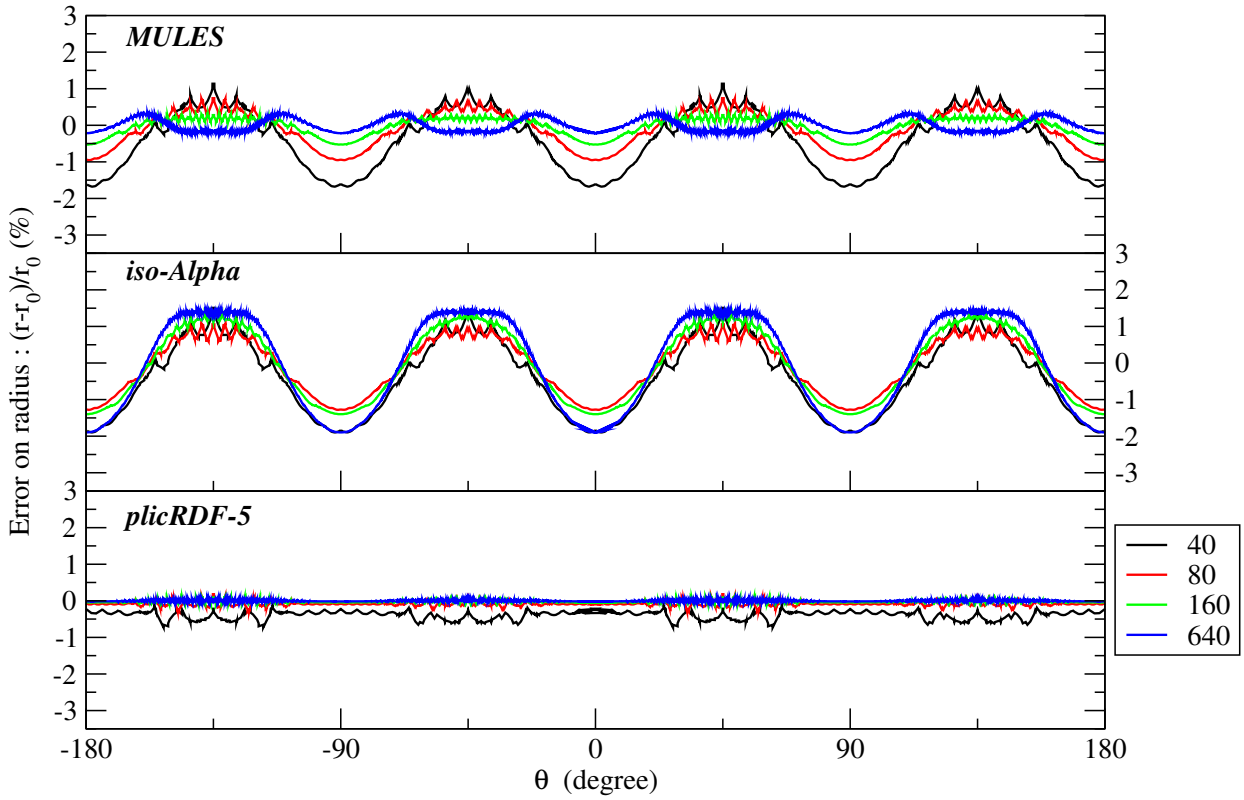

Figure 6.23 – Bubble under 0 gravity : Error on bubble radius for hexahedral grids.

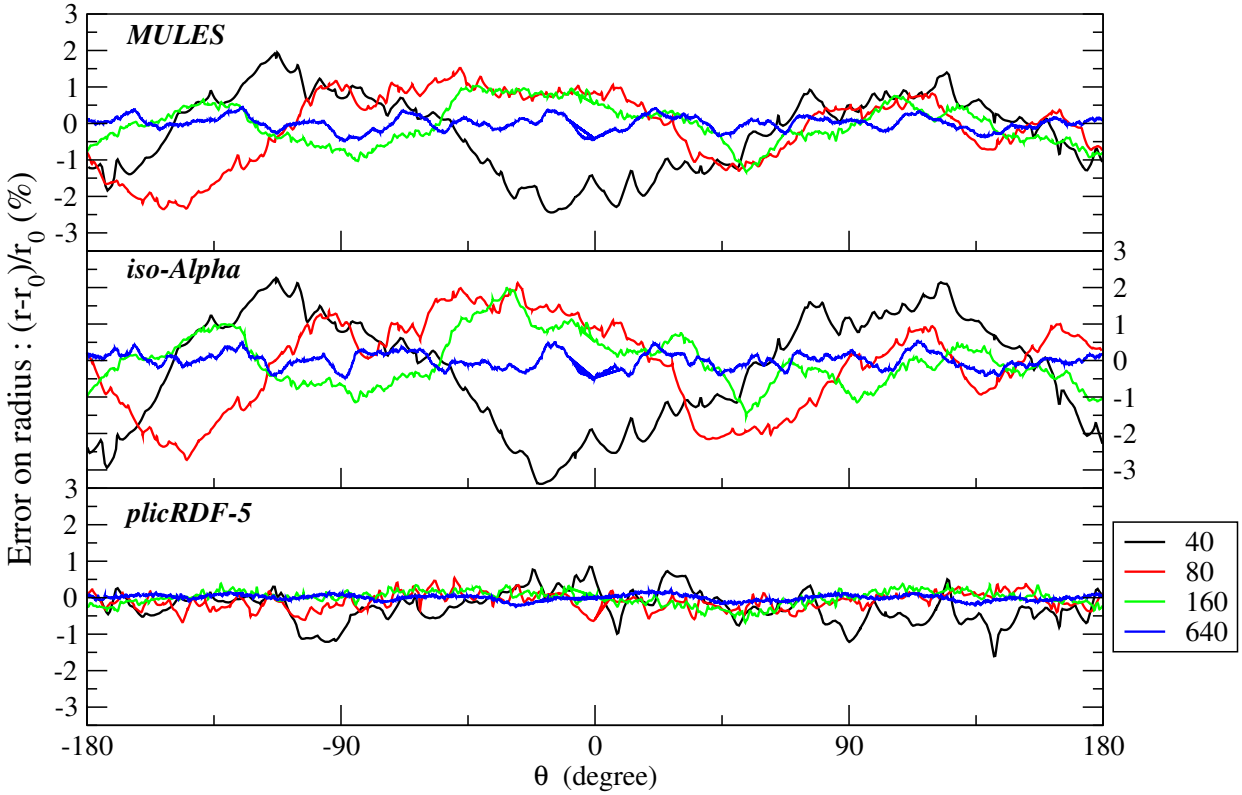

Figure 6.24 – Bubble under 0 gravity : Error on bubble radius for triangular grids.

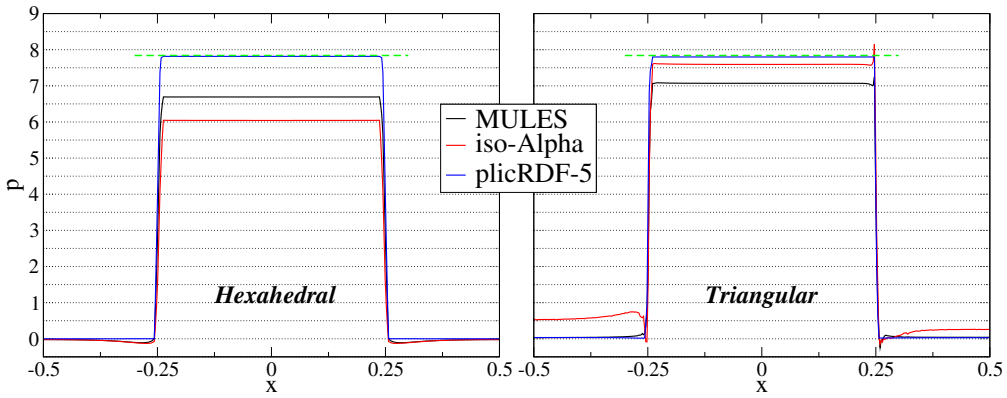

Figure 6.25 – Bubble under 0 gravity : Pressure jump across the bubble at time $t = 3$.

Finally, the plot of figure 6.25 shows the pressure jump across the middle of the bubble along the horizontal direction x. The Young-Laplace law for the pressure discontinuity due to surface tension can be expressed as :

$$\Delta P = \sigma \left(\frac{1}{R_1} + \frac{1}{R_2} \right) \tag{6.1}$$

where R_1 and R_2 are curvature radii along two perpendicular directions. As the present case involves a 2D cylindrical bubble which is infinite in the z direction, one of the curvature radii can thus be taken as infinite. The second curvature radius in the perpendicular direction is the bubble radius, which can be approximated as the initial bubble radius $r_0 = 0.25$m. The

pressure jump across the bubble can so be computed as $\Delta P = 7.84$Pa. This theoretical solution is plotted as the dashed green line in figure 6.25. Both for hexahedral and triangular grids, plicRDF-5 provides the best fit to the theoretical rectangular function of pressure jump across this bubble under zero-gravity. MULES and isoAlpha solvers conduct to underestimated pressure in the gas region, presenting over or undershoot near the pressure discontinuities at the fluids interface.

In conclusion, this validation case aimed at quantifying the spurious currents obtained by the three VoF variants tested here (MULES, isoAlpha and plicRDF-5). This test case was derived from the rising bubble benchmark, using similar physical and numerical parameters, except gravity and fluid domain size. The new reconstruction method, plicRDF-5, significantly reduced the spurious currents due to its more accurate interface curvature calculation. Moreover, the plicRDF-5 reconstruction method demonstrated a better prediction of the pressure jump across the bubble.

6.3 Chapter Summary

The preceding chapter illustrated the validation test cases run in this study. These test cases enabled to assess the performance and validate the VoF solvers in OpenFOAM® against results reported in the literature. Furthermore, they allowed us to compare OpenFOAM® numerical methods, namely *MULES*, *isoAdvector* isoAlpha and *isoAdvector* plicRDF-5.

2D [205] and 3D [206] Hysing benchmark, consisting in a single bubble rising in a quiescent liquid, were selected for validation purposes. Furthermore, a zero-gravity test case was derived from the definition of the single rising bubble. This allowed us to quantify the spurious velocities generated by the VoF solvers.

These benchmarks permitted us to identify the most performing VoF solver : plicRDF-5. Although plicRDF-5 proved to be more effective in terms of spurious currents, isoAlpha (`interIsoFoam`) showed better time-step stability. In fact, time-step oscillations were found using plicRDF-5 (`interFlow`) with fixed CFL.

Chapter 7

CFD results and discussion

In the present chapter, the main CFD results are reported. The structure of this chapter mirrors chapter 4, in order to make more convenient the comparison of experimental and numerical results. In the first sections, the setup of CFD cases and the techniques of mesh generation used are detailed.

7.1 Setup of CFD cases

A geometry similar to that employed for experiments (detailed in section 3.1) was used. A 2D representation of the set-up is outlined in figure 7.1. Liquid phase (n-heptane) properties are $\rho_L = 638.8\,\mathrm{kg/m^3}$, $\mu_L = 4.1 \times 10^{-4}\,\mathrm{Pa/s}$, while gas phase (nitrogen) takes $\rho_G = 1.165\,\mathrm{kg/m^3}$, $\mu_G = 1.76 \times 10^{-5}\,\mathrm{Pa/s}$ as physical parameters. The surface tension is $\sigma = 0.020\,\mathrm{N/m}$. More details are available in table 3.1.

Table 7.1 – Cases investigated.

Case	**Gas flow rate [l/h]**	**Nozzle diameter [mm]**
Bubble column	1	1
2 SMX	1	1
5 SMX	1	1
10 SMX	1	1

The cases are delimited by a cylindrical computational domain defined by two characteristic dimensions : the diameter of the column ($D_c = 16.2\,\mathrm{mm}$) and its length. The latter varied according to the case under investigation. As depicted in figure 7.1, the coordinate system was defined by choosing $+y$ as the rising direction. The other directions x and z define a horizontal plane perpendicular to the column axis. The x (resp. z) direction is perpendicular to all bars of the first (second) element of the static mixer. The coordinate system is thus identical to the coordinate system used in the experiments. The gravity vector $\mathbf{g}$ was therefore pointing towards the negative y direction. The contact angle values for the column (made of glass) and mixer (made of plastic) were measured experimentally. Table 7.2 shows the boundary conditions used for all patches.

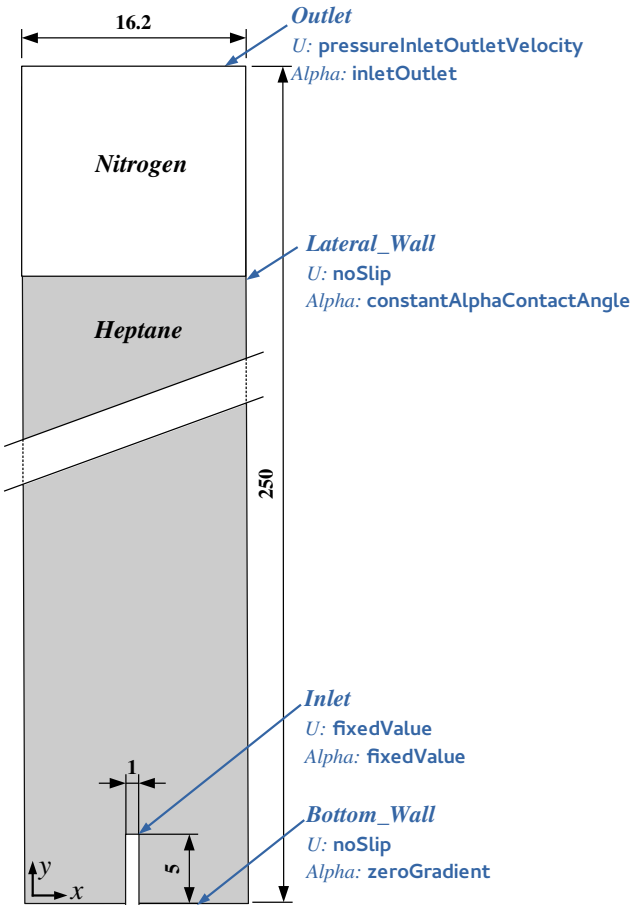

Figure 7.1 – Configuration, size and boundary conditions for the bubble column case. All dimensions are in mm.

Table 7.2 – Boundary conditions adopted in the numerical simulations.

Patch	alpha.heptane	p_rgh	U
Inlet	*fixedValue* *$internalField*	*fixedFluxPressure* *$internalField*	*fixedValue* $u_x\ u_y\ u_z$
Bottom_wall	*constantAlphaContactAngle* *value 90°*	*fixedFluxPressure* *$internalField*	*noSlip*
Injector_wall	*constantAlphaContactAngle* *value 90°*	*fixedFluxPressure* *$internalField*	*noSlip*
Lateral_wall	*constantAlphaContactAngle* *value 70°*	*fixedFluxPressure* *$internalField*	*noSlip*
SMX	*constantAlphaContactAngle* *value 25°*	*fixedFluxPressure* *$internalField*	*noSlip*
Outlet	*inletOutlet* *$internalField*	*totalPressure* *value 0 bar*	*pressureInletOutletVelocity* *value 0 0 0*

At the two sidewalls of the column (`Lateral_Wall` and `Bottom_Wall`), no-slip conditions were applied. The axial velocity (u_y) at the `Inlet` was set to 0.3537 m/s, which corresponds to a 1.0 l/h gas flow rate. Larger flow rates were not explored numerically because of the large increase of the gas-liquid interface surface and therefore of the computational time. All

computations were performed with `interIsoFoam` solver. As mentioned in chapter 6, *isoAdvector* with *isoAlpha* proved to be better performing than the MULES scheme. Although *plicRDF-5* proved to be more effective in terms of spurious currents, `interIsoFoam` was chosen because of its better time-step stability. In fact, significant fluctuations (Δt ranged from 10×10^{-5} to 10×10^{-7} s) were observed using `interFlow` with fixed CFL.

The liquid level was initialized as a cylinder region where $\alpha = 1$ is imposed, by using the `setAlphaField` utility, with `cylinderToCell` mode. Pressure and velocity were initialized as zero everywhere in the domain.

The `Gauss- Crank Nicolson` second order time scheme with blending coefficient 0.9 was selected. `Gauss linear` was used as gradient scheme. The convective term was resolved with `Gauss limitedlinearV 1`. Gauss vanLeer was used for the alpha term. All spatial schemes are second order. The reader is referred to the user's guide [11] for more details on OpenFOAM® numerical schemes.

The GAMG implicit linear solver [11] was used for pressure terms, while the smooth solver was used for the velocity with smoother `symGaussSeidel`. The simulations were run with a constant CFL, namely with CFL = 0.1. The constant CFL option allowed a thorough control of the maximum CFL value throughout the computational domain. Such small CFL combined with the Crank-Nicolson second order scheme reduced the discretization errors due to time scheme.

As for the Hysing benchmark, the PIMPLE algorithm [11] was run with `nOuterCorrectors` set to 3 and with 3 PISO correctors (`nCorrectors` set to 3). Furthermore, the `momentumP- redictor` was set to `true` in order to improve the accuracy of the solution. The number of non-orthogonal correctors (`nNonOrthogonalCorrectors`) was set to 1. All the computations were run up to physical time $t = 4$ s.

7.2 Mesh generation using snappyHexMesh

The mesh was generated by `snappyHexMesh`, which is part of the OpenFOAM® distribution. `snappyHexMesh` generates 3-dimensional meshes containing mainly hexahedra (hex) and split-hexahedra (split-hex). The mesh generation process is automatically made from triangulated surface geometries in STL format. All the STL files were produced by Pointwise® starting from CAD geometries.

The general workflow for creating a mesh with `snappyHexMesh` is the following :

1. A background Cartesian grid is created with the utility `blockMesh`. This grid consists in cubic cells of identical sizes along all directions. The background grid defines a reference refinement level that `snappyHexMesh` uses in the next step to refine the grid in regions specified by the user. The background Cartesian grid must englobe the entire computational domain.

2. `snappyHexMesh` performs the castellating step. The triangulated STL surface is approximated by splitting/refining and removing cells outside the fluid domain.

3. `snappyHexMesh` performs the snapping step. The mesh close to the triangulated STL surface is projected onto the surface.

4. `snappyHexMesh` performs the layer addition step. The mesh is shrunk from the surface and hexahedral cells are introduced at the STL surface to ensure a good capture of the physical boundary layers.

The specification of mesh refinement level is very flexible and the surface handling is robust with a pre-specified final mesh quality [11]. `snappyHexMesh` runs in parallel with a load re-balancing step each time the load disequilibrium exceeds a certain percentage on one of the processors [11]. The background Cartesian grid generated with `blockMesh` and the STL geometry of the static mixer are shown in figure 7.2.

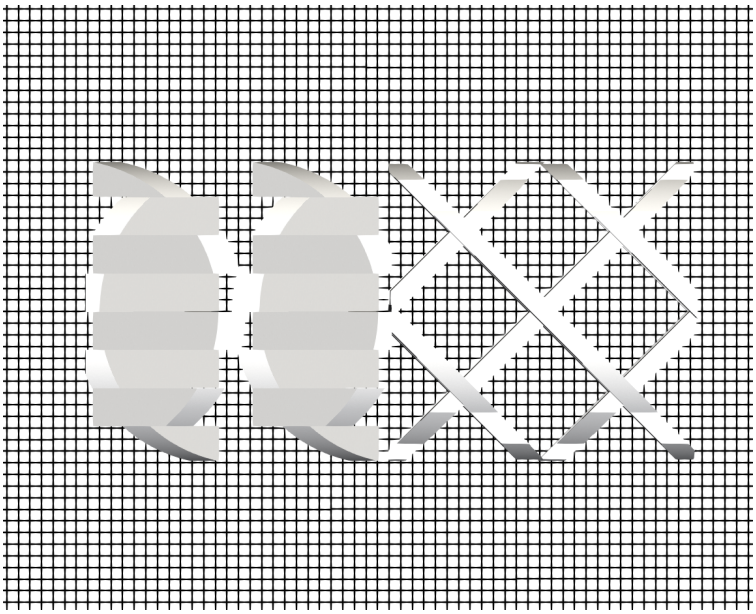

Figure 7.2 – Details of the initial mesh generation in `snappyHexMesh` meshing process (in the background) and of the SMX geometry.

VoF simulations performed on OpenFOAM® require as much hexahedral grid as possible. In fact, the convergence, the stability and the quality of the results on hexahedral grids were greatly improved compared to those on tetrahedral grids. This behaviour was confirmed by the test cases analysed in chapter 6. `snappyHexMesh` allowed us to obtain a uniform and structured grid in most of the fluid domain. The quantity of hexahedra cells reached between 97% to 99% (depending on the case, see table 7.3). Only cells near the wall surfaces were polyhedra with more than 6 faces or, more rarely, tetrahedra. Cells with volume less than $10 \times 10^{-15}\,\mathrm{m}^3$ were removed from the domain.

A grid sensitivity analysis was performed on the Hysing benchmark in order to find the optimum number of cells per bubble diameter d_b. The results reported in chapter 6 suggest an optimal value between 20 to 40 cells/d_b. The latter value led to more reliable results (see chapter 6). Experimental results (see chapter 4) indicate a mean bubble diameter of about 3 mm. Assuming that about 40 cells per diameter are desired, a spatial discretization of 0.075 mm is required. A preliminary estimation of the overall number of cells in the computational domain revealed that the 40 cells/d_b criterion cannot not be met, since the total number of cells would exceed 100 million. For this reason, an intermediate spatial discretization of 0.1 mm was used, corresponding to 30 cells/d_b. Figure 7.3 shows the regular structured grid obtained on the SMX mixer surface. More details on the meshes are given in table 7.3 below. In addition, `snappyHexMesh` generated a slightly smaller cell size of spatial discretization near the walls, which was measured to be around 0.07 mm.

Table 7.3 – Details of the meshes generated by `snappyHexMesh`.

Case	Overall number of cells	Faces per cell	Hexahedra	Prisms	Polyhedra
Column	30788676	5.99118	30491441	289180	8055
2 SMX	32116494	5.98616	31643179	442693	30614
5 SMX	33546609	5.97915	32818452	665286	62864
10 SMX	44270158	5.97275	43036842	1112582	120729

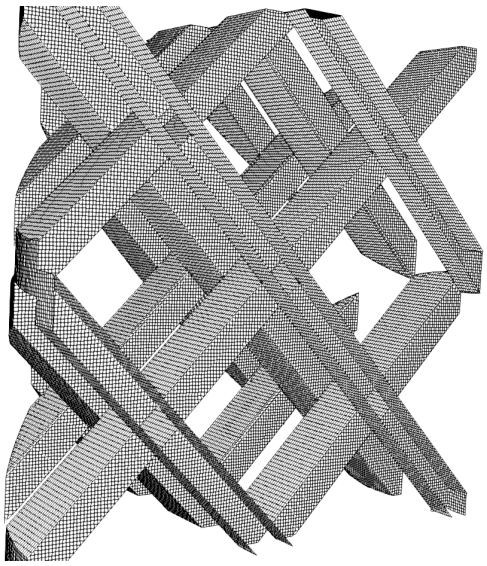

Figure 7.3 – Detailed view of the mesh obtained from `snappyHexMesh` on a section of a static mixer element.

Boundary layers were not added to the surface of the static mixer because they were not considered necessary due to the low value of the Reynolds number. Let's consider the Reynolds number based on the continuous phase, $Re_c = \rho_c U_c L/\mu_c$, where ρ_c is the density of the liquid, μ_c the viscosity of the liquid, U_c a characteristic velocity in the liquid and L a characteristic dimension of the static mixer. Transition to turbulence in the static mixer might occur in the liquid phase when the flow field around the bars experience some detachments. The liquid maximal velocity is of the order of bubble velocities, i.e. around 0.2 m/s. U_c can thus be chosen with this value. The bars dimension along the main flow axis are 1 mm. With these assumptions, Re_c can be estimated to 311.6. In the abundant literature on the transition to turbulence around a cylindrical obstacle, the Reynolds number at which transition to unsteady flow experiencing a Von Karman alley is roughly 300. For Reynolds in the range from 300 to 20 000, the flow becomes more and more turbulent, but the boundary layer remains laminar. This is the reason why prismatic boundary layers cells were not added to the wall surfaces.

Once the mesh was generated, its quality was checked by `meshQualityControls` subdictionary entries in the `snappyHexMeshDict`. `RenumberMesh` function was then run. This tool allowed us to renumber and restructure cell IDs. This procedure drastically decreased the bandwidth of the mesh and helped considerably the calculation OpenFOAM® User's guide [11].

7.3 Bubbles diameters and shapes

As presented in section 5.8, the `functionObject bubbleTracker` allowed to identify the grid cells belonging to the same bubble. Figure 7.4 shows an example of cells of the computational domain coloured by the values of the `VoFColor` field.

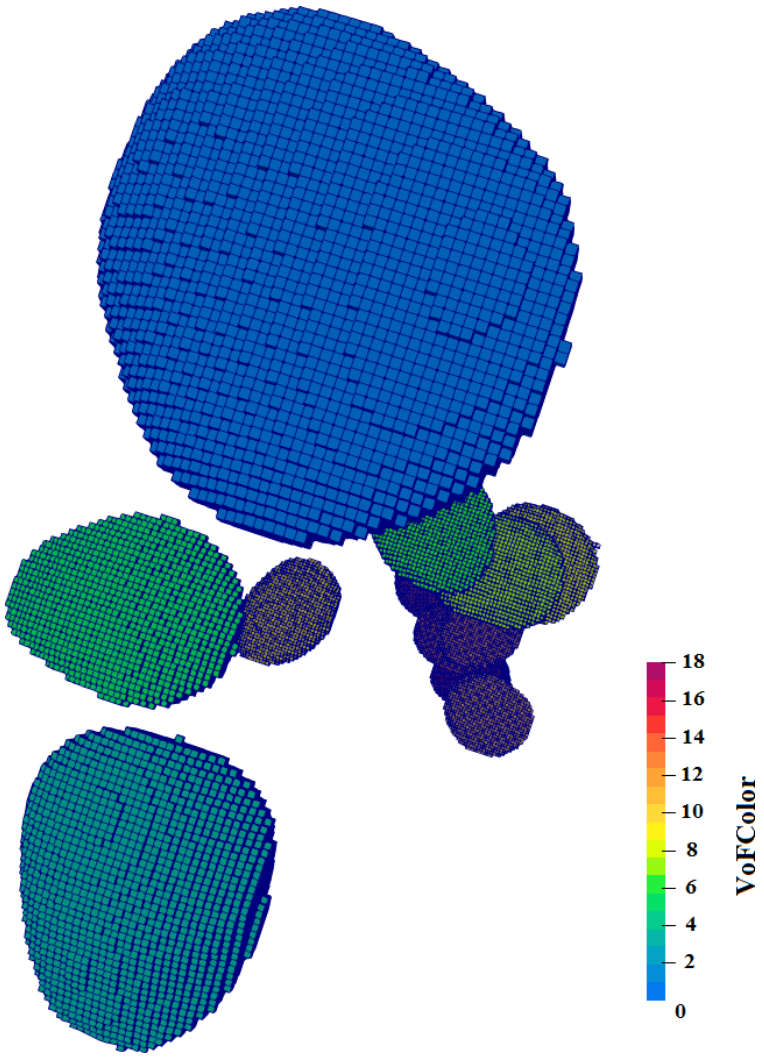

Figure 7.4 – Coloured bubbles according to their ID number. Output of the `FunctionObject bubbleTracker`.

Once the bubbles were isolated, a loop over the ID numbers allowed us to calculate the properties of each bubble. These properties were obtained as a function of time. The conservation of the bubble volumes over time was firstly verified. The collected data indicates a mean volume variation of less than 0.5 % from the moment bubble detached from the injector to the moment it reached the surface of the liquid (if the bubble does not break-up nor coalesce). This confirmed that the geometric reconstruction of the gas-liquid interface is conservative in the *isoAdvector* with *isoAlpha* algorithm.

The sphere equivalent diameter d_V of the bubble was estimated from its volume V_b as :

$$d_V = \sqrt[3]{\frac{6\,V_b}{\pi}} \tag{7.1}$$

Table 7.4 compares the results obtained from numerical simulations and experiments at the exit of the SMX. This table indicates that the average diameter of the bubbles between the inlet (line *Bubble column*) and outlet of the mixer varies slightly. This behaviour was also noted during the experiments (see Sauter mean diameter on figures 4.7, 4.8, 4.9).

Table 7.4 – Comparison of bubble mean diameters obtained through CFD simulations and experiments. Gas flow-rate $Q_G = 1$l/h. Nozzle diameter $d_n = 1$ mm.

Case	**Mean diameter experiments [mm]**	**Mean diameter CFD [mm]**
Bubble column	2.67	2.70
5 elements SMX	2.75	2.82
10 elements SMX	2.73	2.78

Even if the mean diameters remained almost unchanged, the distribution evolved substantially in the presence of the mixer. For example, a significant quantity of bubbles (about 19%) with a mean diameter of less than 2 mm was detected at the outlet of the 5 elements static mixer. These bubbles were generated by break-ups in the mixer. Similarly, a non-negligible amount of bubbles (about 8%) with an average diameter of 4 mm or higher was found. These bubbles were produced by coalescence phenomena. Numerical and experimental PDF at the 5 elements device exit are plotted in figure 7.5. It should be noted that the histogram of the numerical data was not yet converged, due to the insufficient simulated time. The CFD physical time (4 s) is an order of magnitude smaller than the experimental time.

For each bubble, an isosurface corresponding to the value of $\alpha = 0.5$ was generated by the `functionObject` `bubbleTracker`. These allowed us to calculate the area of the bubbles. An example of isosurface is shown in figure 7.6. The upper part highlights the isosurface, such as reconstructed by the `functionObject`. The lower part shows the ensemble of cells belonging to the bubble, which includes completely the isosurface.

From the bubble surfaces, several other important quantities could be calculated, like the specific surface area a [m^2/m^3], the surface-based equivalent diameter d_A (see equation 7.2 below) and the sphericity of the bubble ψ (see equation 5.27). The equivalent diameter d_A of a sphere having the same surface as the bubble's surface is computed by :

$$d_A = \sqrt{\frac{A_b}{\pi}} \tag{7.2}$$

The bubble' diameters, sphericity and surface are determined along with the centroid of mass of the bubble $\mathbf{x}_G$, computed with equation 5.24. The simultaneous knowledge of diameter and position of the bubbles allowed us to track the evolution of the mean diame-

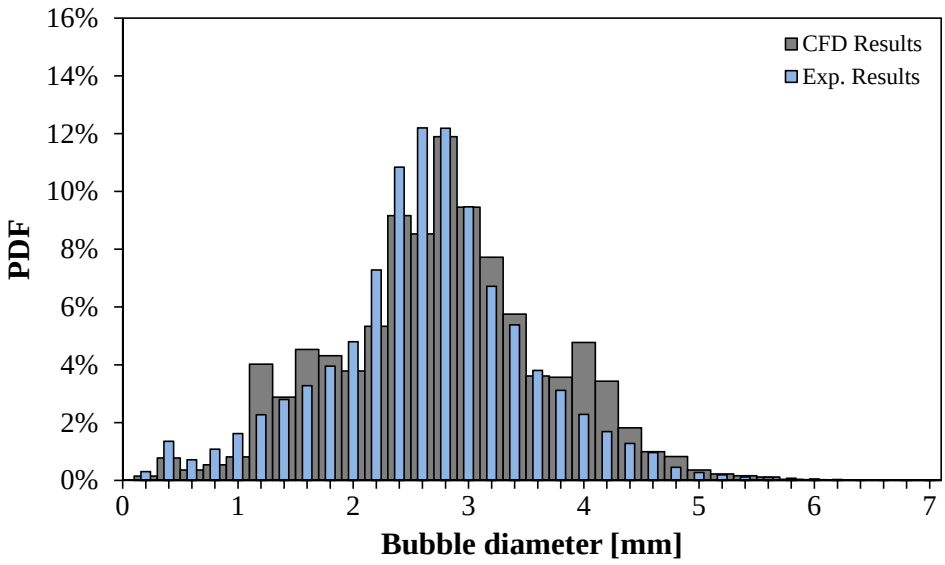

Figure 7.5 – Comparison of the equivalent diameter distributions measured at the 5 SMX elements exit : CFD vs experimental results. $Q_G = 1$ l/h. $d_n = 1$ mm.

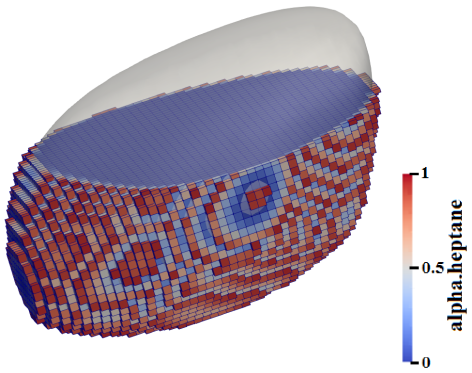

Figure 7.6 – Cells belonging to a bubble coloured with alpha heptane values (bottom half). Isosurface $\alpha = 0.5$ (top half, in grey).

ters according to their position. For example, figure 7.7 shows the evolution of the volume, sphericity and surface of a bubble rising in the 5-element SMX. As can be seen from figure 7.7, the volume of the bubble remains constant over time. This bubble did not undergo any coalescence nor breakup. The bubble sphericity and surface fluctuate considerably in the mixer region, highlighted in light blue. These fluctuations seem to have a periodic nature that could be linked to the structure of the SMX.

The specific surface a area represents the amount of bubble surface per unit volume. Values for a go from $13.75\,\mathrm{m^2/m^3}$ in the bubble column to $22.10\,\mathrm{m^2/m^3}$ in the 5-element mixer and finally to $26.90\,\mathrm{m^2/m^3}$ in the 10-element mixer. This increase is in accordance with the mass transfer coefficients k_La obtained in the experimental investigation (see section 4.6).

Bubbles appear rounder in the mixer : the average sphericity ψ varies from 0.89 in the column (0.86 in the experiments) to 0.92 (0.90 in the experiments) within the SMX mixer. The average sphericity reported is significantly influenced by the small diameter bubbles. These bubbles ($d_V < 1\,\mathrm{mm}$) tend to have a perfectly spherical shape (ψ about 1).

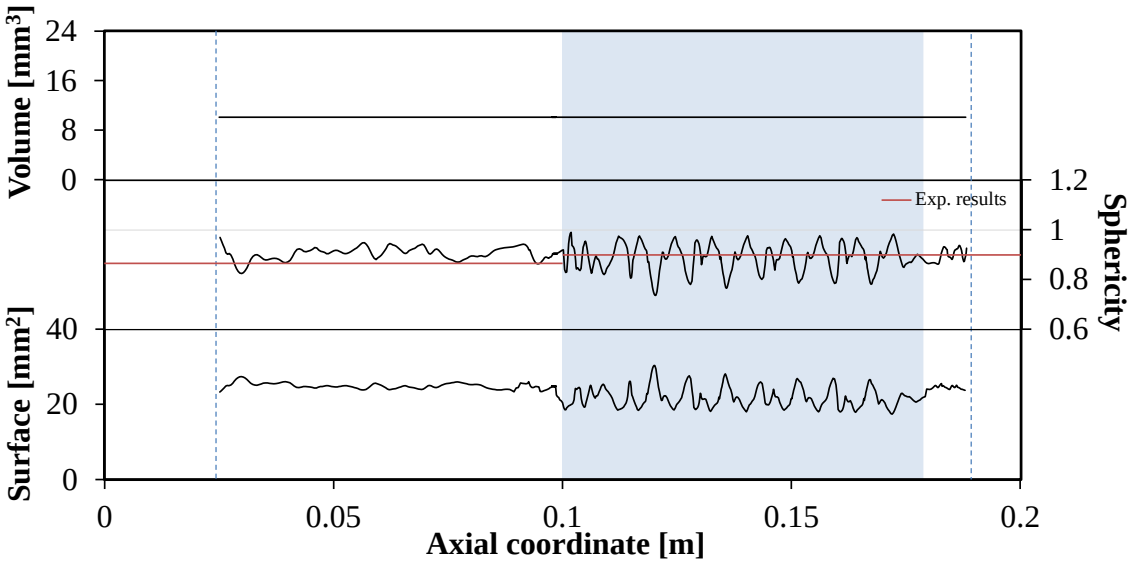

Figure 7.7 – Volume, sphericity and surface of a bubble rising in the 5-element SMX (highlighted in light blue). The two dashed lines in blue delimit the area investigated by the `functionObject`.

7.4 Bubbles velocities

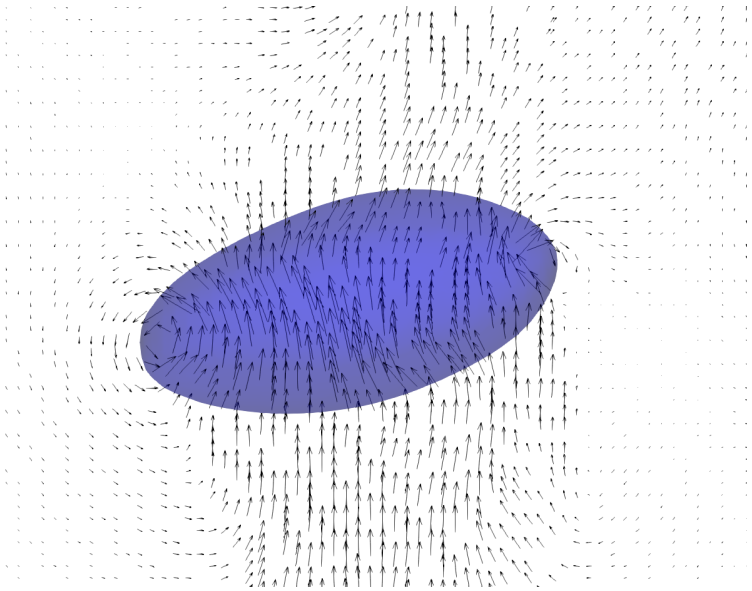

Figure 7.8 – 2D view of the velocity field in a plane passing through the centre of the bubble. Vectors scaled according to their magnitude.

As explained in section 5.3, in the VoF method, the velocity field is unique and shared between the liquid and gas phases. The bubble velocity $\mathbf{U}_b$ was estimated using equation 5.25. As an example, figure 7.8 portrays an instantaneous velocity field recorded in the plane passing through the centre of the blue bubble. The velocity field is continuous between the two phases. The most relevant velocities were observed in the wake (lower part) and in the upstream region of the bubble. This bubble was in the wake of a previous one.

As summarized on table 7.5, the average velocities obtained in numerical simulations were compared with those obtained from experiments (see section 4.2).

Table 7.5 – Comparison of bubble mean axial velocities obtained through CFD simulations and experiments. Gas flow-rate $Q_G = 1\,\mathrm{l/h}$. Nozzle diameter $d_n = 1$ mm.

Case	Mean axial velocity experiments [m/s]	Mean axial velocity CFD [m/s]
Bubble column	0.192	0.196
5 elements SMX	0.091	0.094
10 elements SMX	0.081	0.087

In the bubble column, bubbles instantaneous axial velocities ranged from 0.12 m/s to 0.27 m/s in the CFD. These limits are identical to those found during the experiments. Figure 7.9 shows a comparison between the experimental PDF and the numerical PDF of the bubble velocities in the bubble column. The two trends are fairly similar.

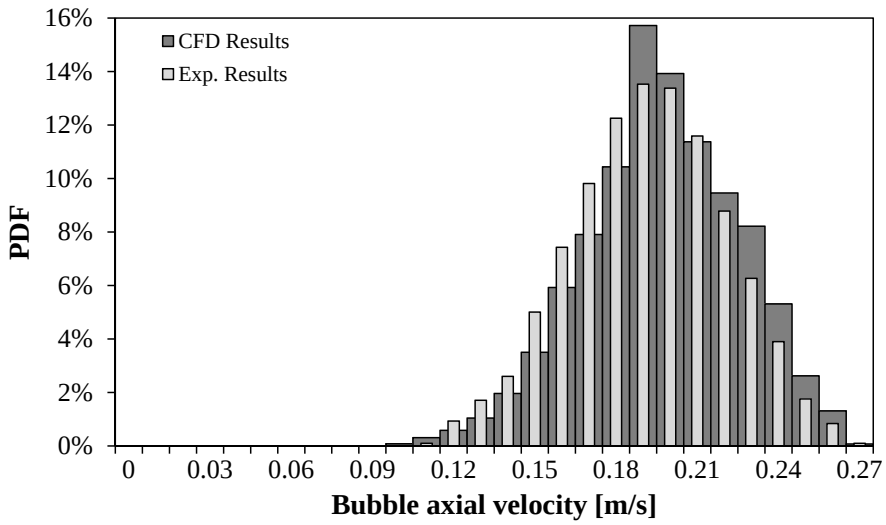

Figure 7.9 – PDF of axial velocity component u_y in the bubble column : CFD vs experimental results. Q_G =1 l/h, $d_n = 1$ mm.

Inside the SMX mixer, the bubbles instantaneous velocities were scattered over the range 0 to 0.24 m/s in the CFD. These limits are similar to those found in the experiments on figure 4.11. Less bubbles with near-zero velocities were observed during the simulations. Experimental results showed that about 5.8% of the bubbles had an axial velocity between 0 and 0.01 m/s in the 10 SMX and 4.48% in the 5 SMX. CFD results indicated a percentage close to 3.5% in the 10 elements SMX and 2.09% in the 5 elements SMX for the same velocity range. For instance, figure 7.10 shows the PDFs of the bubbles' axial velocities in the 5 elements mixer observed in the experiments and in the CFD. This graph reveals an excellent agreement between the experimental and CFD results, which further validates the numerical model.

A detailed analysis of the internal velocity field of the bubbles revealed the existence of velocity gradients. The core of the bubble is usually at higher velocity, due to recirculations within it. Then, the velocity is lower near the gas-liquid interface. This physical

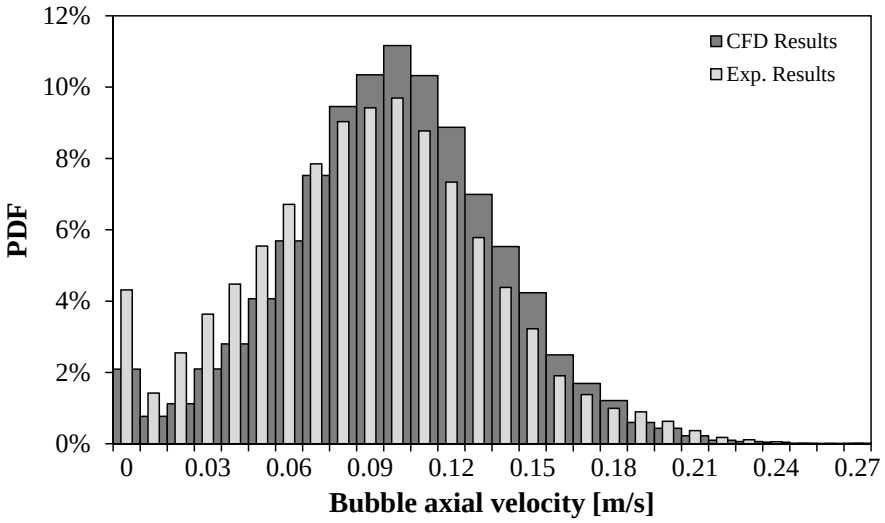

Figure 7.10 – PDF of axial velocity component u_y in the 5 SMX elements : CFD vs experimental results. Q_G =1 l/h, d_n = 1 mm.

phenomenon was already put in evidence in the literature by Li et al. (1999) [218], Seong-Su et al (2009) [219] and Alhendal et al. (2012) [220]. These recirculations inside bubbles may help the internal mixing of the gas phase, and thus improve mass transfer. As an example, figure 7.11 outlines the internal field inside a bubble.

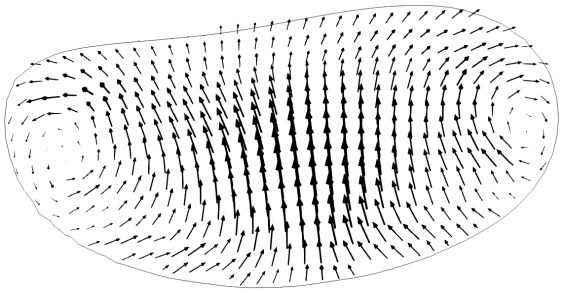

Figure 7.11 – Detailed view of the velocity field inside a bubble on a cutting plane running through the bubble axis.

As can be seen from table 7.5, the mixer decreases the bubbles' velocities, thus favouring coalescence and breakup events. Figure 7.12 shows the evolution of bubble A that rises in the mixer. Once inside the SMX, bubble A coalesces with bubble B, generating bubble A_B. This bubble with a larger diameter then breaks in the mixer and produces bubble C, which is much smaller (d_V = 0.98 mm). The coalescence between A and B led to a 60% increase of gas-liquid interface for bubble A. The bubble A_B has greater fluctuations of velocity and sphericity inside the mixer than the bubble shown in figure 7.7. This behaviour is mainly due to the deformations that the bubble has to endure in order to pass between the gap between the SMX bars.

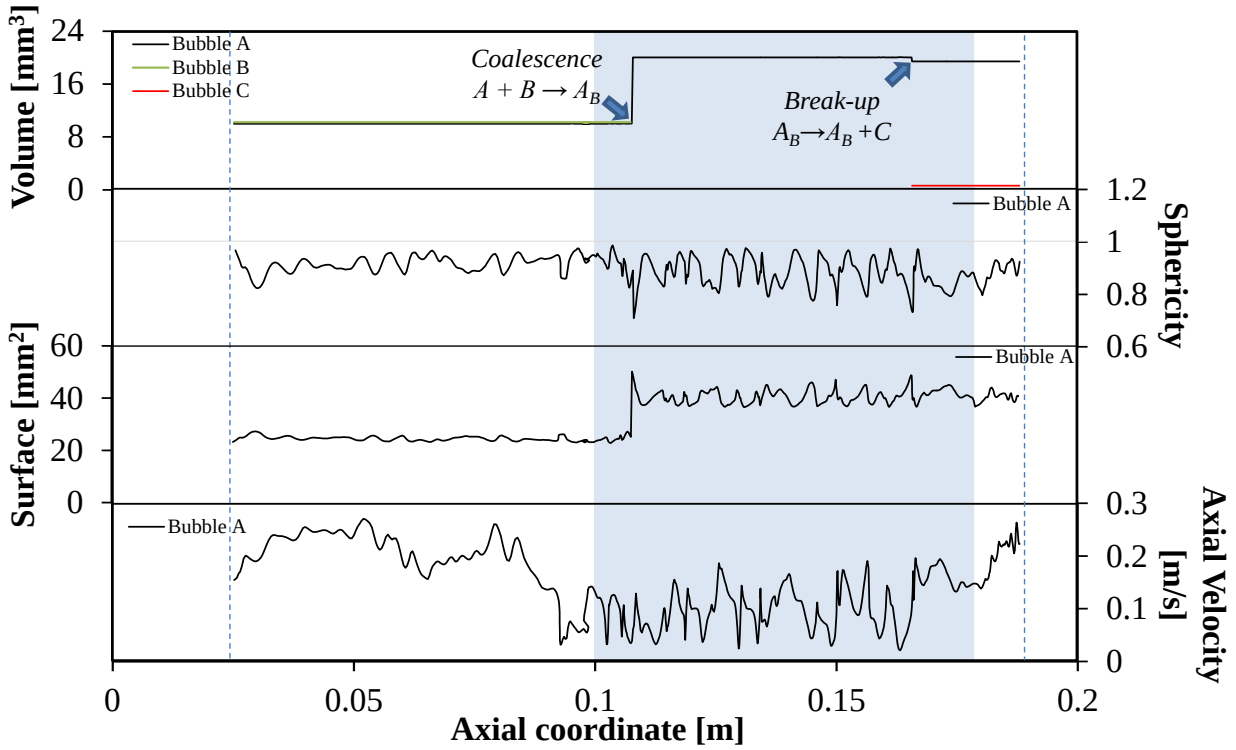

Figure 7.12 – Volume, sphericity, surface and velocity of the bubble A that rises in the 5-element SMX (highlighted in light blue). The two dashed lines in blue delimit the time interval investigated by the `functionObject`.

7.5 Preferential paths

Preferential paths were evaluated in two different ways in the simulations : firstly by analysing the centroid of mass of the bubble $\mathbf{x}_G$ and secondly, by averaging over time the values of the `alpha.heptane` field. Both methods produced qualitatively similar results.

Figures 7.13 and 7.14 report the mean volume fraction isosurface $\overline{\alpha} = 0.5$, coloured by the velocity magnitude $\overline{u}$. The overline symbol denotes the time-average operator. Figure 7.13 outlines the preferential paths of the bubbles identified inside the column without mixer. The preferential paths identified by the numerical simulations are qualitatively analogous to those encountered during experiments (see figure 4.13). The bubbles prefer to pass in the central part of the column. A higher velocity is usually related to a greater frequency of passage of the bubbles. In the vicinity of the injector and for the first centimetres after the detachment, the bubbles advanced on a rectilinear trajectory. Zigzag and/or spiral bubble paths were observed further away from the injector (see figure 7.15).

Numerical simulations highlighted that bubbles rise in the SMX by following preferential paths. As evidenced by the experimental results (see figure 4.14), these preferential paths are mainly close to the mixer-inclined bars. Furthermore, zones with a null probability (about 0.8%) of finding bubbles were evidenced. Down-flows were confirmed in these zones by the averaged velocity field (see section 7.7 below and figure 7.21). The results of the 2 elements and 5 elements SMX are illustrated in figure 7.14.

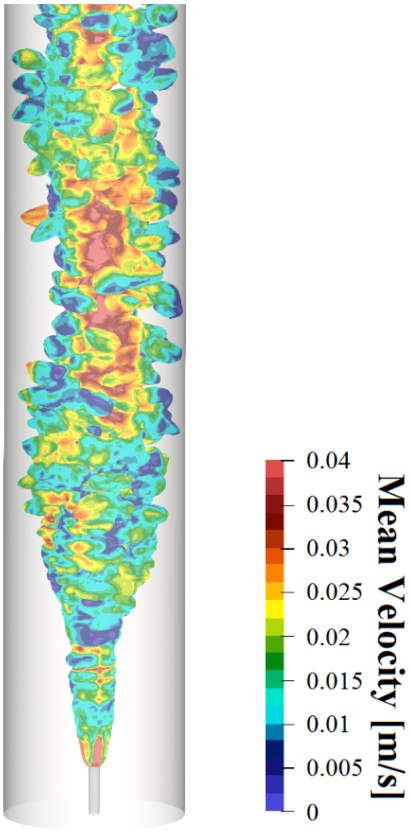

Figure 7.13 – Preferential paths in the bubbles column. $d_n = 1$ mm, $Q_G = 1\,\mathrm{l/h}$. Isosurface $\overline{\alpha} = 0.5$ coloured by the magnitude of mean velocity.

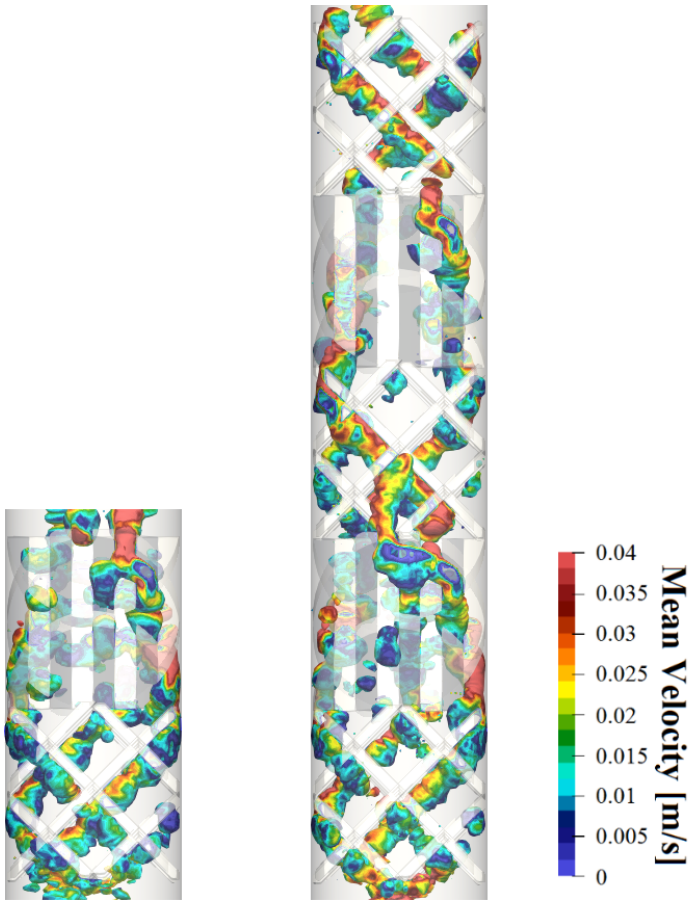

Figure 7.14 – Preferential paths inside the 2 elements (l.h.s.) and 5 elements (r.h.s.) SMX. $d_n = 1$ mm, $Q_G = 1\,\mathrm{l/h}$. Isosurface $\overline{\alpha} = 0.5$ coloured by the magnitude of mean velocity.

The analysis of the centroid of mass of the bubble $\mathbf{x}_G$ confirmed the results obtained from the average of `alpha.heptane` fields. For instance, figure 7.15 depicts the trajectories of the bubbles in the column containing the 5 elements SMX.

Figure 7.15 – Trajectories of bubbles registered in the bubbles column with the 5 elements SMX fed by $d_n = 1$ mm. Gas flow-rate $Q_G = 1\,\mathrm{l/h}$. Coloured according to bubble ID.

7.6 Gas hold-up

Gas hold-up values were evaluated through numerical simulations. Both bubble and liquid volumes were recorded during simulations. The gas hold-up ϵ_G was then estimated as the ratio between the volume of gas $V_G = \sum_{ID=1}^{N} V_{b,ID}$ and the total volume of the system $V_G + V_L$.

The increase in the level of n-heptane was also evident from the results produced by the simulations. This allowed us to double check the values obtained from the `functionObject bubbleTracker`. Figure 7.16 shows the increase of the liquid level in the column containing the 5 elements SMX. The gas hold-up was constantly monitored during the simulations. The graph shown in figure 7.17 describes a typical history of this parameter. Only 1 point out of 50 was reported in order to make the plot of figure 7.17 clearer. The graph reported in figure 7.17 allowed us to identify two distinct phases in the hold-up curve. An initial phase in which the amount of gas retained in the liquid phase increases linearly. This is due to the constant flow rate imposed at inlet and to the filling of the computational volume with bubbles. Then, a second phase where the hold-up oscillates around a steady state value. The two distinct phases were fitted with linear interpolations. The flat interpolation line allowed us to estimate the mean hold-up value.

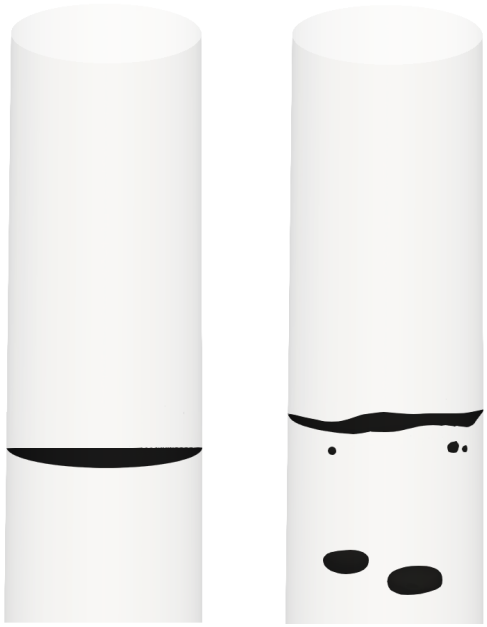

Figure 7.16 – Liquid level in the column containing the 5 elements SMX without (l.h.s.) and with gas flow (r.h.s). Gas flow-rate $Q_G = 1$l/h. Nozzle diameter $d_n = 1$ mm.

Table 7.6 shows a comparison of the results obtained by numerical simulations and experiments. The values obtained exhibit a satisfactory agreement between the experimental and computational results. The maximum deviation encountered is less than 10%.

Table 7.6 – Comparison of hold-up values obtained through CFD simulations and experiments. Gas flow-rate $Q_G = 1$l/h Nozzle diameter $d_n = 1$mm.

Case	**Hold-up experiments**	**Hold-up CFD**
Bubble column	0.52	0.57
2 elements SMX	0.78	0.80
5 elements SMX	1.09	1.06
10 elements SMX	1.31	1.23

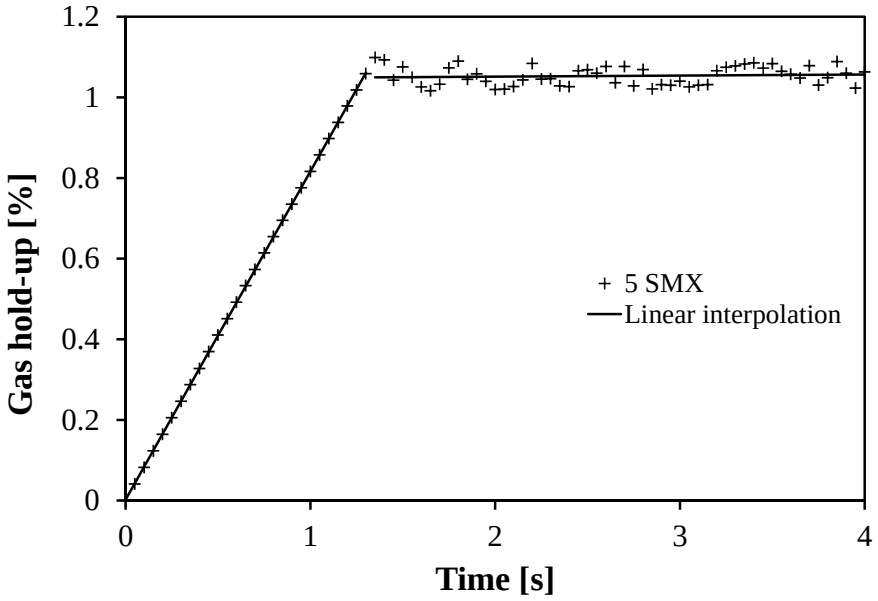

Figure 7.17 – Gas hold-up versus time in the 5 elements SMX. Gas flow-rate $Q_G = 1$ l/h. Nozzle diameter $d_n = 1$ mm.

7.7 Velocity fields

Several authors compared the velocity fields obtained by PIV against CFD in order to validate the computational model, like for example Ranade et al. (2001) [221], Khopkar et al. (2003) [222] and (2004) [223], Silva et al. (2008) [224], Feng et al. (2009) [225], Mendoza et al. (2012) [226]. More references can be found in the literature.

The velocity fields in the liquid phase were investigated in the column with and without the SMX. The velocity component u_y is along the upward vertical direction, i.e. along the axis of the column. The other components u_x and u_z are along planes perpendicular to the axis. The same coordinate system was used in the experiments.

As depicted in figure 7.18, higher average and instantaneous velocities were observed inside the first element. The velocities decrease as we go up along the mixer. Preferential paths were highlighted by dark red regions corresponding to higher axial velocities. At the outlet of the mixer, the bubbles prefer to exit from the side of the column. This phenomenon was also observed in experiments (see figure 4.14). Strong similarities between numerical and experimental average axial velocity fields can be seen from the centre and right images of figure 7.18.

Figure 7.19 (l.h.s.) illustrates a detailed view of the average axial velocity field obtained at the 10 elements SMX inlet with the PIV. The field on the right shows the axial velocity field of the same region obtained through the numerical simulations. The results of the numerical simulations reflect those obtained experimentally by HFPIV as reported in section 4.5, even when the mixer was used.

Numerical and experimental velocity fields are qualitatively equivalent. Furthermore, the average and instantaneous velocities varied in the same interval in both experiments and CFD simulations (see figures 7.18 and 7.19). About 55% of the velocities in the mixer ranged from

-0.02 m/s to 0.02 m/s.

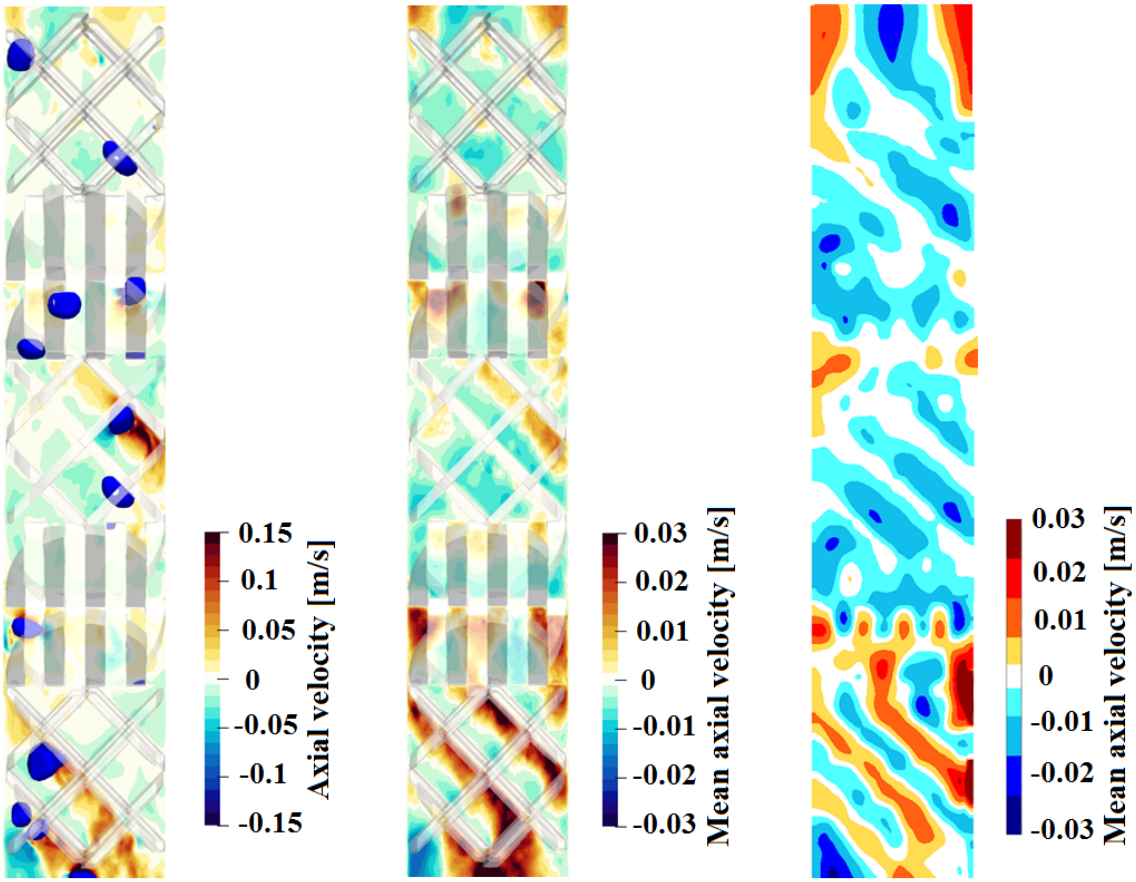

Figure 7.18 – Axial velocity field found in the 5 elements SMX fed by $d_n = 1$ mm. $Q_G = 1$l/h. Left and middle : scalar map of the axial velocity field and of the average axial velocity profile (from CFD). On the right, average velocity obtained through by HFPIV.

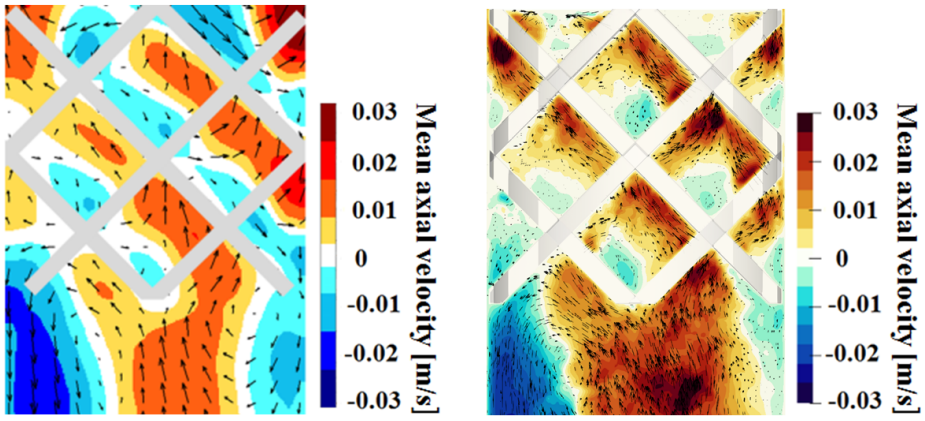

Figure 7.19 – Detailed view of the first element of the 10 elements SMX : experimental results (l.h.s.) and numerical (r.h.s.) results. Cutting plane (passing through the centre of the element) depicting the values of the average axial velocity. $d_n = 1$ mm. $Q_G = 1$l/h

For the column without the mixer, the CFD vertical velocity showed an up-flow in proximity of the axis while a down-flow was generated near the column walls. This result is in

agreement with the experiments. Besides, both the instantaneous and averaged flow fields confirmed the same trend. Figure 7.20 illustrates the mean axial velocity for several cross-sections obtained by the numerical simulations.

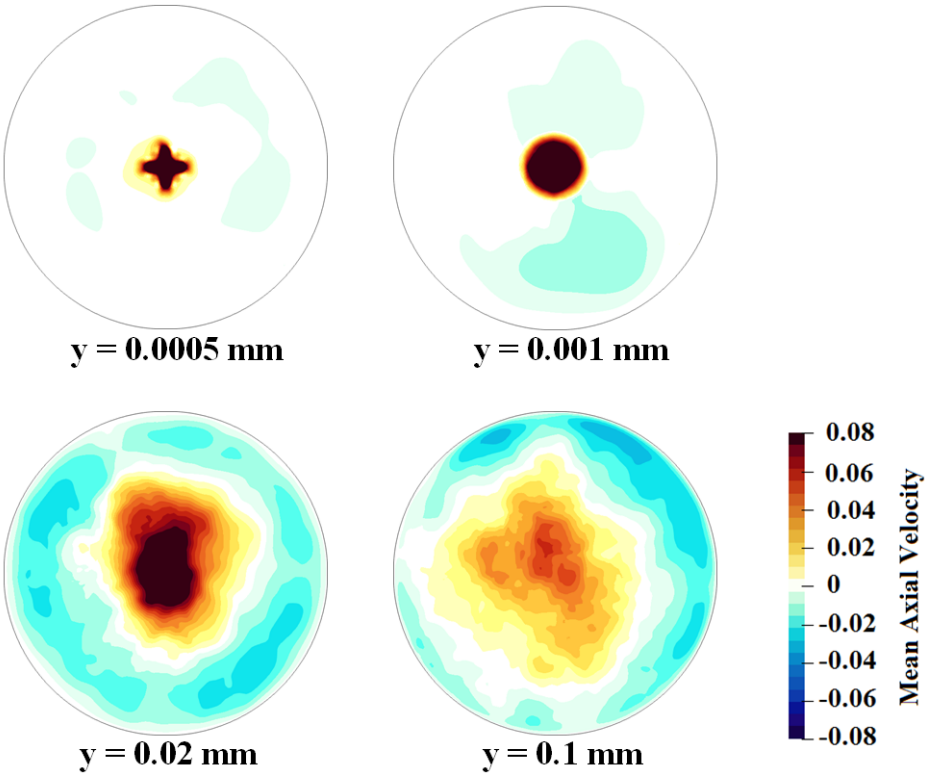

Figure 7.20 – Detailed view of the mean axial velocity field found in 4 horizontal sections of the column without static mixer fed by $d_n = 1$ mm. Gas flow-rate $Q_G = 1\,\mathrm{l/h}$

The first cross section of figure 7.20 is located near the injector. An important up-flow is localized at the centre of the column. The cross shape in this first section is due to a mesh effect explained by bubble detachments occurring preferably along grid lines and not along diagonal directions. In planes further away from the injector, the up-flow zone extends radially. The second axial position shows a rather axisymmetric up-flow field.

A significant down-flow is visible near the walls. In the last image (corresponding to $y = 0.1\,\mathrm{mm}$), the up-flow region is even more spread along the radial direction. It should however be noted that after a physical simulation time of 4 s, the mean velocity statistics are not enough converged to obtain fully axisymmetric fields, as can be seen on the bottom line of figure 7.20. The high computational cost of the VoF method did not allow us to perform sufficiently long simulation times.

The numerical simulations confirmed that the bubbles rise in the wake left by the previous ones. This behaviour led to preferential paths in bubble column and SMX static mixer (see also section 7.5). For instance, these paths can be clearly distinguished from figure 7.21, on which several axial sections of the 5 elements SMX are portrayed. In the section 1 of figure 7.21, it can be clearly seen how the bubbles enter the static mixer from its central zone.

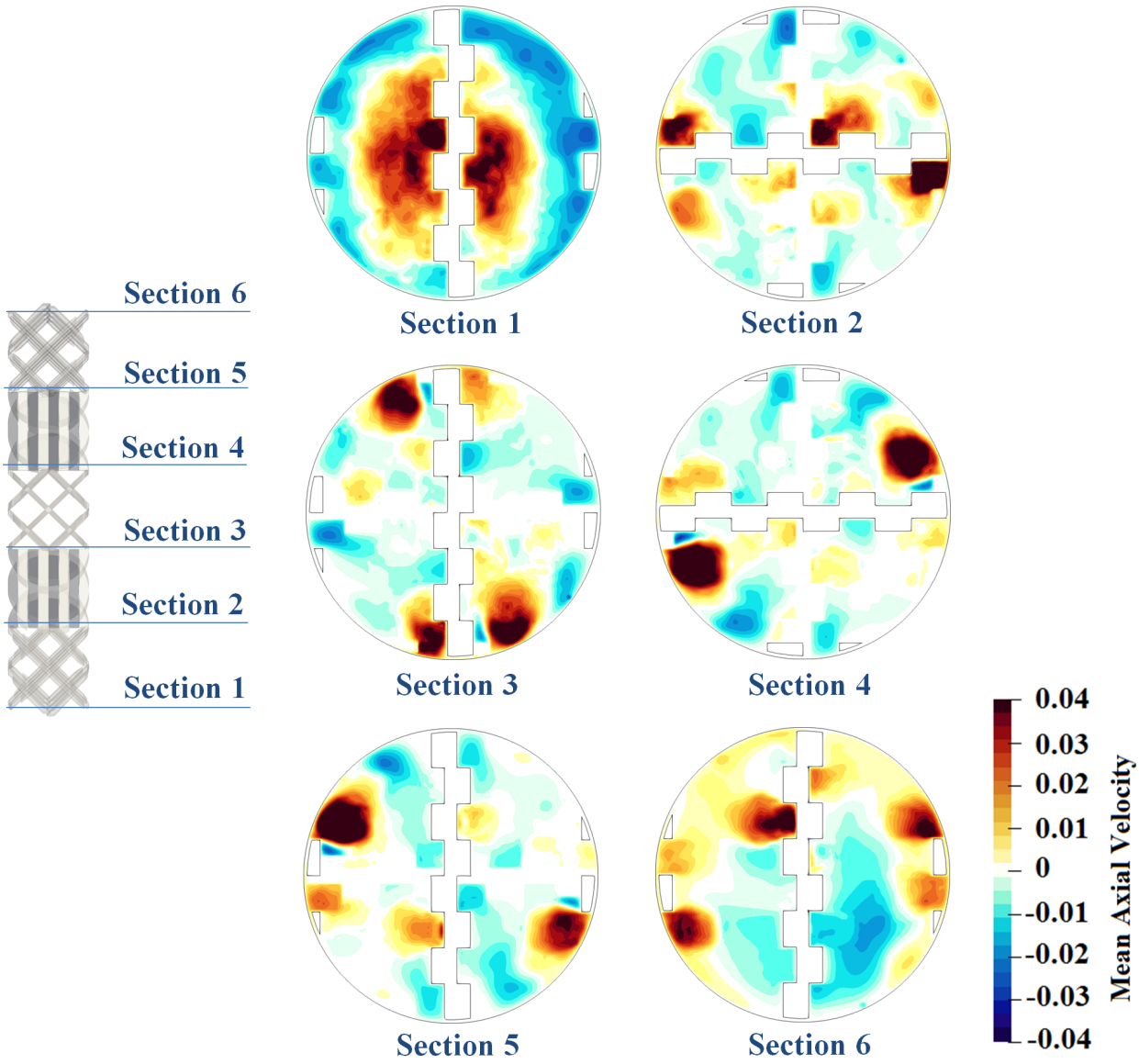

Figure 7.21 – Detailed view of the mean axial velocity field found in 6 horizontal sections of the 5 elements SMX fed by $d_n = 1$ mm. Gas flow-rate $Q_G = 1\,\mathrm{l/h}$

In all simulations, the liquid is stagnant, so that the mean liquid velocity $\overline{U}_L$ is null in a cross section. The inlet gas flow rate Q_G is kept constant in the nozzle. Supposing that the gas flow rate is uniformly spread over a column cross section, we can estimate an average gas velocity $\overline{U}_G$ in the column, downstream the nozzle, by writing $Q_G = \overline{U}_G \pi D_c^2/4$. For $Q_G = 1\,\mathrm{l/h}$, this gives $\overline{U}_G = 1.35 \times 10^{-3}\,\mathrm{m/s}$. Similarly, the average gas volume fraction over a cross section of the column can be estimated from the ratio of surfaces, i.e. $\overline{\alpha}_G = (d_n/D_c)^2$, where d_n is the injector diameter (here 1 mm). The mixture average velocity, such as computed by the VoF model, is then $\overline{U} = \overline{\alpha}_L \overline{U}_L + (1 - \overline{\alpha}_L)\overline{U}_G$. With $\overline{U}_L = 0$ and $\overline{\alpha}_L = 1 - \overline{\alpha}_G$, the mixture average velocity on a section takes the value $\overline{U} = 5.13 \times 10^{-6}\,\mathrm{m/s}$. The flow rate through a disk cross section of the column was computed through an integral of the velocity field $\mathbf{u}$, similar to equation 4.2. The value found was about $5 \times 10^{-6}\,\mathrm{m/s}$.

7.8 Chapter Summary

In the present chapter, we illustrated the main results of 3D simulations of the Sulzer SMX^{TM} static mixer. The mesh generation process with `snappyHexMesh` was detailed as well. A `functionObject` called `bubbleTracker` was developed in order to have an inlined post-processing of the results. This function revealed to be an efficient tool to collect the bubbles properties during the computations.

Shapes, sizes, trajectories and velocities of the bubbles were then calculated numerically and then compared against experimental results. This comparison brought new insight into the flow pattern in a SMX^{TM} static mixer. Bubbles velocities and diameters detected during the experiments were confirmed by numerical simulations. Gas hold-up values returned by CFD were comparable to the experimental values. Preferential paths inside the static mixer were also confirmed by the simulations. Furthermore, thanks to numerical simulation, the specific surface area a was estimated. The results agreed with k_La experimental measures.

Chapter 8

Conclusion

The main goal of the present work was to characterize the gas-liquid hydrodynamics and mass transfers in Sulzer SMX^{TM} static mixers with different lengths. The study aimed at analysing organic liquid phases, namely normal-heptane. Experiments with aqueous systems were also performed to obtain preliminary results and refine the techniques of investigation. The experimental investigation was performed by nitrogen bubbling in stagnant liquid under various operating conditions : different gas flow rates, different mixer lengths, different fluids (water, water + SDS and normal-heptane) and two nozzle sizes.

The bubbles' sizes, shapes, velocities and trajectories were quantified using several experimental techniques, namely PIV, HFPIV and Back Light Shadowgraph. An image post-processing was implemented to estimate the mean Sauter diameter of the bubbles at inlet and outlet of the SMX mixers. The capability to estimate the real sizes, the shapes and velocities of bubbles was verified by conducting several comparisons with empirical correlations and data reported in the literature. The liquid velocities were measured by the PIV technique for the first time in a static mixer thanks to transparent 3D printing. The obtained results revealed that the SMX^{TM} substantially increased the gas hold-up and the residence time of bubbles for all operating conditions. The higher hold-up values achieved in pure water systems were mainly due to the important amount of bubbles stuck on the static mixer surface. By adding the surfactant SDS, the amount of bubbles that were trapped decreased and thus also the gas hold-up. An increase of coalescence and breakup phenomena was observed at high hold-up value under the highest gas flow rate in both liquid phases. The second major finding was the existence of preferential paths inside the mixer. This could potentially affect the mass transfer efficiency throughout the device. In addition, the detailed analysis carried out on the nitrogen-heptane system revealed important insights. For instance, this study suggested that the 15 elements SMX was long enough to ensure a dynamic equilibrium between the coalescence and break-up of bubbles flowing through the device. Furthermore, the static mixer exhibited an efficient redistribution of bubble sizes and positions passing across the mixer. Although the coalescence phenomena in the mixer can lead to large bubbles, a considerable percentage of small-scale bubbles (diameter smaller than 0.5 mm) was detected.

The oxygen transfer performance of the SMX static mixer in air/water mixture was assessed by measures with an oxygen probe. The mass transfer coefficient to the interfacial area k_La was determined. The k_La proved to be twice larger with the mixer than without. Furthermore, the use of a metallic mixer improved the dispersion and thus also the mass

transfer visibly due to the wetting phenomena between the liquid and the mixer surface.

The effect of a mean liquid flow on the bubble shape, velocity, diameter and gas hold-up was evaluated. Different configurations were examined to extend the validity of the results. The tests were performed with heptane flow in two directions, i.e. in co-current and counter-current with respect to the gas. The effect of the liquid flow appeared to be negligible on the bubble size distributions in both configurations. In fact, the main properties (bubbles' velocities, hold-up, diameter distribution) of the system at the outlet of the SMX mixer remained unchanged.

3D Volume-of-Fluid numerical simulations of gas-liquid flows in the mixer were then performed with OpenFOAM®. These 3D simulations focused on the behaviour of the SMX in organic system at low gas flow rate (Q_G=1 l/h). The geometry used in the laboratory was faithfully reproduced in order to allow comparisons with the experiments.

Elementary test cases (Hysing benchmark and stagnant bubble) were firstly run in order to evaluate the numerical methods and schemes, in particular the best settings for the simulations like grid size and solvers.

In a second step, 3D VoF simulations of the Sulzer SMX™ static mixers were realized. `snappyHexMesh` was used to generate the meshes. *isoAdvector* with *isoAlpha* was used in all simulations. A home-made `functionObject` called `bubbleTracker` was developed. This function revealed to be an efficient tool to collect the bubbles properties during the computations. Shapes, sizes, trajectories and velocities of the bubbles were then examined in order to validate the numerical model against experimental results.

The comparison of the numerical and experimental results brought new insight into the flow pattern in a SMX™ static mixer. The average velocities and diameters of the bubbles found during the experiments were confirmed by numerical simulations. The gas hold-up values were comparable to the experimental values. Preferential paths, detected in the mixer by the experiments, were also confirmed by the simulations. The specific surface area a was estimated through the simulations. Using the 10 elements mixer, the specific surface area a is doubled compared to the bubble column. This result is in line with k_La experimental measures.

In order to extend the present results to further studies, it is recommended to use the collected data to develop one-dimensional models that would allow process engineering dimensioning of devices containing gas-liquid static mixers. Further investigation is advised to explore the effects of material and roughness of the SMX mixer. In addition, numerical simulations with the most accurate and precise solver *isoAdvector* with *PLIC-RDF* are strongly encouraged, since it reduces drastically VoF spurious currents.

Bibliography

[1] J. A. Sanchez Perez, E. M. Rodriguez Porcel, J. L. Casas Lopez, J. M. Fernandez Sevilla, and Y. Chisti, "Shear rate in stirred tank and bubble column bioreactors," *Chemical Engineering Journal*, vol. 124, no. 1-3, pp. 1–5, 2006. Quoted at pages V and 1.

[2] R. K. Thakur, C. Vial, K. Nigam, E. B. Nauman, and G. Djelveh, "Static mixers in the process industries—a review," *Chemical Engineering Research and Design*, vol. 81, no. 7, pp. 787–826, 2003. Quoted at pages V, XXVIII, XXXVII, 1, 2, 5, 10, 11, 12, 14, 15, 20, 23, 24, 25, 26, and 27.

[3] A. Heyouni, M. Roustan, and Z. Do-Quang, "Hydrodynamics and mass transfer in gas–liquid flow through static mixers," *Chemical Engineering Science*, vol. 57, no. 16, pp. 3325–3333, 2002. Quoted at pages V and 2.

[4] H. P. Grace, "Dispersion phenomena in high viscosity immiscible fluid systems and application of static mixers as dispersion devices in such systems," *Chemical Engineering Communications*, vol. 14, no. 3-6, pp. 225–277, 1982. Quoted at pages V, XXVIII, 2, 5, 11, 17, 18, 19, 20, 21, and 22.

[5] H. Z. Li, C. Fasol, and L. Choplin, "Hydrodynamics and heat transfer of rheologically complex fluids in a sulzer smx static mixer," *Chemical Reaction Engineering : From Fundamentals to Commercial Plants and Products*, vol. 51, no. 10, pp. 1947–1955, 1996. Quoted at pages V, XXIX, 2, 5, 35, 36, and 37.

[6] J. Legrand, P. Morançais, and G. Carnelle, "Liquid-liquid dispersion in an smx-sulzer static mixer," *Chemical Engineering Research and Design*, vol. 79, no. 8, pp. 949–956, 2001. Quoted at pages V, 2, 26, 27, and 30.

[7] L. Fradette, H.-Z. Li, L. Choplin, and P. Tanguy, "Gas/liquid dispersions with a smx static mixer in the laminar regime," *Chemical Engineering Science*, vol. 61, no. 11, pp. 3506–3518, 2006. Quoted at pages V, XXVIII, XXXVII, 2, 10, 11, 17, 20, 21, 22, 23, 30, and 31.

[8] C. M. R. Madhuranthakam, Q. Pan, and G. L. Rempel, "Hydrodynamics in sulzer smx static mixer with air/water system," *Industrial & Engineering Chemistry Research*, vol. 48, no. 2, pp. 719–726, 2009. Quoted at pages V, XXIX, 2, 17, 37, and 38.

[9] M. Scala, L. Gamet, L.-M. Malbec, and H.-Z. Li, "Hydrodynamics of gas-liquid dispersion in transparent sulzer static mixers smxtm," *Chemical Engineering Science*, vol. 213, p. 115398, 2020. Quoted at pages VIII, XXVII, XXX, 54, and 77.

[10] M. Sathe, J., I. H. Thaker, T. E. Strand, and J. B. Joshi, "Advanced piv/lif and shadowgraphy system to visualize flow structure in two-phase bub-

bly flows," *Chemical Engineering Science*, vol. 65, no. 8, pp. 2431–2442, 2010. Quoted at pages IX, 3, 46, and 65.

[11] *OpenFOAM, The Open Source CFD Toolbox, User Guide. Version v1806*, ESI. [Online]. Available : http://www.openfoam.com/documentation/user-guide Quoted at pages X, 106, 115, 120, 123, 141, 142, and 143.

[12] A. Nienow, *Mass Transfer and Mixing Across the Scales in Animal Cell Culture*, 11 2015, p. 137 – 169. Quoted at pages XIV and 98.

[13] S. Akbulut, Z. Kurt Albayrak, and S. Arasan, "Surfactant modified clays consistency limits and contact angles," *Earth Sciences Research Journal*, vol. 16, pp. 95–101, 12 2012. Quoted at pages XXVII and 7.

[14] P. Di Marco, "Birth, life and death of gas bubbles rising in a stagnant liquid," *International Journal of Heat and Technology*, vol. 23, 2005. Quoted at pages XXVII, 7, and 8.

[15] R. P. website, *www.reactor-physics.com*. Quoted at pages XXVII and 9.

[16] Y. Cengel and J. Cimbala, *Fluid Mechanics : Fundamentals and Applications*, 01 2006. Quoted at pages XXVII and 10.

[17] C. Leonard, J.-H. Ferrasse, O. Boutin, L. Sébastien, and A. Viand, "Bubble column reactors for high pressures and high temperatures operation," *Chemical Engineering Research and Design*, vol. 100, 05 2015. Quoted at pages XXVII, XXVIII, 12, 13, and 14.

[18] StaMixCo, "Static mixer products & technology." Quoted at pages XXVIII and 15.

[19] M. Scala, "Vof methods for the simulation of two phase flows : Application to the smx static mixer," Solaize-France et École Polytechnique de Turin, 2016. Quoted at pages XXVIII and 16.

[20] N. Ioannou, H. Liu, and Y. H. Zhang, "Droplet dynamics in confinement," *Journal of Computational Science*, vol. 17, pp. 463–474, 2016. Quoted at pages XXVIII and 17.

[21] H. Meijer, M. Singh, and P. Anderson, "On the performance of static mixers : A quantitative comparison," *Progress in Polymer Science*, vol. 37, pp. 1333–1349, 10 2012. Quoted at pages XXVIII, 2, 17, 29, and 30.

[22] H. Z. Li, C. Fasol, and L. Choplin, "Pressure drop of newtonian and non-newtonian fluids across a sulzer smx static mixer," *Chemical Engineering Research and Design*, vol. 75, no. 8, pp. 792–796, 1997. Quoted at pages XXIX, 31, 32, 33, 34, and 100.

[23] J. M. Zalc, E. S. Szalai, and F. J. Muzzio, "Mixing dynamics in the smx static mixer as a function of injection location and flow ratio," *Polymer Engineering Science*, vol. 43, no. 4, pp. 875–890, 2003. Quoted at pages XXIX, 39, and 40.

[24] D. Rauline, P. A. Tanguy, J.-M. Le Blevec, and J. Bousquet, "Numerical investigation of the performance of several static mixers," *The canadian journal of chemical engineering*, vol. 76, June 1998. Quoted at pages XXIX, 23, 39, 40, and 41.

[25] D. Rauline, J.-M. Le Blevec, J. Bousquet, and P. A. Tanguy, "A comparative assessment of the performance of the kenics and smx static mixers," *Chemical Engineering Research and Design*, vol. 78, no. 3, pp. 389–396, 2000. Quoted at pages XXIX, 2, 41, and 42.

[26] S. Hirschberg, R. Koubek, F. Moser, and J. Schock, "An improvement of the sulzer smx static mixer significantly reducing the pressure drop," *Chemical Engineering Research Design*, vol. 87, pp. 14–17, 05 2009. Quoted at pages XXIX, 5, 42, and 43.

[27] M. Heniche, P. Tanguy, M. F. Reeder, and J. Fasano, "Numerical investigation of blade shape in static mixing," *AIChE Journal*, vol. 51, pp. 44 – 58, 01 2005. Quoted at pages XXIX, 43, and 44.

[28] S. Liu, A. N. Hrymak, and P. E. Wood, "Drop breakup in an smx static mixer in laminar flow," *The canadian journal of chemical engineering*, vol. 83, 2005. Quoted at pages XXX, 17, 44, and 45.

[29] D. Laupsien, A. Cockx, and A. Line, "Bubble plume oscillations in viscous fluids," *Chemical Engineering & Technology*, 2017. Quoted at pages XXX, 3, 46, and 59.

[30] M. Raffel, C. E. Willert, F. Scarano, C. J. Kahler, S. T. Wereley, and J. Kompenhans, *Particle Image Velocimetry : A Practical Guide*. Springer International Publishing, 2007. Quoted at pages XXX and 47.

[31] Z. Liu and Y. Zheng, "Piv study of bubble rising behavior," *Powder Technology*, vol. 168, no. 1, pp. 10–20, 2006. Quoted at pages XXX, 48, and 49.

[32] R. C. Chen and L. S. Fan, "Particle image velocimetry for characterizing the flow structure in three-dimensional gas-liquid-solid fluidized beds," *Chemical Engineering Science*, vol. 47, no. 13/14, pp. pp. 3615–3622, 1992. Quoted at pages XXX, 3, 47, 48, and 50.

[33] N. Mokhtar, A. Abas, N. Razak, M. Najib Abdul Hamid, and L. Teong Soon, "Effect of different stent configurations using lattice boltzmann method and particles image velocimetry on artery bifurcation aneurysm problem," *Journal of Theoretical Biology*, vol. 433, 09 2017. Quoted at pages XXXI and 71.

[34] Wikipedia contributors, *Wikipedia, The Free Encyclopedia*, 2019, [Online; accessed 10-08-2019]. [Online]. Available : https://en.wikipedia.org Quoted at pages XXXIII, 105, and 106.

[35] S. Mirjalili, S. Jain, and M. Dodd, "Interface-capturing methods for two-phase flows : An overview and recent developments," *Center for Turbulence Research - Annual research brief*, pp. 117–135, 12 2017. Quoted at pages XXXIII and 107.

[36] J. Roenby, H. Bredmose, and H. Jasak, "A computational method for sharp interface advection," *Royal Society Open Science*, vol. 3, no. 11, 2016. Quoted at pages XXXIII, 107, 111, 112, 113, 114, 115, and 116.

[37] H. Scheufler and J. Roenby, "Accurate and efficient surface reconstruction from volume fraction data on general meshes," *Journal of Computational Physics*, vol. 383, pp. 1 – 23, 2019. [Online]. Available : http://www.sciencedirect.com/science/article/pii/S0021999119300269 Quoted at pages XXXIII, 111, 112, 113, 114, and 115.

[38] F. Theron, N. Le Sauze, and A. Ricard, "Turbulent liquid-liquid dispersion in sulzer smx mixer," *Industrial Engineering Chemistry Research*, vol. 49, no. 2, pp. 623–632, 2010. Quoted at pages XXXVII, 11, 16, 26, 27, 28, 30, 33, 35, and 54.

[39] D. M. Hobbs and F. J. Muzzio, "Optimization of a static mixer using dynamical systems techniques," *Chemical Engineering Science*, vol. 53, no. 18, pp. 3199–3213, 1998. Quoted on page 2.

[40] O. Byrde and M. Sawley, "Optimization of a kenics static mixer for non-creeping flow conditions," *Chemical Engineering Journal*, vol. 72, no. 2, pp. 163–169, 1999. Quoted on page 2.

[41] C. U. Ugwu, J. C. Ogbonna, and H. Tanaka, "Improvement of mass transfer characteristics and productivities of inclined tubular photobioreactors by installation of internal

static mixers," *Applied microbiology and biotechnology*, vol. 58, no. 5, pp. 600–607, 2002. Quoted on page 2.

[42] M. Regner, K. Ostergren, and C. Tragardh, "Effects of geometry and flow rate on sec ry flow and the mixing process in static mixers : a numerical study," *Chemical Engineering Science*, vol. 61, no. 18, pp. 6133–6141, 2006. Quoted at pages 2 and 16.

[43] V. Engel, J. Stichlmeir, and W. Geipel, "Fluid dynamics of packings for gas-liquid contactors," *Chemical Engineering & Technology - CHEM ENG TECHNOL*, vol. 24, pp. 459–462, 2001. Quoted on page 3.

[44] G. Wild, S. Poncin, H. Li, and E. Olmos, "Some aspects of the hydrodynamics of bubble columns," *International Journal of Chemical Reactor Engineering - INT J CHEM REACT ENG*, vol. 1, pp. 1–36, 2003. Quoted on page 3.

[45] S. J. Luo, W. Fei, X. Y. Song, and H. Li, "Effect of channel opening angle on the performance of structured packings," *Chemical Engineering Journal*, vol. 144, pp. 227–234, 2008. Quoted on page 3.

[46] E. Delnoij, J. Kuipers, W. van Swaaij, and J. Westerweel, "Measurement of gas–liquid two-phase flow in bubble columns using ensemble correlation piv," *Chemical Engineering Science*, vol. 55, no. 17, pp. 3385–3395, 2000. Quoted on page 3.

[47] T. Boëdec and S. Simoëns, "Instantaneous and simultaneous planar velocity field measurements of two phases for turbulent mixing of high pressure sprays," *Experiments in Fluids*, vol. 31, no. 5, pp. 506–518, Nov 2001. [Online]. Available : https://doi.org/10.1007/s003480100311 Quoted on page 3.

[48] C. Boyer, A.-M. Duquenne, and G. Wild, "Measuring techniques in gas–liquid and gas–liquid–solid reactors," *Chemical Engineering Science*, vol. 57, no. 16, pp. 3185–3215, 2002. Quoted on page 3.

[49] J. Aubin, N. Sauze, J. Bertrand, D. Fletcher, and C. Xuereb, "Piv measurements of flow in an aerated tank stirred by a down- and an up-pumpxxing axial flow impeller," *Experimental Thermal and Fluid Science*, vol. 28, 04 2004. Quoted at pages 3, 47, 49, and 65.

[50] A. Zaruba, E. Krepper, H.-M. Prasser, and B. N. Reddy Vanga, "Experimental study on bubble motion in a rectangular bubble column using high-speed video observations," *Flow Measurement and Instrumentation*, vol. 16, no. 5, 2005. Quoted at pages 3 and 46.

[51] J. Aubin, M. Ferrando, and V. Jiricny, "Current methods for characterising mixing and flow in microchannels," *Chemical Engineering Science*, vol. 65, no. 6, pp. 2065 – 2093, 2010. [Online]. Available : http://www.sciencedirect.com/science/article/pii/S0009250909008458 Quoted on page 3.

[52] P. Sobieszuk, J. Aubin, and R. Pohorecki, "Hydrodynamics and mass transfer in gas-liquid flows in microreactors," *Chemical Engineering & Technology*, vol. 35, no. 8, pp. 1346–1358, 2012. Quoted on page 3.

[53] M. Sathe, J. Joshi, and G. Evans, "Characterization of turbulence in rectangular bubble column," *Chemical Engineering Science*, vol. 100, pp. 52–68, 2013. Quoted at pages 3 and 46.

[54] A. A. Ayati, J. Kolaas, A. Jensen, and G. W. Johnson, "Combined simultaneous two-phase piv and interface elevation measurements in stratified gas/liquid pipe flow," *International Journal of Multiphase Flow*, vol. 74, pp. 45–58, 2015. Quoted on page 3.

[55] D. Green, *Perry's Chemical Engineers' Handbook*, 01 2007. Quoted at pages 6 and 7.

[56] D. Gerlach, N. Alleborn, V. Buwa, and F. Durst, "Numerical simulation of periodic bubble formation at a submerged orifice with constant gas flow rate," *Chemical Engineering Science*, vol. 62, no. 7, pp. 2109–2125, 2007. Quoted on page 8.

[57] R. B Bird, W. E Stewart, and E. Lightfoot, *Transport Phenomena*, 01 2002. Quoted on page 9.

[58] C. Marculescu, B. Tincu, A. Avram, T. Burinaru, and M. Avram, "Computational prediction of capillary number impact on droplets formation in microchannels," *Energy Procedia*, vol. 85, pp. 339–349, 2016. Quoted at pages 10 and 11.

[59] Y. T. Shah, S. P. Kelkar, B. G. Godbole, and W. D. Deckwer, "Design parameters estimations for bubble column reactors," *AlChE journal*, vol. 28, pp. 353–379, 05 1982. Quoted on page 12.

[60] N. Kantarci, F. Borak, and K. Ulgen, "Bubble column reactors," *Process Biochemistry*, vol. 40, pp. 2263–2283, 08 2005. Quoted at pages 12 and 13.

[61] L. T. Fan, H. H. Hsu, and K. B. Wang, "Mass transfer coefficient and pressure drop data of two-phase oxygen-water flow in buble column packed with static mixers," *Journal of Chemical and Engineering Data - J CHEM ENG DATA*, vol. 20, pp. 26–28, 01 1975. Quoted on page 12.

[62] B. Bhatia, K. Nigam, D. Auban, and G. Hébrard, "Effect of a new high porosity packing on hydrodynamics and mass transfer in bubble columns," *Chemical Engineering and Processing : Process Intensification*, vol. 43, pp. 1371–1380, 11 2004. Quoted on page 12.

[63] K. Onda, H. Takeuchi, and O. Y., "Mass transfer coefficients between gas and liquid phases in packed columns," *Journal of Chemical Engineering of Japan*, pp. 56 – 62, 1968. Quoted on page 12.

[64] S. Goto and J. M. Smith, "Trickle-bed reactor performance. part i. holdup and mass transfer effects," *AIChE Journal*, vol. 21, pp. 706 – 713, 07 1975. Quoted on page 12.

[65] J. Charpentier, "Recent progress in two phase gas—liquid mass transfer in packed beds," *The Chemical Engineering Journal*, vol. 11, no. 3, pp. 161 – 181, 1976. Quoted on page 12.

[66] K. Wang and L. Fan, "Mass transfer in bubble columns packed with motionless mixers," *Chemical Engineering Science*, vol. 33, no. 7, pp. 945 – 952, 1978. Quoted on page 12.

[67] C. L. Hyndman, F. Larachi, and C. Guy, "Understanding gas-phase hydrodynamics in bubble columns : a convective model based on kinetic theory," *Chemical Engineering Science*, vol. 52, no. 1, pp. 63 – 77, 1997. [Online]. Available : http://www.sciencedirect.com/science/article/pii/S0009250996003879 Quoted on page 13.

[68] B. Thorat and J. Joshi, "Regime transition in bubble columns : Experimental and predictions," *Experimental Thermal and Fluid Science*, vol. 28, pp. 423–430, 04 2004. Quoted on page 13.

[69] T. Abadie, J. Aubin, D. Legendre, and C. Xuereb, "Hydrodynamics of gas-liquid taylor flow in rectangular microchannels," *Microfluidics and Nanofluidics*, vol. 12, 01 2011. Quoted on page 13.

[70] X. Luo, D. J. Lee, R. B. F. Lau, G. Yang, and L.-S. Fan, "Maximum stable bubble size and gas holdup in high-pressure slurry bubble columns," *Fluid Mechanics and Transport Phenomenon*, vol. 45, pp. 665 – 680, 1999. Quoted on page 13.

[71] H. Hikita, S. Asai, K. Tanigawa, K. Segawa, and M. Kitao, "Gas hold-up in bubble columns," *The Chemical Engineering Journal*, vol. 20, no. 1, pp. 59 – 67, 1980. Quoted on page 14.

[72] A. Ghanem, T. Lemenand, D. Della Valle, and H. Peerhossaini, "Static mixers : Mechanisms, applications, and characterization methods – a review," *Chemical Engineering Research and Design*, vol. 92, no. 2, pp. 205–228, 2014. Quoted on page 15.

[73] T. Park, Y. Sung, T. Kim, I. Lee, G. Choi, and D. Kim, "Effect of static mixer geometry on flow mixing and pressure drop in marine scr applications," *International Journal of Naval Architecture and Ocean Engineering*, vol. 6, no. 1, pp. 27–38, 2014. Quoted on page 16.

[74] V. Stamilla, "Gas-liquid dispersion by static mixers in the laminar regime : Application to the smx static mixer," Solaize-France et École Polytechnique de Turin, 2016. Quoted on page 16.

[75] G. I. Taylor, "The formation of emulsions in definable fields of flow," *Proc. Roy. Soc.*, vol. 29, 1934. Quoted on page 18.

[76] J. M. Rallison, "The deformation of small viscous drops and bubbles in shear flows," *Ann. Rev. Fluid Mech.*, vol. 16, pp. 45–66, 1984. Quoted on page 20.

[77] I. Manas-Zloczowe, "Studies of mixing efficiency in batch and continuous mixers," *Rubber Chemistry and Technology*, vol. 67, pp. pp. 504–528, 1994. Quoted on page 20.

[78] D. H. Sharp, "An overview of rayleigh-taylor instability," *Physica D : Nonlinear Phenomena*, vol. 12, pp. pp. 3–18, 1984. Quoted on page 20.

[79] J. C. Beale and R. Reitz, "Modeling spray atomization with the kelvin-helmholtz/rayleigh-taylor hybrid model," *Atomization and Sprays*, vol. 9, pp. 623–650, 11 1999. Quoted on page 20.

[80] M. Mutsakis, G. Schneider, and F. A. Streiff, "Advances in static mixing technology," *Chemical Engineering Progress*, vol. 82, pp. 42–48, 1986. Quoted on page 22.

[81] W. D. Mohr, R. L. Saxton, and C. H. Jepson, "Mixing in laminar-flow systems," *Ind. Eng. Chem.*, vol. 49, no. 11, pp. 1855–1856, 1957. Quoted on page 23.

[82] M. F. Edwards, N. Harnby, and Nienow A. W., *Mixing in the process Industries : Laminar flow and distributive mixing (Chapter 11)*, 2nd ed., Oxford, 1992. Quoted on page 24.

[83] L. Filippa, A. Trento, and A. M. Álvarez, "Sauter mean diameter determination for the fine fraction of suspended sediments using a lisst-25x diffractometer," *Measurement*, vol. 45, no. 3, pp. 364–368, 2012. Quoted on page 26.

[84] J. G. Daly, S. A. Patel, and D. B. Bukur, "Measurement of gas holdups and sauter mean bubble diameters in bubble column reactors by dynamics gas disengagement method," *Chemical Engineering Science*, vol. 47, no. 13, pp. 3647–3654, 1992. Quoted on page 26.

[85] R. Schäfer, C. Merten, and G. Eigenberger, "Bubble size distributions in a bubble column reactor under industrial conditions," *Experimental Thermal and Fluid Science*, vol. 26, no. 6, pp. 595–604, 2002. Quoted on page 26.

[86] M. Bouaifi, G. Hebrard, D. Bastoul, and M. Roustan, "A comparative study of gas hold-up, bubble size, interfacial area and mass transfer coefficients in stirred gas–liquid reactors and bubble columns," *Chemical Engineering and Processing : Process Intensification*, vol. 40, no. 2, pp. 97–111, 2001. Quoted at pages 26 and 77.

[87] G. M. Evans, G. J. Jameson, and B. W. Atkinson, "Prediction of the bubble size generated by a plunging liquid jet bubble column," *Chemical Engineering Science*, vol. 47, no. 13, pp. 3265–3272, 1992. Quoted on page 26.

[88] S. Middleman, "Drop size distributions produced by turbulent pipe flow of immiscible fluids through a static mixer," *Industrial Engineering Chemistry Process Design and Development*, vol. 13, no. 1, pp. 78–83, 1974. Quoted on page 27.

[89] A. Pacek and A. Nienow, *Measurement of drop size distribution in concentrated liquid-liquid dispersions : Video and capillary techniques*, 1995, vol. 73. Quoted on page 30.

[90] J. M. Zalc, E. S. Szalai, F. J. Muzzio, and S. Jaffer, "Characterization of flow and mixing in an smx static mixer," *AIChE Journal*, vol. 48, no. 3, pp. 427–436, 2002. Quoted at pages 31, 32, and 45.

[91] S. M. Hosseini, K. Razzaghi, and F. Shahraki, "Design and characterization of a low-pressure-drop static mixer," *AIChE Journal*, vol. 65, 12 2018. Quoted on page 31.

[92] H.-S. Song and S. Phil Han, "A general correlation for pressure drop in a kenics static mixer," *Chemical Engineering Science*, vol. 60, pp. 5696–5704, 11 2005. Quoted on page 31.

[93] V. Kumar, V. Shirke, and K. Nigam, "Performance of kenics static mixer over a wide range of reynolds number," *Chemical Engineering Journal - CHEM ENG J*, vol. 139, pp. 284–295, 06 2008. Quoted at pages 31, 42, and 43.

[94] P. Moracancias, H. Khaled, G. Carnelle, and J. Legrand, "Friction factor in static mixer and determination of geometric parameters of smx sulzer mixers," *Chemical Enginnering Communications*, vol. 171, pp. 77–93, 02 1999. Quoted on page 31.

[95] M. K. Singh, P. D. Anderson, and H. E. H. Meijer, "Understanding and optimizing the smx static mixer," *Macromolecular rapid communications*, vol. 30, no. 4-5, pp. 362–376, 2009. Quoted at pages 31 and 54.

[96] N. Shah and D. Kale, "Pressure drop for laminar flow of non-newtonian fluids in static mixers," *Chemical Engineering Science*, vol. 46, no. 8, pp. 2159 – 2161, 1991. Quoted on page 32.

[97] F. Streiff, S. Jaffer, and G. Schneider, "The design and application of static mixer technology," *Society of Chemical Engineers*, no. 1, pp. 107 – 114, 1999. Quoted on page 32.

[98] C. M. R. Madhuranthakam, Q. Pan, and G. L. Rempel, "Residence time distribution and liquid holdup in kenics kmx static mixer with hydrogenated nitrile butadiene rubber solution and hydrogen gas system," *Chemical Engineering Science*, vol. 64, no. 14, pp. 3320–3328, 2009. Quoted on page 37.

[99] B. Gourich, C. Vial, N. El Azher, M. Belhaj Soulami, and M. Ziyad, *Biochemical Engineering Journal*, vol. 39, no. 1, pp. 1–14, 2008. Quoted on page 37.

[100] A. Lakota, M. Jazbec, and J. Levec, "Impact of structured packing on bubble column mass transfer characteristics. part 2. analysis of gas-liquid mass transfer measurements," *Acta Chim. Slov.*, vol. 49, pp. 587–604, 2002. Quoted on page 38.

[101] A. Martin, S. Camy, and J. Aubin, "Hydrodynamics of co 2 -ethanol flow in a microchannel under elevated pressure," *Chemical Engineering Science*, vol. 178, 12 2017. Quoted on page 46.

[102] M. J. W. Harleman, R. Delfos, Terwisga, T J C van, and J. Westerweel, "Dispersion of bubbles in fully developed channel flow," *Journal of Physics : Conference Series*, vol. 318, no. 5, p. 052007, 2011. Quoted on page 46.

[103] S. Li, Y. Ma, S. Jiang, T. Fu, C. Zhu, and H. Z. Li, "The drag coefficient and the shape for a single bubble rising in non-newtonian fluids," *Journal of Fluids Engineering*, vol. 134, 2012. Quoted on page 46.

[104] A. M. Leitch and W. D. Baines, "Liquid volume flux in a weak bubble plume," *Journal of Fluid Mechanics*, vol. 205, no. -1, p. 77, 1989. Quoted on page 46.

[105] V. Strubel, S. Simoëns, P. Vergne, N. Fillot, F. Ville, M. El Hajem, N. Devaux, A. Mondelin, and Y. Maheo, "Fluorescence tracking and µ-piv of individual particles and lubricant flow in and around lubricated point contacts," *Tribology Letters*, vol. 65, no. 3, p. 75, May 2017. [Online]. Available : https://doi.org/10.1007/s11249-017-0859-z Quoted at pages 46, 47, and 69.

[106] C. Senatore, M. Wulfmeier, I. Vlahinc, J. Andrade, and K. Iagnemma, "Design and implementation of a particle image velocimetry method for analysis of running gear–soil interaction," *Journal of Terramechanics*, vol. 50, no. 5-6, pp. 311–326, 2013. Quoted on page 47.

[107] R. Lindken and W. Merzkirch, "A novel piv technique for measurements in multiphase flows and its application to two-phase bubbly flows," *Experiments in Fluids*, vol. 33, no. 6, pp. 814–825, 2002. Quoted on page 49.

[108] L. Gui, J. Longo, and F. Stern, "Towing tank piv measurement system, data and uncertainty assessment for dtmb model 5512," *Experiments in Fluids*, vol. 31, no. 3, pp. 336–346, 2001. Quoted on page 49.

[109] B. B. Amira, D. Zied, and M. Salah Abid, "Piv study of the turbulent flow in a stirred vessel equipped by an eight concave blades turbine," *Fluid Mechanics*, vol. 1, no. 2, pp. pp. 5–10, 2015. Quoted on page 49.

[110] J. Chen, A. Kemoun, M. H. Al-Dahhan, M. P. Duduković, D. J. Lee, and L.-S. Fan, "Comparative hydrodynamics study in a bubble column using computer-automated radioactive particle tracking (carpt)/computed tomography (ct) and particle image velocimetry (piv)," *Chemical Engineering Science*, vol. 54, no. 13-14, pp. 2199–2207, 1999. Quoted on page 49.

[111] S. Liu, A. N. Hrymak, and P. E. Wood, "Design modifications to smx static mixer for improving mixing," *AIChE Journal*, vol. 52, no. 1, pp. 150–157, 2006. Quoted on page 54.

[112] G. S. Settles and E. Covert, *Schlieren and Shadowgraph Techniques : Visualizing Phenomena in Transport Media*, 01 2002, vol. 55. Quoted on page 59.

[113] A. Buffo and V. Alopaeus, "Experimental determination of size distributions : Analyzing proper sample sizes," *Measurement Science and Technology*, vol. 27, no. 4, p. 045301, 2016. Quoted on page 61.

[114] H. Wadell, "Volume, shape, and roundness of quartz particles," *The Journal of Geology*, vol. 43, no. 3, pp. 250–280, 1935. Quoted on page 62.

[115] T. Brox, A. Bruhn, N. Papenberg, and J. Weickert, "High accuracy optical flow estimation based on a theory for warping," *Proceedings of the European Conference on Computer Vision (ECCV)*, vol. 3024, 2004. Quoted on page 63.

[116] J. Link, C. Zeilstra, N. Deen, and H. Kuipers, "Validation of a discrete particle model in a 2d spout fluid bed using non intrusive optical measuring techniques," *The Canadian Journal of Chemical Engineering*, vol. 82, 2008. Quoted on page 65.

[117] D. Funfschilling and H. Z. Li, "Flow of non-newtonian fluids around bubbles : Piv measurements and birefringence visualisation," *Chemical Engineering Science*, vol. 56, no. 3, pp. 1137–1141, 2001. Quoted at pages 65, 66, and 96.

[118] M. Raffel, C. Willert, and J. Kompenhans, *Particle Image Velocimetry : A Practical Guide*, 1998. Quoted on page 66.

[119] G. Stokes, "On the effect of internal friction of fluids on the motion of pendulums," *Trans Camb Philos Soc*, vol. 9, 1850. Quoted on page 70.

[120] S. P. Godbole, A. Schumpe, Y. T. , and N. L. Carr, "Hydrodynamics and mass transfer in nonnewtonian solutions in a bubble column," *AlChe Journal*, vol. 30, pp. 213–220, 03 1984. Quoted on page 74.

[121] J. Dudley, "Mass transfer in bubble columns : A comparison of correlations," *Water Research*, vol. 29, pp. 1129–1138, 1995. Quoted on page 74.

[122] H. Chaumat, A. M. Billet, F. Augier, C. Mathieu, and H. Delmas, "Mass transfer in bubble column for industrial conditions effects of organic medium, gas and liquid flow rates and column design," *Chemical Engineering Science*, vol. 60, p. 5930–5936, 11 2005. Quoted on page 74.

[123] H. Dhaouadi, S. Poncin, J. Hornut, and N. Midoux, "Gas–liquid mass transfer in bubble column reactor : Analytical solution and experimental confirmation," *Chemical Engineering and Processing : Process Intensification*, vol. 47, pp. 548–556, 04 2008. Quoted on page 74.

[124] D. Pinelli, L. Z., and F. Magelli, "Analysis of kla measurement methods in stirred vessels : The role of experimental techniques and fluid dynamic models," *International Journal of Chemical Reactor Engineering*, vol. 8, 2010. Quoted at pages 74, 75, and 76.

[125] P. Kovats, D. Thevenin, and K. Zahringer, "Characterizing fluid dynamics in a bubble column aimed for the determination of reactive mass transfer," *Heat and Mass Transfer*, 09 2017. Quoted on page 74.

[126] A. L. Marquez, G. Wild, and N. Midoux, "A review of recent chemical techniques for the determination of the volumetric mass-transfer coefficient kla in gas—liquid reactors," *Chemical Engineering and Processing : Process Intensification*, vol. 33, pp. 247–260, 1994. Quoted on page 76.

[127] G. Grund, A. Schumpe, and W.-D. Deckwer, "Gas-liquid mass transfer in a bubble column with organic liquids," *Chemical Engineering Science*, vol. 47, no. 13, pp. 3509–3516, 1992. Quoted on page 77.

[128] P. Lage and R. O. Espósito, "Experimental determination of bubble size distributions in bubble columns : prediction of mean bubble diameter and gas hold up," *Powder Technology*, vol. 101, pp. 142–150, 1999. Quoted on page 77.

[129] N. A. Kazakis, A. A. Mouza, and S. V. Paras, "Experimental study of bubble formation at metal porous spargers : Effect of liquid properties and sparger characteristics on the initial bubble size distribution," *Chemical Engineering Journal*, vol. 137, no. 2, pp. 265–281, 2008. Quoted on page 77.

[130] P. G. Saffman, "On the rise of small air bubbles in water," *Journal of Fluid Mechanics*, vol. 1, no. 3, pp. 249–275, 1956. Quoted at pages 85 and 86.

[131] G. Mougin and J. Magnaudet, "Path instability of a rising bubble," *Physical Review Letters*, vol. 88, no. 1, p. 014502, 2001. Quoted on page 85.

[132] M. K. Tripathi, K. C. Sahu, and R. Govindarajan, "Dynamics of an initially spherical bubble rising in quiescent liquid," *Nature communications*, vol. 6, p. 6268, 2015. Quoted on page 85.

[133] T. Z. Harmathy, "Velocity of large drops and bubbles in media of infinite or restricted extent," *AIChE Journal*, vol. 6, no. 2, pp. 281–288, 1960. Quoted on page 85.

[134] H. D. Mendelson, "The prediction of bubble terminal velocities from wave theory," *AIChE Journal*, vol. 13, 1967. Quoted on page 85.

[135] G. B. Wallis, "The terminal speed of single drops or bubbles in an infinite medium," *International Journal of Multiphase Flow*, vol. 1, no. 4, pp. 491–511, 1974. Quoted on page 85.

[136] A. Tomiyama, I. Kataoka, I. Zun, and T. Sakaguchi, "Drag coefficients of single bubbles under normal and micro gravity conditions," *JSME International Journal Series B*, vol. 41, 1998. Quoted on page 85.

[137] J. Raymond and J.-M. Rosant, "A numerical and experimental study of the terminal velocity and shape of bubbles in viscous liquids," *Chemical Engineering Science*, vol. 55, no. 5, pp. 943–955, 2000. Quoted on page 85.

[138] A. Tomiyama, "Single bubbles in stagnant liquids and in linear shear flows," *Workshop on Measurement Technology (MTWS5)*, 2002. Quoted on page 85.

[139] A. Tomiyama, G. P. Celata, S. Hosokawa, and S. Yoshida, "Terminal velocity of single bubbles in surface tension force dominant regime," *International Journal of Multiphase Flow*, vol. 28, no. 9, pp. 1497–1519, 2002. Quoted on page 85.

[140] R. Clift, J. R. Grace, and M. E. Weber, *Bubbles, drop and particles*. New York : Academic Press, 1978. Quoted on page 86.

[141] K. Lunde and R. J. Perkins, "Shape oscillations of rising bubbles," in *In Fascination of Fluid Dynamics : A Symposium in Honour of Leen van Wijngaarden*, A. Biesheuvel and G. F. van Heijst, Eds. Springer Netherlands, 1998, pp. 387–408. Quoted on page 86.

[142] *OpenFOAM Wiki : This Wiki collects information about the OpenSource CFD toolbox OpenFOAM and provides a platform for collaborations*, Unofficial OpenFOAM wiki. [Online]. Available : https://openfoamwiki.net Quoted at pages 105, 106, and 115.

[143] D. Marchisio and R. Fox, *Computational Models for Polydisperse Particulate and Multiphase Systems*, 03 2013. Quoted on page 107.

[144] D. Pfleger, S. Gomes, N. Gilbert, and H.-G. Wagner, "Hydrodynamic simulations of laboratory scale bubble columns fundamental studies of the eulerian–eulerian modelling approach," *Chemical Engineering Science*, vol. 54, no. 21, pp. 5091 – 5099, 1999. Quoted on page 107.

[145] Z. Jaworski and P. Pianko-Oprych, "Two-phase laminar flow simulations in a kenics static mixer : Standard eulerian and lagrangian approaches," *Chemical Engineering Research and Design*, vol. 80, no. 8, pp. 910 – 916, 2002, fluid Mixing VII. [Online]. Available : http://www.sciencedirect.com/science/article/pii/S0263876202722703 Quoted on page 107.

[146] F. Kerdouss, A. Bannari, and P. Proulx, "Cfd modeling of gas dispersion and bubble size in a double turbine stirred tank," *Chemical Engineering Science*, vol. 61, no. 10, pp. 3313 – 3322, 2006. [Online]. Available : http://www.sciencedirect.com/science/article/pii/S000925090500922X Quoted on page 107.

[147] J. Ding, X. Wang, X.-F. Zhou, N.-Q. Ren, and W.-Q. Guo, "Cfd optimization of continuous stirred-tank (cstr) reactor for biohydrogen production," *Bioresource Technology*, vol. 101, no. 18, pp. 7005 – 7013, 2010. Quoted on page 107.

[148] L. Gemello, V. Cappello, F. Augier, D. Marchisio, and C. Plais, "Cfd-based scale-up of hydrodynamics and mixing in bubble columns," *Chemical Engineering Research and Design*, vol. 136, 06 2018. Quoted on page 107.

[149] M. Shiea, A. Buffo, E. Baglietto, D. Lucas, M. Vanni, and D. Marchisio, "Evaluation of hydrodynamic closures for bubbly regime cfd simulations in developing pipe flow," *Chemical Engineering Technology*, 04 2019. Quoted on page 107.

[150] T. Wang and J. Wang, "Numerical simulations of gas–liquid mass transfer in bubble columns with a cfd–pbm coupled model," *Chemical Engineering Science*, vol. 62, no. 24, pp. 7107 – 7118, 2007, 8th International Conference on Gas-Liquid and Gas-Liquid-Solid Reactor Engineering. [Online]. Available : http://www.sciencedirect.com/science/article/pii/S0009250907006616 Quoted on page 107.

[151] M. Bhole, J. Joshi, and D. Ramkrishna, "Cfd simulation of bubble columns incorporating population balance modeling," *Chemical Engineering Science*, vol. 63, no. 8, pp. 2267 – 2282, 2008. [Online]. Available : http://www.sciencedirect.com/science/article/pii/S0009250908000298 Quoted on page 107.

[152] M. Petitti, A. Nasuti, D. Marchisio, M. Vanni, G. Baldi, N. Mancini, and F. Podenzani, "Bubble size distribution modeling in stirred gas-liquid reactors with qmom augmented by a new correction algorithm," *AIChE Journal*, vol. 56, pp. 36 – 53, 01 2009. Quoted on page 107.

[153] D. Li, A. Buffo, W. Podgórska, Z. Gao, and D. Marchisio, "Droplet breakage and coalescence in liquid-liquid dispersions : Comparison of different kernels with eqmom and qmom," *AIChE Journal*, vol. 63, 10 2016. Quoted on page 107.

[154] A. Buffo, M. Vanni, and D. Marchisio, "Simulation of a reacting gas–liquid bubbly flow with cfd and pbm : Validation with experiments," *Applied Mathematical Modelling*, vol. 44, 12 2016. Quoted on page 107.

[155] D. Li, A. Buffo, W. Podgórska, D. Marchisio, and Z. Gao, "Investigation of droplet breakup in liquid-liquid dispersions by cfd - pbm simulations : The influence of the surfactant type," *Chinese Journal of Chemical Engineering*, 05 2017. Quoted on page 107.

[156] M. Basavarajappa and S. Miskovic, "Investigation of gas dispersion characteristics in stirred tank and flotation cell using a corrected cfd-pbm quadrature-based moment method approach," *Minerals Engineering*, vol. 95, pp. 161 – 184, 2016. [Online]. Available : http://www.sciencedirect.com/science/article/pii/S0892687516301789 Quoted on page 107.

[157] V. Buwa, D. Deo, and V. Ranade, "Eulerian–lagrangian simulations of unsteady gas–liquid flows in bubble columns," *International Journal of Multiphase Flow*, vol. 32, pp. 864–885, 07 2006. Quoted on page 107.

[158] T. Shao, Y. Hu, W. Wang, Y. Jin, and Y. Cheng, "Simulation of solid suspension in a stirred tank using cfd-dem coupled approach," *Chinese Journal of Chemical Engineering*, vol. 21, no. 10, pp. 1069 – 1081, 2013. Quoted on page 107.

[159] D. Kafui, S. Johnson, C. Thornton, and J. Seville, "Parallelization of a lagrangian–eulerian dem/cfd code for application to fluidized beds," *Powder Technology*, vol. 207, no. 1, pp. 270 – 278, 2011. [Online]. Available : http://www.sciencedirect.com/science/article/pii/S0032591010005887 Quoted on page 107.

[160] G. Boccardo, F. Augier, Y. Haroun, D. Ferre, and D. Marchisio, "Validation of a novel open-source work-flow for the simulation of packed-bed reactors," *Chemical Engineering Journal*, vol. 279, 05 2015. Quoted on page 107.

[161] L. Pezo, M. Pezo, A. Jovanovic, N. Kosanić, A. Petrovic, and L. Levic, "Granular flow in static mixers by coupled dem/cfd approach," *Hemijska industrija*, vol. 70, pp. 60–60, 01 2015. Quoted on page 107.

[162] V. Bhusare, M. Dhiman, D. Kalaga, S. Roy, and J. Joshi, "Cfd simulations of a bubble column with and without internals by using openfoam," *Chemical Engineering Journal*, vol. 317, 02 2017. Quoted on page 107.

[163] C. Hirt and B. Nichols, "Volume of fluid (VOF) method for the dynamics of free boundaries," *J. Comp. Phys.*, vol. 39, no. 1, pp. 201 – 225, 1981. Quoted on page 107.

[164] A. Bourlioux, "A coupled level-set volume-of-fluid algorithm for tracking material interfaces," *International symposium on Computational Fluid Dynamics*, vol. 4, no. 1, pp. 15 – 22, 1995. Quoted at pages 107 and 108.

[165] H. G. Weller, "A new approach to vof-based interface capturing methods for incompressible and compressible flow," *OpenCFD Ltd., Report TR/HGW/04*, 2008. Quoted at pages 107 and 110.

[166] G.-H. Cottet and E. Maitre, "A semi-implicit level set method for multiphase flows and fluid–structure interaction problems," *Journal of Computational Physics*, vol. 314, pp. 80 – 92, 2016. [Online]. Available : http://www.sciencedirect.com/science/article/pii/S0021999116001546 Quoted at pages 107 and 108.

[167] S. Osher and J. A. Sethian, "Fronts propagating with curvature-dependent speed : Algorithms based on Hamilton-Jacobi formulations," *J. Comp. Phys.*, vol. 79, no. 1, pp. 12 – 49, 1988. Quoted at pages 107 and 108.

[168] B. A. Nichita, I. Zun, and J. R. Thome, "A level set method coupled with a volume of fluid method for modeling of gas-liquid interface in bubbly flow," *Journal of Fluids Engineering*, vol. 132, no. 8, 08 2010. [Online]. Available : https://doi.org/10.1115/1.4002166 Quoted at pages 107 and 108.

[169] H. Takahira, T. Horiuchi, and S. Banerjee, "An improved three-dimensional level set method for gas-liquid two-phase flows," *Journal of Fluids Engineering*, vol. 126, no. 4, pp. 578–585, 09 2004. [Online]. Available : https://doi.org/10.1115/1.1777232 Quoted on page 108.

[170] I. Chakraborty, G. Biswas, and P. Ghoshdastidar, "A coupled level-set and volume-of-fluid method for the buoyant rise of gas bubbles in liquids," *International Journal of Heat and Mass Transfer*, vol. 58, no. 1, pp. 240 – 259, 2013. [Online]. Available : http://www.sciencedirect.com/science/article/pii/S0017931012008824 Quoted on page 108.

[171] M. Sussman and E. G. Puckett, "A coupled level set and volume-of-fluid method for computing 3d and axisymmetric incompressible two-phase flows," *Journal of Computational Physics*, vol. 162, no. 2, pp. 301 – 337, 2000. [Online]. Available : http://www.sciencedirect.com/science/article/pii/S0021999100965379 Quoted on page 108.

[172] G. Son and N. Hur, "A coupled level set and volume-of-fluid method for the buoyancy-driven motion of fluid particles," *Numerical Heat Transfer, Part B : Fundamentals*, vol. 42, no. 6, pp. 523–542, 2002. Quoted on page 108.

[173] J. Brackbill, D. Kothe, and C. Zemach, "A continuum method for modeling surface tension," *Journal of Computational Physics*, vol. 100, no. 2, pp. 335–354, 1992. Quoted at pages 108, 115, 116, and 117.

[174] C. Hirt and B. Nichols, "Volume of fluid (VOF) method for the dynamics of free boundaries," *Journal of Computational Physics*, vol. 39, no. 1, pp. 201–225, 1981. Quoted on page 109.

[175] S. Afkhami and Y. Renardy, "A volume-of-fluid formulation for the study of co-flowing fluids governed by the hele-shaw equations," *Physics of Fluids*, vol. 25, no. 8, p. 082001, 2013. Quoted on page 110.

[176] M. Wörner, "Numerical modeling of multiphase flows in microfluidics and micro process engineering : a review of methods and applications," *Microfluidics and Nanofluidics*, vol. 12, no. 6, pp. 841–886, 2012. Quoted on page 110.

[177] D. Suraj, A. Lakshman, and T. Mario, "Evaluating the performance of the two-phase flow solver interfoam," *Comp. Sc. & Discovery*, vol. 5, no. 1, p. 014016, 2012. [Online]. Available : http://stacks.iop.org/1749-4699/5/i=1/a=014016 Quoted at pages 110 and 115.

[178] H. Marschall, K. Hinterberger, C. Schüler, F. Habla, and O. Hinrichsen, "Numerical simulation of species transfer across fluid interfaces in free-surface flows using openfoam," *Ch. Eng. Sc.*, vol. 78, pp. 111 – 127, 2012. Quoted on page 111.

[179] A. Q. Raeini, M. J. Blunt, and B. Bijeljic, "Modelling two-phase flow in porous media at the pore scale using the volume-of-fluid method," *J. Comp. Phys.*, vol. 231, no. 17, pp. 5653 – 5668, 2012. Quoted on page 111.

[180] D. A. Hoang, V. van Steijn, L. M. Portela, M. T. Kreutzer, and C. R. Kleijn, "Benchmark numerical simulations of segmented two-phase flows in microchannels using the volume of fluid method," *Computers & Fluids*, vol. 86, pp. 28 – 36, 2013. Quoted on page 111.

[181] C. Bilger, M. Aboukhedr, K. Vogiatzaki, and R. Cant, "Evaluation of two-phase flow solvers using level set and volume of fluid methods," *J. Comp. Phys.*, vol. 345, pp. 665 – 686, 2017. Quoted on page 111.

[182] J. Roenby, B. E. Larsen, H. Bredmose, and H. Jasak, "A new Volume-of-Fluid method in OpenFOAM," in *VII International Conference on Computational Methods in Marine Engineering, MARINE 2017*, 2017. Quoted on page 111.

[183] J. Roenby, H. Bredmose, and H. Jasak, "Isoadvector : Geometric vof on general meshes," 2018. Quoted on page 111.

[184] W. F. Noh and P. Woodward, "Slic : Simple line interface calculation," in *Proceedings of the Fifth International Conference on Numerical Methods in Fluid Dynamics June 28 – July 2, 1976 Twente University, Enschede*, A. I. van de Vooren and P. J. Zandbergen, Eds. Berlin, Heidelberg : Springer Berlin Heidelberg, 1976, pp. 330–340. Quoted on page 111.

[185] R. Debar, "Fundamentals of the kraken code," California Univ., Livermore (USA). Lawrence Livermore Lab., Tech. Rep., 1974. Quoted on page 111.

[186] F. Xiao, Y. Honma, and T. Kono, "A simple algebraic interface capturing scheme using hyperbolic tangent function," *International Journal for Numerical Methods in Fluids*, vol. 48, no. 9, pp. 1023–1040, 2005. Quoted on page 111.

[187] K. Yokoi, "Efficient implementation of THINC scheme : A simple and practical smoothed VOF algorithm," *Journal of Computational Physics*, vol. 226, no. 2, pp. 1985–2002, 2007. Quoted on page 111.

[188] J. E. Pilliod, "An analysis of piecewise linear interface reconstruction algorithms for volume-of-fluid methods," *Master's thesis, Univ of California, Davis*, 1992. Quoted on page 111.

[189] J. E. Pilliod and E. G. Puckett, "Second-order accurate volume-of-fluid algorithms for tracking material interfaces," *Journal of Computational Physics*, vol. 199, no. 2, pp. 465–502, 2004. Quoted on page 111.

[190] S. J. Cummins, M. M. Francois, and D. B. Kothe, "Estimating curvature from volume fractions," *Computers Structures*, vol. 83, no. 6, pp. 425 – 434, 2005, frontier of Multi-Phase Flow Analysis and Fluid-Structure. [Online]. Available : http://www.sciencedirect.com/science/article/pii/S0045794904004110 Quoted on page 114.

[191] D. Sun and W. Tao, "A coupled volume-of-fluid and level set (voset) method for computing incompressible two-phase flows," *International Journal of Heat and Mass Transfer*, vol. 53, no. 4, pp. 645 – 655, 2010. [Online]. Available : http://www.sciencedirect.com/science/article/pii/S0017931009005717 Quoted on page 114.

[192] R. F. Engberg and E. Y. Kenig, "Numerical simulation of rising droplets in liquid–liquid systems : A comparison of continuous and sharp interfacial force models," *International Journal of Heat and Fluid Flow*, vol. 50, pp. 16–26, 2014. Quoted on page 115.

[193] C. Wang and A. K. Mitra, "Estimates of surface normal and curvature, reconstruction of continuum surface force model, and elimination of spurious currents," *International Journal for Numerical Methods in Fluids*, vol. 75, 06 2014. Quoted on page 115.

[194] B. Lafaurie, C. Nardone, R. Scardovelli, S. Zaleski, and G. Zanetti, "Modelling merging and fragmentation in multiphase flows with surfer," *Journal of Computational Physics*, vol. 113, no. 1, pp. 134–147, 1994. Quoted on page 115.

[195] X.-D. Liu, R. P. Fedkiw, and M. Kang, "A boundary condition capturing method for poisson's equation on irregular domains," *Journal of Computational Physics*, vol. 160, no. 1, pp. 151 – 178, 2000. Quoted on page 115.

[196] M. Kang, R. P. Fedkiw, and X.-D. Liu, "A boundary condition capturing method for multiphase incompressible flow," *Journal of Scientific Computing*, vol. 15, no. 3, pp. 323–360, Sep 2000. Quoted on page 115.

[197] L. Chen, J. Zang, A. Hillis, G. Morgan, and A. Plummer, "Numerical investigation of wave–structure interaction using openfoam," *Ocean Engineering*, vol. 88, pp. 91 – 109, 2014. [Online]. Available : http://www.sciencedirect.com/science/article/pii/S0029801814002169 Quoted on page 116.

[198] P. Schmitt and B. Elsaesser, "On the use of openfoam to model oscillating wave surge converters," *Ocean Engineering*, vol. 108, pp. 98 – 104, 2015. [Online]. Available : http://www.sciencedirect.com/science/article/pii/S0029801815003686 Quoted on page 116.

[199] Z. Z. Hu, D. Greaves, and A. Raby, "Numerical wave tank study of extreme waves and wave-structure interaction using openfoam," *Ocean Engineering*, vol. 126, pp. 329 – 342, 2016. [Online]. Available : http://www.sciencedirect.com/science/article/pii/S0029801816303936 Quoted on page 116.

[200] B. Lalanne, L. R. Villegas, S. Tanguy, and F. Risso, "On the computation of viscous terms for incompressible two-phase flows with level set/ghost fluid method," *Journal of Computational Physics*, vol. 301, pp. 289 – 307, 2015. [Online]. Available : http://www.sciencedirect.com/science/article/pii/S002199911500563X Quoted at pages 116 and 117.

[201] H. Deconinck and E. Dick, *Computational fluid dynamics 2006. Proceedings of the fourth international conference on computational fluid dynamics*, 01 2006. Quoted on page 116.

[202] F. Denner and B. G. van Wachem, "Numerical time-step restrictions as a result of capillary waves," *Journal of Computational Physics*, vol. 285, pp. 24 – 40, 2015. [Online]. Available : http://www.sciencedirect.com/science/article/pii/S002199911500025X Quoted at pages 116 and 117.

[203] C. Galusinski and P. Vigneaux, "On stability condition for bifluid flows with surface tension : Application to microfluidics," *Journal of Computational Physics*, vol. 227, no. 12, pp. 6140–6164, 2008. Quoted on page 117.

[204] L. Gamet, M. Scala, J. Roenby, H. Scheufler, and J.-L. Pierson, "On 2d validation of volume-of-fluid openfoam isoadvector solvers using single bubble benchmark," *submitted to Computers and Fluids*, 2019. Quoted on page 121.

[205] S. Hysing, S. Turek, D. Kuzmin, N. Parolini, E. Burman, S. Ganesan, and L. Tobiska, "Quantitative benchmark computations of two-dimensional bubble dynamics," *I.J.N.M.F.*, vol. 60, no. 11, pp. 1259–1288, 2009. [Online]. Available : http://www.featflow.de/en/benchmarks/cfdbenchmarking/bubble.html Quoted at pages 121, 122, 123, 126, and 138.

[206] J. Adelsberger, P. Esser, M. Griebel, S. Groß, M. Klitz, and A. Rüttgers, "3D incompressible two-phase flow benchmark computations for rising droplets," 2014, proceedings of the 11th World Congress on Computational Mechanics (WCCM XI), Barcelona, Spain, also available as INS Preprint No. 1401 and as IGPM Preprint No. 393. [Online]. Available : http://wissrech.ins.uni-bonn.de/research/projects/risingbubblebenchmark/ Quoted at pages 121, 122, 130, and 138.

[207] W. Dijkhuizen, E. Van den Hengel, N. Deen, M. van Sint Annaland, and J. Kuipers, "Numerical investigation of closures for interface forces acting on single air-bubbles in water using volume of fluid and front tracking models," *Chemical Engineering Science*, vol. 60, no. 22, pp. 6169–6175, 2005. Quoted on page 121.

[208] C. K. Svihla and H. Xu, "Simulation of free surface flows with surface tension with ansys cfx," in *2006 International ANSYS Conference, Pittsburg*, 2006. Quoted on page 121.

[209] J. Hua, J. F. Stene, and P. Lin, "Numerical simulation of 3d bubbles rising in viscous liquids using a front tracking method," *Journal of Computational Physics*, vol. 227, no. 6, pp. 3358 – 3382, 2008. Quoted on page 121.

[210] L. Amaya-Bower and T. Lee, "Single bubble rising dynamics for moderate reynolds number using lattice boltzmann method," *Computers & Fluids*, vol. 39, no. 7, pp. 1191–1207, 2010. Quoted at pages 121 and 132.

[211] B. Andersson, R. Andersson, L. Håkansson, M. Mortensen, R. Sudiyo, and B. Van Wachem, *Computational fluid dynamics for engineers*. Cambridge University Press, 2011. Quoted on page 121.

[212] A. M. Thomas, J. Fang, J. Feng, and I. A. Bolotnov, "Estimation of shear-induced lift force in laminar and turbulent flows," *Nuclear Technology*, vol. 190, no. 3, pp. 274–291, 2015. Quoted on page 121.

[213] H. Badreddine, Y. Sato, B. Niceno, and H.-M. Prasser, "Finite size lagrangian particle tracking approach to simulate dispersed bubbly flows," *Chemical Engineering Science*, vol. 122, pp. 321 – 335, 2015. Quoted on page 121.

[214] S. Popinet and S. Zaleski, "A front-tracking algorithm for accurate representation of surface tension," *International Journal for Numerical Methods in Fluids*, vol. 30, no. 6, pp. 775 – 793, 1999. Quoted on page 133.

[215] M. Herrmann, "A balanced force refined level set grid method for two-phase flows on unstructured flow solver grids," *Journal of Computational Physics*, vol. 227, no. 4, pp. 2674 – 2706, 2008. Quoted on page 133.

[216] A. Albadawi, D. Donoghue, A. Robinson, D. Murray, and Y. Delauré, "Influence of surface tension implementation in volume of fluid and coupled volume of fluid with level set methods for bubble growth and detachment," *International Journal of Multiphase Flow*, vol. 53, pp. 11 – 28, 2013. Quoted on page 133.

[217] T. Abadie, J. Aubin, and D. Legendre, "On the combined effects of surface tension force calculation and interface advection on spurious currents within volume of fluid and level set frameworks," *Journal of Computational Physics*, vol. 297, 05 2015. Quoted on page 133.

[218] Y. Li, J. Zhang, and L.-S. Fan, "Numerical simulation of gas–liquid–solid fluidization systems using a combined cfd-vof-dpm method : bubble wake behavior," *Chemical Engineering Science*, vol. 54, no. 21, pp. 5101 – 5107, 1999. [Online]. Available : http://www.sciencedirect.com/science/article/pii/S0009250999002638 Quoted on page 149.

[219] S.-S. Jeon, S.-J. Kim, and G.-C. Park, "Cfd simulation of condensing vapor bubble using vof model," *World Acad. Sci.*, vol. 60, 12 2009. Quoted on page 149.

[220] Y. Alhendal and A. Turan, "Volume-of-fluid (vof) simulations of marangoni bubbles motion in zero gravity," 03 2012. Quoted on page 149.

[221] V. Ranade, M. Perrard, N. L. Sauze, C. Xuereb, and J. Bertrand, "Trailing vortices of rushton turbine : Piv measurements and cfd simulations with snapshot approach," *Chemical Engineering Research and Design*, vol. 79, no. 1, pp. 3 – 12, 2001. [Online]. Available : http://www.sciencedirect.com/science/article/pii/S0263876201720114 Quoted on page 154.

[222] A. Khopkar, J. Aubin, C. Xuereb, N. Sauze, J. Bertrand, and V. Ranade, "Gas-liquid flow generated by a pitched-blade turbine : Particle image velocimetry measurements and computational fluid dynamics simulations," *Industrial Engineering Chemistry Research*, vol. 42, 09 2003. Quoted on page 154.

[223] A. Khopkar, J. Aubin, C. Rubio-Atoche, C. Xuereb, N. Sauze, J. Bertrand, and V. Ranade, "Flow generated by radial flow impellers : Piv measurements and cfd simulations," *Int. J. Chem. React. Eng.*, vol. 2, 01 2004. Quoted on page 154.

[224] G. Silva, N. Leal, and V. Semiao, "Micro-piv and cfd characterization of flows in a microchannel : Velocity profiles, surface roughness and poiseuille numbers," *International Journal of Heat and Fluid Flow*, vol. 29, no. 4, pp. 1211 – 1220, 2008. Quoted on page 154.

[225] J. Feng, F. K. Benra, and H. J. Dohmen, "Unsteady flow visualization at part-load conditions of a radial diffuser pump : by piv and cfd," *Journal of Visualization*, vol. 12, no. 1, pp. 65–72, 03 2009. Quoted on page 154.

[226] F. Mendoza, A. L. Banales, E. Cid, C. Xuereb, M. Poux, D. Fletcher, and J. Aubin, "Hydrodynamics in a stirred tank in the transitional flow regime," *Chemical Engineering Research and Design*, vol. 132, pp. 865 – 880, 2018. [Online]. Available : http://www.sciencedirect.com/science/article/pii/S0263876217306755 Quoted on page 154.